Sterile neutrino search with KATRIN – modeling and design-criteria of a novel detector system

Zur Erlangung des akademischen Grades eines
DOKTORS DER NATURWISSENSCHAFTEN (Dr. rer. nat.)

von der KIT-Fakultät für Physik des
Karlsruher Instituts für Technologie (KIT)
angenommene

DISSERTATION
von

M. Sc., Korzeczek, Marc

Eidesstattliche Versicherung gemäß § 13 Absatz 2 Ziffer 3 der Promotionsordnung des Karlsruher Instituts für Technologie (KIT) für die KIT-Fakultät für Physik:

1. Bei der eingereichten Dissertation zu dem Thema
   Sterile neutrino search with KATRIN – modeling and design-criteria of a novel detector system
   handelt es sich um meine eigenständig erbrachte Leistung.

2. Ich habe nur die angegebenen Quellen und Hilfsmittel benutzt und mich keiner unzulässigen Hilfe Dritter bedient. Insbesondere habe ich wörtlich oder sinngemäß aus anderen Werken übernommene Inhalte als solche kenntlich gemacht.

3. Die Arbeit oder Teile davon habe ich bislang nicht an einer Hochschule des In- oder Auslands als Bestandteil einer Prüfungs- oder Qualifikationsleistung vorgelegt.

4. Die Richtigkeit der vorstehenden Erklärungen bestätige ich.

5. Die Bedeutung der eidesstattlichen Versicherung und die strafrechtlichen Folgen einer unrichtigen oder unvollständigen eidesstattlichen Versicherung sind mir bekannt.

Ich versichere an Eides statt, dass ich nach bestem Wissen die reine Wahrheit erklärt und nichts verschwiegen habe.

_____   _____
Ort und Datum   Unterschrift

Acknowledgments

I sincerely thank

- the KSETA graduation school for supporting my doctorate as well as for organizing and enabling various seminars and activities - it is a wonderful research environment. Special thanks for facilitating my parental leave.

- my mentor and first reviewer *Guido Drexlin* for his guidance in physics as well as his subtle influence that shaped the friendly working atmosphere at KATRIN. Thank you for introducing astroparticle physics as well as the KATRIN experiment to me and for giving me the opportunities to travel abroad.

- my second reviewer *Marc Weber* for his continued curiosity in my research topic. Thank you also for your electronics teaching course at university - a great combination of theoretical knowledge and hands-on experience.

- *Susanne Mertens* and *Thierry Lasserre*. Both of you have been my mentors during my master thesis and I feel privileged to know you two. Special thanks to you Susanne for your encouragements and for the inspiring physics discussions.

- *Thomas Thümmler* for his repeated personal and scientific inputs. Special thanks for sharing your experiences with me.

- *Joachim Wolf* for the baptism in experimental physics. Without you I would have missed out on the physical, experimental side of physics.

- my colleagues *Anton Huber*, *Martin Descher* and *Leonard Köllenberger*. Both for friendship and for the fun time together.

- all physicist, technicians and staff who not only supported me directly but also indirectly, enabling the day-by-day operation of KATRIN and the KIT as a whole.

Abstract

A fundamental phenomenon in particle physics is the absence of massive objects in our universe: Dark Matter. A promising candidate that could explain these observations are sterile neutrinos with a mass of several keV/c^2. While it is presumed that sterile neutrinos do not interact via the weak force, they, due to their mass, still partake in neutrino oscillation.

Consequently, it is experimentally possible to investigate their imprint in beta-decay experiments, such as the Karlsruhe tritium neutrino experiment (KATRIN). A dedicated search for sterile neutrinos however ensues a steep increase in the electron rate and thus requires the development of a new detector system, the TRISTAN detector. In addition, as the imprint of sterile neutrinos is presumably $< 10^{-7}$, systematic uncertainties have to be understood and modeled with high precision.

In this thesis systematics prevalent at the detector and spectrometer section of KATRIN will be discussed and their impact to a sterile neutrino sensitivity illuminated. The derived model is compared with data of the current KATRIN detector and with characterization measurements of the first TRISTAN prototype detectors, seven pixel silicon drift detectors. It is shown that the final TRISTAN detector requires a sophisticated redesign of the KATRIN detector section. Moreover, the combined impact of the back-scattering and electron charge-sharing systematic lead to an optimal detector magnetic field of $B_{\mathrm{det}} = 0.7 \dots 0.8\,\mathrm{T}$, which translates to a pixel radius of $r_{\mathrm{px}} = 1.5 \dots 1.6\,\mathrm{mm}$ (s. sc. 7.2).

The sensitivity analysis discusses individual effects as well as the combined impact of systematic uncertainties. It is demonstrated that the individual effects can be largely mitigated by shifting the tritium beta-decay energy spectrum above the beta-decay endpoint. In contrast, their combined impact to the sensitivity leads to an overall degradation and only mixing amplitudes of $\sin^2\theta < 3 \cdot 10^{-6}$ would be reachable, even in an optimized case with very low and homogeneous detection deadlayer $z_{\mathrm{dl}} = 20 \pm 1\,\mathrm{nm}$ (s. sc. 7.1). Assessing sterile neutrino mixing amplitudes of $\sin^2\theta < 10^{-7}$ thus requires disentangling of systematic effects. In a future measurement this could be for example achieved by vetoing detector events with large signal rise-times and small inter-event times (s. sc. 8.1).

Contents

Chapter 1

Introduction

While first ideas on the nature of matter, consisting of elementary particles, date back several millennia [Ter03], it was not before the 19th century that scientists were able to test these experimentally [Zub11]. In the 20th century, accelerated by the success of high-energy experiments, a consistent model of elementary particles was formed: the Standard Model of Particle Physics (SM) [Eck19]. It contains both, fundamental matter particles (fermions) and interaction particles (bosons). With the discovery of the Higgs boson in 2012 [Aad12; Cha12] all elementary particles contained in the SM were discovered. This should, in principle, mark the completeness of the SM. Interestingly, a stark contradiction to that resides in the fermion sector: a particle known from radioactive decay, the neutrino. Whilst the SM assumes neutrinos to be massless, experiments in the 1980s proved otherwise [Mik86]. Observations of solar, atmospheric as well as reactor and accelerator neutrinos contributed to a model of neutrino oscillation, wherein the existence of masses is a mandatory prerequisite.

To this day the absolute neutrino mass has yet to be determined. With KATRIN, a tritium beta-decay based experiment situated in Karlsruhe (Germany), particle masses down to 200 meV (90% CL) will be tested [Ang05]. Similar to the predecessor experiments at Mainz and Troitsk, but improving the sensitivity by a factor of 10, a non-observation of a finite neutrino mass would yield a new experimental upper limit.

Another remarkable feature of neutrinos is related to their spin-momentum property: the particle handedness or chirality in the massless limit. Typically, one would assume all interactions to be independent of chirality. An investigation of ^{60}Co beta-decay in the 1950s [Wu57], albeit, has lead to the concept of "parity violation" and to the understanding that neutrinos with right-handed chirality do not seem to exist.

A new paradigm would be the existence of sterile neutrinos [Sha13; Adh16], hypothetical particles introduced as counterparts to standard neutrinos. They are assumed to be right-handed in nature and non-interacting with standard matter – literally "sterile". If, however, sterile neutrinos take part in neutrino oscillations, one might find their imprint in beta-decay-like experiments.

KATRIN, with its high statistics tritium beta-decay source, is ideally matched for investi-

gating sterile neutrinos in the keV mass range. Contrary to the nominal operation mode, focusing on the region close to the endpoint, sterile neutrinos require the examination of the full beta-decay spectrum. Most notable, this entails a redesign of the detector and data acquisition system, referred to as TRISTAN project. In the envisioned silicon detector upgrade the number of pixels increases to roughly 3500, reaching statistical sterile neutrino sensitivities down to $\sin^2 \theta = 10^{-7}$ [Mer19].

Major design criteria for TRISTAN stem from the mode of operation: measuring the energy of tritium beta-decay electrons. Roughly, it encompasses charge deposition [Ren11; Kor16], charge collection [Alt19; Urb19], as well as DAQ [Dol16; Des19]. An electron impinging on the detector creates measurable electron-hole-pairs, i.e. charges, along its scattering path inside the detector. These are then drifted to electrodes on the sides and the measured electric current allows for an estimation of the incident electrons kinetic energy.

In the first chapters of this thesis, the current status of neutrino physics (s. ch. 2), the KATRIN experiment (s. ch. 3) and the future detector upgrade TRISTAN for subsequent sterile neutrino investigation (s. ch. 4) are introduced.

Chapter 5 is centered around simulation and modeling systematic effects prevalent at the detector section of KATRIN. The model comprises individual electron trajectory simulations as well as analytic back-scattering and -reflection, charge sharing, electronic noise and pile-up. At first the systematics are characterized (s. sc. 5.2) and then their influence to the observed electron energy response is discussed (s. sc. 5.3).

In chapter 6 measurements with the seven-pixel TRISTAN prototype detector are presented. Both spectra from x-rays and electrons are shown and compared with the model.

The impact of detector systematics to the design of the TRISTAN upgrade is illuminated in chapter 7. It is based on first principles from the electromagnetic field settings at KATRIN as well as an in-depth sensitivity study (s. sc. 7.1).

The last chapter 8 addresses the influence of detector-related systematics to the sterile neutrino search with first KATRIN data.

Chapter 2

Neutrino Physics

Following a historical timeline, in this chapter the postulation and the experimental discovery of neutrinos is discussed. Afterwards, a central concept of neutrino physics, the phenomenon of flavor oscillation, is explained [Fuk03; Zub11; Obe19]. Lastly, the current Standard Model of particle physics (SM) [Tan18; Eck19] and how it could be extended in the neutrino sector is outlined [Dre13; Adh16; Boy19].

2.1   History

The history of neutrinos is strongly tied to advances in particle and quantum physics of the late 18th and early 19th century.

The dawn of modern particle physics began with the discovery of electrons in 1897. Independently, E. Wiechert [Wie97] and J. J. Thomson [Tho97] investigated the emission of cathode rays. By subjecting the cathode ray to varying electric potentials and magnetic fields they proved its negative charge and measured its mass. The particle character of electrons was deduced from the fact that their measurements were independent of the cathode material.

In 1911 the subatomic particle nature of atoms was established by E. Rutherford [Rut11]. He observed the scattering profile of alpha particles off a gold foil. To allow scattering angles up to 190° an atom must contain a heavy and positively charged nucleus. Two years later, together with N. Bohr, an atomic model was introduced [Boh13]. Therein atoms should consist of heavy, positively charged nuclei that are orbited by much lighter, negatively charged electrons.

Steering away from a pure particle nature, the 1920s lead to the discovery of quantum physics. Experiments, such as the Stern-Gerlach experiment [Ger22] were the incentive to describe the quantum nature of particles. Notably, L. de Broglie [Bro26] described the particle-wave dualism, W. Heisenberg [Hei25] formulated a mathematical model, and E. Schrödinger [Sch26] adapted the theory to construct the quantum model for the hydrogen atom.

Only thereafter neutrinos were first proposed, marking the start of neutrino physics.

Figure 2.1: Differential electron energy spectrum from beta-decay. The maximum rate and energy are normalized to one. In the early 19th century a discrete, mono-energetic energy distribution was expected (red). On the contrary, experiments measured continuous beta-decay spectra (black), which lead to the discovery of neutrinos.
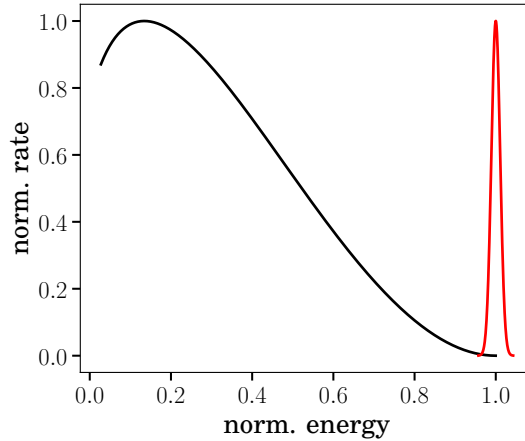
Postulation and discovery

In 1930 W. Pauli [Pau30] tried to explain long-standing discrepancies in beta-decay experiments [Cha14]. In a letter to the Technical University of Zurich, he hypothesized the existence of ghost-like particles, which he addressed as "neutron" - later renamed to neutrino. Pauli suggested a decaying atom would emit, in addition to the known electron, a light unobserved particle. The decay energy would be shared among the two, which would conform with the observed continuous energy spectra of electrons (s. fig. 2.1).

J. Chadwick in 1932 then discovered the "real" neutron [Cha32]. He found neutrons to be charge-less and slightly heavier than protons. Moreover he deduced that an atomic nucleus is made up of both protons and neutrons. Two years later, E. Fermi formulated a quantum theory of beta-decay [Fer34]. Therein the beta-decay of an atom is driven by the decay of a single nucleon:

$$n \rightarrow p + e^- + \overline{\nu}_e \,, \tag{2.1}$$
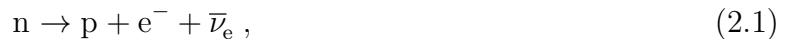
where a neutron n decays into a proton p, an electron e^- and a neutrino ν - here more specifically labeled as electron antineutrino $\overline{\nu}_e$.

Roughly 22 years after their postulation, indirect evidence for neutrinos was found in electron capture reactions on argon atoms: $^{37}\text{Ar} + e- \rightarrow^{37} \text{Cl} + \nu_e$ [Rod52]. With a time-of-flight measurement G. Rodeback and J. Allen measured the recoil energy E_{Cl} of the produced chlorine atoms. The observed discrete recoil energy $E_{\text{Cl}} = 9.67\,\text{eV}$ matched well the hypothesis of a two-particle process.

The direct discovery of neutrinos happened in 1956 in an experiment by F. Reines and C. Cowan [Cow56]. Situated next to a nuclear reactor, providing an abundance of antineutrinos $\overline{\nu}_e$, their goal was to search for the products of inverse beta-decay

$$\overline{\nu}_e + p \rightarrow n + e^+ \,. \tag{2.2}$$

In their detector, both the neutron n and the positron e^+ were causing characteristic gamma rays. Positrons promptly produce gamma rays upon annihilation with electrons,

whereas the gamma signal from neutrons is delayed as their capture on cadmium atoms happens only after several scatterings in the detector bulk. Analyzing delayed time coincidences between two events allowed for background discrimination and enabled the discovery.

Theory of weak interaction

During the 1950s the concept of neutrinos further evolved. Of central importance was the formulation of an underlying theory of weak interactions. Urged by puzzling observations of kaon decay, the so-called $\tau - \theta$ puzzle [Da54], the physicists T. Lee and C. Yang [Lee56] started to question if parity is conserved in weak interactions.

In a cryogenic experiment headed by C.-S. Wu in 1957, the decay properties of polarized ^{60}Co atoms was investigated [Wu57]. Applying an external magnetic field and other means to orient the spin direction of ^{60}Co atoms, Madame Wu could show that the decay preferably leads to the emission electrons in the direction opposite to the nuclear spin.

A similar result was reported by R. Garwin, L. Lederman and M. Weinrich within the same month [Gar57], through the investigation of the decay of π-mesons.

One year later, the Goldhaber experiment measured the helicity of neutrinos [Gol58]. In particular the electron capture of ^{152}Eu was investigated. The direction of the emitted photons of the daughter atom ^{152}Sm led to the conclusion that neutrinos display a negative helicity $\mathcal{H} = -1$.

In 1958, incorporating the distinct neutrino helicity in Fermi's theory of interaction, the V-A theory (vector minus axial vector) was introduced. It was first presented by E. Sudershan and R. Marshak [Sud94], and later by R. Feynman and M. Gell-Mann [Fey58]. S. Glashow [Gla59], A. Salam [Sal59] and S. Weinberg [Wei67] further advanced the theory by formulating a model of unified electroweak interaction in the mid-1960s. A major prediction of their theory was the existence of massive gauge bosons W$^{\pm}$ and Z, responsible for mediating weak interaction between particles that carry weak charge.

At CERN several experiments set out to investigate these bosons. In 1973 first evidence of a Z boson mediated neutral current reaction was presented by the Gargamelle bubble chamber experiment [Has73]. Ten years later, at the SPS proton-antiproton collider, all three "electroweak" massive bosons were directly discovered by the UA1 and UA2 experiments [Arn83; Bag83; Ban83]. At the electron-positron collider LEP, the number of neutrino flavors N_ν was experimentally determined in 1989 by the ALEPH [Dec89], DELPHI, L3 and OPAL collaborations. They investigated the decay width of the Z boson and reported a value $N_\nu = 2.984 \pm 0.0082$ in a joint analysis [Ale05].

Neutrino flavors and oscillation

The first ideas on neutrino flavor oscillation date back to 1956, when B. Pontecorvo hypothesized that a muonium, i.e. a bound state of an antimuon μ^+ and an electron e$^-$, might transform, with respect to neutrinos and the weak interaction, to its antiparticle (μ^- & e$^+$) [Pon57]. Over the following years, with notable contributions of Z. Maki, M.

Nakagawa and S. Sakata [Mak62], the conceptual framework of neutrino flavor oscillation was shaped.

Until 1962 it was questioned whether neutrinos from beta-decay (ν_e) and pion decay (ν_μ) are one and the same particle. J. Steinberger, M. Schwartz and L. Lederman could first proof the inequality of the two particles [Dan62]. Using spark chambers, they investigated the tracks of electrons and muons, originating from pion and kaon decays. The mesons were created by focusing a 15 GeV proton beam, from the Brookhaven AGS, on a beryllium target.

The last neutrino flavor was measured only in 2001 by the DONUT experiment [Kod01]. Using the ring accelerator Tevatron at Fermilab, they investigated neutrino-induced tracks of charged particles in an emulsion-based detector.

On the non-accelerator side in 1968, the Homestake experiment of R. Davis was prone to a first effect from neutrino oscillation [Dav68]. The experiment counted the number of ^{37}Ar atoms that formed due to incident solar neutrinos. Comparing the experimental rate to prevalent flux estimations from J. Bahcall a deficit of roughly two third was observed. This finding is often called the solar neutrino deficit and was theoretically explained 20 years later by the MSW-effect (S. Mikheyev, A. Smirnov and L. Wolfenstein). It describes matter-induced neutrino oscillation [Wol78], that is resonantly enhanced in the solar matter [Mik86].

Another major event, marking the dawn of astroparticle physics occurred on February 24th 1987. Several solar neutrino experiments, most prominently the water Cerenkov detector Kamiokande [Hir87], measured a sharp excess in neutrinos, from the core-collapse super-nova SN1987A. Interestingly, this event played a vital role in understanding the impact of neutrinos during the collapse of late-phase stellar objects.

While the absolute mass scale of neutrinos is yet to be measured, neutrino oscillation experiments determined the mass splittings and mixing angles. Notable are:

- the Super Kamiokande experiment in Japan, which investigated oscillations of atmospheric neutrinos $\nu_\mu \to x$ in 1998 [Fuk98].

- the MINOS [Mic06] and K2K [Ahn06], later followed by Opera [Aga10] and T2K [Abe14], experiments. They investigated high-energy neutrino beams in the ν_μ-disappearance and ν_e-appearance channels.

- the Double Chooz [Abe12], Daya Bay [An12] and Reno [Ahn12] experiments. Within a few months they published their findings on reactor neutrino oscillations $\overline{\nu}_e \to x$ in 2012.

2.2   Standard Model

The Standard Model of particle physics (SM) describes the baryonic matter of our universe by elementary particles, referred to as fermions. Similarly, forces between them are conveyed

Figure 2.2: Illustration of elementary particles in the SM, with matter particles (fermions) and interaction particles (bosons). The SM assumes neutrinos to be massless and right-handed neutrinos to be non existent (adapted from [Sha13]).

by another set of elementary particles, the bosons. Altogether they are discriminated by their rest mass, electric charge and spin (s. fig. 2.2).

The SM counts twelve fermions subdivided in three mass generations, each containing a doublet of quarks and leptons. Higher mass generations can decay into the corresponding lighter sets, thus leaving us with (u, d) & (ν_e, e) as the prevalent matter constituents in the universe. In addition a fermion f with the same mass but opposite electric charge is called anti-fermion $\bar{f}$ and lastly fermions are also distinguished by their helicity, being either left- or right-handed.

Neutrons and protons correspond to (valence) quark triplets, e.g. the proton has two up quarks and one down quark. While bound states of triplets are called baryons, there exist also mesons: bound doublets of a quark and an antiquark $(q, \bar{q})$, a prominent meson being the pion $\pi^+ = (u, \bar{d})$.

The SM includes three fundamental forces of nature, conveyed by its interaction particle and charge: the strong force by gluons g which couple to color charge (red, blue, green), the weak force by W- and Z-bosons coupling to the weak charge, and lastly, electromagnetism by photons that couple to electric charge.

The weak force plays a special role, as it only couples to neutrinos with left-handed helicity, denoted by blanks in figure 2.2. In the SM right-handed neutrinos are assumed to be non-existent and neutrino masses collectively set to zero.

Symmetries in the Lagrangian

The SM is a quantum field theory, where elementary particles are represented by fields and observable quantities determined by applying non-commutable operators (e.g. momentum operator P) to the fermion fields ψ. Based on the principle of least action, the fields and their derivatives make up the Lagrangian density $\mathcal{L}$.

A special property in the Lagrange formalism is derived from Noether's theorem [Noe18]. E. Noether showed that conservation laws in physics (e.g. conservation of energy) are directly connected to transformations of the Lagrangian density that leave it invariant. Or, differently phrased, conservation laws are connected to symmetries in the Lagrange

density.

Global symmetries for the whole SM Lagrangian are described by the Poincaré group. It includes translations, rotations as well as boosts. It ensues energy, momentum and angular-momentum conservation. In contrast, local transformations of the Lagrangian are called gauge symmetries. Each interaction in the SM follows the global as well as an individual local symmetry.

The strong interaction is represented by an SU(3) gauge symmetry and color charge conservation. Electromagnetism and the weak interaction are jointly described by the SU(2)xU(1) symmetry. W-, Z- bosons and photons convey the interaction, with the conserved quantities weak isospin and hypercharge.

Notably, the current set of Lagrangians in addition follow a global U(1) symmetry, with baryon and lepton number as conserved quantities. This signifies, that at each point in time an interaction must not change the number of leptons or quarks.

Investigations on new physics often imply the search of new symmetries and Lagrangian terms. Interestingly, the SU(3)xSU(2)xU(1) symmetry in its most general form slightly differs from SM Lagrangian. Concerning neutrinos, additional terms include a Dirac and Majorana mass.

Beyond SM

Almost all observed phenomena in nature can be explained as excitations of quantum fields. The recent discoveries of the top quark, the tau neutrino and the Higgs boson further set the SM on an exalted experimental ground. In spite of that, the SM fails to encompass a quantum theory of gravity. Instead, general relativity is treated as a classical background. In addition, the SM is not able to explain several observational facts [Dre13]:

- **Dark Matter**: Starting with F. Zwicky in 1933 [Zwi33], astrophysical observations have established that the contribution of baryonic matter only corresponds to roughly 16% of all gravitating masses in the universe [Agh18]. The missing 84% is referred to as Dark Matter (DM). Currently, DM is assumed to consist of unknown elementary particles (e.g. WIMPs, axions or sterile neutrinos).

- **Dark Energy** (DE) is behind the accelerated expansion of the universe. While a constant expansion rate was measured in 1929 by E. Hubble [Hub29], its accelerated behavior was only discovered in the 1990s (e.g. [Paa92]). Similar to DM, DE contributes to the measurable energy-mass content of the universe. Both are described in the Lambda Cold Dark Matter (Λ-CDM) model of cosmology [Agh18].

- **Matter-antimatter asymmetry** describes the question, why our universe is devoid of antimatter. According to the Big Bang theory from Lemaitre in 1927 [Lem27], matter and antimatter should be produced equally. Criteria for generating these asymmetries were postulated by A. Sakharov in 1967 [Sak67].
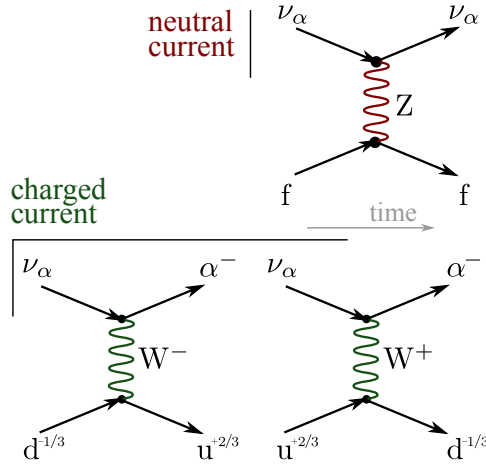
Figure 2.3: Exemplary Feynman diagrams of the weak interaction. The neutral current reaction via Z boson exchange, similar to scattering, leaves the particles unchanged. Charged currents via W^+/W^- bosons and transform quarks and leptons into their weak iso-doublet partners.

- **Neutrino flavor violation**: solar neutrino observations first uncovered the theory of flavor oscillation (s. sc. 2.1). It requires non-zero masses and allows flavor changes.

2.3 Flavor and mass

Neutrinos are extremely light neutral particles, that only interact via weak interactions (s. fig. 2.3). In the late 20th century, experiments making use of the flavors (ν_e, ν_μ, ν_τ) measured an oscillatory flavor change pattern.

Neutrino oscillation

The framework of neutrino mixing, based on the works B. Pontecorvo, Z. Maki, M. Nakagawa and S. Sakata (s. sc. 2.1), depicts neutrinos occurring in flavor eigenstates, taking part in the weak interaction, as well as mass eigenstates, describing their propagation through space. The two triplets are connected - in honor of above scientists - by the U_{PMNS} matrix:

$$\nu_\alpha = \sum_{i=1}^{3} U_{\alpha i} \cdot \nu_i \text{ or } \begin{pmatrix} \nu_e \\ \nu_\mu \\ \nu_\tau \end{pmatrix} = \begin{pmatrix} U_{e1} & U_{e2} & U_{e3} \\ U_{\mu 1} & U_{\mu 2} & U_{\mu 3} \\ U_{\tau 1} & U_{\tau 2} & U_{\tau 3} \end{pmatrix} \begin{pmatrix} \nu_1 \\ \nu_2 \\ \nu_3 \end{pmatrix}, \tag{2.3}$$

where ν_α ($\alpha = e, \mu, \tau$) denotes the three neutrino flavor eigenstates and ν_i ($l = 1, 2, 3$) the mass eigenstates. Thus, each flavor is formed by a specific superposition of the mass states.

Flavor change probabilities $P_{\alpha\beta}$ of an α flavored neutrino can be calculated using propagation of mass eigenstates $|\nu_\alpha(t)\rangle$ and subsequent projection onto the new flavor state $\langle \nu_\beta |$.

Figure 2.4: Neutrino oscillation probabilities $P_{\alpha\beta}$ along the ratio L/E, distance over neutrino energy. In blue the probability P_{ee} of the ν_e flavor survival for the three neutrino flavor model is depicted. Correspondingly, in black the simplified probability $P_{ee}^{e\mu}$ in the two neutrino approximation, i.e. only ν_e and ν_μ flavors, is illustrated.
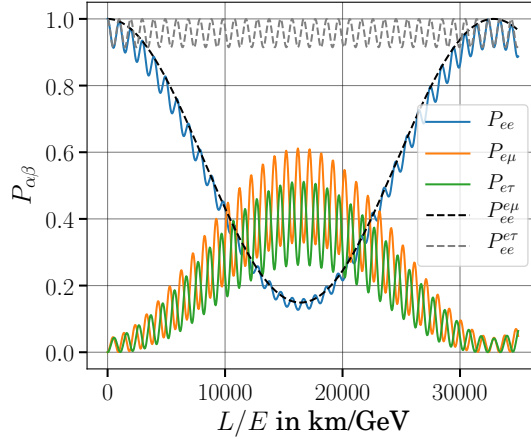
$$P_{\alpha\beta} = \left| \langle \nu_\beta | \nu_\alpha(t) \rangle \right|^2 = \left| \sum_{j=1}^{3} U_{\beta j}^* \langle \nu_j | \sum_{i=1}^{3} U_{\alpha i} | \nu_i(t) \rangle \right|^2$$

$$= \left| \sum_{i,j=1}^{3} U_{\alpha i} e^{-i(m_i^2 L)/(2E)} \langle \nu_j | \nu_i \rangle \right|^2 = \left| \sum_{i=1}^{3} U_{\beta i}^* U_{\alpha i} e^{-i(m_i^2 L)/(2E)} \right|^2 \qquad (2.4)$$

Here E denotes the neutrino energy, L the distance to the source and m_i are the mass eigenvalues. As the mass eigenstates are orthonormal, $\langle \nu_j | \nu_i \rangle$ yields the Kronecker delta δ_{ij}. Moreover the relativistic limit was used. Often flavor oscillations are discussed in a simplified scenario with only two different neutrino flavors ($\tau\kappa$) and mass eigenstates:

$$P_{\alpha\beta}^{\tau\kappa} = \sin^2(2\theta) \sin^2 \left(1.27 \cdot \Delta m_{\alpha\beta}^2 / \text{eV}^2 \frac{L/\text{km}}{E/\text{GeV}} \right) , \qquad (2.5)$$

with the difference of squared masses $\Delta m_{\alpha\beta}^2 = m_\alpha^2 - m_\beta^2$ and mixing angle θ between the flavor eigenstates. In figure 2.4 both the simplified two and standard three neutrino oscillation probabilities are shown. A combined analysis of current experimental parameters can be found in [Est19].

As the sign of Δm_{23}^2 is yet to be determined, two different mass ordering scenarios are distinguished: the normal $\Delta m_{23}^2 > 0$ and the inverted $\Delta m_{23}^2 < 0$ mass hierarchy (s. fig. 2.5).

For the scope of this thesis it is important to note that oscillation experiments are not sensitive to the absolute mass scale of neutrinos.

Neutrino mass

The laboratory based methods to asses the mass scale is separated in single and double beta-decay experiments. It is complemented by cosmological and astrophysical observations. To date these approaches only yield upper limits:
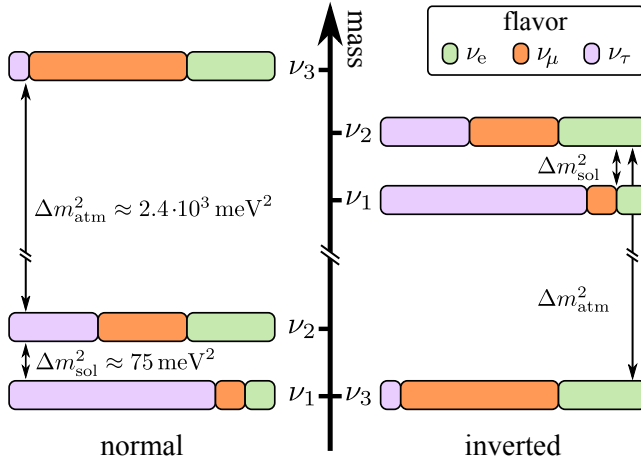
Figure 2.5: Depending on the sign of the squared mass difference Δm_{23}^2 from atmospheric neutrinos, two different scenarios of mass ordering are feasible. In the normal hierarchy scenario the lightest neutrino mass eigenstate is given by ν_1, and in the inverted case by ν_3. Each mass eigenstate is a superposition of different neutrino flavors, illustrated in green (ν_e), orange (ν_μ) and violet (ν_τ) colors.

- *Beta-decay*: The most model independent approach is the investigation of the electron spectrum from single beta-decay $n \rightarrow p + e^- + \overline{\nu}_e$. As mass and energy are related via $E = mc^2$, a massive neutrino would reduce the maximal possible kinetic energy of electrons. The current best upper limit is provided by KATRIN [Ake19b]:

$$m_\beta = \sqrt{\sum_{i=1}^{3} |U_{ei}| m_{\nu i}^2} \leq 1.1 \, \text{eV} \, (95\%\text{CL}). \tag{2.6}$$

- *Neutrinoless double-beta-decay*: In case neutrinos are their own antiparticles, the observation of a zero neutrino double beta-decay ($0\nu\beta\beta$) would point to a special scenario where two "neutrinos" annihilate within the nucleus. A calorimetric measurement of the summed kinetic electron energy from double beta-decay would then consist of two components: a continuous part for the $2\nu\beta\beta$ process and a mono energetic part $0\nu\beta\beta$ at the endpoint. An evaluation from KamLAND-Zen has given the upper limit of [Gan16]

$$m_{0\nu\beta\beta} = \left| \sum_{i=1}^{3} U_{ei}^2 m_i \right| = \sum_{i=1}^{3} \left| |U_{ei}|^2 \cdot e^{i\delta_{Mi}} \right| m_i \leq 0.05\text{-}0.16 \, \text{eV} \, (90\%\text{CL}). \tag{2.7}$$

- *Cosmology*: Based on the Λ-CDM model of cosmology it is possible to extract information of neutrino masses. The Planck satellite experiment results on the CMB together with data from gravitational lensing and baryonic acoustic oscillations gives a combined upper limit of [Agh18]

$$\sum_\nu m_\nu \leq 0.12 \, \text{eV} \, (95\%\text{CL}). \tag{2.8}$$

- *Supernovae*: Lastly, the arrival times from supernovae explosions within our galactic neighborhood allow to infer neutrino masses. In core collapse models of supernovae the bulk of neutrinos are emitted over a short interval of a few seconds only. Knowing the distance to the explosion thus allows to determine the neutrino mass. An analysis on data from the SN1987A event yields an upper limit of [Lor02]

$$m_{\bar{\nu}_e} \leq 5.7 \, \text{eV} \ (95\%\text{CL}). \tag{2.9}$$

A notable investigation that combines the above experimental findings in a joint model obtains a more conservative upper limit of $\sum_\nu m_\nu < 0.26 \, \text{eV} \ 95\% \, \text{CL}$ [Lou19].

2.4 Sterile neutrinos

From a theoretical point of view experimental results on neutrino mass and mixing lead to two prominent questions:

- why are neutrino masses so small (mass puzzle) - more than 10^8 times lighter than an electron - and

- why is flavor mixing so large (flavor puzzle) - U_{pmns} matrix without distinct shape.

While it is in principle possible to add new gauge symmetries to the Lagrange density, more fundamental theories should be able to address the above questions while at same time minimize the introduction of new parameters.

Seesaw mechanism and the νMSM
A well known extension to the Lagrangian to answer the mass puzzle is provided by the seesaw mechanism (type 1), which introduces right-handed sterile neutrinos. Technically, the same singlet terms known from weak interaction but with switched chiralities are added to the Lagrangian.
The Lagrange mass term generated by the Higgs mechanism after electroweak symmetry breaking can then be written in matrix form

$$\frac{1}{2}\begin{pmatrix} \bar{\nu}_L & \bar{\nu}_R^c \end{pmatrix} A \begin{pmatrix} \nu_L^c \\ \nu_R \end{pmatrix} + h.c. = \frac{1}{2}\begin{pmatrix} \bar{\nu}_L & \bar{\nu}_R^c \end{pmatrix} \begin{pmatrix} 0 & m_D \\ m_D & M_M \end{pmatrix} \begin{pmatrix} \nu_L^c \\ \nu_R \end{pmatrix} + h.c. \, , \tag{2.10}$$

with the left-/right-handed neutrino fermion fields $\nu_{L/R}$, the Dirac mass m_D and the Majorana mass M_M. Switching to mass eigenstates diagonalizes A and predicts the mass eigenvalues
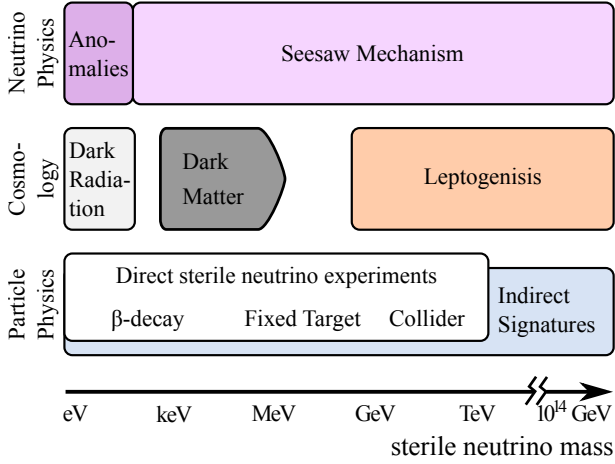
Figure 2.6: Depiction of the right-handed sterile neutrino mass range and corresponding influence to neutrino physics, cosmology as well as particle physics. A sterile neutrino with a mass $m_4 = \mathcal{O}(\text{keV})$ would explain low neutrino masses via the seesaw mechanism and establish a candidate for DM. Experimentally this mass range is accessible in beta-decay (adapted from [Dre19]).

$$\lambda_{\pm} = \frac{m_{\mathrm{D}} \pm \sqrt{m_{\mathrm{D}}^2 + 4M_{\mathrm{M}}^2}}{2} \ . \tag{2.11}$$

Assuming $m_{\mathrm{D}}/M_{\mathrm{M}} \ll 1$ gives the two disproportionate solutions $\lambda_+ \approx M_{\mathrm{M}}$ and $\lambda_- \approx -m_{\mathrm{D}}^2/M_{\mathrm{M}}$. Literally similar to a seesaw, increasing the Majorana mass M_{M} leads to a smaller mass eigenstates λ_-. Thus the smallness of a neutrino mass eigenvalue $m_{\mathrm{L}} = \lambda_-$ could be explained by a right-handed partner with mass eigenvalue $m_{\mathrm{R}} = \lambda_+$.

While this mechanism works down to sterile masses $m_{\mathrm{R}} > \mathcal{O}(keV)$ (s. fig. 2.6), it requires a right-handed partner for each neutrino with non-zero mass. In total, three right-handed neutrino singlets correspond to 18 new parameters: three Majorana masses, three diagonal Yukawa couplings, six mixing angles as well as six CP-violating phases.

A notable theory based on low-scale seesaw mechanism is the neutrino minimal standard model (νMSM) [Asa05a; Asa05b]. By fine tuning the parameters it tries to explain current observational facts and problems within a single framework. In it, the three right-handed neutrinos are responsible for neutrino oscillation. Two of them have degenerate masses below the electroweak scale and produce the baryon asymmetry in the universe. The third neutrino represents warm DM (WDM). Its mass is chosen in the keV/c^2 range, with tiny mixing angles to SM left-handed neutrinos (s. fig. 2.6).

Cosmology

Since the 1930s an ever-increasing suite of astrophysical observations points to the existence of Dark Matter (DM). Its imprint, referred to as missing mass, manifests on all spatial scales in the universe: in rotation curves of spiral galaxies [Cor00]; through the velocity dispersion of stars and galaxies [Fab76]; in galaxy clusters through x-ray mass determination (e.g. bullet cluster [Clo06]) and (weak) gravitational lensing [Tay98]; in the amount of formed galaxies [Kly99]; and, on the cosmic scale, in distinct anisotropies of the cosmic microwave background (CMB) [Hin12].

Over the years baryonic matter (black holes, red stars) was ruled out as a candidate for DM, and similarly modified theories of gravitation [Sko06] fail to fit all data. Currently,
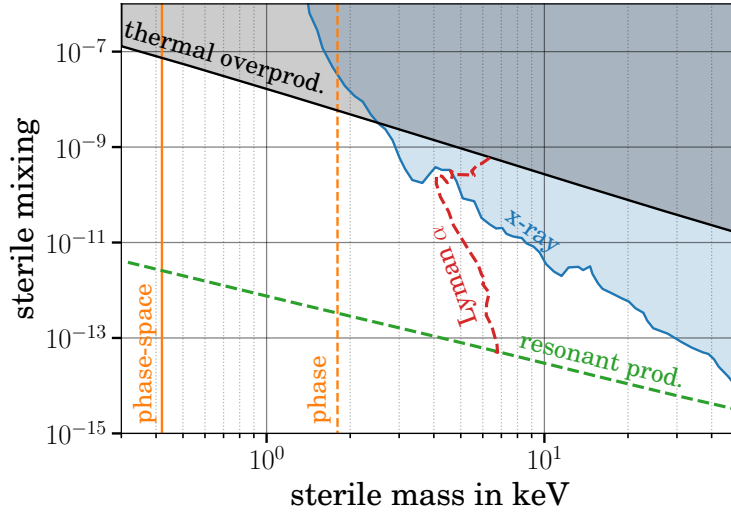
Figure 2.7: Constraints on sterile neutrino sensitivity. Solid lines correspond to more robust, model-independent assumptions. In contrast, marked with dashed lines, limits are displayed that depend on the implied production mechanism. The empty white region around $m_4 = 3\,\mathrm{keV}$ and $\sin^2\theta = 10^{-11}$ signifies the most viable parameters for sterile neutrino WDM candidate (adapted from [Boy19]).

the best guess is that DM is constituted of a yet unknown elementary particle. One assumes they have been produced at the start of the universe and must be hence long-lived enough to survive till today. Furthermore, since direct search experiments fail to measure a genuine signal, DM candidates must have an exceedingly small interaction with baryonic matter. Current studies show that DM particles with masses of several keV/c^2 would be able to explain astrophysical observations (e.g. [Lov12; Adh16; Boy19]).

By definition, a light right-handed sterile neutrino fits these criteria. Typically, it is defined by its mixing angle $\sin^2\theta$ to standard neutrinos and by its mass m_4. Sensible parameters for sterile neutrinos as WDM particle is illustrated in figure 2.7. The listed constraints come from

- phase space considerations, i.e. assuming maximal density of fermionic gas within Pauli's exclusion principle,

- non-observation of x-ray lines, from sterile neutrino decays via $\nu_{\mathrm{s}} \to \nu + \gamma$,

- production mechanisms, where a standard thermal production yields a lower limit and, a combination thermal+resonant mechanism results in upper and lower bounds,

- and Lyman α-lines, i.e. the mass determination of galactic matter via hydrogen absorption lines.

Chapter 3

KATRIN

The Karlsruhe Tritium Neutrino experiment (KATRIN) is ideally suited to investigate, both, the light SM neutrino mass as well as the mass of a hypothetical light right-handed sterile neutrino.

Building up on the experience from its predecessors, the Los Alamos [Rob91], Mainz [Kra05] and the Troitsk [Ase11] experiments, a collaboration together with KIT as host laboratory was formed. The letter of intent [Osi01] from 2001 and the design report in 2005 [Ang05] illustrate the working principle and key features of KATRIN. Notably, the requirement of a high luminosity tritium source led to the decision to build the experiment at "Tritium Laboratory Karlsruhe" (TLK) [Bor06; Bor11], which was already operating at that time.

While the pre-spectrometer arrived already in 2003 and the main spectrometer (MS) in 2006, other components were not delivered before 2015. The CPS and WGTS were thus the last to be connected to the 70 m long beam line. With the "first light" measurement campaign 2016, the functionality of KATRIN was successfully tested [Are18a]. The commissioning and calibration phase was rounded up with a dedicated Krypton campaign in 2017 [Are18b] and a first tritium run at low purity in 2018 [Ake19a]. The recent science run [Ake19b] is presented in more detail in section 3.4.

In this chapter the concept of KATRIN, its experimental setup and model, and lastly the current status is presented at first. The detector upgrade to search for sterile neutrinos is later discussed in a separate chapter (s. ch. 4).

3.1   Concept

KATRIN is optimized to the spectroscopy of electrons from tritium beta-decay and to search for the imprint of neutrino masses therein. The projected mass sensitivity after an effective measurement time of three years is $m_{\text{eff}} = 200\,\text{meV}$ (90 % CL). This translates to a total experiment time of about 5 years, i.e. including yearly maintenance periods [Ang05].

The experimental setup of KATRIN is fundamentally adjusted to the kinematics of the

(a) differential energy spectrum

(b) spectrum endpoint region
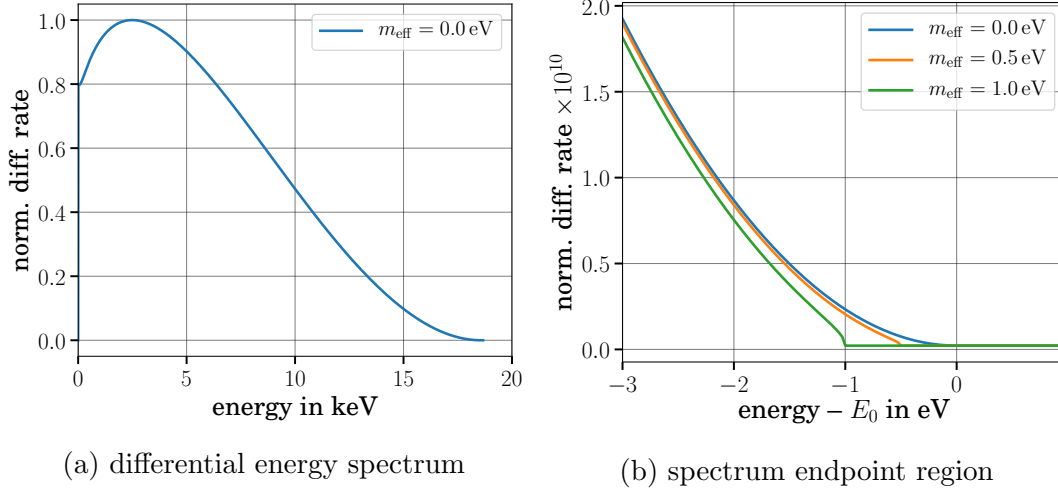
Figure 3.1: (a) Energy spectrum of electrons originating from tritium beta-decay. The maximum differential rate is normalized to unity. A non-zero neutrino mass leads to a slight modification in the region close to the spectrum endpoint $E_0 \approx 18.6\,\text{keV}$, illustrated in (b). Compared to the whole spectrum, the last $30\,\text{eV}$ where the neutrino signature is most distinct constitutes a tiny fraction of all events: only 1 out of about 100 million decay events.

beta-decay kinetic energy spectrum (s. fig 3.1a). A non-zero neutrino mass reduces the maximal observable kinetic energy of electrons and in addition distorts the spectral shape in the last few eV below the kinematic energy endpoint E_0. This requires the electrons energy to be preserved along the entire experimental setup and to be measured with eV precision. Moreover, as the count rate is drastically reduced close to the endpoint, a high luminosity beta-decay source is required.

Three criteria make tritium a well suited β-emitter: first, its energy endpoint is low enough $E_0 \approx 18.6\,\text{keV}$ to apply precision electric potentials [Mye15]; second, its beta-decay half-life time $t_{1/2} \approx 12\,\text{a}$ [Luc00] facilitates both the source stability as well as high decay rates [Ott08]; and third, tritium beta-decay is super-allowed, which simplifies the mathematical description [Ott08].

3.2   Beamline

KATRINs experimental setup is divided in two major sections: the source and transport section (STS) as well as the spectrometer and detector section (SDS) (s. fig. 3.2).

The STS must provide a stable, high luminosity tritium source and ensure lossless electron guidance to the spectrometers. It is further subdivided into: Rear Section (RS), windowless gaseous tritium source (WGTS), differential pumping section (DPS) and finally the cryogenic pumping section (CPS).

The SDS is tasked to measure the electron energies with eV precision. It is formed by
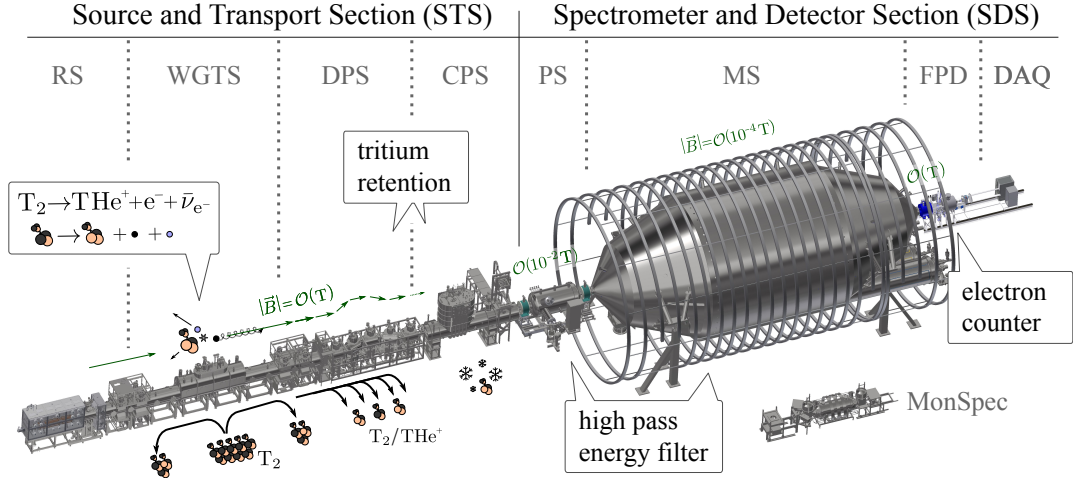
Figure 3.2: Overview of the 70 m long KATRIN beamline. From left to right it encompasses the Rear Section (RS), windowless gaseous tritium source (WGTS), differential pumping section (DPS), cryogenic pumping section (CPS), pre-spectrometer (PS), main spectrometer (MS), focal plane detector (FPD) and the data acquistion (DAQ) system. The monitor spectrometer (MonSpec) is situated in a neighboring building.

pre-spectrometer (PS), main spectrometer (MS), monitor spectrometer (MonSpec) and the focal plane detector (FPD), which includes the data acquistion (DAQ) system.

Rear section

The RS is situated at the upstream end of the beamline [Bab14]. A gold coated Rear Wall (RW) hast the task to define the plasma potential and to keep the source potential stable. In order to compensate possible space charge effects the RW can be illuminated by ultra-violet light (UV) [Sch16b; Kuc18].

The RW acts as "beam dump" for $> 99\%$ of the electrons. A Beta-Induced X-ray Spectroscopy (BIXS) system makes us of this effect to monitor the in-situ activity of the tritium source [Roe13].

Lastly, an electron gun is attached to the RS. It features adjustable electron rates, energies and angles [Bab14; Sch16b]. Together with dipole magnetic fields the complete KATRIN beamline can be calibrated. The electron gun has been successfully used for measuring the transmission function of the spectrometer [Beh17] as well as the electron energy loss function for inelastic scattering of electrons off tritium molecules in the source [Han17].

Tritium source

Almost all of the tritium molecules propagate only within the inner 10 m of the 16 m long WGTS. While tritium is inserted at its center and pumped out on both ends, this part only represents a small section of the closed tritium loop operation. Together with pressure controls, purification and monitoring devices it forms the Loop System (LS) [Bor06; Stu10; Pri15]. An exemplary monitoring device therein is the LAser RAman spectroscopy (LARA) system [Sch13; Fis14].

Of special emphasis for the energy measurement of beta-decay electrons is the thermal motion of the injected molecules. In order to reduce their movement the WGTS is designed as a cryostat. Surrounded by multiple cooling stages, the 10 m long beam-tube is stabilized at about 30 K [Ang05; Gro11].

Along the WGTS beam-tube several superconducting magnets are operated at about 3 T. They are tuned for maximal longitudinal homogeneity to provide identical conditions in the source. The magnets at both ends are optimized to allow adiabatic electron motion to the neighboring sections [Are18c].

Transport section

The transport section must guarantee an adiabatic magnetic guidance of beta-decay electrons, while removing tritium molecules. The first task is achieved via multiple super conducting magnets around 5 T [Are18c] and the second task via a two-staged pumping approach located in the WGTS, DPS and CPS [Ang05]. In combination the amount of tritium is reduced by more than 14 orders of magnitude [Jan15].

The turbomolecular pumps on both ends of the WGTS remove roughly 99% of the tritium molecules. In downstream direction, the removal is further magnified by the DPS. It consists of five 1 m long superconducting magnets [Kos12; Jan15; Hac15]. Its second and fourth section are tilted and thus create a chicane in the beamline that block the transmission of neutral particles. Again turbomolecular pumps are used to remove residual tritium molecules, reducing the overall flow through the DPS by a factor of 10^5 [Jan15]. Within the 7 m long CPS the tritium flow is further reduced by a factor of $> 10^7$ [Gil10; Jan15]. It consists of seven super conducting magnets, and similarly has a chicane between the second and forth segmentation. The CPS inner wall is covered with a layer of argon frost operated at 3 K. Neutral tritium molecules that touch the wall are adsorbed and before the argon layer reaches a predefined activity the frost layer is renewed [Roe19].

Charged tritium ions in contrast can be blocked by applying electric potentials. In addition, the DPS houses dipole electrodes that reflect positive ions, and a (non-functional) Fourier Transformation Ion Cyclotron Resonance (FTICR) unit [Ubi09] that allow regulation of the ion flux [Hac17; Are18a; Kle19b].

Finally, at the downstream end of the CPS a vacuum port allows the insertion of the Condensed Krypton Source (CKrS) and the Forward Beam Monitor (FBM). The FBM can be inserted and moved across the beamline laterally [Ell17]. In spite of the significant electron count rates it allows monitoring the source activity. The detector board was
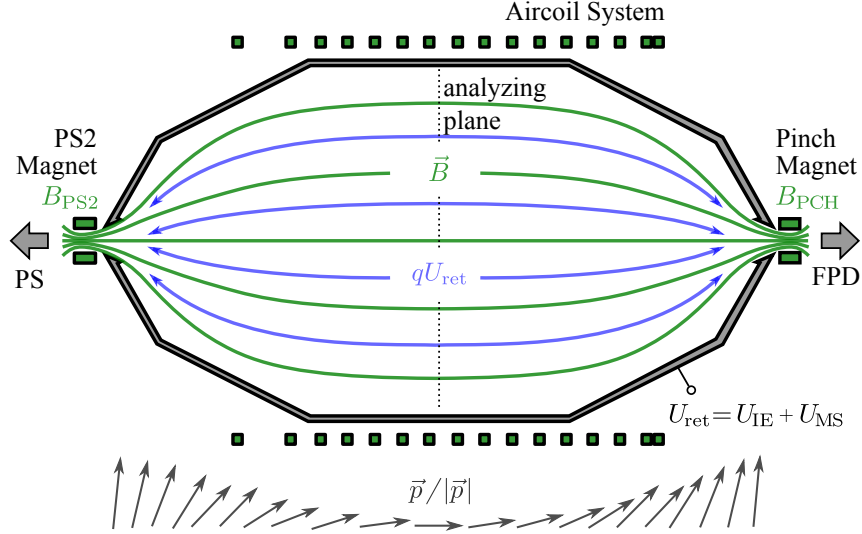
Figure 3.3: Schematic display of the MAC-E filter principle of the MS. Electrons enter from the STS on the left. If their aligned momentum is larger than the applied retarding potential U_{ret}, they may reach the FPD. The best filter process occurs at the analyzing plane (dotted line), where the magnetic field reaches its lowest value (adapted from [Ang05]).

recently replaced by a 7 pixel TRISTAN detector [Urb19].

Spectrometers
As a whole the KATRIN setup hosts three spectrometers: the PS, MS and the MonSpec. They are all based on the same high-pass energy filter principle, i.e. magnetic adiabatic collimation with electrostatic (MAC-E) filter (s. fig. 3.3). Electron momenta are collimated in longitudinal direction, while at the same time experiencing an increasing electrostatic potential. If their longitudinal momenta overcome the largest retention voltage U_{ret} at the position of maximum collimation ($E_{\mathrm{kin}} \gtrapprox U_{\mathrm{ret}}$) they are transmitted through the spectrometer, otherwise they are reflected back.

The PS is operated at a smaller potential. Its task is to reduce the electron flux into the MS and thereby diminishes the background created by scattering from electrons off residual gas in the MS [Ang05]. Historically, the PS acted as a prototype for the bigger MS and proved that the stringent vacuum requirements of $p < 10^{-11}$ mbar can be met [Fla03; Pra12].

Energy filtering of beta-decay electrons is performed in the center of the MS. The region of minimum magnetic field $\vec{B}$ and maximum retardation $|\vec{E}| = q \cdot U_{\mathrm{ret}}$ is called the analyzing plane. The magnetic field is shaped by the low field correction system (LFCS) and a specialized earth magnetic field compensation system (EMCS) [Glu13; Erh18]. Along the building stationary and, directly attached to the LFCS, several mobile sensor units (MobSU) are installed for inferring the magnetic flux [Osi12; Rei13; Erh16; Let18].

The retarding potential is formed by the vessel potential, i.e. the voltage of the entire

outer hull of the MS, and the offset applied to the inner electrode system (IE) [Val10]. As the IE is operated at a more negative potential, negatively charged electrons created at the vessel surface are blocked. This concept, in concert with the magnetic guidance, shields the fiducial spectrometer volume from secondaries induced by cosmic rays or electrons from radioactive decays in the hull [Wan09].

The high voltage system is equipped with sophisticated power supplies that a are tuned to reach ppm level stability (parts per million) [Kra16]. The accuracy is monitored by a self designed voltage divider [Thu09; Bau13] as well as the MonSpec, which is situated in a separate building but shares the high voltage vessel potential with the MS. The MonSpec is designed to continuously scan over a conversion line from ^{83m}Kr and thereby accurately infer the high voltage [Zbo13; Erh14; Sle15; Are18b]. In 2020 the MonSpec detector will upgraded with a second-generation TRISTAN detector system.

Detector and data acquistion

At the downstream end of the KATRIN beamline is the detector and DAQ part. It is designed to count electrons that overcome the MS retarding potential and impinge on the installed focal plane detector (FPD). The detector is encased by a post acceleration electrode (PAE) structure, which shapes an electric field for incoming electrons and accelerates them by 10 kV [Ang05; Sch14; Ams15] (s. fig. 3.4).

The FPD consists of a silicon based pin-diode multi-pixel detector. Similar in layout to a dartboard, it is structured in 148 evenly sized 44 mm^2 segments. Except for the bulls-eye with 4 pixels, all other rings are subdivided in twelve pixel. Intrinsically the FPD measures the charge deposition of incident particles and thus also their initial energy with a resolution (FWHM) of several keV [Ams15].

The detector section also houses a muon veto system, a vacuum port for inserting monitoring and measurement devices (e.g. a radioactive source), and the first stage amplification electronics. As electric boards and cables would increase the pressure around the FPD and propagate to the MS, they are mounted in a separated chamber directly behind the detector. To decouple the high voltage potential from the DAQ, the electric signal is converted to an optical signal before being shaped and analyzed in the DAQ rack [Ang05; Ams15].

Adopted from the Pierre Auger observatory, the DAQ rack is divided into several first level trigger (FTL) cards and a single second level trigger (STL) card [Gem01]. While the STL is solely required for initializing the 10 FTL cards, the latter are responsible for signal conversion and shaping. The FTLs sample at 20 MHz with a 12 bit precision and the signal analysis is based on trapezoidal filters applied via FPGAs on the boards [Ams15].
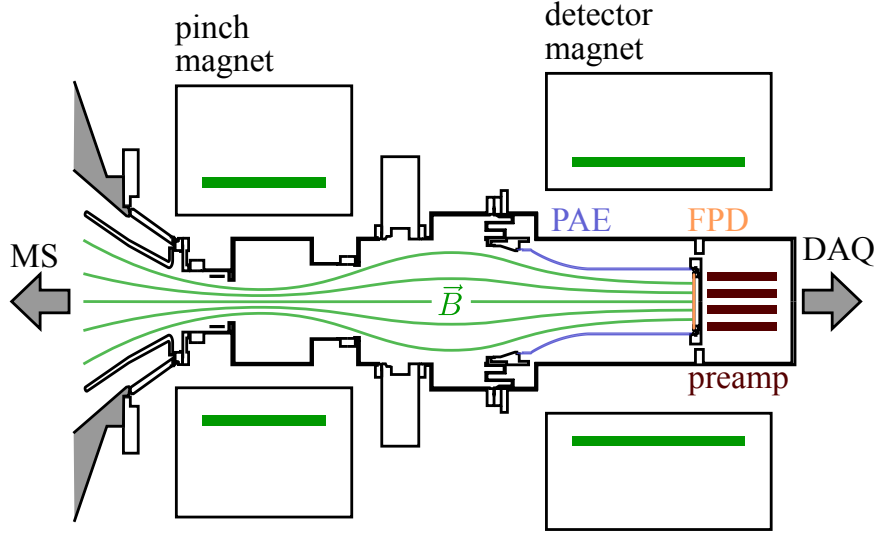
Figure 3.4: Schematic view of the detector part from KATRIN. Electrons are guided along the magnetic field lines (green), accelerated by the PAE (blue) and registered at the FPD (orange). Preamplification electronics (dark red) are mounted behind the detector.

3.3 Model

The measured energy of electrons at KATRIN is fundamentally based on the beta-decay of tritium and the rate is thus described by Fermi's Golden Rule [Dir27; Fer50]. It yields the differential electron energy spectrum

$$\frac{\mathrm{d}\Gamma(E)}{\mathrm{d}E} \quad \propto \quad H(E)\sqrt{(E_0 - E)^2 - m_{\nu_\mathrm{e}}^2} \cdot \Theta(E_0 - E - m_{\nu_\mathrm{e}}) \text{ , with} \tag{3.1}$$

$$H(E) \quad \widehat{=} \quad \frac{G_\mathrm{F}^2 \cos^2\theta_\mathrm{C}}{2\pi^3} \cdot \mathcal{M} \cdot F(Z, E) \cdot p_\mathrm{e} \cdot (E + m_\mathrm{e}) \cdot (E_0 - E) \tag{3.2}$$

incorporating the neutrino mass independent factors from weak coupling, the Fermi constant G_F and Cabbibo angle θ_C, the nuclear transition via the matrix element $\mathcal{M}$, and the electron phase space contribution, with $p_\mathrm{e}, m_\mathrm{e}$ being its momentum respective rest mass. The Fermi function $F(Z, E)$ describes the Coulomb interaction between outgoing electrons and the daughter nucleus [Ott08]. For the KATRIN analysis energy-independent proportionality factors are absorbed by normalizing to the expected tritium source activity, which is derived from the WGTS column density ρd and the life time τ of tritium.

Neutrino oscillation results allow to incorporate the mixing element $U_{\mathrm{e}i}$ to the mass eigenstates m_i, while the ensuing phase space factors are to be summed over:

$$\frac{\mathrm{d}\Gamma(E)}{\mathrm{d}E} \quad \propto \quad \sum_{i=1}^{N_\nu} |U_{\mathrm{e}i}|^2 \cdot H(E)\sqrt{(E_0 - E)^2 - m_i^2} \cdot \Theta(E_0 - E - m_i) \tag{3.3}$$

$$\approx \quad H(E)\sqrt{\Delta E^2 - m_{\mathrm{eff}}^2} \cdot \Theta(E_0 - E - m_{\mathrm{eff}}) \ . \tag{3.4}$$

The observable is the effective neutrino mass $m_{\mathrm{eff}}^2 = \sum_{i=1}^{3} |U_{\mathrm{e}i}|^2 \cdot m_i^2$ in the case of three neutrino mixing $N_\nu = 3$. The description via an "effective neutrino mass" reflects the smallness of neutrino mass splittings known from neutrino oscillation relative to the eV-scale energy resolution of KATRIN. Accordingly, one is not able to resolve individual mass decay rate branches in the beta-decay electron spectrum.

In figure 3.1a the differential energy spectrum for a set of effective masses is illustrated. The dependence of the phase space distortion as function of $E_0 - E$ in equation 3.3 explains the necessity to measure close to the spectral endpoint E_0. Moreover, it implies small signal rates and the requirement of an excellent energy resolution $\mathcal{O}(\mathrm{eV})$.

Transmission function

The KATRIN MS achieves the requited resolution by applying the MAC-E filter principle [Ang05]. It is based on the adiabatic movement of electrons along the prevalent magnetic field lines and the conservation of the magnetic moment μ (in non-relativistic approximation).

$$E = E_\parallel + E_\perp = E_\parallel - \vec{\mu}\vec{B} \longrightarrow \quad E_\perp \propto |\vec{B}| \ . \tag{3.5}$$

The cyclotron motion component of electrons perpendicular to the magnetic field $E_\perp$ is thus directly related to the local field strength $|\vec{B}|$: a decrease in the magnetic field leads to an increase of the longitudinal, parallel component and allows applying electrostatic fields. The energy resolution $\Delta E/E$ is then defined by the ratio of maximal magnetic field B_{PCH} and minimal value in the MS analyzing plane B_{a}:

$$\frac{B_{\mathrm{a}}}{B_{\mathrm{PCH}}} = \frac{B_{\mathrm{min}}}{B_{\mathrm{max}}} \stackrel{3.5}{=} \frac{E_{\perp,\mathrm{min}}}{E_{\perp,\mathrm{max}}} = \frac{E - E_{\parallel,\mathrm{max}}}{E_{\perp,\mathrm{max}}} = \frac{\Delta E}{E_{\perp,\mathrm{max}}} \ . \tag{3.6}$$

Here ΔE signifies the resolution of the MS and only electrons with energies $E_{\mathrm{kin}} \lessgtr qU_{\mathrm{ret}}$ overcome the electrostatic potential in the analyzing plane and are transmitted through the spectrometer.

For $E = 18.6\,\mathrm{keV}$ electrons created isotropically in the WGTS, $B_{\mathrm{PCH}} = 6\,\mathrm{T}$ and $B_{\mathrm{a}} = 6 \cdot 10^{-4}\,\mathrm{T}$, the resolution in the MS is thus $\Delta E \approx 0.93\,\mathrm{eV}$[1]. In the case of electrons without

---

[1]The technical examples are based on parameter values specified in the design report [Ang05]. At present values of 0.7 times their nominal value are chosen.

perpendicular component, i.e. emitted only in longitudinal direction, this values becomes $\Delta E \approx 0\,\text{eV}$.

Similarly, electrons experience an increase in their perpendicular momentum component when moving along increasing magnetic field strengths. As an electron's transversal energy component $E_\perp$ does not exceed the total energy, it is reflected when being created with a large pitch angle $\theta > \theta_\text{max}$. This effect is known as magnetic mirror.

$$\frac{B_\text{s}}{B_\text{PCH}} = \frac{B_\text{min}}{B_\text{max}} \overset{3.5}{=} \frac{E_{\perp,\text{min}}}{E_{\perp,\text{max}}} = \frac{E_{\perp,\text{min}}}{E} = \sin^2 \vartheta_\text{max} \tag{3.7}$$

Source electrons are created at $B_\text{s} = 3.6\,\text{T}$. The largest magnetic field is given by the pinch magnet $B_\text{s} = 6\,\text{T}$ in the MS. As a consequence electrons that are emitted under angles of $\vartheta > \vartheta_\text{max} = 50.77°$ from beta-decay are magnetically reflected and do not reach the detector.

In summary beta-decay electrons are only transmitted through the MS when their kinetic energy is larger than the retarding potential $E > qU_\text{ret}$ at the analyzing plane, and if their momenta lie in the forward pointing acceptance cone $\vartheta < \vartheta_\text{acc} = \vartheta_\text{max}$ where magnetic reflection is avoided. For an isotropic source it is possible to write the transmission probability $T(E, qU_\text{ret})$ of the MS in analytic form [Ang05; Gro15; Beh17; Kle19]

$$T(E, qU_\text{ret}) = \int_{\vartheta=0°}^{\vartheta_\text{max}} \text{d}\vartheta \; \mathcal{T}(E, qU_\text{ret}, \vartheta) \cdot \sin \vartheta \tag{3.8}$$

$$= \begin{cases} 0 & , E - qU_\text{ret} < 0 \\ \dfrac{1 - \sqrt{1 - \frac{E - qU_\text{ret}}{E} \cdot \frac{B_\text{s}}{B_\text{a}}}}{1 - \sqrt{1 - \frac{B_\text{s}}{B_\text{PCH}}}} & , 0 \le E - qU_\text{ret} < \Delta E \\ 1 & , E - qU_\text{ret} > \Delta E \end{cases} \tag{3.9}$$

At fixed retarding potential U_ret, the number of electrons that is transmitted through the MS is counted (s. fig. 3.5a). Scanning across different U_ret for a certain time $\Delta t \cong \Delta t(U_\text{ret})$, also called Measurement Time Distribution (MTD), yields the integral form of the beta-decay electron energy spectrum

$$\Gamma(qU_\text{ret}) \propto \int_{qU_\text{ret}}^{\infty} \text{d}E \; \frac{\text{d}\Gamma(E)}{\text{d}E} \cdot T(E, qU_\text{ret}) \cdot \Delta t(qU_\text{ret}) \,. \tag{3.10}$$

The most basic MTD would be to allow equal measurement times for all potentials U_ret within the relevant spectrum region $[E_0 - 40\,\text{eV}, E_0]$. An example for the region of a few eV around the endpoint for ten potential set points is depicted in figure 3.5b[2]. The MTD used in neutrino mass runs is primarily optimized with respect to the neutrino mass

---

[2]Effects of final state excitations are neglected

(a) MS transmission function

(b) beta-decay spectrum
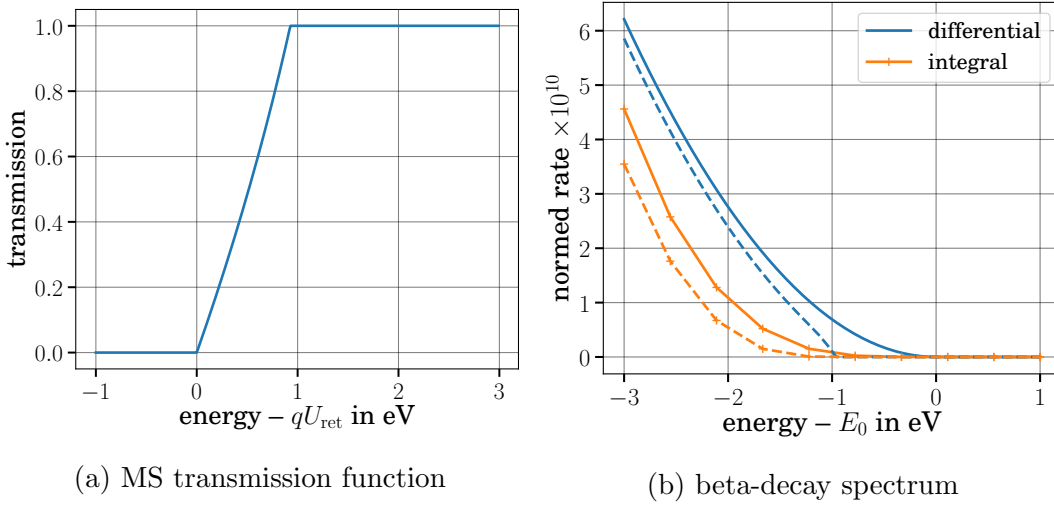
Figure 3.5: (a) Illustration of the KATRIN transmission as a function of surplus energy. The depiction corresponds to $\Delta E \approx 0.93\,\text{eV}$ spectrometer resolution. (b) Differential (blue) and integral (orange) beta-decay electron energy spectrum close to the spectrum endpoint. The integral spectrum is based on the depicted transmission function and a flat MTD with $0.5\,\text{eV}$ steps. The dashed lines represent the influence of non-zero neutrino masses $m_{\text{eff}} = 1\,\text{eV}$.

sensitivity and thus most of the measuring time is spent in a region of a few eV below the endpoint. Additional set points at low U_{ret} and at potentials slightly above the spectrum endpoint are requited to improve constrain the overall normalization respective to the background rate [Ang05; Kle14].

Response function

The full model further accommodates a large set of theoretical corrections to the differential spectrum (e.g. nuclear recoil, molecular final states) as well as systematic effects (e.g. Doppler shift, synchrotron radiation) [Ang05; Ott08; Gro15; Sei19; Kle19].

Experimental effects are incorporated in the so-called response function $R(\dots)$, which can be modified to include systematics dependent on parameters such as time and temperature. The analytical model thus becomes

$$\Gamma(qU_{\text{ret}}) \propto \int_{qU_{\text{ret}}}^{E_0} dE\ \frac{d\Gamma(E)}{dE} \cdot R(E, qU_{\text{ret}}, \dots) \cdot \Delta t(qU_{\text{ret}})\ . \tag{3.11}$$

For KATRIN the response function is the result of folding the MS transmission with source scattering, the latter describing inelastic scattering from beta-decay electrons off tritium gas within the WGTS [Kle19]:
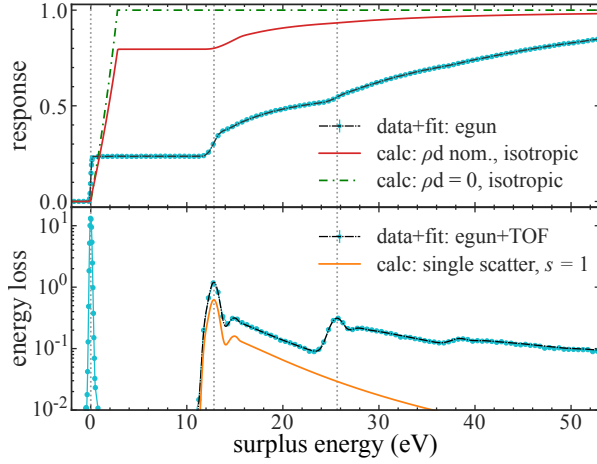
Figure 3.6: RS electron gun data (cyan) and model (black) over the electrons surplus energy $E - qU_{\text{ret}}$. The top shows the response function. Its derived form for isotropic electrons (red) and the contribution from MS transmission (green) is also added. The bottom uses time-of-flight (TOF) information to extract the energy loss function and shows single scattering in orange (adapted from [Ake19b]).

$$R(E, qU_{\text{ret}}) = T(E, qU_{\text{ret}}) \times [P_0 + P_1 \cdot f(E) + P_2 \cdot (f(E) \times f(E)) + \dots]$$
$$= \int_{\epsilon=0}^{E-qU_{\text{ret}}} \mathrm{d}\epsilon \int_{\theta=0}^{\theta_{\max}} \mathrm{d}\theta \; \mathcal{T}(E - \epsilon, qU_{\text{ret}}, \theta) \cdot \sin\theta \cdot \sum_s P_s(\theta) f_s(\epsilon) \; . \tag{3.12}$$

Here, source scattering is described by the probability $P(\theta)$ and its energy loss function $f(\epsilon)$ for an electron to scatter once within its flight through the source. $f_s(\epsilon)$ signifies the energy loss function for multiple scattering, i.e. its s-times self convoluted form. Electrons that do not scatter do not lose energy $f_0(\epsilon) = \delta(\epsilon)$.

3.4 Status

After years of preparation and commissioning, KATRIN took the last step and measured electrons from tritium beta-decay during the so called "First Tritium" campaign in 2018. There, it could successfully be demonstrated that all requirements, except for background rate Γ_{bkg}, are within their limits or better [Ake19a].

The experiment was operated at nominal column density of $\rho d = 5 \cdot 10^{-17}\,\text{cm}^{-2}$, using a reduced $1\,\%\,\text{DT}$ tritium content with $99\%\,\text{D}_2$ gas. In particular it was demonstrated that the WGTS can be stabilized at the $10^{-3}/h$-level. Moreover, the RS electron gun was used to measure the response function of the entire apparatus (s. fig. 3.6 (top)). A novel time-of-flight (TOF) measurement with a pulsed electron gun source allowed to obtain the electron loss function (s. fig. 3.6 (bottom)).

The first regular science neutrino mass measurements lasted from April 10 to May 13 in 2019, internally referred to as the "KATRIN Neutrino Mass 1" campaign (KNM1) [Ake19b]. The WGTS was operated at $\rho d = 1.11 \cdot 10^{-17}\,\text{cm}^{-2}$, with a very high tritium purity of $\epsilon_{\text{T}} = 0.976$. During the campaign an integral tritium beta-decay spectrum was measured with retarding energies qU_{ret} within the range $[E_0 - 90\,\text{eV}, E_0 + 50\,\text{eV}]$. The MTD as well as the measured integral spectrum are illustrated in figure 3.7.

Figure 3.7: Illustration of the measured count rate (top), the residuals relative to the model (middle) and the applied MTD (bottom) over retarding energies qU_{ret}. The data (black dots) is well represented by the model (blue line), as residuals fall within the statistical and systematic uncertainty bounds (blue shaded) (adapted from [Ake19b]).
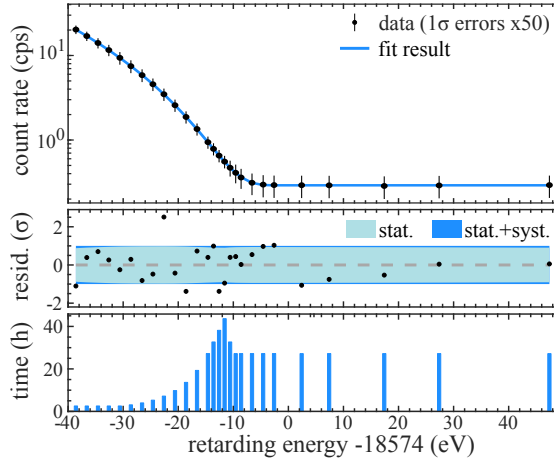
To prevent the influence of a bias in the entire analysis chain, the measured data was blinded with a smeared final state distribution (FSD) and the full analysis was performed by three teams with independent fitting routines. At first a "twin MC data-set" allowed the teams to benchmark their code. Following in a weak-long analysis workshop and a sufficient understanding of systematic effects, the go-ahead to analyze the "real" data was given.

The "MC data" is generated by combining the source scattering model with a subsequent particle propagation software, called KASSIOPEIA [Fur17]. The tracking model incorporates slow control readings from magnetic currents and electric potentials.

The reported value of the observable $m_{\text{eff}}^2 = -1.0_{-1.1}^{+0.9}\,\text{eV}^2/c^4$ represents a 1σ fluctuation from the expectation of $m_{\text{eff}} = 0\,\text{eV}$. Applying the robust Lokhov-Tkachov method [Lok15] allows to derive an upper limit on the effective neutrino mass of $m_{\text{eff}} \leq 1.1\,\text{eV}/c^2$ at 90% CL. The best fit of the spectral endpoint is given for $E_0 = (18573.7 \pm 0.1)\,\text{eV}$ [Ake19b].

In the following years KATRIN will continue its tritium beta-decay measurements on a regular basis of three measurement campaigns per year. The projected goal is $m_{\text{eff}} \leq 0.2\,\text{eV}/c^2$ at 90% CL. A first task to achieve this is to reduce the prevalent non-Poissonian background from Radon [Ake19b].

Chapter 4

TRISTAN upgrade

A viable new field of research of KATRIN is centered on the investigation of non-standard neutrinos with masses in the keV range, namely sterile neutrinos (s. sc. 2.4) [Mer15a; Mer15b]. Tritium beta-decay allows the exploration of neutral fermions with masses up to $\approx 18.6\,\text{keV}/c^2$, limited by the kinematic endpoint. In contrast to the nominal operation mode of KATRIN, the search for a sterile neutrinos signature requires the measurement of the entire tritium beta-decay electron energy spectrum.

This chapter first discusses the concept of such an investigation. The second part is centered on the technical realization of the projected detector system, explaining the working principle of SDDs and the DAQ system (s. sc. 4.2). Lastly, the status of the current detector design is presented (s. sc. 4.3).

4.1 Concept

Assuming neutrino mixing to hold for sterile neutrinos, one can look for an additional mass eigenstate m_4 contributing to the phase space factor of neutrinos (s. eq. 3.3). In this case the differential electron rate

$$\frac{\mathrm{d}\Gamma(E)}{\mathrm{d}E} \propto H(E) \cdot \left(\cos^2\theta \cdot \sqrt{(E_0 - E)^2 - m_{\text{eff}}^2} \cdot \Theta(E_0 - E - m_{\text{eff}}) \right.$$
$$\left. + \sin^2\theta \cdot \sqrt{(E_0 - E)^2 - m_4^2} \cdot \Theta(E_0 - E - m_4) \right) \tag{4.1}$$

gains an additional term. Here the neutrino mixing matrix element $U_{\text{e}4}$ yields the factor $\sin^2\theta$ while the three standard neutrino mass eigenstates are jointly represented with an effective mass m_{eff} and an effective mixing $\cos^2\theta = 1 - \sin^2\theta$ (s. eq. 3.4).

An example of such a sterile neutrino imprint in a differential electron spectrum with unrealistically large mixing is shown in figure 4.1. While an additional mass eigenstate would result in a overall rate reduction, the source stability and systematic effects at
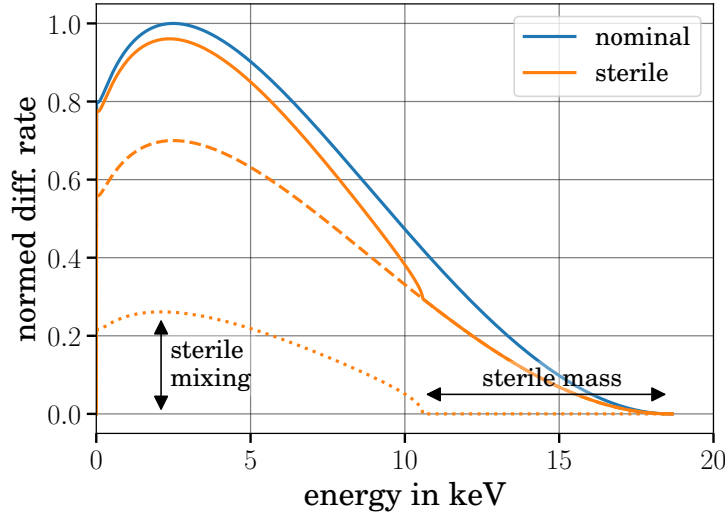
Figure 4.1: Kinematic energy spectrum of electrons from tritium beta-decay. The spectra are normalized with respect the case if massless neutrinos (blue). A hypothetical sterile neutrino would introduce an additional decay branch and manifest below $E_0 - m_4$ with an admixture of $\sin^2 \theta$. Here a sterile mass of $m_4 = 8\,\text{keV}$ and a large mixing of $\sin^2 \theta = 30\%$ is selected (orange).

KATRIN only allow the analysis of a sterile neutrino imprint due to its change of the spectral shape, most notably the kink at $E_0 - m_4$.

The sensitivity to detect a sterile neutrino is governed by the mixing amplitude $\sin^2 \theta$ and also depends on its mass m_4 (s. sc. 2.4). In order to be accessible with KATRIN, the sterile neutrino mass eigenstate would have to fall into the few keV/c^2 mass range. A challenge its the expected tiny mixing amplitude $\sin^2 \theta \leq 10^{-7}$, if we consider that the sterile neutrino is the sole DM particle.

For a sterile neutrino search using beta-decay electrons this entails . . .

1. . . . a source with high *luminosity*. The statistical uncertainty of a counting experiment is described by a Poisson distribution and thus the sensitivity driven by the total standard deviation $\sin^2 \theta \propto \sigma = \sqrt{N} = \sqrt{\Gamma \cdot \Delta t}$ of the number N of decays observed. Both the decay rate Γ and the measurement time Δt affect the statistical uncertainty via their square root value [Mer15a].

2. . . . that model deviations through *systematics* must be understood and/or mitigated with great precision. The information of a sterile neutrino is encoded by the steep rise in electron rate at $E_0 - m_4$ (s. fig. 4.1). Consequently, effects that lead to signal smearing or add discontinuities require special attention. For example effects that lead to Gaussian-like smearing must be reduced by requiring an energy resolution of FWHM $\leq 500\,\text{eV}$[Mer15b].

The tritium source of KATRIN is well suited for a sterile neutrino search and allows testing masses up to $m_4 \leq 18.6\,\text{keV/c}^2$. From bare statistics, a three-year measurement with

maximal source strength of $\Gamma_{\text{src}} = 10^{11}$ Bq would allow to reach a statistical sensitivity down to $\sin^2 \theta = 10^{-8}$ [Mer15a].

Measuring the entire beta-decay spectrum with KATRIN would translate to a MS retarding potential of $U_{\text{ret}} = 0$ kV and a detector rate of $\Gamma_{\text{det}} = 10^{10}$ cps. The FPDs system, however, was designed for rather low rates and its dynamic range is limited to roughly $\Gamma_{\text{det}} < 10^6$ cps. Using the FPD would thus require a rate reduction by 4 orders of magnitude. Also, it would be affected by the rather moderate energy resolution of roughly FWHM ≈ 2 keV. While it would be possible to use the excellent energy resolution of the spectrometer, this would correspond to an integral scan and cut-off spectrum information at $E_{\text{kin}} < qU_{\text{ret}}$ and thus would lead to reduced sensitivity [Mer15b].

In order to reach best sterile neutrino sensitivity a new detector and readout system is required. In addition to featuring an improved energy resolution and high rate compatibility, the system must be compatible with ultra high vacuum pressures $\mathcal{O}(10^{-10}\,\text{mbar})$ and magnetic fields $\mathcal{O}(1\,\text{T})$ [Are18c]. A viable solution for detecting keV-scale electrons are silicon detectors.
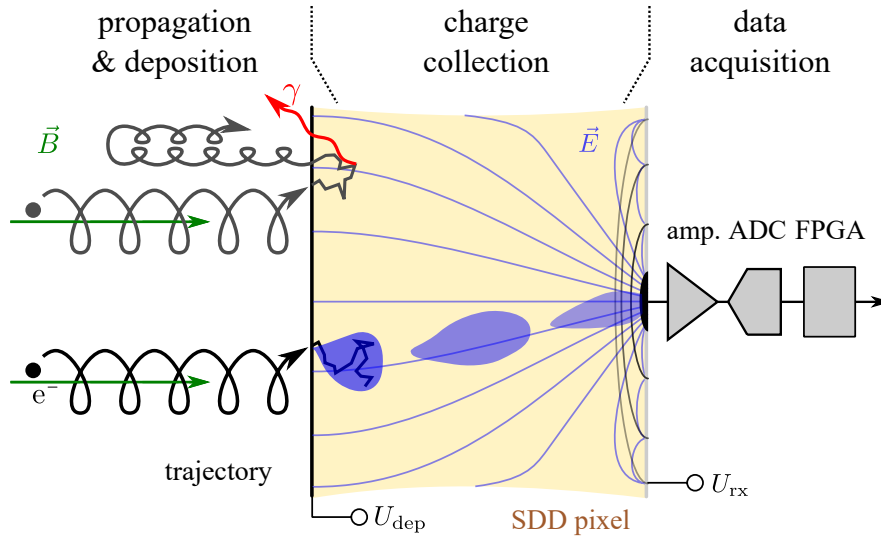
Figure 4.2: Schematic to depict the different steps from the initial charge creation to the final energy determination of an incident electron. Electrons (black) start on the left and are magnetically guided (green) to the detector. They deposit their energy in a multitude of scatterings in the silicon bulk and create electron-hole pairs, with a slight probability for them to back-scatter (gray) or that created Silicon x-ray excitations escape (red line). The charge carriers in the silicon bulk (electrons or holes) form a thermally expanding charge cloud (blue area), which deforms while drifting along the electric field lines (blue lines) to the readout electrode. Finally the collected charge signal is amplified, digitized, shaped and analyzed (gray boxes).
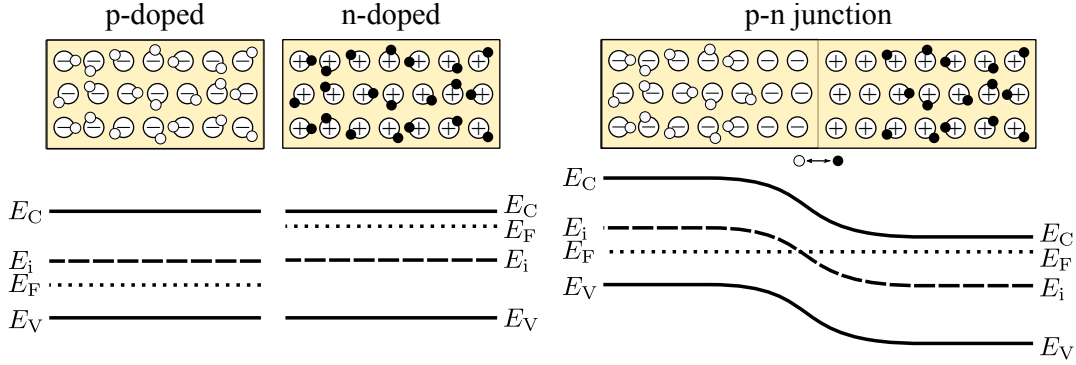
Figure 4.3: Schematic energy bands for holes (white balls) and electrons (black dots) within two differently doped silicon bulks (left). Joining the two in the middle (right) leads to an electron-hole exchange and ensues shifted energy bands (adapted from [Lut07]).

4.2   Technical realization

The detection principle of the TRISTAN detector is based on pn-junctions known from electric diodes. The bulk of a semiconductor functions as the particle detection medium while two opposing surfaces are operated as electrodes to shape an electric field. An external particle traveling through the detector scatters off atoms in the bulk and thereby creates electron-hole pairs that are collected by the electrodes. Particle detection and energy determination is then accomplished by electronically measuring the current flow. The readout encompasses amplification, signal shaping and digitization in separate processes [Lut07]. An example of the entire signal creation process is illustrated in figure 4.2.

Detector
Semiconductors typically come in crystalline form with their atoms being periodically structured, forming a characteristic lattice. The physical properties of charge carriers, more specifically of free electrons and holes, are described by the band model. Therein the electronic properties depend on charge carriers within the conductance band, denoted by the minimal energy E_C. Typically only valence electrons with an energy E_V may enter the conduction layer due to thermal or external excitation.

Thermal excitation can be discussed on the basis of the Fermi-Dirac distribution, which depends on temperature T and the Fermi energy E_F, and by distributing the electron energies within momentum space. In order to use a semiconductor as a detector, the Fermi energy is shifted by introducing impurities into the bulk or near the surface. This process is called doping and it leads to a shift of the Fermi energy level. Compared to intrinsic semiconductors, a positive dotation leads to a negative shift $E_F < E_i$ and vice versa for a negative dotation. P-doping gives an excess of holes while n-doping gives electrons as charge carriers. Joining two differently doped regions together results in recombination of free holes and electrons near the contact area (s. fig. 4.3). This region thus becomes void
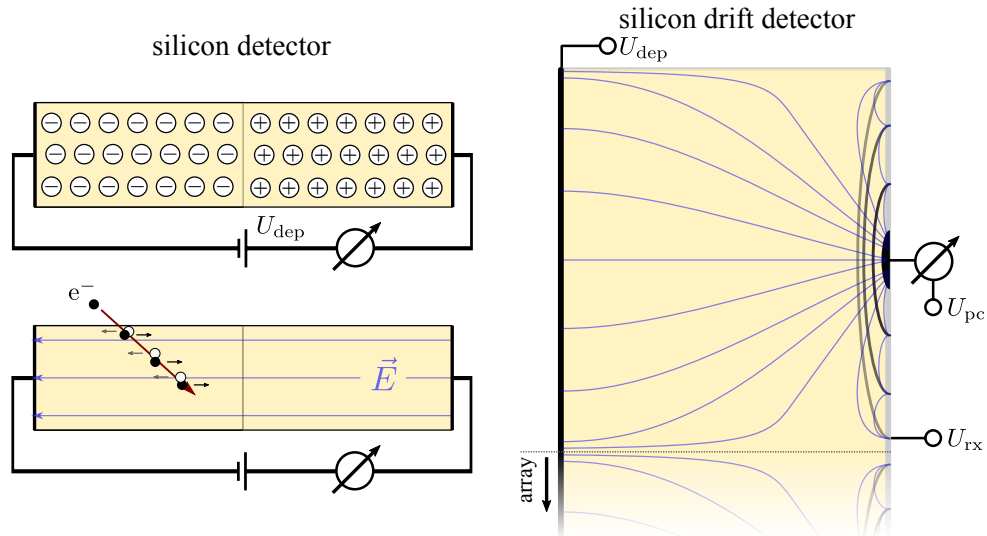
Figure 4.4: Illustration of a pn-junction based silicon detector (left). Applying high reverse bias potentials depletes the bulk from prevalent charges (left top) and allows to measure newly created electron hole pairs from external sources (left bottom). Scaling up the detector size while also reducing the readout point contact size requires shaping of the inner electric field via so-called drift rings (right).

of mobile charge carriers.

By applying an external voltage to the pn-junction, the size of the charge-free region can be either decreased or increased. For particle detection it is best to fully deplete the bulk of free charge carriers. Consequently, a negative potential U_{dep} is applied to the p-doped side. In addition this increases the electric field within the bulk and allows for a quick collection of created charge carriers by an external particle that passes through the bulk (s. fig. 4.4).

In order to shrink the readout electrode while increasing the detector area, the electric field in the bulk has to be shaped accordingly: electrons have to drift "side ways" [Gat84]. Silicon drift detectors (SDD) are based on this principle. On the readout side, several drift electrodes are added and powered at different, increasing potentials. They encase the central point contact and affect the charge collection process dependent on the particles point of incidence (s. fig. 4.4). Charge carriers created in the center of the detector travel in a straight line to the electrode, whereas for charges created at a distance to the electrode have an increased collection path.

(a) active reset
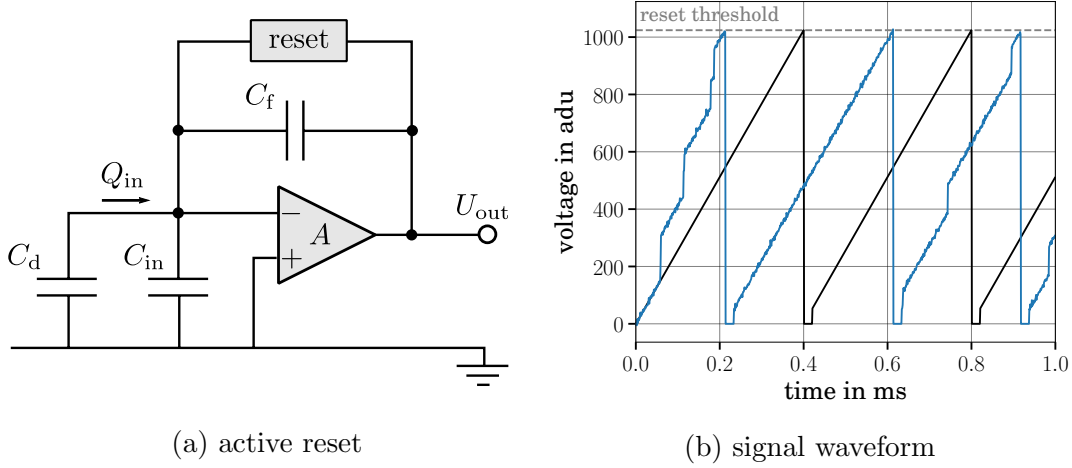
(b) signal waveform

Figure 4.5: (a) Schematic of active amplifier with active reset adapted from [Lut07]. (b) Typical signal waveform U_{out} in analog digital units (adu). The detector is denoted by its capacity C_d, the gray box denotes a dedicated reset circuit for discharging the feedback capacity C_f at a given threshold $U_{res} = 2^{10}$ adu, i.e. before saturating the ADC (here 10 bit). Leakage currents induce a slope in the output voltage (black) and events in the detector show a step-like increase (blue).

Amplification

The advantage of a reduced readout electrode size is the subsequent decrease of the detectors capacitive load C_d, which in turn allows for larger signal amplification in case of charge-sensitive amplifier:

$$U_{out} = -\frac{Q_{in}}{C_f + (C_d + C_{in} + C_f)/A} \longrightarrow \frac{Q_{in}}{C_f} \, , \tag{4.2}$$

where Q_{in} is the amount of charges created by an external particle in the detector, C_{in} is the electronics capacity to ground and C_f the feedback capacity of the amplifier. The output voltage U_{out} is proportional to the input $U_{out} = -AU_{in}$. For an effective charge amplification the capacitive load is chosen smaller than the input impedance: $C_d < (A + 1)C_f + C_{in}$ [Lut07].

In figure 4.5a an electronic schematic of the charge sensitive amplifier is illustrated. As the capacitor C_f charges over time (s. fig. 4.5b), it is mandatory to include a reset mechanism. The so-called continuous reset consists of a parallel resistor R_f, which ensues an exponential decay shape with a decay time of $\tau = R_f \cdot C_f$. The reconstruction of a particle energy in this case is consequently affected by modeling of τ and thus by production uncertainties on R_f and C_f.

Alternatively it is possible to use active reset schemes. These require special integrated circuits that "manually" reset the capacitor after it reaches a certain voltage. This adds a small time frame where incoming signals will not be detected. The feedback is continuously

charged by leakage currents from the detector, which adds a slope to the output voltage. Charge collection from external events happen within a few ns.

Shaping

The deposited energy in the detector is inferred by the voltage increase U_{out} caused by an external particle (s. fig. 4.5b). The measured energy, however, is affected by statistical fluctuations. The spread of the observed energy is described by the energy resolution:

$$\text{FWHM}/2.355 \approx \sigma = \sqrt{\sigma_{\text{fano}}^2 + \sigma_{\text{noise}}^2} \; , \tag{4.3}$$

where the term σ_{fano} is the co-called Fano-noise contribution and σ_{noise} describes the impact of voltage fluctuations, electronic noise.

Fano-noise stems from the energy deposition process of incident particles, the scattering off lattice atoms in the detector bulk. A part of this energy will end-up exciting valence electrons and thus elevate charge carriers into the conductance band. As the energy loss in silicon is limited by discrete energy levels of the atoms, the number of created electron-hole pairs diverges from a classical Poisson distribution and ensues the so-called Fano factor f [Fan47; Ali80]. The electron-hole creation process alone thus adds to the detectors energy resolution:

$$\sigma_{\text{fano}} = \sqrt{f E_{\text{eh}} E_{\text{in}}} \; , \tag{4.4}$$

where E_{in} is the deposited energy of the incident particle and E_{eh} the mean energy for creating electron-hole pairs. In silicon one finds the constants $f = 0.115$ and $E_{\text{eh}} = 3.63\,\text{eV}$. For an incident electron with energy of $E_{\text{in}} = 10\,\text{keV}$ the detector energy resolution is thus limited by Fano-noise to FWHM $> 152\,\text{eV}$.

The contribution of electronic noise largely depends on various experimental parameters, such as temperature and biasing voltage. Typically, the point contact of an SDD is directly connected (as close as possible) to the amplifier, for example by wire bonds of a few millimeter length. The distance can be further reduced, thus improving the noise performance, by integrating signal amplification electronics into the detector substrate [Lec96; Lec01; Lut07].

In general one distinguishes electronic noise according to the periodic time structure visible in the output voltage $U_{\text{out}}(t)$, or differently phrased by their dependency on the frequency f. To compensate uncertainties from electronic noise with high frequencies, the signal is extracted by averaging over several voltage values before and after the event.

An exemplary averaging schema is the trapezoidal filter. It describes two averaging intervals with P-voltages separated by an F-samples long gap. The difference of the two averages is proportional to the energy of the particle

$$E \propto \Delta U = \frac{1}{P} \left(- \sum_{j=0}^{P} U_j + \sum_{j=P+F}^{2P+F} U_j \right). \qquad (4.5)$$

The proportionality constant can derived by calibration measurements and the discrete values $P\&F$ are translated into the so called shaping time t_{sh} and the flattop/gap time t_{ft}. Filters can be implemented as analogue electric components as well as encoded digitally. Independent thereof, the calculated event energy is often recorded with respect to the digital n bit representation, requiring the conversion of potentials to digital values. This is performed by analogue-digital-converters (ADC). Two core properties of an ADC is its clock cycle, which determines the voltage sampling speed, and the resolution, which corresponds to the number of bits an given potential is converted to.

4.3   Status

The effort of redesigning the KATRIN detector section as well as the DAQ system is referred to as the TRISTAN project, short for TRitium Investigation on STerile (A) Neutrinos[1]. The development is organized in an R&D like fashion with several different institutions in Germany (KIT, IPE, MPP, TUM, HLL), Italy (XGLab, UNIMIB and PoliMi) and recently the US (CMU). While the physics runs will be performed at the KATRIN beamline, the MPP is centrally involved in the design and commissioning of the system. The detectors (s. fig. 4.6) are produced by the HLL and the DAQ electronics are designed by XGLab, PoliMi and IPE.

The final detector is projected to consist of 21 modules positioned side-by-side in a grid. Each module consists of an array of hexagonally shaped Silicon Drift Detectors (SDD), which are connected to dedicated amplification and DAQ boards. Finally, each SDD, referred to as a detector pixel, has its individual amplification line which feeds an electric signal of an electron into a separated ADC and a module-wide DAQ channel [Mer19].

The first modules with this SDD technology and dedicated DAQ systems will become available and are expected to be commissioned in 2020. Most importantly, a module will be mounted at the monitor spectrometer. It signifies an important milestone for TRISTAN as it provides a KATRIN-like spectrometer-detector setup on a smaller scale. The insights gained there will be tied to several R&D fields: modeling, SDD design, cooling, electronic amplification, DAQ programming and vacuum specifications. Of special interest are long-term measurements of the detector response, i.e. its energy resolution, and its time dependence.

Since 2016 the first SDD prototypes have been tested. They consist of detectors with seven hexagonally shaped cells, forming one inner and six outer pixels. Several cell sizes

---

[1]The abbreviation is not unique and several different forms are eligible. Safe to say, the team focusing on sterile neutrinos and the ensuing detector upgrade for KATRIN are internally labeled TRISTAN.
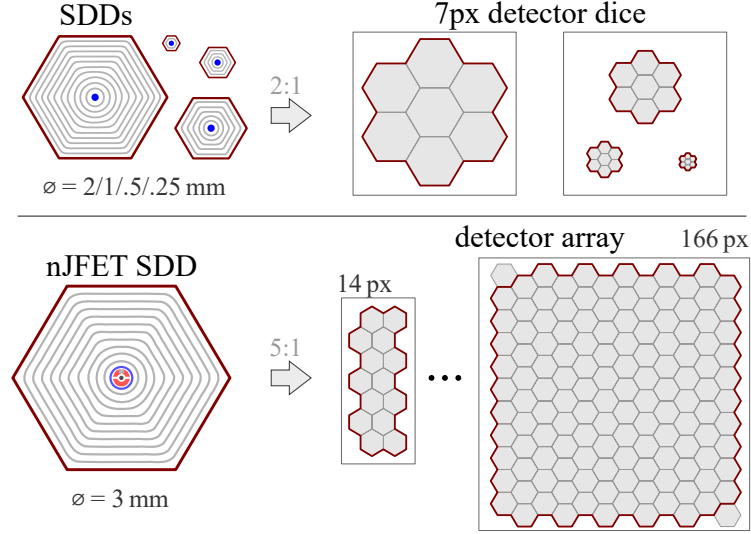
Figure 4.6: Schematics of the TRISTAN detectors. The first production (upper half) included SDDs with varying cell diameters $2r_{px} = 2/1/.5/.25$ mm and numbers of drift rings (black). The readout anode is in the center (blue) and the guard ring (red) marks the boundary to the rest of wafer. Bundled on detector boards (individual pixels only outlined), the detectors come each with seven pixels. In the bottom the current production line is illustrated. It is based on $2r_{px} = 3$ mm SDD pixels with integrated nJFET (red) amplifiers. The detector arrays come with varying pixel numbers. The largest with $n_{px} = 166$ represents the first prototype for the final TRISTAN modules. It misses two corner pixels to facilitate instrumentation.

($r_{px} = 0.125/0.25/0.57/1$ mm) and different production technologies were investigated [Kor16; Alt19; Sie19]. These detectors have proved the overall feasibility of this new design. In particular, an exceptionally good energy resolution FWHM $= 139$ eV (5.9 keV gammas at -30°C) was achieved, while the energy non-linearity was found to be below 0.1%. Finally, a small electronic noise could be confirmed at high frequencies $\mathcal{O}(\mathrm{MHz})$ [Mer19].

The achievable sterile neutrino sensitivity with such a detector is illustrated in figure 4.7. The tritium source is designed to provide decay rates of $\Gamma_{\mathrm{src}} = 10^{11}$ Bq, which would translate to electron count rates of roughly $\Gamma_{\mathrm{det}} = 10^{10}$ cps at the detector and a sensitivity of $\sin^2 \theta = 10^{-8}$ [Mer15a]. An increase in luminosity is prohibited due to inelastic scattering in the source as well as extended tritium handling.

A minimalist approach would be to use KATRIN as is, i.e. without hardware modifications. In this scenario, the FPD would clearly be the limiting factor, as the DAQ was specifically developed for low count rates. Assuming a tolerable detector count rate of $\Gamma_{\mathrm{det}} = 10^5$ cps, ensues an overall rate reduction by five orders of magnitude. The sensitivity would thus be smaller and this approach is thus more interesting as an intermediary step. An exemplary short-scale, i.e. measurement time of several weeks, sensitivity analysis is illustrated in figure 4.7.
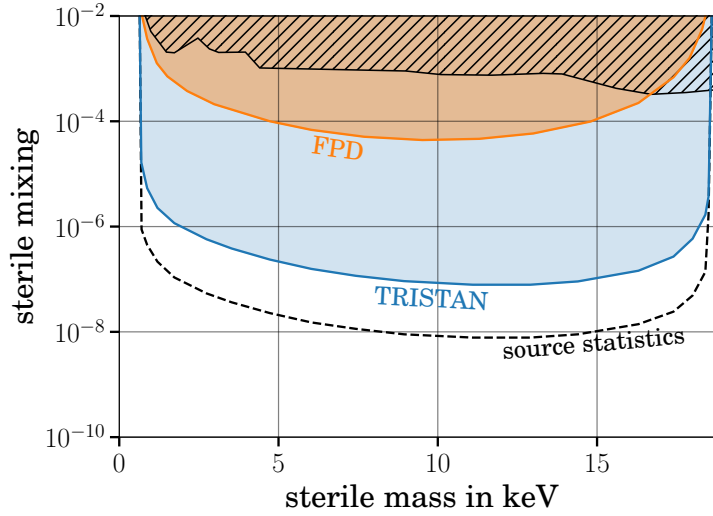
Figure 4.7: Statistical sensitivity (90% CL) for a sterile neutrino search with KATRIN. The theoretical best sensitivity is limited by the overall statistics of the tritium source (dashed). Reducing the rate by a factor 100 will allow to operate of the TRISTAN detector (blue). In the present setup, a reduction of more than 10^5 would be required to use the existing FPD (orange) for a differential spectrum measurement. Current laboratory limits (hatched) are well below $\sin^2\theta = 10^{-4}$ (adapted from [Mer19]).

Even with the TRISTAN detector being optimized for higher signal rates, recent analyses of pile-up and source scattering suggest a source strength reduction by a factor of 100. The projected sterile neutrino sensitivity is hence limited to about $\sin^2\theta = 10^{-7}$, corresponding to an effective measurement time of three years [Mer19].

Chapter 5

Modeling

As sterile neutrinos are to be investigated with admixtures of $\sin^2\theta = 10^{-7}$, systematics have to be tested with high precision. In this chapter a model is presented that focuses on effects related to the detector section and combines simulated data with analytic descriptions.

The first section (s. sc. 5.1) presents the simulation framework KASSIOPEIA and gives a short overview of particles propagation at the detector section of KATRIN. The investigated systematics are introduced in-detail in section 5.2. Here, the presented detector response reflects the current realization with the FPD.

Section 5.3 focuses on a semi-analytical approach that allows time-efficient calculation of the detector response. A novel simulation-interpolation approach is introduced, which is essential for the TRISTAN detector characterization as well as the systematic sensitivity studies presented in the subsequent chapters.

5.1 Simulation framework

KASSIOPEIA is a modular particle tracking framework entirely written in C++. It was originally developed to track multi-keV energy electrons for KATRIN and features complex geometries as well es efficient algorithms for electromagnetic field derivation [Fur17].

KASSIOPEIA
Individual particles are defined by inherent values, such as mass m and electric charge q, as well as parameters that are dynamically changing, such as momentum $\vec{p}$ and position $\vec{x}$. In order to facilitate the creation of secondaries and ease surface and bulk interactions, the whole simulation process is structured into steps, tracks, events and runs.

- Step: The smallest hierarchy in the simulation is a step. It signifies a single evolution step of a particle's dynamic variables from their initial to the final state. A particle's movement $\vec{x}_{\text{in}} \rightarrow \vec{x}_{\text{fi}}$ is calculated with respect to the surrounding environment's

```xml
<define name="path" value="folder/"/>          <!-- XML: VAR -->
<include name="[path]magnet.xml"/>             <!-- &NESTING -->
<geometry>                                     <!-- GEO: OBJECTS -->
  <cylinder_space name="world" z1="-5" z2="5" r="2"/>
  <space name="world_space" node="world">
    <space name="file_magnets" tree="magnet_space"/>
  </space>
</geometry>
<kassiopeia>                                    <!-- SIM: MAGNETS -->
  <ksfield_electromagnet name="field_magnet">
    <zonal_harmonic_field_solver/>
  </ksfield_electromagnet>
  <!-- ...                          (E-FIELDS, FORCES, etc.) -->
</kassiopeia>
```

Listing 5.1: Exemplary code of typical KASSIOPEIA simulation configuration file. C++-objects and their parameters are accessible through xml-tags and their attributes. ⟨geometry⟩ marks a namespace and the container class ⟨space⟩ is filled with geometric objects. The XML-parser classes related to ⟨include⟩ and ⟨define⟩ allow nesting of multiple configuration files, respective variable definitions, therein.

matter, interactions and fields. On each step a complex decision tree is evaluated: "New object entered?", "Continue simulation/Terminators?", "Write output?", etc.

- Track: A track expresses a particle's evolution from creation to termination and consists of a multitude of steps. A particle is either directly created by the user with so-called "generators", or it is being created as a secondary particle due to interactions (e.g. ionization) or artificially (e.g. if transmitted through or reflected off an object's surface).

- Event: An event is directly created by the "generators" defined by the user. It combines the tracks and steps of the primary simulation particle(s) and all its subsequent secondaries.

- Run: The highest level of organization is defined within a run. It represents a single simulation execution and consists of multiple user-defined events.

The definition of the whole simulation is specified by the user within configuration files, following the syntax of the extensible markup language (XML). Such a file generally starts with the definition of geometrical objects, within ⟨geometry⟩ ...⟨/geometry⟩ tags, followed by o the overall definition of a particle's generation and interactions within ⟨kassiopeia⟩ ...⟨/kassiopeia⟩ tags (s. lst. 5.1).

In KASSIOPEIA the particle's propagation is implemented within trajectory classes. A notable algorithm for calculating a charged particle's movement along electromagnetic field
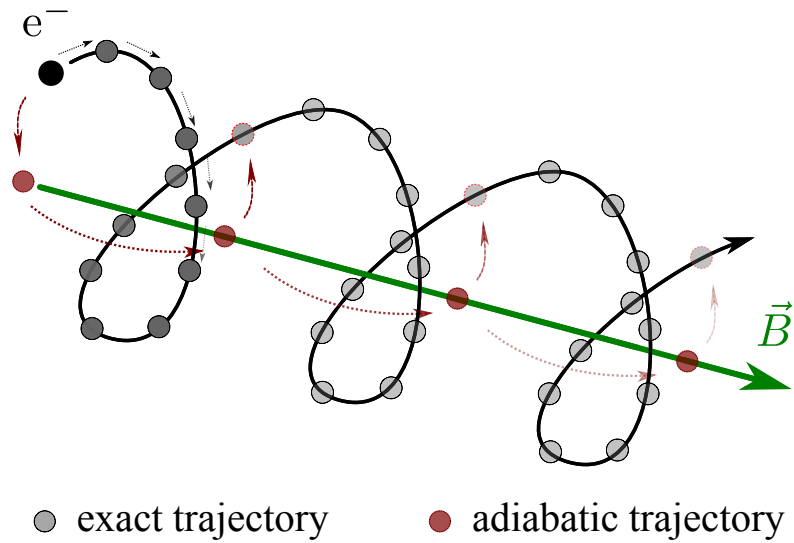
Figure 5.1: Electron propagation along a magnetic field line in the KASSIOPEIA framework. The particle's cyclotron motion depends on its pitch angle and its trajectory is simulated in small 'exact' steps aligned with its path. A quicker implementation projects the particles position on the magnetic field line and reconstructs the true position every other 'adiabatic' step.

lines is the adiabatic trajectory. It differs from a typical exact calculation by advancing the particle along a modified momentum vector. The adiabatic trajectory is based on the assumption that low energy particles move in a periodic cyclotron motion around magnetic field lines. Instead of following their exact circular path, the adiabatic trajectory propagates only the movement of the guiding center. The real position is determined with respect to magnetic drift and the initial circular motions phase (s. fig. 5.1).

Simulation geometry

The simulation results presented in this thesis are based on KASSIOPEIA and make use of an axial-symmetric KATRIN model. The geometry includes the SDS electrodes and magnets with high accuracy. This simulation focuses solely on detector systematics and the STS can be neglected in order to decrease computation time. Electrons are generated in the PS instead.

The simulated chamber at the position of the PS section hence completes the simulation geometry in downstream direction. It functions as a smooth transition for the electromagnetic fields, where the first magnet is used to emulate the field strength of the tritium source: $B_{\text{ps},1} = B_{\text{src}}$.

Just like in the source, electrons are generated isotropically within the magnets center with energies according to tritium beta-decay:

$$
\begin{aligned}
& r_{\text{in}} \in [0\,\text{m}, r_{\text{ps1}}) \text{ homogeneous} && E_{\text{in}} \in [qU_{\text{ret}}, E_0) \text{ beta-decay/uniform} \\
& \varphi_{\text{x,in}} \in [-180°, 180°) \text{ homogeneous} && \varphi_{\text{p,in}} \in [-180°, 180°) \text{ isotropic} && (5.1) \\
& z_{\text{in}} \approx -16.5\,\text{m} && \vartheta_{\text{p,in}} \in [0°, \vartheta_{\text{acc}}] \text{ isotropic}
\end{aligned}
$$

Here the initial radial position of the simulated particles corresponds to homogeneously distributed disc and its size is based on the conservation of the magnetic flux $\phi = B_{\text{src}} \cdot \pi r_{\text{src}}^2 = B_{\text{ps1}} \cdot \pi r_{\text{ps1}}^2$.

In order to reduce computation time only electrons with energies above or equal to the retarding potential $E_{\text{in}} \geq qU_{\text{ret}}$ and only polar angles pointing in forward direction within the cone of magnetic acceptance $\vartheta_{\text{p,in}} \leq \vartheta_{\text{acc}}$ are generated.

In total two different geometries where investigated:

1. A standard KATRIN geometry with electromagnetic field settings according to the "1.6 keV" run during the First Tritium campaign (s. tb. A.1). In addition two different electron generators are investigated: tritium beta-decay electrons which were started in the center of the tuned first PS magnet, as well as a Rydberg background scenario, where electrons are generated the volume of the MS with low initial energies $\mathcal{O}(\text{eV})$.

2. A slightly modified geometry for the future TRISTAN detector [Kor16; Mer19]. The SDD array is positioned a few centimeters $d_1 = z_{\text{SDD}} - z_{\text{det},1}$ downstream of the detector magnet, its vacuum chamber as well as the PAE are enlarged, and a second detector magnet is added at $d_2 = z_{\text{det},2} - z_{\text{SDD}} \overset{!}{=} d_1$. The two magnets are simulated assuming identical magnetic field strengths $B_{\text{det},1} = B_{\text{det},2}$, which ensures perpendicular magnetic field lines at the detector surface.

A typical simulation of electrons traveling in downstream direction is illustrated in figure 5.2. Here the effects of the electric qU_{ret} and magnetic reflection ϑ_{acc} are highlighted.
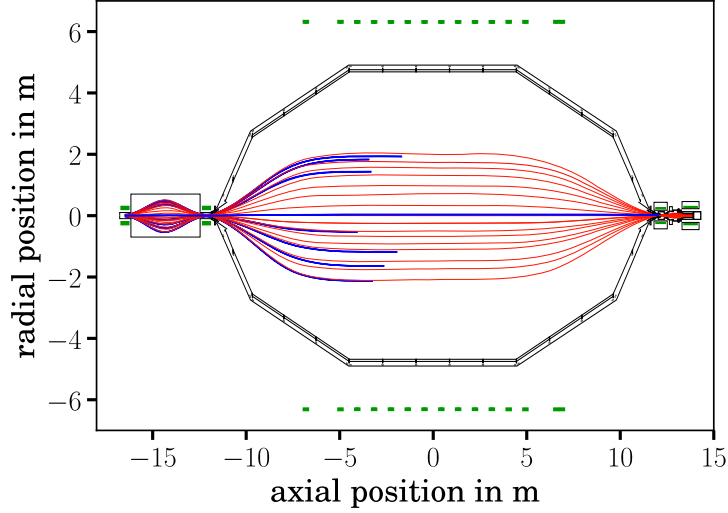
Figure 5.2: Simulated electron trajectories in the SDS with respect to First Tritium settings. Electrons are initialized at $-16.5\,\mathrm{m}$ with conditions similar to the WGTS. Their tracks are colored red if they are transmitted through the MS and blue if they are electrically (U_{ret}) or magnetically (B_{pch}) reflected. A close up of the DS is shown in figure 5.3.

The track simulation is terminated either if an electron travels in upstream direction and exceeds the axial position $z < z_{\mathrm{in}}$ or if it loses all its energy $E_{\mathrm{kin}} < 110\,\mathrm{eV}$.

The energy loss is governed by electron interactions within the silicon bulk of the detector (s. sc. 5.2.1). Internally it is defined as a cylinder consisting of pure silicon with a special set of interactions. The simulated geometry is further sub-divided into a fiducial volume so that only interactions within this volume account for the registered kinetic energy by the detector. For the FPD the fiducial volume starts at $z_{\mathrm{dl}} = 100\,\mathrm{nm}$ into the bulk [Sch14].

A specialty in the simulation is the splitting of tracks upon transmission into the detector's surface as well as into the fiducial volume. It allows for an offline analysis of simulated electron tracks. Especially the effect of back-scattering off the detector leads to a complex position and timing structure (s. sc. 5.2.2) of subsequent detector hits (s. fig. 5.3).

For KATRIN back-scattered electrons travel in upstream direction and are mostly (s. sc. 5.2.2) magnetically ($B_{\mathrm{det}},B_{\mathrm{pch}}$) or electrically reflected ($U_{\mathrm{pae}},U_{\mathrm{ret}}$) back to the FPD.

Accordingly, these particles will deposit their energy multiple times within the detector and thus create a more complex event structure. For the FPD, this structure is function of its 148 pixels and the DAQ system's event time discrimination $t_{\mathrm{min}} = 2 \cdot t_{\mathrm{sh}} + t_{\mathrm{ft}}$.

5.2 Detector related systematics

The complex nature of electromagnetic guidance as well as the subsequent detector scattering inhibit a description with an analytic formula alone. As a consequence, the
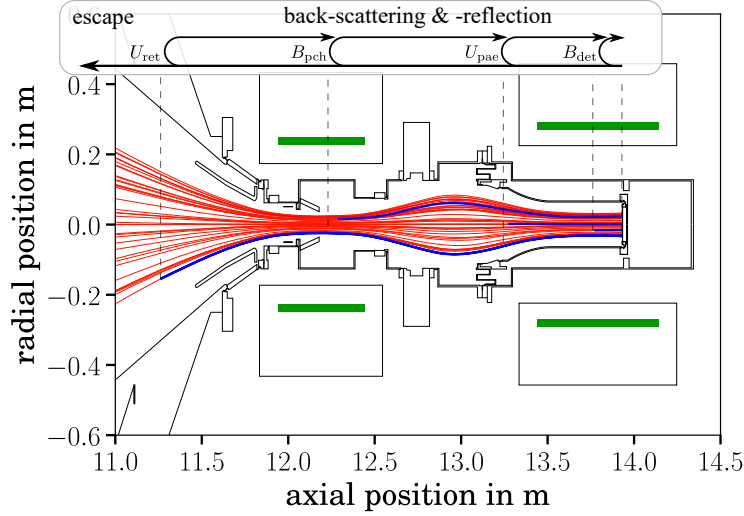
Figure 5.3: Detailed view of simulated electron trajectories including an electron back reflection schema. Electrons originating from the WGTS are colored in red. Tracks of electrons that back-scatter off the FPD and are electromagnetically reflected back to it are colored in blue. In more than $90\,\%$ of all cases they are reflected electrically (U_{pae},U_{ret}) or magnetically (B_{det},B_{pch}) and only a small fraction escapes into the STS.

following analysis comprises both: a part based on simulation as well as an analytic part. Simulations are used in order to derive a realistic energy deposition spectrum of the incident electrons and has three major steps:

- The initial **electromagnetic guidance** of electrons to the detector (s. a.),

- the energy deposition process of electrons by **scattering off silicon** in the detector (see 5.2.1), and

- the subsequent electromagnetic guidance of detector **back-scattered** electrons (see 5.2.2).

The analytic part of the response modeling is based on four systematic effects:

- The charge creation process governed by Fano-like noise (see 5.2.1),

- the process of subsequent **charge-sharing** across neighboring detector pixels (see 5.2.3),

- the contribution of **electronic noise** (see 5.2.4), and

- the impact of signal **pile-up** (see 5.2.4).

In the following the above effects are discussed in detail and their impact to the observed energy response is illuminated. The simulation scenario of detector back-scattering closely

reflects measurement conditions during the First Tritium campaign. Consequently, the presented exemplary energy responses are based on FPD specifications [Eno19; Ake19a]: deadlayer $z_{dl} = 100\,\mathrm{nm}$, energy resolution FWHM $= 2.7\,\mathrm{keV}$ and DAQ timing $t_{min} = 3.6\,\mu\mathrm{s}$.

5.2.1 Electron scattering in silicon

The program KESS, an acronym for KATRIN electron silicon scattering, was specifically developed for the investigation of energy deposition within the detector and is fully integrated in KASSIOPEIA. It features elastic as well as inelastic scattering processes. Several interactions such as photo ionization, delta rays, Auger cascades and surface transmissions are implemented [Ren11].

Scattering profile

Electrons deposit their energy via a multitude of scattering processes. On each interaction they lose some energy and change their direction they travel in. As a consequence the flight path of an electron in the bulk is quite "erratic" and might lead to it exiting the detector, referred to as back-scattering. Thus only some part of the initial kinetic energy E_{in} is deposited while the rest escapes with the back-scattered electron E_{bs}:

$$E_{dep}(E_{in}, \vartheta_{p,in}) = E_{in} - E_{bs}(E_{in}, \vartheta_{p,in}) \,. \tag{5.2}$$

Scattering is non-trivially dependent on the initial energy as well as on the incident angle relative to the surface normal $\vartheta_{p,in}$ [Ren11]. For now the energy dependence is discussed and only perpendicular incidence $\vartheta_{p,in} = 0\,^\circ$ considered.

The simulated detector response for a $E_{in} = 30\,\mathrm{keV}$ is illustrated in figure 5.4b. The effect of back-scattering splits the energy spectrum into two separate regions. Electrons that deposit their whole energy in the detector show a delta-like peak, whereas electrons that have undergone back-scattering show contribute to a low-energy tail.[1]

In figure 5.4b individual simulated trajectories are illustrated. Each corner in the electron track signifies an interaction in the bulk. As scattering and energy loss are stochastic processes the depth and lateral spread of individual electron tracks sharply diverge. While some deposit their whole energy in the bulk, others travel less than a μm and back-scatter after a timescale of ps.

A common approach for characterizing a particle's trajectory in a medium is their energy loss per unit distance, the stopping power $S(E) = \mathrm{d}E/\mathrm{d}x$. For ions with energies $E = \mathcal{O}(\mathrm{MeV})$ the stopping power is mathematically described by the Bethe-Bloch formula [Bet30]. The energy loss curve reaches a maximum just before the particle is fully stopped, which is referred to as Bragg peak [Bra05].

---

[1]Here the simulation of secondary electrons was suppressed. They are more likely to exit the detector with a few $\mathcal{O}(100\,\mathrm{eV})$ and thus slightly spread the delta-like peak to lower energies.

(a) electron energy spectrum

(b) trajectories in silicon
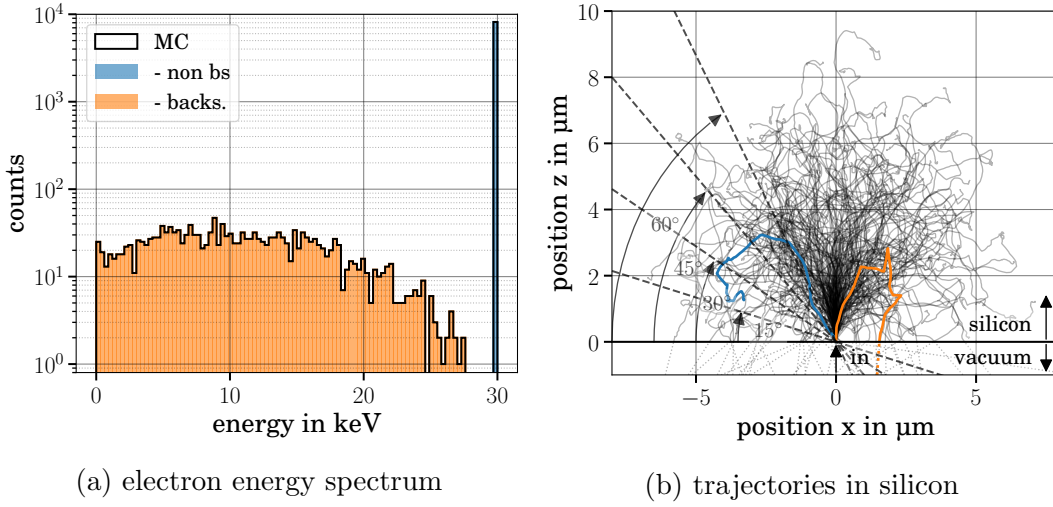
Figure 5.4: (a) Deposited energy histogram of $N_{\text{sim}} = 10^4$ electrons scattering in silicon and (b) subset of 200 individual electron trajectories simulated with KESS. Electrons are initialized at $(0\,\mu\text{m}, 0\,\mu\text{m})$ with perpendicular incidence $\vartheta_{\text{p,in}} = 0\,^\circ$ and constant energy $E_{\text{kin}} = 30\,\text{keV}$. For illustration the partial energy deposition of electrons that back-scatter is highlighted in orange - for a single track on the right. Similarly for non back-scattering in blue. The impact of skewed particle incidence $\vartheta_{\text{p,in}} = 15/30/45/60\,^\circ$ is visually approximated by a rotated detector surface (dashed).

The simulated stopping power of low-energy electrons in vertical and lateral direction for perpendicular incidence is illustrated in figure 5.5a respective 5.5b. An electron with $E_{\text{kin}} = 3\,\text{keV}$ will deposit half its energy within the first $z \approx 150\,\text{nm}$ into the detector. On average it is fully stopped at a depth of $z \approx 200\,\text{nm}$ and similarly in lateral direction for $x \approx 1\,\mu\text{m}$.

The simulated stopping power may be expressed in terms of a polynomial function fitted to the simulated data (s. fig. A.2a):

$$z^{50\%}/\text{nm} \approx 2.45 \cdot (E_{\text{in}}/\text{keV})^2 + 18.1 \cdot (E_{\text{in}}/\text{keV}) + 5.75 \tag{5.3}$$

In case of electrons with a kinetic energy of $E_{\text{in}} = 20\,\text{keV}$, which impinge perpendicular onto the detector $\vartheta_{\text{p,in}} = 0\,^\circ$, they will deposit on average half of their energy within the first $z^{50\%}(20\,\text{keV}) = 1.3\,\mu\text{m}$ into the detectors bulk. Similarly the radial spread of the deposited energy has on average half the energy lost within a distance of $r^{50\%} \approx 1.1\,\mu\text{m}$ to the initial impingement position.

(a) detector depth

(b) lateral direction
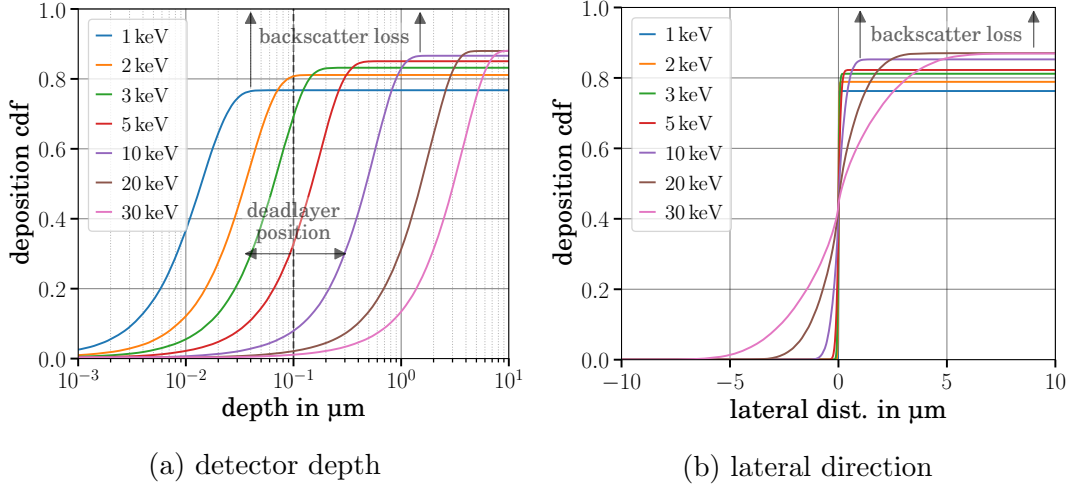
Figure 5.5: Cumulative energy deposition of electrons in silicon along the detectors depth (left) and lateral direction x (right). The stopping power corresponds to point where the the energy loss of back-scattered electrons leads to a plateau below one. Different simulated electron energies E_{kin} are represented in color.

Deadlayer

An important characteristic of electron energy measurements with solid state detectors, including SDDs, is the detection deadlayer. It describes region near the surface where created electron-holes are not or only partly collected.

On an atomic level the surface of the detector consists of a small layer of oxidized silicon SiO_2. It forms in a natural way when the detector is exposed to air. As this layer is electrically insulating charge carriers are not collected and the layer contributes a dead region. Further inside the bulk electron-hole pairs start to feel the inner electric fields created by the electrodes. Close to the surface charge collection is however influenced by the doping profile. A Gaussian profile with a mean at $\mu = 50\,\mathrm{nm}$ depth would lead to low charge collection efficiencies at shallow depths $z < \mu$ and quickly converge to 100% for $z > \mu$ [Lec98; Pop00].

In this thesis a basic effective model was assumed, neglecting depth-dependent charge collection. In the simulation the silicon bulk is divided into a fiducial detector volume that starts at a certain depths $z > z_{\mathrm{dl}}$, and all interactions in the insensitive part $z < z_{\mathrm{dl}}$ are discarded. The measured energy is thus diminished by the amount lost in the deadlayer E_{dl}:

$$E_{\mathrm{meas}} = E_{\mathrm{dep}} - E_{\mathrm{dl}} = E_{\mathrm{in}} - E_{\mathrm{bs}} - E_{\mathrm{dl}} \ . \tag{5.4}$$

In figure 5.6a the influence of a non-zero detection deadlayer to the detector response is depicted. In particular electrons that do not back-scatter would still lose some energy within the deadlayer and might be even stopped entirely therein. The amount lost in the

(a) electron energy spectrum   (b) deposition along detectors depth
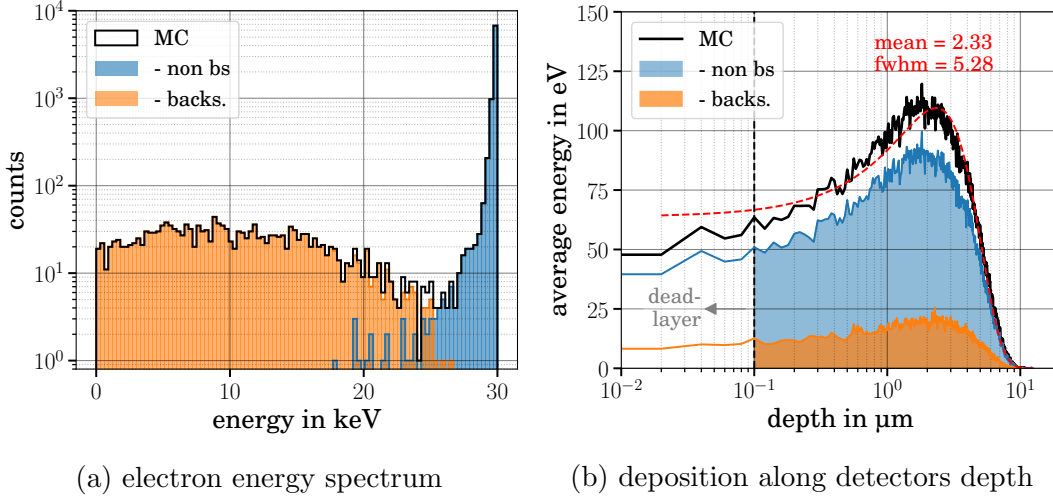
Figure 5.6: Impact of a detector deadlayer on ()a) the measured electron energy spectrum and (b) the average energy deposited in slices along the detectors depth z. A non-zero deadlayer $z_{dl} = 100\,\text{nm}$ broadens the registered energy peak $E_{in} = 30\,\text{keV}$ of non back-scattered electrons (shaded blue). For comparison the energy deposition along the depth of the detector is fitted with a Gaussian (red dashed).

deadlayer depends on its thickness (s. fig. 5.6a) and in case of $z_{dl} = 100\,\text{nm}$ electrons would lose on average about $340\,\text{eV}$ therein.

Using parameterization 5.3 the kinetic energy where the impact of the deadlayer starts to dominate can be mathematically derived:

$$z^{50\%} \overset{!}{=} z_{dl} \longleftrightarrow \quad \frac{E_{in}}{\text{keV}} = \frac{-21.6 \, (\overset{+}{_-}) \sqrt{21.6^2 - 4 \cdot 2.36 \cdot (36.4 - z_{dl}/\text{nm})}}{2 \cdot 2.36} \,. \tag{5.5}$$

Thus a deadlayer thickness $z_{dl} = 50\,\text{nm}$ ($100\,\text{nm}$) ensues that low-energy electrons with roughly $E_{in} = 1.9\,\text{keV}$ ($3.5\,\text{keV}$) would lose on average half of their total energy within the deadlayer.

Energy response

Finally, silicon detectors are not sensitive to the deposited energy but the number of charge carriers N_{eh} created within the sensitive bulk. This leads to a small energy dependent broadening over the entire energy spectrum (s. eq. 4.4).

Analytically Fano-like broadening may be incorporated by an energy dependent convolution approach or by randomly drawing the number of created electron-hole pairs. Both are based on a normal distribution with mean μ and standard deviation σ:

$$N_{eh} = \frac{E_{meas}}{E_{eh}} \longrightarrow \quad \mu = E_{meas} \quad \& \quad \sigma = \sqrt{f E_{eh} E_{meas}} \,. \tag{5.6}$$
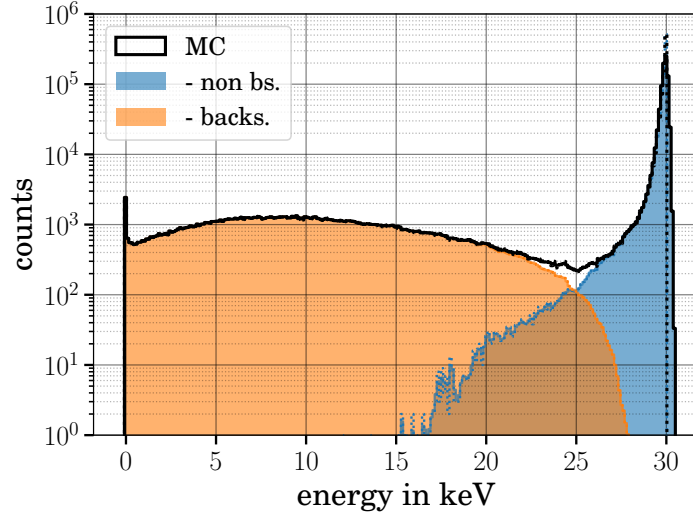
Figure 5.7: Simulated energy response of $E_{kin} = 30\,keV$ electrons for statistics of $N_{sim} = 10^6$ (black). The introduction of Fano-noise broadens the non back-scattering region (blue shaded) and is less visible in the back-scattering part (orange shaded).

In figure 5.7 a simulation with $N_{sim} = 10^6$ electrons, a deadlayer of $z_{dl} = 100\,nm$ and perpendicular incidence $\vartheta_{p,in} = 0\,°$ is depicted. The underlying simulation processes include the tracking of ionized secondary electrons and leads to an increase at the lowest energies $E_{meas} \approx 0\,keV$. Apparently, Fano-like noise has a higher contribution at large energies and visibly broadens the peak at $E_{meas} \approx E_{kin}$.

A complication of the measured energy response is the electrons incidence angle onto the detector. On average it may be described by a tilt of its trajectory within the bulk (s. fig. 5.4b). In the effective deadlayer model this procedure would virtually enlarge its movement therein:

$$z_{dl}^{virt} \approx z_{dl}/\cos(\vartheta_{p,in}) \,, \tag{5.7}$$

where the incidence angle $\vartheta_{p,in}$ is defined with respect to the surface normal vector - perpendicular incidence $\vartheta_{p,in} = 0\,°$.

In particular the detector response for non back-scattered electrons may be approximated by this virtual deadlayer thickness (s. fig. 5.8).

In summary, the response of electron scattering off silicon is coarsely distinguished between the fraction $(1 - P_{bs})$ that deposits all of the energy in the bulk and the fraction P_{bs} that deposits only some part of its initial energy and escapes the detector. The former shows a sharp maximum at the incident energy E_{kin}, while the latter gives a tail to lower energies. The insensitive region at the first $100\,nm$ of the detector largely suppresses low-energy electrons $E_{kin} \lesssim 3.5\,keV$. For higher energies the suppression decreases and the response can be described by a one-sided broadening and shift of the maximum deposited energy to lower values. This effect is further accentuated by a skewed particle incidence $\vartheta_{p,in} \neq 0\,°$.
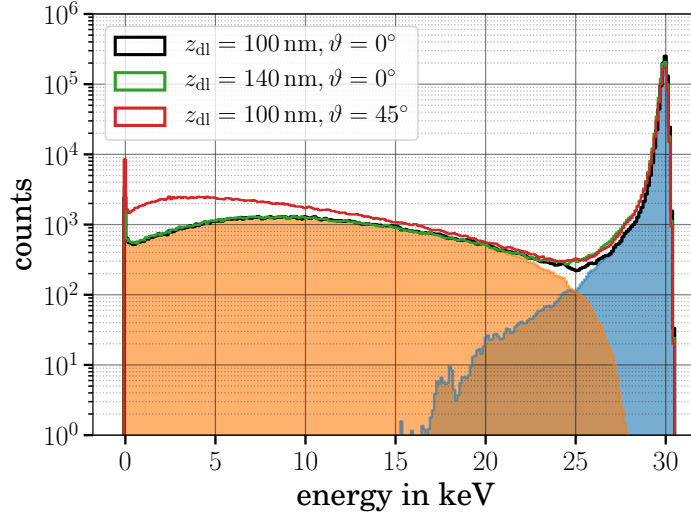
Figure 5.8: Simulation of the detector energy response to $N_{\text{sim}} = 10^6$ electrons with $E_{\text{kin}} = 30\,\text{keV}$. The case $z_{\text{dl}} = 100\,\text{nm}$ and $\vartheta_{\text{p,in}} = 0\,^\circ$ is given in black and the fraction of (non) back-scattered electrons is shaded in (blue) orange. An increase of the deadlayer $z_{\text{dl}} = 140\,\text{nm}$ (green) and similarly a skewed incidence $\vartheta_{\text{p,in}} = 45\,^\circ$ (red) result in a broadening of the non back-scattered peak.

5.2.2   Electron back-scattering and -reflection

Electron scattering off silicon atoms ensues a probability P_{bs} that the incident electron back-scatters. The back-scattered electron is described by its energy E_{bs} as well as the direction $\vartheta_{\text{p,bs}}$, forming a two dimensional distribution ρ_{bs}:

$$P_{\text{bs}}(E_{\text{in}}, \vartheta_{\text{p,in}}) \overset{>10\,\text{keV}}{\approx} 20\% + \left[P_{\text{bs}}(\vartheta_{\text{p,in}}) - P_{\text{bs}}(0^\circ) \right] \tag{5.8}$$

$$\rho_{\text{bs}}(E_{\text{bs}}, \vartheta_{\text{p,bs}}) \equiv \rho_{\text{bs}}(E_{\text{bs}}, \vartheta_{\text{p,bs}}, E_{\text{in}}, \vartheta_{\text{p,in}}) . \tag{5.9}$$

Both are depended on the incident electrons energy E_{in} and angle $\vartheta_{\text{p,in}}$ [Ren11] as well as on the orientation of crystal layers in the silicon detector [Ber02] (s. fig. A.3).

At KATRIN back-scattered electrons experience a strong magnetic B_{sur} and an electric potential $U = U_{\text{pae}} + U_{\text{BF}}$ prevalent at the detector surface. According to ρ_{bs} they would travel in upstream direction where they undergo a magnetic field change induced by the detector and pinch magnet ($B_{\text{det}}, B_{\text{pch}}$) and similarly a electric potential field change induced by the detector bias, the PAE and the MS retardation potential ($U_{\text{BF}}, U_{\text{pae}}, U_{\text{ret}}$) (s. fig. A.4).

Similarly to the MS transmission function, the magnetic and electric potentials act like a transmission barrier. Electrons that are back-scattered with low energies E_{bs} or under shallow angles $\vartheta_{\text{p,bs}}$

$$E_{\text{bs}} < qU_{\text{pae}} + qU_{\text{BF}} \quad \& \quad E_{\text{bs}} < qU_{\text{ret}}$$
$$180 - \vartheta_{\text{p,bs}} < \vartheta_{\text{acc}}^{\text{pch}} \quad \& \quad 180 - \vartheta_{\text{p,bs}} < \vartheta_{\text{acc}}^{\text{det}} \tag{5.10}$$

are electromagnetically reflected back to the detector (s. fig. 5.3), whereas the transmitted electrons escape to the RW.

Back reflection

The probability of being reflected back to the detector P_{ref} depends on the back-scattered parameters ρ_{bs} and its evolution along the electric retardation (U_{pae},U_{ret}) and adiabatic magnetic guidance (B_{det},B_{pch}). Although the reflection is a combination of both fields, it can be approximated as the sum of individual components:

$$P_{\text{ref}} = P_{\text{ref}}^{\text{ret}} + P_{\text{ref}}^{\text{pch}} + P_{\text{ref}}^{\text{pae}} + P_{\text{ref}}^{\text{det}} . \tag{5.11}$$

Depending on the exact reflection mechanism, electrons travel further upstream so that their inter-event time back onto the detector will show characteristic peaks (s. fig. 5.9b). The shortest inter-event times $\Delta t < 0.3\,\mu$s are associated to magnetic reflection $P_{\text{ref}}^{\text{det}}$ within the detector magnet. Next, a sharp peak is visible at $\Delta t = 0.3\,\mu$s, which corresponds to the position of the PAE and represents electric reflection $P_{\text{ref}}^{\text{pae}}$. In a similar fashion the impact of the pinch magnet $\Delta t \approx 0.6\,\mu$s and the retardation voltage $\Delta t \gtrsim 0.9\,\mu$s become visible.

Back-scattered electrons that are back-reflected will re-hit the detector at a new location. In contrast to the inter-event time, the positional change at the detector Δx is less affected by the reflection mechanism (s. fig. 5.9a). In adiabatic approximation the particles movement is separated into a cyclotron component $\vec{x}_{\text{L}}$ around the magnetic field as well as the drift of the guiding center x_{gc} [Fur17]. The position change at the detector is then given as

$$\Delta x \quad = \quad |\vec{x}_{\text{L}} + \vec{x}_{\text{gc}}| \ , \text{with} \tag{5.12}$$

$$|\vec{x}_{\text{L}}| \quad = \quad r_{\text{L}} = \frac{m_{\text{e}}c\sqrt{\gamma_0^2 - 1}}{eB_{\text{sur}}} \ \text{and} \tag{5.13}$$

$$\frac{\text{d}\vec{x}_{\text{gc}}}{\text{d}t} \quad = \quad \frac{\vec{E} \times \vec{B}}{B^2} + \frac{2p_\parallel^2 + p_\perp^2}{qm(\gamma + 1)B^3}\vec{B} \times \vec{\nabla}B \ . \tag{5.14}$$

Here $\vec{E}$ and $\vec{B}$ are the electromagnetic fields defined with respect to the guiding center and γ is the relativistic Lorentz factor. At the SDS the positional change of the cyclotron component is larger and the drift of the guiding center ensues a radially increasing clockwise displacement [Kor16].

(a) FPD position shift

(b) FPD inter-event time
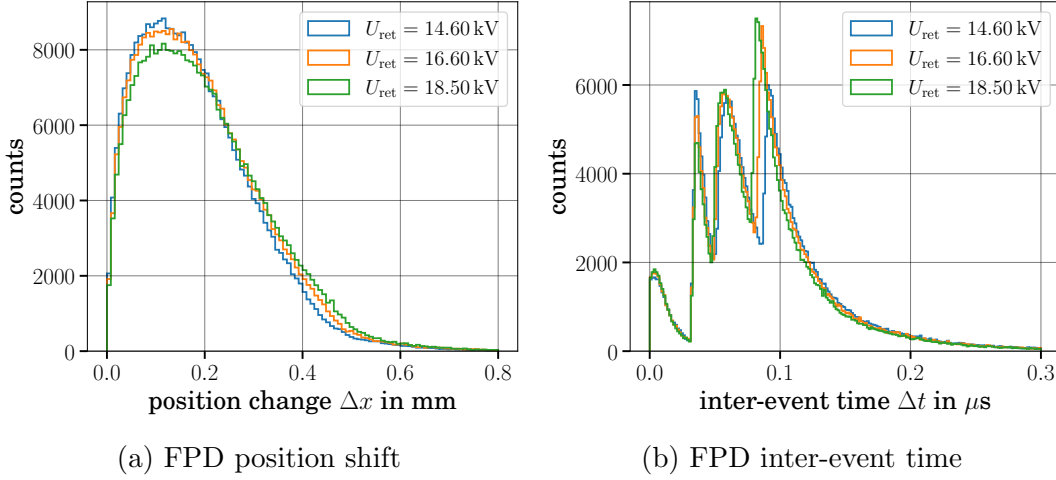
Figure 5.9: Tritium beta-decay electrons with "1.6 keV" run field settings: position change $\Delta x = x_\mathrm{fi} - x_\mathrm{in}$ (a) and inter-event time $\Delta t = t_\mathrm{fi} - t_\mathrm{in}$ (b) for electrons that back-scatter off the detector $(x_\mathrm{in}, t_\mathrm{in})$ and are back-reflected onto it $(x_\mathrm{fi}, t_\mathrm{fi})$ (s. fig. 5.3). Both slightly depend on the retarding potential values U_ret.

In order to determine the detector energy response, the position change has to be compared to the detector pixel geometry and the inter-event time to DAQ energy filter. A back-scattered electron would only show as two events, if the position change moves the second hit to a neighboring detector pixel or if the subsequent hit in the same pixel is distinguishable by the DAQs filter.

For the FPD in the tritium beta-decay scenario with "1.6 keV" run field settings . . .

- . . . the overall *multiplicity* of individual beta-decay electrons is illustrated in figure 5.10a. Electrons that do not back-scatter and electrons that back-scatter but re-hit the same pixel are illustrated at a multiplicity of zero. The fraction of high multiplicities $m \geq 1$ is around 1% and is more pronounced for high retarding potentials U_ret (s. eq. 5.12) as well as FPD pixels in the outer rings, since the pixels at the rim are thinner compared to the inner counterparts.

- . . . the inter-arrival time of electrons is illustrated in figure 5.10b. Here electrons that deposit their contribute to the peak at $t = 0\,\mu\mathrm{s}$, whereas back-scattering with subsequent back-reflection creates non zero inter-arrival times. The maxima related to the point of reflection are smeared by multiple scattering processes. The inter-arrival times are independent of U_ret and centered around $t \approx 0.3\,\mu\mathrm{s}$. Only a small fraction $\approx 0.1\%$ of electrons contribute to larger values $t \gtrsim 0.4\,\mu\mathrm{s}$.

Comparing the minimum discrimination time

$$t_\mathrm{min} = 2 \cdot t_\mathrm{sh} + t_\mathrm{ft} = (3.2 + 0.2)\,\mu\mathrm{s} \tag{5.15}$$

(a) FPD event multiplicity

(b) inter-arrival time
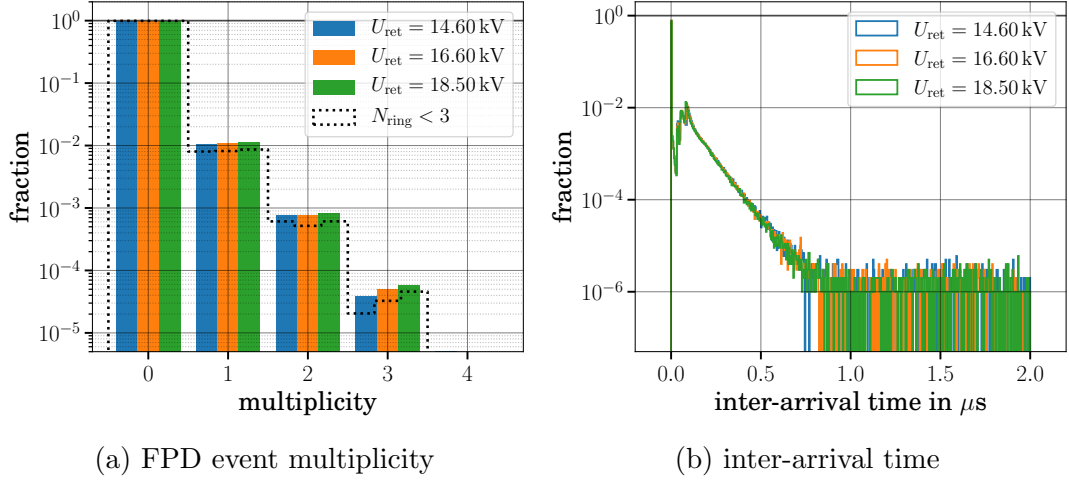
Figure 5.10: Tritium beta-decay "4 keV" run: Overall multiplicity (a) and inter-arrival times (b) of simulated electrons. Here three exemplary retarding potential settings are depicted in color. In addition the multiplicity shows the same distribution but for the innermost FPD rings (+bullseye). The inter-arrival time is calculated relative to the first impingement on the detector and the peak at $t = 0\,\mu\text{s}$ thus corresponds to the $\approx 80\%$ of electrons that don't back-scatter.

of the FPD system with the simulated inter-event time and inter-arrival times shows that back-reflected electrons are not discriminated by the DAQ system. Instead the short timings $\mathcal{O}(0.3\,\mu\text{s})$ are more likely to impact the energy determination of the DAQ system (s. sub-sc. 5.2.4).

Electron escape

An important characteristic of back-scattering is the fraction P_{esc} of electrons that escape into the STS part and are not back-reflected P_{ref} to the detector. The escape fraction is determined by counting the number of electrons that escape after their first back-scattering as well as subsequent back-reflection/-scattering escapees:

$$
\begin{aligned}
P_{\text{esc}} = \frac{N_{\text{esc}}}{N_{\text{in}}} &= 1 - P_{\text{ref}} \\
&= P_{\text{bs},1}(1 - P_{\text{ref},1}) + P_{\text{bs},1}P_{\text{ref},1}P_{\text{bs},2}(1 - P_{\text{ref},2}) + \dots \, .
\end{aligned}
\tag{5.16}
$$

Here N_{in} represents the number of electrons that initially reach the detector and N_{esc} are all events that exit the MS in upstream direction. Similarly, the number may be expressed by the recursive sum of i-times back-scattering $P_{\text{bs},i}$ and back reflection $P_{\text{ref},i}$.

Electrons escaping into the STS are most likely only stopped within the RW. The small fraction that back-scatters off the RW is unlikely to be registered at the detector as it is suppressed by magnetic reflection ($B_{\text{rw}},B_{\text{pch}}$) and retardation ($U_{\text{ret}}$). Electron escape thus signifies a real loss of rate that has to be accounted for.
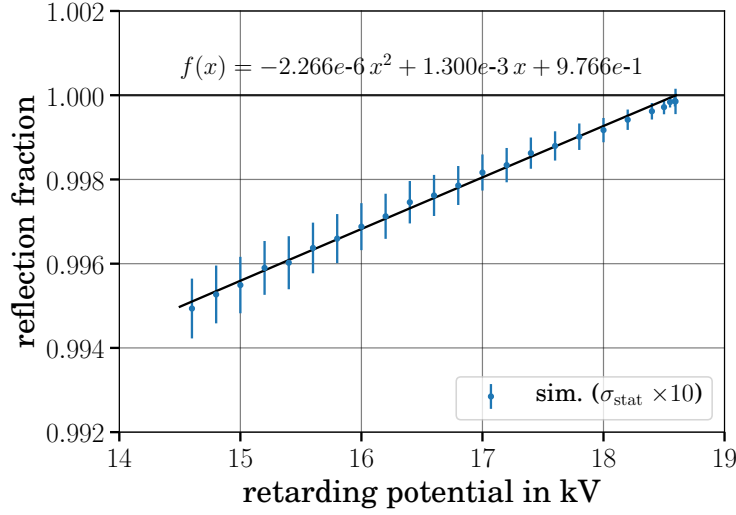
Figure 5.11: Displayed is the fraction of back-reflected electrons P_{ref}. Electrons that are not reflected will escape detection with the probability $P_{\text{esc}} = 1 - P_{\text{ref}}$. A second order polynomial fit is given in black.

In figure 5.11 the fraction of electron escape for different simulated retardation potentials U_{ret} is illustrated as the fraction $1 - P_{\text{esc}}$.

As back-scattered electrons have lost some energy within the detector, the fraction of electron escape becomes zero at the spectrum endpoint $P_{\text{esc}}(qU_{\text{ret}} = E_0) = 0$. In contrast a potential of $U_{\text{ret}} = 14.6\,\text{kV} = E_0 - 4\,\text{keV}$ ensues that roughly $P_{\text{esc}} = 0.5\,\%$ of back-scattered electrons escape. Due to reflection at the magnets and the PAE (s. fig. 5.9b), the overall fraction of electron escape is limited to

$$P_{\text{esc}} \lessapprox 30\% \cdot P_{\text{bs}} \approx 6\% \;. \tag{5.17}$$

Energy response

For multiple back-reflection processes the measured energy in the detector must account for the number of times i that an electron hits the detector:

$$E_{\text{meas}}^{(i)} = E_{\text{in}}^{(i)} - E_{\text{bs}}^{(i)} - E_{\text{dl}}^{(i)} = E_{\text{in}}^{(i)} - E_{\text{in}}^{(i+1)} - E_{\text{dl}}^{(i)} \;, \tag{5.18}$$

where $E_{\text{bs}}^{(i)} = E_{\text{in}}^{(i+1)}$ and $E_{\text{in}}^{(0)} = E_{\text{kin}}$. The overall amount of energy deposited in the detector for an electron that is stopped ($E_{\text{bs}}^{(m)} = 0$) or that escapes ($E_{\text{bs}}^{(m)} = E_{\text{esc}}$) on its m-th incidence is then given by the sum over the individual contributions

$$E_{\text{meas}} = \sum_{i=0}^{m} E_{\text{meas}}^{(i)} = E_{\text{kin}} - E_{\text{esc}} - \sum_{i=0}^{m} E_{\text{dl}}^{(i)} \;. \tag{5.19}$$
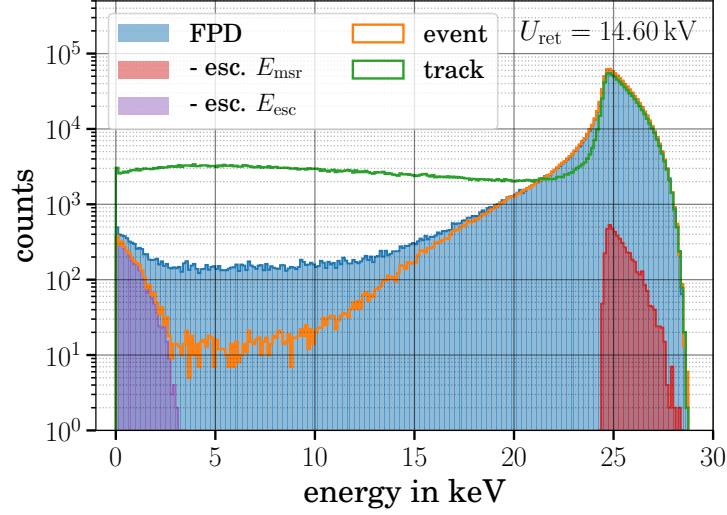
Figure 5.12: Simulated beta-decay electron response with respect to back-reflection. The blue graph represents the total amount of energy that electrons deposit in the sensitive silicon bulk. Back-scattering is marked on track level in KASSIOPEIA and consequently leads to more low energy events (green). Lost energy E_{esc} due to electron escape is colored in orange and the measured fraction colored red.

The overall measured energy is reduced by m-times passing through the deadlayer as well as the energy E_{esc} lost by electrons that escape to the STS.

An exemplary energy spectrum $U_{ret} = 14.6\,\text{kV}$ for the FPD is shown in figure 5.12. The underlying simulation framework allows for an investigation of E_{meas} on several levels:

- The response at track-level is dominated by the effect of silicon scattering and shows the characteristic low energy tail and peak (s. fig. 5.8).

- On event-level back-reflection suppresses the back-scattered energy tail while ensuing an increased loss in the detection deadlayer (s. eq. 5.19).

- The 148 pixels of the FPD in concert with the DAQ filter length $t_{min} = 3.6\,\mu\text{s}$ gives a spectrum shape situated in-between the pure track- and event-level response.

- Independent of the event structure is the energy loss E_{esc} due to back-scattering escape. In KASSIOPEIA this contribution is selected via terminator flag and the loss occurs at the highest $\geq qU_{ret} + qU_{pae} + qU_{BC}$.

In summary the detector response at KATRIN is strongly affected by the electromagnetic settings, by the detector geometry and by the DAQ timing. In particular, the inter-event time as well as the position change have to be considered. Notably, the guiding center drift (s. eq. 5.14) which introduces a radial dependent position change.

The consequences of back-reflection are encoded in equation 5.19: the back-scattering low-energy tail is suppressed $E_{bs}^{(i)} \longrightarrow E_{esc}$ and the impact of the detection deadlayer increases $\sum_{i=0}^{m} E_{dl}^{(i)}$.

5.2.3   Pixel charge-sharing

Another characteristic of silicon detectors is related to the profile of the created charge carriers and the propagation of charges while traveling to the readout electrode. In silicon an incident electron with $E_{\mathrm{kin}} = 30\,\mathrm{keV}$ will roughly create $N_{\mathrm{eh}} = 8 \cdot 10^3$ electron-hole pairs (s. sc. 4.2). The spatial distribution of these charges is referred to as charge cloud and its dimensions are described by the charge cloud radius r_{cc}.

Both the FPD and the TRISTAN detectors are sub-divided into pixels. If an incident particle impinges within a distance Δx to an adjacent pixel, the charge cloud may cover both pixels sot that the charges are split among the two readout electrodes ($\Delta x < \mathcal{O}(r_{\mathrm{cc}})$). Overall the expansion of the charge cloud is affected by the initial energy deposition profile from electron-silicon scattering (s. sc. 5.2.1) and by the charge clouds expansion during the drift to the electrodes [Gat84; Gat87] - described by thermal diffusion as well as electric repulsion.

- *Thermal diffusion* is a temperature dependent stochastic scattering process of charge carriers during charge collection. It may be described as a Gaussian broadening of the cloud over time

$$n(x,t) \quad = \tfrac{1}{\sqrt{2\pi}\cdot\sigma} \exp\!\Big(-\tfrac{(x-\mu E_x t)^2}{2\cdot\sigma^2}\Big) \,, \quad \sigma(t) = \sqrt{2Dt} \,, \tag{5.20}$$

  where μ signifies the mobility and D the diffusion coefficient of charge carriers in silicon [Gat87]. The charge cloud radius can be identified by the standard deviation of the Gaussian broadening and in some detector scenarios it is possible to remove the time dependence and replace it with the bias potential U_{BF} applied to the back frame and the detector wafer thickness d [Ini07]

$$\sigma = \sqrt{2Dt_{\mathrm{drift}}} \longleftrightarrow \quad \sigma = d\frac{k_{\mathrm{B}}T}{qU_{\mathrm{BF}}} \,. \tag{5.21}$$

  For a $d = 450\,\mu\mathrm{m}$ thick detector operated at room temperature $T = 300\,\mathrm{K}$ and $U_{\mathrm{BF}} = -100\,\mathrm{V}$, gives a standard deviation of $\sigma = 10\,\mu\mathrm{m}$. The same applies for a drift time of $t_{\mathrm{drift}} = 20\,\mathrm{ns}$ and diffusion coefficient of $D = 36\,\mathrm{cm}^2/\mathrm{s}$.

- The charge spread due to *mutual repulsion* can be approximated by describing the created charge carriers $N_{\mathrm{eh}}\,(E_{\mathrm{kin}}/E_{\mathrm{eh}})$ with a basic spherical model. The resulting distribution has a well-defined radius

$$r(t) = \sqrt[3]{\frac{3\mu q}{4\pi\epsilon} \cdot N_{\mathrm{eh}} \cdot t_{\mathrm{drift}}} \,, \tag{5.22}$$

with the absolute permittivity $\epsilon = \epsilon_0 \cdot \epsilon_r$. For the case of a $t_{drift} = 20\,\text{ns}$ drift time and an electron energy of $E_{kin} = 30\,\text{keV}$ ($N_{eh} = 8 \cdot 10^3$) a radius of $r = 20\,\mu\text{m}$ is expected [Gat87].

The assumption of an initial spherical charge cloud however is not appropriate as charges are created along the elongated path of the incident particle. For electrons individual tracks are spread over several μm (s. fig. 5.4b).

- The initial energy *deposition profile* is given by scattering from the incident particle off silicon atoms in the detector, as discussed in 5.2.1. The overlap to a neighboring pixels would be then determined by its lateral distribution (s. A.1). The simulated average 90% energy deposition volume is approximately given by a second order polynomial:

$$x^{90\%}/\text{nm} = 3.47 \cdot (E_{kin}/\text{keV})^2 + 24.7 \cdot (E_{kin}/\text{keV}) - 25.9 \,. \tag{5.23}$$

In case of a $E_{kin} = 30\,\text{keV}$ electron 90% of the charges would be thus created within a lateral distance of $\leq 3.84\,\mu\text{m}$ to the point of impact.

In addition to the above effects one has to distinguish between the drift of electrons or holes to the readout electrode. The FPD is based on hole collection parallel to the surface normal. The TRISTAN detectors are based on electron collection and charges experience an additional lateral drift field component. Such a field will electrically guide charges away from the pixel boundary. At the boundary between pixels the lateral electric field however cancels out.

To study this effect first charge-sharing estimates were performed in [Sch14] for the FPD and in [Alt19; Urb19] for the TRISTAN prototype detectors (s. also [Gat84; Gat87; Mat02; Ini07]).

In figure 5.13 the standard deviation from thermal diffusion, the radius from mutual repulsion and the energy deposit quantile from scattering are illustrated for different drift times as well as electron energies.

For a direct comparison of the effects it is vital to transform σ, r and $x^{90\%}$ to a common quantity. A sensible way to achieve this is the definition of the charge cloud radius via the coverage of the respective distributions.

Model

In this thesis only charge-sharing of two pixels is modeled and the charge cloud is assumed to be defined solely by a normal distribution $\mathcal{N}(x, \mu, \sigma)$ along a single given axis x. The charge cloud radius r_{cc} is than defined as

$$r_{cc} = \text{FWHM}/2 = \sqrt{2\ln 2} \cdot \sigma \,. \tag{5.24}$$
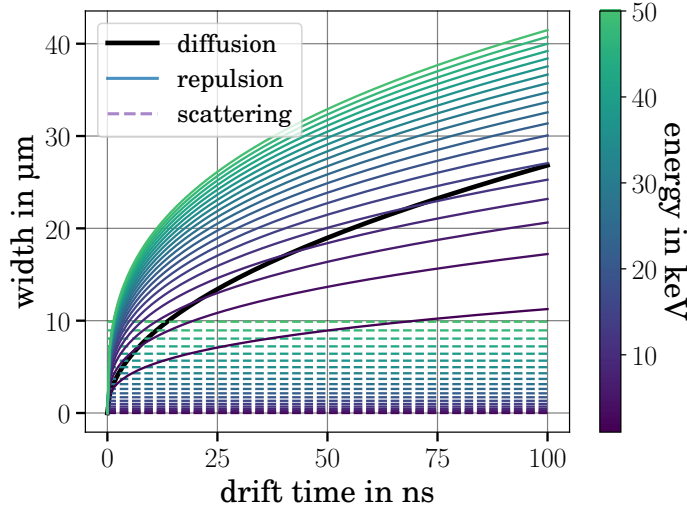
Figure 5.13: Charge cloud distribution width over the drift time for a silicon based detector with electron collection. The energy dependence is given in color for electric repulsion (solid lines) as well as scattering (dashed lines). For diffusion its standard deviation σ (black), for electric repulsion the sphere radius r and for scattering $x^{90\%}$ are illustrated.

As a consequence charge-sharing events are only counted as such, once the number N_{cs} of charge carriers that spill over to a neighboring pixel exceed a certain threshold, here at roughly 12% of the created charges.

Mathematically, the number of charges shared depends on the relative distance Δx of a particle's incidence to the pixel boundary

$$N_{cs} = N_{eh} \cdot \eta(\Delta x) = N_{eh} \int_{\Delta x}^{\infty} \mathcal{N}(x, \mu, \sigma) \mathrm{d}x \tag{5.25}$$

where η is defined as the fraction of shared charges.

To characterize charge-sharing the probability distribution of spilled charges $P(\eta(\Delta x))$ is investigated:

$$\frac{\mathrm{d}P}{\mathrm{d}\eta} = \frac{\mathrm{d}P}{\mathrm{d}\Delta x} \cdot \frac{\mathrm{d}\Delta x}{\mathrm{d}\eta} = \frac{\mathrm{d}P}{\mathrm{d}\Delta x} \cdot \frac{\mathrm{d}}{\mathrm{d}\eta} \left[\eta^{-1}(\Delta x) \right] , \tag{5.26}$$

where η^{-1} denotes the inverse function (s. eq. 5.25) and $\frac{\mathrm{d}P}{\mathrm{d}\Delta x}$ describes the positional distribution of particle incidence. A homogeneous detector illumination will give a constant factor $\frac{\mathrm{d}P}{\mathrm{d}\Delta x} = 1/s$, according to a uniform distribution with width s.

The fraction of charge-sharing η, its inverse η^{-1} as well as the final differential thereof can easily be calculated numerically. For a given window length of $s = 2\,\mathrm{mm}$ the resulting probability is illustrated in figure 5.14.
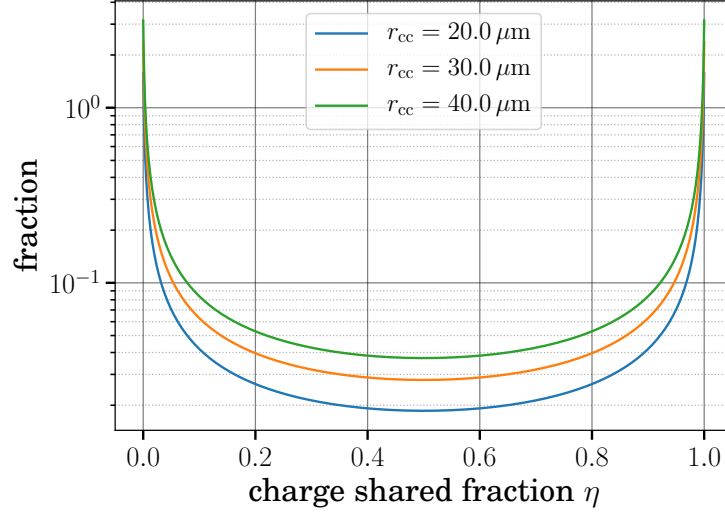
Figure 5.14: Probability density of the charge-sharing fraction η, for uniform particle incidence $s = 2\,\mathrm{mm}$ and normal-distributed charge cloud.

Finally, the detector geometry is included via normalization. It was assumed that the uniform approximation holds for all positions along a pixel's perimeter L_{px}. The expected probability of charge-sharing P_{cs} can then be calculated with respect to the pixels surface area A_{px}:

$$P_{\mathrm{cs}} \approx \frac{L_{\mathrm{px}} \cdot 2 r_{\mathrm{cc}}}{A_{\mathrm{px}}} = 2 \cdot \int_{0.12}^{0.88} \mathrm{d}\eta \; \frac{\mathrm{d}P}{\mathrm{d}\eta} \; . \tag{5.27}$$

Here the integration boundaries for the normalization are rough estimates of the charge cloud's coverage within the radius r_{cc} (s. eq. 5.24).

Energy response
The number of charges shared with neighboring pixels N_{cs} directly results in a reduction of the measured energy

$$E_{\mathrm{meas}} = E_{\mathrm{kin}} - E_{\mathrm{bs}} - E_{\mathrm{dl}} - E_{\mathrm{cs}} \; , \tag{5.28}$$

where the shared energy is $E_{\mathrm{cs}} \equiv E_{\mathrm{cs}}(\Delta x) = E_{\mathrm{eh}} \cdot N_{\mathrm{cs}}(\Delta x)$. As a consequence, the detector will measure two separate events related to the same initial particle, but with two distinct energies

$$E_{\mathrm{meas},1} = E_{\mathrm{meas}} \quad \mathrm{and} \quad E_{\mathrm{meas},2} = E_{\mathrm{cs}} \; . \tag{5.29}$$

In figure 5.15 the resulting detector response is illustrated. The model includes the analytic model of charge-sharing as well as the simulated effect of electron scattering in silicon and
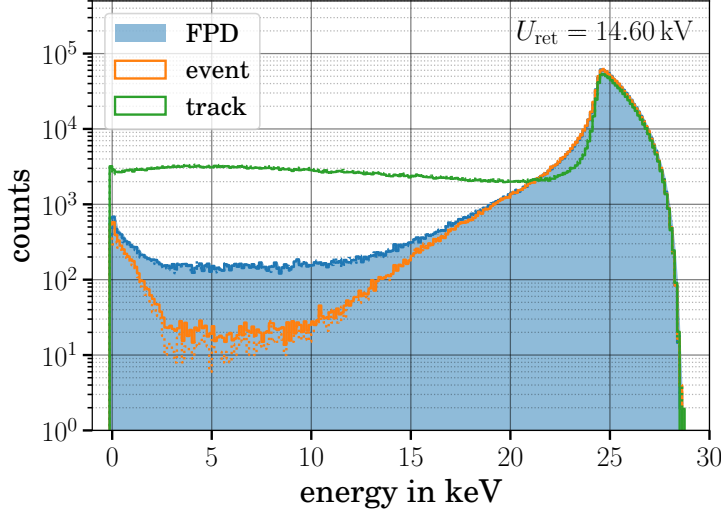
Figure 5.15: Simulated beta-decay electron response with respect to detector scattering, back-scattering and charge-sharing. Event (track) level simulation is depicted in orange (green) and the response without charge-sharing is shown as dotted lines ($3\%/N_{\mathrm{bin}}$-effect visible around $E_{\mathrm{kin}} = 5\,\mathrm{keV}$).

back-scattering off the detector. On average roughly 3% charge-sharing events is expected for a charge cloud radius of $r_{\mathrm{cc}} = 20\,\mu\mathrm{m}$ at the FPD (s. fig. A.11).

The addition of charge-sharing to the response leads to a small broadening of the non back-scattered regions and a slight rate increase at low energies $E < E_{\mathrm{dep}}/2$. In principle it is possible to discriminate events related to charge-sharing by applying energy- ($E_1 + E_2 \approx E_{\mathrm{kin}}$) and time-coincidence ($t_2 - t_1 < 0.2\,\mu\mathrm{s}$) filters. This approach however fails for events below the detector threshold $E_{1,2} < E_{\mathrm{thres}}$.

5.2.4 Electronic signal shaping

The last step in the detection chain is the determination of current flow by the DAQ system (s. sc. 4.2). Roughly the DAQ chain can be divided into three stages: amplification, digitization and signal filter [Vel19].

- Signal amplification occurs at several position in the DAQ chain. To ensure high fidelity and stability the first amplification is performed close to the detector. Systematics related to this stage are electronic noise as well as cross-talk between geometrically close readout channels.

- Signal digitization represents the transition from a continuous voltage to a discrete binary form. An import systematic for sterile neutrino investigation at this stage results from non-linearity of this transformation [Dol16; Dol17].

- The signal increase related to the energy deposit is gathered by applying signal filters, for example by a trapezoidal filter. An essential systematic introduced at this

stage is signal pile-up, describing the occurrence of two events within the energy reconstruction time $t_{\text{min}} = 2 \cdot t_{\text{sh}} + t_{\text{ft}}$.

The influence of each effect on the measured energy spectrum depends on the exact realization of the detector and DAQ system. A detailed characterization of the DAQ-effects for the FPD were performed in [Sch14] and for TRISTAN in [Des19].

Electronic noise

The detector response of electronic noise is considered with respect to constant normal distributed noise and the energy determination assumed to scale linear with the signal voltage. The registered energy hence similarly follows a scaled normal distribution

$$E_{\text{meas}} \propto \mathcal{N}(\mu, \sigma) \ . \tag{5.30}$$

Analytically, the impact to the entire energy spectrum $\Gamma(E)$ is included via convolution

$$\Gamma(E_{\text{meas}}) = \int \mathrm{d}E \ \Gamma(E_{\text{meas}} - E) \cdot \mathcal{N}(E_{\text{meas}}, \sigma) \ . \tag{5.31}$$

The resulting energy response for a resolution of FWHM $= 2.6\,\text{keV}$ is illustrated in figure 5.16. The influence of electronic noise is most prominent at sharp structures in the energy spectrum. Both the signature of the MS retardation potential at $E_{\text{meas}} \approx qU_{\text{ret}} + qU_{\text{pae}}$ and the energy threshold at $E_{\text{thres}} = 0\,\text{keV}$ are broadened.

In addition the size of electronic noise σ ensues a lower limit for detecting events. The detection threshold E_{thres} is typically chosen around 2σ. Depending on the implementation of the trigger logic in the DAQ, the signal discrimination has to be applied before or after the noise convolution.

Signal pile-up

The signal processing within the DAQ is driven by the ADC's sampling rate as well as by the energy filter settings. If two incident particles impinge within a shortly after another Δt, a small probability will exist that the two events are indistinguishable $\Delta t < t_{\text{min}}$. They would be thus registered as a single event with a combined energy.

This process is referred to as signal pile-up with a probability P_{pu}. For a constant count rate Γ_{px} per pixel the it is determined by integration of the exponential inter-arrival time distribution

$$P_{\text{pu}} = \int_0^{t_{\text{min}}} \mathrm{d}t \ \Gamma_{\text{px}} e^{-t\Gamma_{\text{px}}} \ . \tag{5.32}$$

The simplest form of pile-up is the exact addition of two separate events from tritium beta-decay. This can be described through self convolution of the electron spectrum $\Gamma(E)$
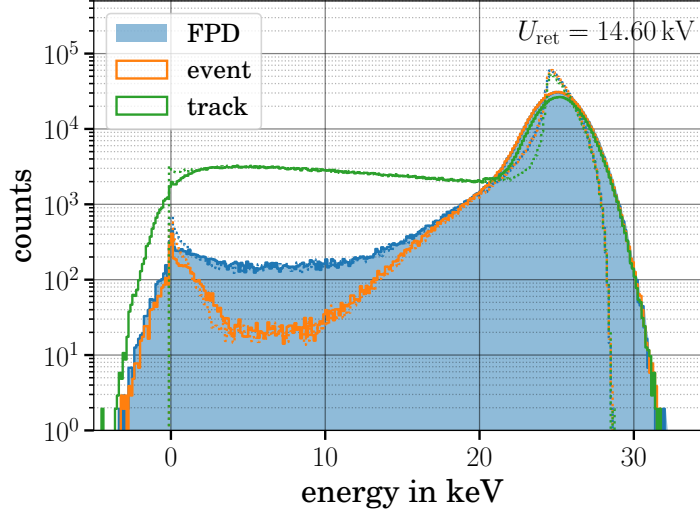
Figure 5.16: First tritium "1.6 keV" run $U_{\text{ret}} = 14.6\,\text{kV}$: Simulated beta-decay electron response with respect to detector scattering, back-scattering, charge-sharing and electronic noise FWHM $= 2.6\,\text{keV}$. Event (track) level simulation is depicted in orange (green) and the response without electronic noise is shown in dotted line style.

$$\Gamma = (1 - P_{\text{pu}}) \cdot \Gamma + P_{\text{pu}} \cdot \int \text{d}\tau \ \Gamma(E - \tau) \cdot \Gamma(E) \ . \tag{5.33}$$

This approach however neglects:

1. The exact timing between two events. Compared with the DAQ filter flattop time only the smallest time differences $t_2 - t_1 \ll t_{\text{ft}}$ can be approximated by a simple summation of the individual energies. For a intermediate times $t_2 - t_1 \approx \mathcal{O}(t_{\text{ft}})$ a the registered energy is reduced $E < E_1 + E_2$ [Eno14; Eno19; Des19].

2. The signal rise-time t_{rise} is dependent on the charge cloud's drift within the detector and the signal amplification stage[2]. Its influence to the energy determination is mitigated by choosing an appropriate flattop time in the trapezoidal filter setting $t_{\text{ft}} > t_{\text{rise}}$.

3. The inter-event time of back-scattered electrons (s. sc. 5.2.2). For the simulated setup it is around $\Delta t = \mathcal{O}(0.1\mu s)$ (s. fig. 5.9b). Similarly, its influence may be mitigated for an appropriate choice of the flattop time $t_{\text{ft}} > \Delta t$.

Overall the exact energy response of signal pile-up depends on the pixel rate Γ_{px} from tritium beta-decay as well as on the inter-event times Δt from back-reflection. For high count rates Γ_{px}, systematic effects that increase the number of perceived events (e.g.

---

[2]rise-times of $t_{\text{rise}} = \mathcal{O}(20\,\text{ns})$ were measured with a TRISTAN detector (s. sc. 6.3.4).

charge-sharing) would have to be considered. Still, the correct choice of the trapezoidal filter parameters $(t_{\text{sh}}, t_{\text{ft}})$ allow to mitigate the impact of systematics.

For modeling the detector response it would be best to include signal pile-up on the track-level by running subsequent electronic signal simulations. Such an investigation was performed for the FPD (s. fig. A.10). As an outcome one can state that the applied trapezoidal filter of the FPD leads to an underestimate of the registered energy, it broadens and shifts the spectrum response to lower energies $\Delta E = \mathcal{O}(100 \, \text{eV})$.

5.2.5 X-rays

The interaction of x-rays with silicon is of special interest as detector energy calibrations are often based on x-ray emitters with well-known spectral lines. In addition, silicon detectors are affected by x-ray escape, as de-excitation of silicon lattice atoms creates characteristic x-rays with energies of $E_{\text{kin}} = 1.74 \, \text{keV}$.

For x-rays with kinetic energies below $E_{\text{kin}} = 100 \, \text{keV}$ their interaction with silicon is dominated by photoelectric absorption [Ber10]. They transfer their entire energy to a prime electron, which subsequently deposits energy via multiple scatterings off silicon. The main difference between an incident x-ray and electron is thus the depth z into the detector where the conversion occurs. The exact position is not fixed but rather given by an exponential attenuation distribution $I(z)$

$$I(z) = I_0 \cdot e^{-z/\lambda} \, , \tag{5.34}$$

where I_0 denotes the total incident intensity and λ is the so called attenuation length. For $z = \lambda$ the intensity drops by a factor of $1/e = 37\%$. The attenuation length is material and energy dependent. For silicon an incident x-ray with $E_{\text{kin}} = 1/5/10/20 \, \text{keV}$ the attenuation length is given as $\lambda = 3.5/18/132/1000 \, \mu\text{m}$ [Ber10]. Relating the attenuation length to the detector properties, its detection deadlayer $\mathcal{O}(50 \, \text{nm})$ and the wafer thickness $d = 450 \, \mu\text{m}$, allows to infer the characteristic behavior for x-rays.

In figure 5.17 the energy dependent attenuation lengths [Ber10] are used to evaluate the fraction of the incident beams intensity at different positions into the silicon bulk (s. eq. 5.34. The lower energy limit $E_{\text{kin}} = 1 \, \text{keV}$ is a consequence of the higher increasing uncertainties in the database.

The fraction of interactions within the deadlayer reflects the characteristic energy transition of $E_{\text{kin}} = 1.74 \, \text{keV}$, as they occur close enough to the surface a small fraction of the resulting x-rays will escape the bulk. It is visible that only low energy gammas $E_{\text{kin}} < 5 \, \text{keV}$ are affected by the detection deadlayer $< 6\%$ ($z_{\text{dl}} = 100 \, \text{nm}$).

For increasing energies the interaction points first shifts to the second half of the detectors bulk (at $E_{\text{kin}} = 13.6 \, \text{keV}$) and at $E_{\text{kin}} = 17.2 \, \text{keV}$ half of the x-rays won't interact in the detector at all but are transmitted. For an x-ray that deposits its energy at half depth into the detector $z = d/2$, one would expect a subsequent twice reduction of the charge
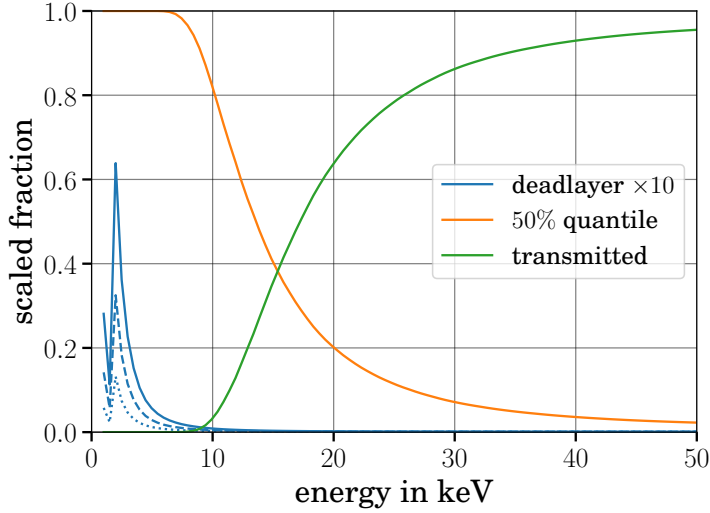
Figure 5.17: Energy dependent fraction of incident x-rays that interact within the detection deadlayer (blue), that interact within the first half of the silicon bulk (orange), and, that are transmitted without interacting at all $d = 450\,\mu\mathrm{m}$ (green). For visibility the interaction in the deadlayer is scaled by 10 and three different deadlayer thicknesses $z_{\mathrm{dl}} = 20/50/100\,\mathrm{nm}$ (dotted/dashed/solid) are depicted.

clouds drift time t_{drift} and consequently a smaller charge cloud radius and thus an impact to charge-sharing (s. sec. 5.2.3).

The detector response model to incident x-rays is implemented as simplified fashion, where an incident x-ray will deposit its entire energy within the sensitive detector bulk, the detection deadlayer as well as electron back-scattering become irrelevant. Charge-sharing is only modeled for low energy x-rays $E_{\mathrm{kin}} < 10\,\mathrm{keV}$, where the first interaction occurs closer to the surface.

$$E_{\mathrm{meas}}^{x\text{-}ray} = E_{\mathrm{in}} - E_{\mathrm{cs}} \tag{5.35}$$

The escape of silicon transition x-rays is modeled by a basic superposition of a second spectrum that is shifted by $E_{\mathrm{kin}} = 1.74\,\mathrm{keV}$ and occurs with a certain probability $P_{\mathrm{esc}}^{\mathrm{Si}}$:

$$\Gamma(E) = \Gamma(E) \cdot (1 - P_{\mathrm{esc}}^{\mathrm{Si}}(E)) + \Gamma(E - 1.74\,\mathrm{keV}) \cdot P_{\mathrm{esc}}^{\mathrm{Si}}(E) \ . \tag{5.36}$$

This approach however neglects subsequent interactions of $E_{\mathrm{kin}} = 1.74\,\mathrm{keV}$ x-rays close to surface.

5.3 Semi-analytical description

The differential sterile neutrino search with KATRIN requires the modeling of the observed electron energy spectrum with high precision. In addition, in order to apply the model for

sensitivity studies and online-analyses quick evaluation times are necessary.

In this section a first approach to combine the above systematics, excluding back-reflection, into a joint model is discussed (s. sc. 5.3.1). In order to incorporate an accurate and time-efficient response calculation of electron scattering in silicon, a novel technique is presented (s. sc. 5.3.2). It is based on a generic approach for transforming simulated data into a continuous empiric model with several free parameters.

5.3.1 Implementation

A core concept of the analytic description is the response function formalism (s. eq. 3.11), where each systematic effect contributes a characteristic response. In the code this is implemented with respect to their discrete form along the energy axis:

$$\Gamma(E) \longrightarrow \vec{\Gamma} \quad \text{and} \quad \vec{\Gamma}_{\text{syst}} = \mathbf{R}_{\text{syst}} \cdot \vec{\Gamma} \ . \tag{5.37}$$

Here "$\cdot$" implies the matrix multiplication of a response matrix $\mathbf{R}_{\text{syst}}$ associated to a certain systematic with the discrete energy spectrum $\vec{\Gamma}$.

In order to facilitate the computation event timings and electron back-reflection are neglected.

1. At first an initial energy spectrum $\Gamma(E)$ is constructed. For tritium beta-decay electrons the formalism from equation 3.1 is used, whereas mono energetic lines are created using Gaussian profile with defined mean $\mu = E_{\text{kin}}$, standard deviation σ and a normalization factor n. The sum over several Gaussian distributions $\mathcal{N}_i$ is used to model the spectrum of radioactive sources:

$$\Gamma_{\text{xray}}(E) = \sum_i n_i \cdot \mathcal{N}(E, \mu_i, \sigma_i) \ , \text{with} \quad \sum_i n_i = 1 \ . \tag{5.38}$$

   The composite energy spectrum is first normalized to unity and subsequently scaled to a given detector rate Γ_{det} and measurement time t_{msr}

$$\vec{N} = \Gamma_{\text{det}} \cdot t_{\text{msr}} \cdot \frac{\vec{\Gamma}}{|\vec{\Gamma}|} \ . \tag{5.39}$$

2. The first systematic considered is the initial scattering of electrons off silicon lattice atoms in the detectors bulk. The model is based on the simulation interpolation approach (s. sub-sc. 5.3.2), where KESS simulations are performed along a discrete three dimensional grid of input parameters: the incident energy E_{kin}, the angle of incidence $\vartheta_{\text{p,in}}$, and a fixed detector deadlayer z_{dl}.

For simulating x-rays, the scattering response is scaled by the probability P_{scat} and switched off for $P_{\text{scat}} = 0\%$. In this scenario, the contribution of Fano-like noise is integrated separately:

$$\vec{\Gamma}_{\text{scat,fano}} = \mathbf{R}_{\text{scat+fano}} \cdot \vec{\Gamma} \cdot P_{\text{scat}} + \mathbf{R}_{\text{fano}} \cdot \vec{\Gamma} \cdot (1 - P_{\text{scat}}) \,. \tag{5.40}$$

The simulation interpolation database currently includes types of responses: the entire detector response, the response to back-scattered electrons and the response to electrons that do not back-scatter (e.g. s. fig. 5.18).

3. The impact of charge-sharing is considered with respect to the analytic function described in subsection 5.2.3. Its response is internally normalized to give two events for an electron that shares its charge. The spectrum with charge-sharing is calculated according to

$$\vec{\Gamma}_{\text{cs}} = \mathbf{R}_{\text{cs}} \cdot \vec{\Gamma}_{\text{scat,fano}} \cdot \frac{3}{2} P_{\text{cs}} + \cdot \vec{\Gamma}_{\text{scat,fano}} \cdot (1 - \frac{3}{2} P_{\text{cs}}) \,. \tag{5.41}$$

Here the factor $3/2$ is given by the numeric implementation of the response function. The integral of the charge-sharing probability $P(\eta)$ is evaluated such that a coverage of 33.33% is given for $\eta \in [0.12, 0.88]$. The range corresponds to the initial charge cloud coverage $r_{\text{cc}} = \text{FWHM}/2$ of the normal distribution.

Likewise to the scattering flag, applying a charge-sharing probability $P_{\text{cs}} = 0\,\%$ will switch the response off. Furthermore it is possible to specify, that only the energy spectrum of charge shared electrons is modeled. This allows for a direct comparison of the charge-sharing model, in conjunction with a DAQ model, to measurements.

4. Electronic noise is implemented separately for its impact on the trigger and energy smearing. This enables modeling DAQ systems where trigger- and energy-readout are handled by independent filters.

The trigger results in an energy threshold E_{thres} for registering electrons. It is implemented using the cumulative of a normal distribution $\Phi(E, \mu, \sigma)$. Its mean corresponds to the energy threshold $E_{\text{thres}} = \mu$, while the standard deviation σ allows modeling sharp trigger cut-off as well as smooth transitions:

$$\Gamma_{\text{thres,i}} = \Phi_i \cdot \Gamma_{\text{cs,i}} \,. \tag{5.42}$$

The energy smearing is calculated using a response matrix derived from a normal distribution $\mathcal{N}(E, \mu, \sigma)$

$$\vec{\Gamma}_{\text{noise}} = \mathbf{R}_{\text{noise}} \cdot \Gamma_{\text{thres}} \,. \tag{5.43}$$

5. Lastly, signal pile-up is considered in a simplified manner, where the underestimation of pile-up event energies due to insufficient pulse overlap is neglected. This assumption holds for sufficiently good pile-up rejection [Des19].

   The convolution is performed for the energies $E \in [0, E_{\max}]$ according to equation 5.33. The defining property of pile-up is the minimal time resolution $t_{\min}$ and results, together with the detector rate $\Gamma_{\det}$, in the probability for pile-up to occur P_{pu} (s. eq. 5.32).

5.3.2 Simulation interpolation

While simulations allow for in-detail studies of complex geometries and parametric $\vec{p} = p_1, p_2, p_3, \ldots$ dependencies, their accuracy σ_{sim} is limited by the number N_{sim} of simulated particles:

$$\sigma_{\mathrm{sim}} = \sigma_{\mathrm{stat}} + \sigma_{\mathrm{syst}} \gtrless \sqrt{N_{\mathrm{sim}}} \ . \tag{5.44}$$

A quantitative comparison with measurement thus demands a high number of simulated particles. As N_{sim} is directly proportional to the calculation time, modeling via simulation is rendered infeasible for live measurements and sensitivity studies.
In order to retain the advantages of simulations two mechanisms are used:

- *spline-interpolation* of simulated responses along axis x for reducing σ_{sim}, and

- *shape-interpolation* of precalculated splines along $\vec{p}$ for a continuous model.

Time efficiency is achieved by caching the spline-interpolated simulated responses into a database. The calculation time is given by the shape-interpolation step.
In the following the simulation-interpolation approach is explained with respect to electron scattering in silicon. Here the energy response $x = E_{\mathrm{dep}}$ of $N_{\mathrm{sim}} = 10^7$ simulated electrons is of interest. The simulation is repeated at different parameters in a discrete three dimensional grid $p_1 \times p_2 \times p_3$ of incident electron energies $p_1 = E_{\mathrm{kin}}$, incident angles $p_2 = \vartheta_{\mathrm{p,in}}$ and deadlayer thicknesses $p_3 = z_{\mathrm{dl}}$:

$$
\begin{aligned}
E_{\mathrm{kin}}/\mathrm{keV} &\in [0.5, 1.0, \ldots, 10, 11, 12, \ldots, 50] \ , \\
\vartheta_{\mathrm{p,in}}/^{\circ} &\in [0, 5, \ldots, 90] \ , \mathrm{and} \\
z_{\mathrm{dl}}/\mathrm{nm} &\in [0, 10, \ldots, 200] \ .
\end{aligned}
\tag{5.45}
$$

Overall, the simulation database thus contains $60 \times 19 \times 21 \approx 24k$ spline-interpolated energy responses.
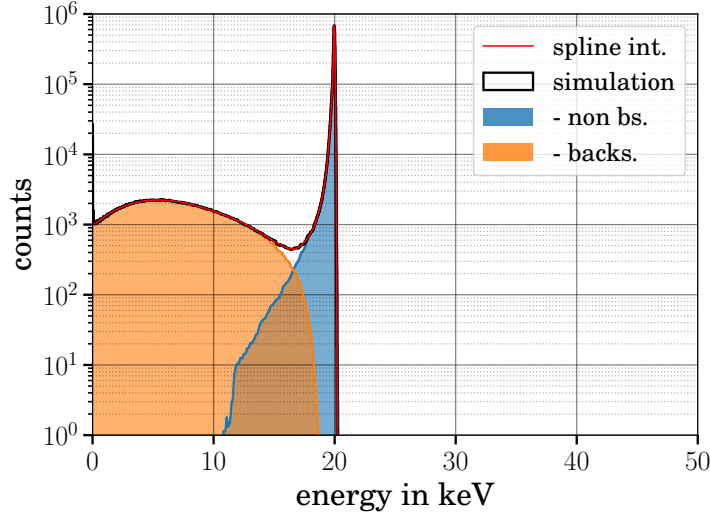
Figure 5.18: Spline interpolation (red) of the simulated energy deposition (black): highlighted in blue are deposits of electrons that are stopped in the detector, whereas the orange part corresponds to electrons that back-scatter.

Spline interpolation

The first step of the modeling approach comprises simulating N_{sim} electrons with fixed parameters. The energy response is then binned and spline-interpolated with respect to its characteristic features. For fast changing shapes it is advisable to spline-interpolate the logarithm of the response instead.

In figure 5.18 the detector simulation resulting from KESS with an added Fano-like noise convolution step is depicted. The shape is largely defined by the steep increase of the non back-scattering peak and its width $\sigma_{\text{nonbs.}}$.

The illustrated electron energy response corresponds to a simulation with parameters ($E_{\text{kin}} = 20\,\text{keV}$, $\vartheta_{\text{p,in}} = 0\,°$, $z_{\text{dl}} = 100\,\text{nm}$) and its output energy response histogram was chosen in accordance to the expectations at KATRIN:

$$N_{\text{bin}} = 4096 \quad \text{and} \quad E \in [0\,\text{keV}, 50\,\text{keV}] \,. \tag{5.46}$$

Here the energy range E is derived from the maximal energy expected at KATRIN $E_{\text{dep}}^{\text{max}} \approx E_0 + qU_{\text{pae}}$, and the number N_{bin} of histogram bins takes the specific shape of the energy response into account: the width $\sigma_{\text{nonbs.}}$ of the sharp non back-scattering peak at $E_{\text{dep}} \approx E_{\text{kin}}$. The lower limit is given by the deadlayer broadening as well as the added Fano-like noise convolution (s. eq. 4.4).

For achieving a sufficient description at all different simulated energy responses it is demanded, that the bin width ΔE should be small enough to have at least five bins within the non back-scattering peak:
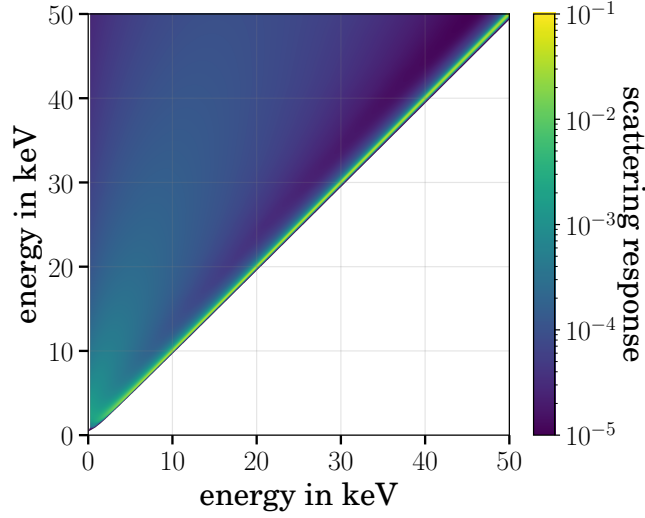
Figure 5.19: Normalized response matrix for a given set of deadlayer $z_{\mathrm{dl}} = 50\,\mathrm{nm}$ and incident angle $\vartheta_{\mathrm{p,in}} = 0\,^\circ$. Each energy on the y-axis, ie. each row, translates to a simulated MC simulation for a different incident energy, where each point is divided by the number of simulated electrons.

$$\frac{\sigma_{\mathrm{nonbs.}}(E_{\mathrm{kin}}, \vartheta_{\mathrm{p,in}}, z_{\mathrm{dl}})}{\Delta E} \gtrapprox \frac{\sigma_{\mathrm{fano}}(10\,\mathrm{keV})}{\Delta E} \approx \frac{152\,\mathrm{eV}}{\Delta E} \gtrapprox 10 \longrightarrow N_{\mathrm{bin}} \gtrapprox \frac{50 \cdot 10^3}{15.2} = 3300 \,. \quad (5.47)$$

Repeating the simulation and spline interpolations along the energy $p_1 = E_{\mathrm{in}}$ axis then yields the typical discrete response matrix as illustrated in figure 5.19.
At this end another spline interpolation step is performed: namely, the interpolation of the normalization along the incident energy E_{kin} axis (s. fig. 5.20).

Shape interpolation
The second step of the modeling approach transforms the discrete parameter $\vec{p}$ axis into a continuous form. This is achieved by shape interpolating between two neighboring, previously calculated spline interpolations.
Defining the shape of a curve via its coordinates (x, y), allows to shape interpolate its new form at $\hat{p}_1$ from the neighboring splines (x_1, y_1) and (x_2, y_2):

$$\begin{aligned}
x &= \frac{x_1 \cdot (p_{1,n+1} - \hat{p}_1) + x_2 \cdot (\hat{p}_1 - p_{1,n})}{p_{1,n+1} - p_{1,n}} \text{ and} \\
y &= \frac{y_1 \cdot (p_{1,n+1} - \hat{p}_1) + y_2 \cdot (\hat{p}_1 - p_{1,n})}{p_{1,n+1} - p_{1,n}} \,.
\end{aligned} \quad (5.48)$$

Here n is chosen as such that $\hat{p}_1$ directly lays between the two precalculated splines $\hat{p}_1 \in [p_{1,n}, p_{1,n+1}]$.
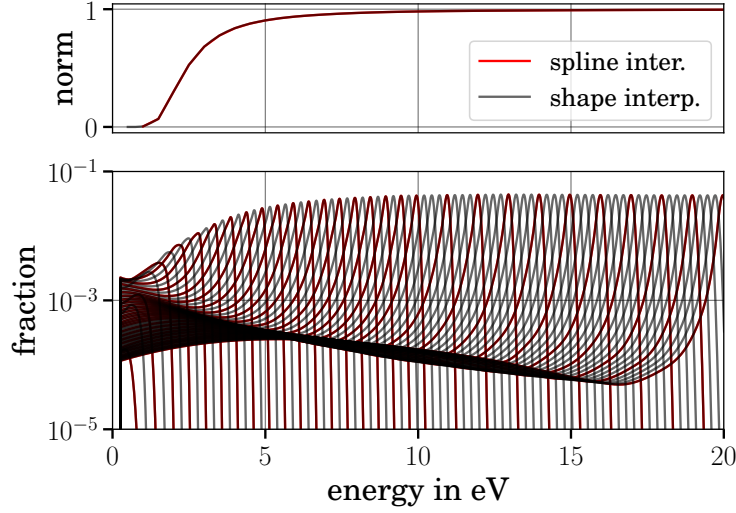
Figure 5.20: Fraction of simulated electrons that deposit their energy in the detector with respect to the spline interpolation (red). Each line corresponds to a simulation of 10 million electrons for fixed parameters of the incident energy $E_{\mathrm{in}} = 1/2/3/\ldots$ keV, deadlayer $z_{\mathrm{dl}} = 50\,\mathrm{nm}$ and incident angle $\vartheta_{\mathrm{p,in}} = 0\,^\circ$. Additionally, the shape interpolated spectra are illustrated in gray. The overall normalization illustrated in the top follows a spline interpolation along different simulated energies E_{in}.

To increase the precision of the shape interpolation, it is important to consider the exact form of the underlying curve. For the detector energy response the curve was split at the peak position of the non back-scattering peak and the shape interpolation performed separately on both halves.

In figure 5.20 several shape-interpolated responses and the neighboring spline-interpolated spectra are illustrated. The shape-interpolation enables a continuous description of the investigated system along the parameter $p_1 = E_{\mathrm{in}}$. This step is responsible for the low evaluation time of the semi-analytical model: $\mathcal{O}(200\,\mu\mathrm{s})$.

Additional parameter dependencies $p_2/p_3/\ldots$ are included by repeating the shape-interpolation along a second/third/$\ldots$ axis. However, they add complexity to the calculation and the evaluation time t_{calc} thus scales exponentially with the number d of parameters

$$t_{\mathrm{calc}} = \mathcal{O}(200\,\mu\mathrm{s}) \cdot 2^{d-1} \; . \tag{5.49}$$

An example for the simulation-interpolation result is illustrated in figure 5.21, where the response model is evaluated at 65 arbitrary incident energies E_{kin}, polar angles $\vartheta_{\mathrm{p,in}}$ and deadlayer thicknesses z_{dl}.
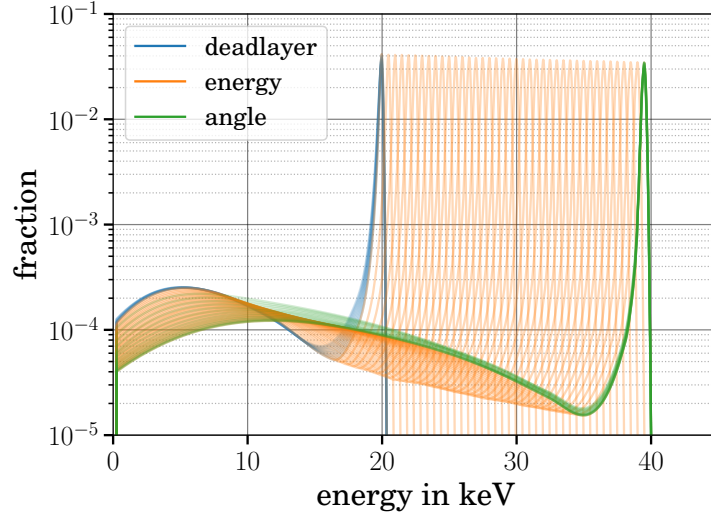
Figure 5.21: Example set of energy spectra evaluated according to the simulation-interpolation approach and based on KESS simulations. Starting at a set of parameters $(z_{dl} = 100\,\mathrm{nm}$, $E = 20\,\mathrm{keV}$, $\vartheta = 0\,^{\circ})$, the deadlayer is first reduced to $z_{dl} = 50\,\mathrm{nm}$ (blue), then the incident energy increased to $E = 40\,\mathrm{keV}$ (orange), and finally the incident angle increased $\vartheta = 45\,^{\circ}$ (green). In total the figure shows 120 different simulation-interpolated energy responses.

Accuracy

The overall database of spline-interpolated simulations amounts to a reasonable compressed size of $35\,\mathrm{MB}$. Combined with the shape-interpolation technique along the parameters $\vec{p} = (E_{in}, \vartheta_{p,in}, z_{dl})$ it yields evaluation times of roughly $\mathcal{O}(1\,\mathrm{ms})$.

This allows to use the model for live comparisons of measurements and sensitivity analyses, where - depending on the incident energy distribution - the model would be repeatedly called to build a response matrix (s. sc. 5.3.1).

In chapter 6 the comparison with measurement data shows, that the interpolations give a quite good fit with data. Still, the technique described above is but a first approach for modeling the detector response. Regions within the grid of parameters $\vec{p}$ as well as the simulation itself could be further improved:

- For low simulated incident electron energies $E_{kin} < 5\,\mathrm{keV}$ an increasing fraction of electrons lose their entire energy within the detection deadlayer. The energy response thus is based on smaller statistics and the relative uncertainty of the simulation increases. This could be compensated by increasing the number of simulated electrons in this region.

- For small deadlayer thicknesses the peak width of non back-scattered electrons decreases. In consequence, the spline-interpolation is more sensitive towards individual energy response bins in the peak and thus more sensitive to statistical fluctuations. This was partially compensated by including Fano-like noise and could

be further improved by extending the shape-interpolation to next-to-next neighbors (e.g. $\hat{p}_1 \in [p_{1,n-1}, p_{1,n}, p_{1,n+1}]$).

- Inherently the simulation is based on a set of interactions and assumptions. The accuracy of the simulation-interpolation is thus predetermined by the simulation itself. For KESS improvements can, for example, be made by including the energy-loss of elastic scatterings [Ren11].

5.4   Conclusion

The presented detector response model is based on various first order systematics prevalent at the detector section of KATRIN. As illustrated in figure 4.2, the entire response would have to consider the propagation and energy deposition of electrons from tritium beta-decay. Moreover, the model should include a detailed description of charge collection as well as the DAQ step.

Particle propagation and energy deposition in silicon was investigated based on MC simulations with KESS [Ren11] and KASSIOPEIA [Fur17]. The process of charge collection in the detector is approximated by introducing a discrete detection deadlayer z_{dl} and by considering the movement of charges solely with respect to their spilling into neighboring pixels, i.e. charge-sharing. Investigated DAQ effects include a basic model electronic noise, energy threshold as well as signal pile-up.

Section 5.2 introduces the above systematics, while in parallel focusing on the detector response of the FPD. Of special interest for tritium beta-decay measurements with KATRIN is the process of electron back-scattering and back-reflection 5.2.2. The energy response and its influence to the detection efficiency is further described in chapter 8.

Notably, a detailed eV precision of the underlying simulations requires improvements in KESS. In particular, elastic electron-silicon scattering should include energy-losses and silicon lattice orientations as well as tracking of x-rays could be implemented.

The description of electron back-scattering (s. fig. A.3) would profit from this especially in the region close to the spectrum endpoint, where the smallest energy-loss in the detector would lead to the suppression of back-reflection.

Section 5.3 focuses on a time-efficient description of the detector response. To do so a database of simulated responses is created and the response evaluated using the simulation-interpolation technique. While this approach signifies a first step in direction of a detector model, enabling online analysis (s. ch. 6) as well as sensitivity studies (s. ch. 7.1), a future model should include electron back-reflection as well as a description of charge-sharing at the intersection of three pixels.

Chapter 6

Characterization

Central to a sterile neutrino search at KATRIN is the TRISTAN detector upgrade and its characterization. In particular, a deep understanding of the detector response to incident electrons is mandatory.

In this chapter the measured energy response to incident x-rays (s. sc. 6.2) as well as to electrons (s. sc. 6.3) is investigated and compared with predictions from the semi-analytical response model (s. sc. 5.3).

6.1 Detector system

For the first prototyping step several detectors were produced by HLL, which differ in pixel size and doping techniques for reducing the detection deadlayer at the detectors entrance window. The measurements presented in the following are based on the $r_{px} = 1\,mm$ sized detector with standard entrance window technology. It is referred to as the "F-02" detector, according to the nomenclature of the HLL production.

The detector comes on a small 8 mm by 8 mm die (s. fig. 4.6) and is glued to the back of a PCB with slightly smaller sized cut-out. The charge sensitive amplifiers, CUBEs from XGLab, are accommodated on the same board and soldered directly next to the cut-out region. They are connected to the SDDs readout electrode via a few mm long wire bounds. Similarly, electric potentials are supplied via wire bonds from the PCB to the detector and amplifiers (s. fig. 6.1b). Except for the bonds to the biasing and back-frame potentials, all the electronics are placed on the back side of the detector board.

For ease of experimental operation the detector board is fixated on to a bigger base plate that can be inserted into a mount (s. fig. 6.1a). For operation the detector requires four voltages: back frame $U_{BF} \approx -100\,V$, back contact $U_{BC} \approx -110\,V$, inner drift ring $U_{R1} \approx -20\,V$ and the outer drift ring $U_{RX} \approx -90\,V$ voltage. Here U_{BC} functions as a hurdle separating the SDD from the rest of the die and the two drift voltages automatically define the potentials for the other rings via integrated diodes between the rings.

On the detector board all signal and power supplies lines are connected to a 26 pin socket strip with a 2 mm pitch. Via a ribbon cable the board can be thus connected to another
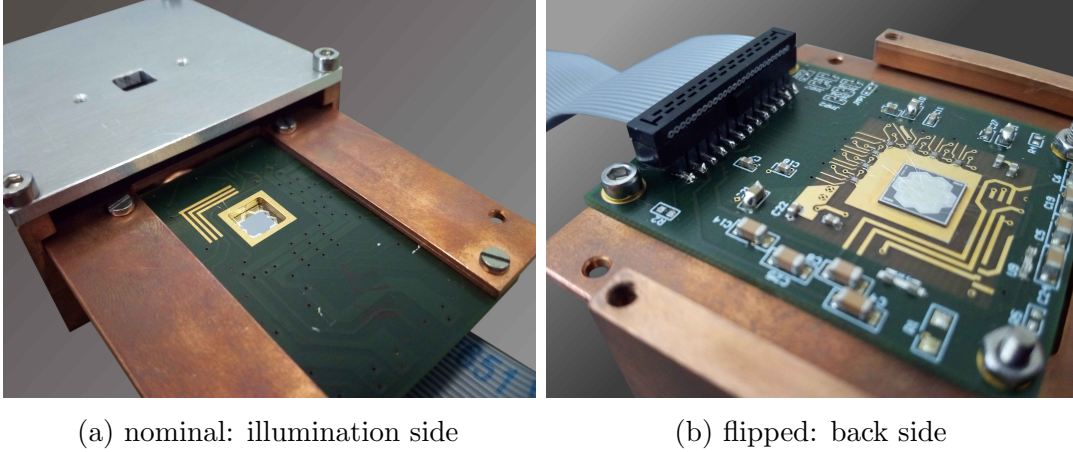
(a) nominal: illumination side   (b) flipped: back side

Figure 6.1: Picture of the detector board with mounted seven pixel $r_{px} = 1\,\mathrm{mm}$ TRISTAN detector. The board is screwed to a copper base plate that, similarly to a cartridge, can be inserted into a copper mount. The four screw holes on the mounts top allow fixing an aluminum aperture. The nominal operation mode is illustrated in (a). The base plate protrudes two thirds out of the cartridge, showing the illumination side of the detector. In (b) the base plate is flipped around to show the backside of the detector, revealing the seven CUBE preamplifiers and the ribbon cable connector.

device, the biasing board (s. fig. 6.2). It encompasses second stage amplifiers, reset electronics for the CUBEs and several voltage trimmers for configuration.

A nine pin D-Sub connector links to an external low noise power source. Thereof two lines are reserved for high power and supplied to the detector. Consequently, fine tuning the detector voltages is performed via voltage trimmers, using two trimmers to split one high voltage line for U_{BF}-U_{BC} and similarly for U_{R1}-U_{RX}.

Lastly, the amplified signal from the readout anodes trace to SMA sockets on the biasing board. Via coaxial cables these are then connected to the pulse processing and digitization component: the DANTE box from XGLab. In the setup used, the box includes seven interconnected pulse processor boards, synchronizing their timing to the first processors clock[XGL18].

Each processor comes with a 16 bit ADC that samples at 16 ns. Online the signal is interpolated for a virtual 8 ns sampling. Subsequently two trapezoidal filters are applied: one for the standard energy determination and another for more precise time triggering, referred to as fast-filter (s. eq. 4.5).

For DANTE the energy filter peaking t_{pk} and flattop t_{ft} times can be freely chosen in multiples of 32 ns samples, likewise for the fast-filter in multiples of 8 ns. The advantage of this combination is a drastic improvement for rejecting signal pile-up, as the minimum time resolution is given by the quicker fast-filter $t_{min} = 2 \cdot t_{ff,pk} + t_{ff,ft}$ settings (s. eq. A.9) [Des19]. With respect to electronic noise the fast-filter is however less accurate and thus the energy resolution at the detection threshold is thus given by the fast-filter.
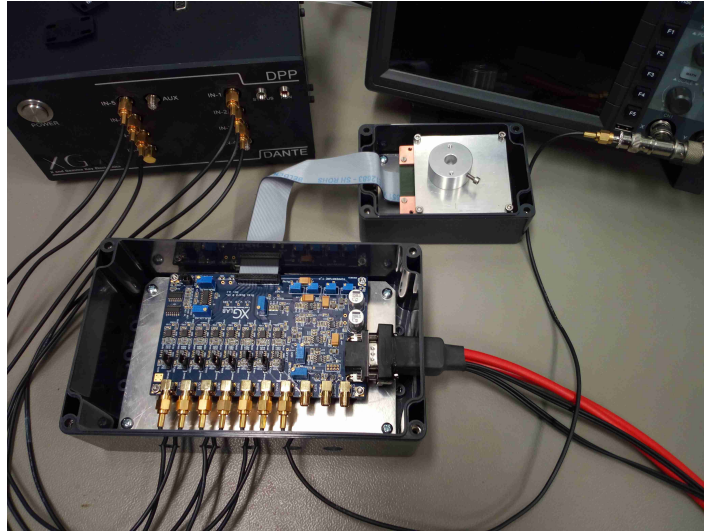
Figure 6.2: Overview photograph showing the detector mount with a radioactive source holder screwed in place onto the aperture plate. The ribbon cable links to the detector biasing board, that is similarly mounted on a grounded base plate. It supplies reset electronics for the CUBEs and distributes various voltages and signals. The power cable (red) is connected to the board via a D-Sub plug with nine pins. The amplified signal is then passed over SMA coaxial cables to the DANTE box (top left). Here a single line is connected to an oscilloscope (top right).

Another feature of the pulse processor is the so called maximum rise-time rejection. Internally it is derived from the area below the fast-filter output. This allows to further reduce the minimum time t_{min} resolution, improving the discrimination of pile-up and charge-sharing events.

6.2 Response to x-rays

A good way to characterize SDDs is the use of x-rays from radioactive sources. Their sharp spectral lines allow calibrating the recorded signal amplitudes and calculate an accurate value for the initial energy. Unlike electrons, x-rays penetrate far into the detector and are thus not affected by the deadlayer nor by back-scattering 5.2.5. On-site measurements were performed with the radioactive isotopes ^{241}Am (s. fig. A.14a) and ^{55}Fe. For model comparisons, however, low energy x-rays from ^{55}Fe are much better suited.

^{55}Fe decays via electron capture into ^{55}Mn, leaving an empty electronic K shell, which is subsequently filled by electrons from higher orbitals. Three characteristic x-rays are distinguishable: $E_{\mathrm{kin}}^{L} = 0.64\,\mathrm{keV}\ (0.66\%)$[1], $E_{\mathrm{kin}}^{K\alpha_{1+2}} = 5.90\,\mathrm{keV}\ (24.5\%)$ and $E_{\mathrm{kin}}^{K\beta_{1+3}} = 6.49\,\mathrm{keV}\ (2.85\%)$ [Jun08].

This corresponds to attenuation lengths of $\lambda = 3.5/29/37\,\mu$m and leads to x-ray interactions

---

[1]X-rays from the L orbital typically fall below the energy threshold and are not observed.

within the first $\lambda/d \lesssim 10\%$ ($d = 450\,\mu\text{m}$) of the detector and only a small fraction $< 0.18\%$ of interacts within the first $50\,\text{nm}$ (s. fig. 5.17). The two effects allow to reduce the impact of the deadlayer and back-scattering, while still being sensitive to the full charge collection process. In consequence x-rays from ^{55}Fe are well suited for investigating charge-sharing.

Inter-event time

Experimentally investigating charge-shared events requires the analysis of short time coincidences between neighboring pixels. In the used setup the DAQ returns the event times and amplitudes for each pixel separately. In the analysis the output is thus manually merged into a joint form 6.1. As each pixel comes with individual clock-cycles a small timing correction t_ch^off between readout channels is applied.

Table 6.1: Exemplary, time sorted event structure ($t_2^\text{off} - t_0^\text{off} < 1$) that is used for analyzing measurements. The individual channels are related to a physical pixel, the timing corrected and the measured amplitude A calibrated to an energy, using a channel dependent function E_ch^cal. Typically, the central pixel is wired to channel 0 of the DAQ and the other pixel are connected in a clockwise motion, starting at the north-pixel (1=nn,2=ne, ...). Assuming an incident energy $E_\text{kin} = 10\,\text{keV}$, then event 1 and 2 are subject to charge-sharing ($E_1 + E_2 = E_\text{kin} = 10\,\text{keV}$), while event 6 and 7 are purely coincidental $E_6 + E_7 > E_\text{kin}$.

event	channel	pixel	clock	time	amplitude	energy
1	2	ne	2	$2+t_2^\text{off}$	60	$E_2^\text{cal}(60)$
2	0	cc	1	$1+t_0^\text{off}$	42	$E_0^\text{cal}(42)$
3	1	nn	19	$19+t_1^\text{off}$	105	$E_1^\text{cal}(105)$
4	4	ss	50	$50+t_4^\text{off}$	98	$E_4^\text{cal}(98)$
5	0	cc	100	$100+t_0^\text{off}$	100	$E_0^\text{cal}(100)$
6	4	ss	120	$120+t_4^\text{off}$	99	$E_4^\text{cal}(99)$
7	6	nw	122	$122+t_6^\text{off}$	90	$E_6^\text{cal}(90)$
...	...	...	...	...	...	...

The correction is derived from analyzing the inter-event times Δt observed in each pixel, which should be ideally centered around $\Delta t = 0$ for a homogeneous detector illumination. A measurement of the inter-event times Δt, including a correction of $t_\text{ch}^\text{off} \approx N_\text{ch} \cdot 5.9\,\mu\text{s}$, is depicted in figure 6.3a. Here, depending on order of detecting the coincident event in a given pixel, the arrival times are considered positive for first registering the event and a negative sign is applied $-\Delta t$ if it triggers second.

In order to focus on timing of charge-shared events, an energy cut $E_1 + E_2 \in [5\,\text{keV}, 8\,\text{keV}]$ on the sum of individual events was applied. This allows for a decent discrimination of random coincidence, which showed oscillatory noise with a frequency of $12.5\,\text{MHz}$. This noise slightly affects the timing of each clock separately and thus leads to a spread

(a) inter-event time

(b) pixel map
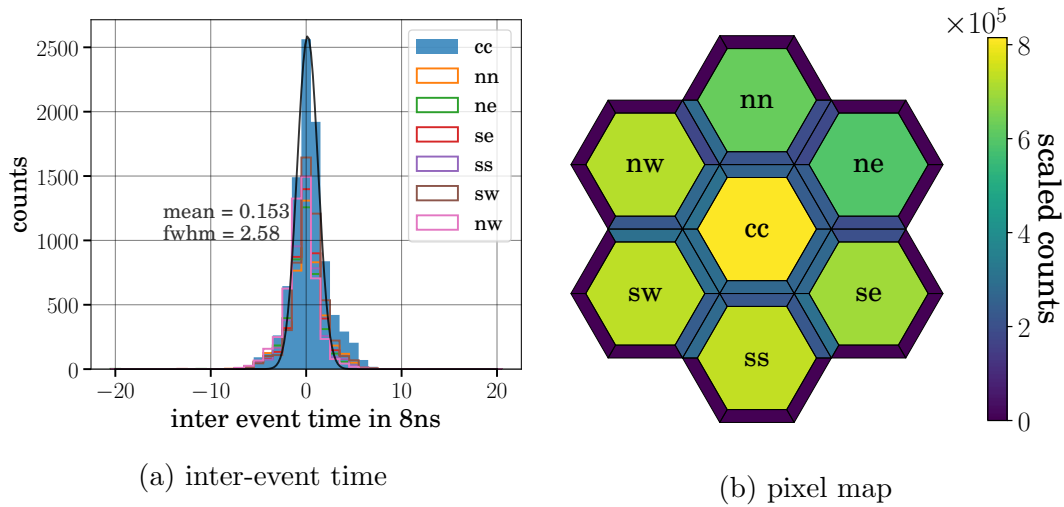
Figure 6.3: (a) inter-event times charge-shared electrons measured with ^{55}Fe x-rays. The time is given in multiples of the DAQ samples. (b) Illustration of the count rate of each detector pixels as well as the number of events N_{cs} with short coincidence times $t_{coin} < 0.2\,\mu s$ to a following event in the adjacent pixel. For visualization N_{cs} is scaled by 100.

in the observed inter-event times. The fitted normal distribution shows that the most charge-sharing events occur within short time frame $< 21\,ns = 2.58 \cdot 8\,ns$.

For visualizing the fraction of charge-shared events measured in each pixel the investigation of the observed count-rate is required. In figure 6.3b the detected rates in each pixel as well as the rate of charge-shared events is depicted. For selecting coincident events related to charge-sharing only small inter-event times of $\Delta t < 0.2\,\mu s = t_{coin}$ are considered. The order of the inter-event times is given by showing only the rates of the pixel that triggers first.

The pixel map nicely demonstrates, that the number of charge-shared events in the central pixel is approximately twice the amount compared to the outer pixels (nn, ne, etc.), as it has twice the number of neighboring pixel. However this does not imply that outer pixels are less affected by charge-sharing. Charge-sharing may still occur on all six sides of the hexagonal shaped pixels. It is just not possible to investigate the rate with a coincidence measurement.

The probability for charge-sharing to occur is based on a homogeneous incident of particles on the entire detector (s. eq. 5.27). Here x-rays illuminate the detector homogeneously but with a small offset to the central pixel and a roughly 10% radial rate decrease to outer pixels, both originating from the positioning of the source at about 1 cm distance to the detector.
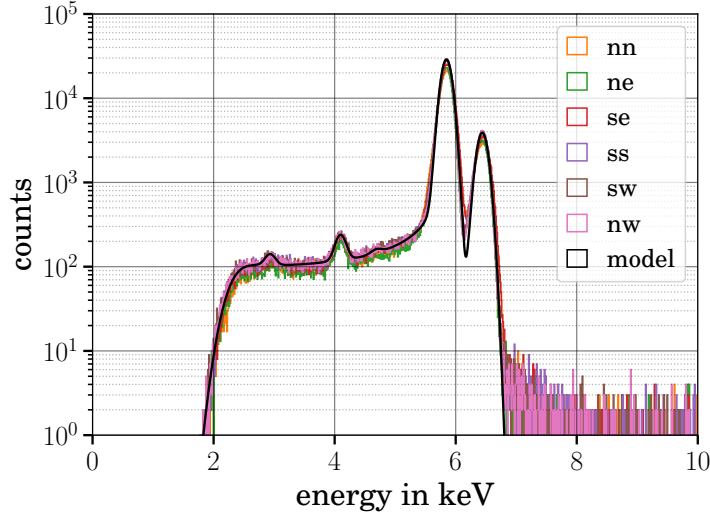
Figure 6.4: Self calibrated x-ray energy spectrum from ^{55}Fe. The energy response of the different detector pixels are given in color and the fitted energy response for pixel "nw" is given in black.

Response

Assuming a homogeneous incidence, the response model can be compared with measured energy response (s. fig. 6.4). Here, the response of the central pixel was omitted, due to a characteristic noise component that, in combination with the fast-filter settings, lead to a shift in the measured spectrum (s. fig. A.15).

The fitted model includes the two x-ray lines from ^{55}Fe as well as their respective silicon x-ray escape peaks $E_{\mathrm{kin}} - 1.7\,\mathrm{keV}$. In addition an x-ray line according to the transition energy of argon $E_{\mathrm{kin}}^{K\alpha_{1,2}} = 2.96\,\mathrm{keV}$ is included. It originates from ^{55}Fe x-ray scattering off argon molecules in ambient air. The observed excess of 0.1% can be estimated by multiplying the fraction of argon molecules in air ($\approx 1\%$) with the probability ($\approx 30\%$) to excite argon with ^{55}Fe x-rays and the probability ($\approx 30\%$) of argon x-rays to reach the detector[2].

As discussed above, keV-scale x-rays penetrate far enough into the bulk to suppress the influence of the detection deadlayer as well as the back-scattering of secondary electrons. Consequently the observed low energy tail is fully described by charge-sharing. Accordingly, only the response contribution of electronic noise and charge-sharing are considered (s. sc. 5.3). Fitting to the measurement gives a charge-sharing probability of $P_{\mathrm{cs}} = 8.0 \pm 0.4\,\%$. According to equation 5.27, this translates to a charge cloud radius of $r_{\mathrm{cc}} = 19 \pm 1.2\,\mu\mathrm{m}$, the uncertainty being related to the accuracy of the pixel rate estimation $\Gamma_{\mathrm{px}} = 12.6 \pm 0.3\,\mathrm{kcps}$. Although charge-sharing across three pixels was not modeled, its impact should be small. One, since a probability for them to occur is (s. eq. 5.27) is limited by the charge cloud

---

[2]The source is situated at about $1\,\mathrm{cm}$ distance to the detector and an attenuation length $\lambda = 2.3\,\mathrm{cm}$ for $5.9\,\mathrm{keV}$ x-rays was used.

radius, here $< 0.3\%$. And two, since the used detection threshold of $E_{\mathrm{thres}} = 2.2\,\mathrm{keV}$ was chosen high enough to suppress the impact of a the three-split energy $E_{\mathrm{thres}} > 6.4\,\mathrm{keV}/3$.

6.3 Response to electrons

In contrast to x-rays, the response of electrons is largely affected by their initial energy and incident angle. These two parameters strongly influence the energy-loss within the insensitive detector region, the detection deadlayer (s. sc. 5.2.1), as well as probability for back-scattering of the detector (s. sc. 5.2.2). For the detector characterization, hence, a high-precision electron source is required.

In this section the detector response to electrons is investigated using a scanning electron microscope, see 6.3.1. In addition to the incident angle and kinetic energy, the microscope allows for focusing the electron beam from a few mm down to a few nm in size. While illuminating the entire detector gives the most realistic energy response (s. sc. 6.3.2), a focused beam allows studying the detector response at different positions: at the center of an SDD the response is mostly given by the scattering process (s. sc. 6.3.3), whereas the response at the intersection of two pixels is dominated by pixel charge-sharing (s. sc. 6.3.4).

6.3.1 Scanning electron microscope

The electron source is the commercial scanning electron microscope (SEM) "JSM-IT300" from JEOL [Jeo19]. It is situated at HLL and was used in previous studies to investigate the detection deadlayer [Sie19].

Overall the SEM features electron energies within $E_{\mathrm{kin}} \in [0.3\,\mathrm{keV}, 30\,\mathrm{keV}]$, variable beam spot sizes from $\mathcal{O}(\mathrm{nm})$ to $\mathcal{O}(\mathrm{mm})$, as well as an eucentric goniometer stage. The stage allows the probes displacement over several mm as well as its rotation $\varphi \in [0, 360°]$ and tilt $\vartheta \in [-10°, 90°]$. The detector is screwed onto a special specimen holder, which in turn can be easily slid into a central position on the stage.

With the available hardware and software it is only possible to illuminate two dimensional regions on the probe. These regions are referred to as photos and come with different presets for scanning rasterization $w \times h$ and time t_{scan}: by default a sensible frame of $1280 \times 960\,\mathrm{px}$ and the highest time of $t_{\mathrm{scan}} = 160\,\mathrm{s}$ was chosen. By varying the magnification parameter of the SEMs the photographs frames width and height can be easily modified: a value of $\mathrm{mag} = 10^3$ thus corresponds to a frame size of $64 \times 48\mu\mathrm{m}$.

In figure 6.5a a picture of the SEMs vacuum chamber is given. The detector is mounted in the center and moreover has the radioactive calibration source holder (red) placed directly on top of it. While it is removed during SEM operation, the source allows to verify in-situ influence of electronic noise.

In fact the SEM is not optimized for low-noise operation and largely affected the detected signal waveforms, introducing several oscillatory noise components. The best performance
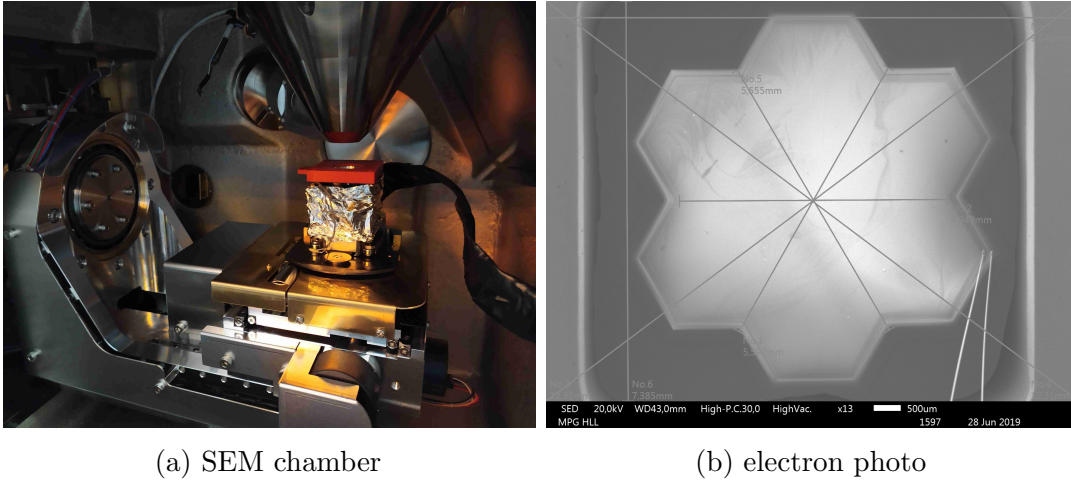
(a) SEM chamber   (b) electron photo

Figure 6.5: (a) Photograph of the internal vacuum chamber with a mounted detector in the center. The red source holder for ^{241}Am is removed during electron scans. (b) Electron photo of the $r_{px} = 1\,\text{mm}$ large "F-02" detector taken with the SEM.

was achieved by electrically decoupling the detector holder from the positioning stage and sharing the detectors ground line with an encompassing aluminum cover. Similarly, the ribbon cables connecting the bias board to the detector board were shielded with aluminum and insulated with black tape.

Lastly, the SEMs electron rate is changed via the filament current I_{fil}. For high values $I_{fil} = \mathcal{O}(\text{nA})$ it is possible to visually inspect the detector with electrons, as depicted in figure 6.5b. Here the SDD is operated at nominal bias potentials, which results in a visible glow of the entrance window. Furthermore, the depicted guiding lines were used to center the detector with respect to the middle of the rasterization frame.

In figure 6.6 an exemplary rasterization schema is superimposed to the measured pixel map. Here the scanning framing is chosen large enough for homogeneous detector illumination. The scan begins at the upper left corner moves along the grid from left-to-right and line-by-line. During a typical measurement the filament current $I_{fil} = 1.5 \pm 0.1\,\text{pA}$ was adjusted to ensure electron rates of $\Gamma_{det} = 10^4\,\text{cps}$. The uncertainty reflects minor current adjustments with respect to the used acceleration voltage.

The detector TRISTAN detector "F-02" was operated at $U_{BF} = -105\,\text{V}$, $U_{BC} = -100\,\text{V}$, $U_{RX} = -90\,\text{V}$ and $U_{R1} = -20\,\text{V}$. Notably, the feedback reading of the inner electrode differed from the external voltage applied and $-30\,\text{V}$ measured. The energy calibration was performed based on an one hour long measurement with ^{241}Am (s. fig. A.14a).

6.3.2   Homogeneous illumination

At KATRIN the initial electrons are homogeneously created within the STS. Correspondingly, after traveling along the beamline, they will thus homogeneously impinge onto the detector. With the SEM a homogeneous illumination is achieved at low magnifications
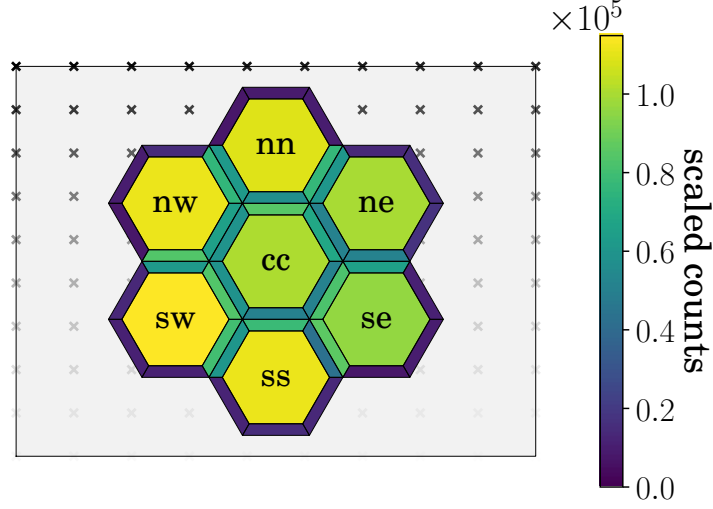
Figure 6.6: Count rates of the individual detector pixels and charge-shared rate scaled by 100. A rasterization of the measurement with the SEM is artistically depicted with black crosses. In total scan includes a grid of 1280×960 individual pixels within the illustrated gray shaded frame.

mag = 15 as illustrated in figure 6.6. Notably, the measured rates show a $\approx 10\%$ decrease from the on one side. This hints to a slight asymmetric scanning procedure of the SEM.

Charge-sharing

Similar to the characterization of charge-shared events performed with x-rays (s. sc. 6.2), the investigation of short inter-event times allows selecting charge-shared events. The initial energy $E_{\mathrm{in}} \approx E_{\mathrm{meas}}$ of the incident electron can be reconstructed by summation of the individual measured energies of the two pixels $E_{\mathrm{meas}} \approx E_1 + E_2$.

Drawing the recorded energies for events with short time coincidences in a scatter plot, thus allows to visually locate charge-shared events along a diagonal line. For electrons with perpendicular incidence and energy $E_{\mathrm{in}} = 20\,\mathrm{keV}$, an exemplary measurement is illustrated in figure 6.7a. Here only events with inter-event times smaller $t_{\mathrm{coin}} = 0.2\,\mu\mathrm{s}$ are selected, which suppresses random coincidences. The observed excess at low energies is partly related to a electrons that back-scatter $E_{\mathrm{meas}} - E_{\mathrm{bs}}$ off the detector, and partly due to electrons that hit the detector at the intersection of three pixels, triple charge-sharing. In the measurement (s. fig. 6.7a) the number of low energy coincidences amounts to roughly $N(E_{\mathrm{dep}} < 19\,\mathrm{keV})/\sum N = 34\%$ of all coincident events. Assuming a rough back-scattering probability of 20% would predict a 14% contribution of triple charge-shared events. Multiplied with the probability of twin charge-sharing the magnitude of triple charge-sharing is thus $\mathcal{O}(0.1\%)$.

In order to further discriminate twin and triple charge-sharing, the energy response of all charge-sharing events is selected with consideration of short time coincidences between two respective three events (s. fig. 6.7b). Here the contribution of back-scattering was

(a) energy scatter

(b) energy spectrum
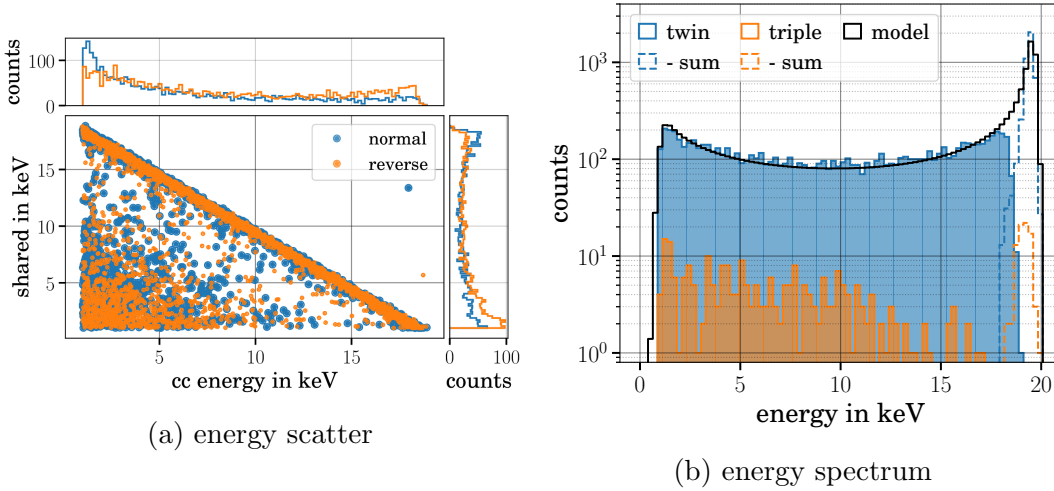
Figure 6.7: Coincidence time analysis for $t_{\mathrm{coin}} = 0.2\,\mu\mathrm{s}$ in the central pixel. In (a) the observed energy in the center is plotted over the energy of the coincident event. Here events registered first (second) in the center pixel are blue (orange). The energy spectrum of all signals that fall into the diagonal band $\sum E_i \in [19\,\mathrm{keV}, 20\,\mathrm{keV}]$ is illustrated in (b). In addition the model expectation for twin (black) and the histogram of triple charge-sharing (orange) is given.

suppressed by only selecting coincident events E_i where the sum of individual pixels $\sum E_i \in [18\,\mathrm{keV}, 20\,\mathrm{keV}]$ add to the initial electrons energy.

The measurement is in excellent agreement with the modeled response (s. fig. 6.7b). Here only the response of electrons that deposit their entire energy in the detector are considered within the model, the analytical response of electron back-scattering is excluded (s. sc. 5.3). Fitting the modeled response to the data gives a charge-sharing probability of $P_{\mathrm{cs}} = 7.6 \pm 0.5\,\%$. The uncertainty is directly correlated with the expected count rate Γ, here the rate was estimated by counting energies above a certain threshold E_{min}:

$$\Gamma \approx t_{\mathrm{meas}} \cdot \int_{E_{\mathrm{min}}}^{E_{\mathrm{dep}}} \mathrm{d}E \; \frac{\mathrm{d}\Gamma}{\mathrm{d}E\mathrm{d}t} \; . \tag{6.1}$$

Typically, all registered events should be counted and $E_{\mathrm{min}} = 0\,\mathrm{keV}$ chosen. However, for charge-sharing boundaries smaller than $E_{\mathrm{min}} \approx 1/2 \cdot E_{\mathrm{dep}}$ would ensue counting charge-shared events twice. As a compromise a lower bound of $E_{\mathrm{min}} = 5 \pm 2\,\mathrm{keV}$ is selected which results in a rate of $\Gamma_{\mathrm{px}} = 554 \pm 50\,\mathrm{cps}$. Translated to the charge cloud radius (s. eq. 5.27) a value of $r_{\mathrm{cc}} = 18.1 \pm 1.2\,\mu\mathrm{m}$ is obtained. Compared to the characterization with x-rays ($r_{\mathrm{cc}} = 19 \pm 1.2\,\mu\mathrm{m}$), the radii agree within their uncertainties. This suggests that the charge cloud radius is dominated by thermal diffusion for energies below $E_{\mathrm{kin}} = 20\,\mathrm{keV}$. Assuming the same charge cloud radius for triple charge-sharing events, one can calculate its probability as $P_{\mathrm{cs}} = 6 \cdot (2r_{\mathrm{cc}})^2 / A_{\mathrm{px}} = 0.25\%$ (cf. eq. 5.26). This compares to roughly 0.09% detected coincident events in the measurement (s. fig. 6.7b). A more accurate
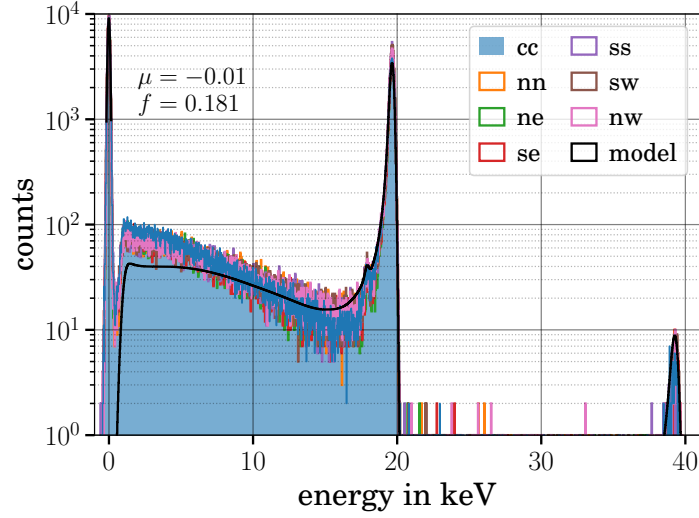
Figure 6.8: Energy spectrum of $E_{\text{kin}} = 20\,\text{keV}$ electrons measured at the SEM with the "F-02" detector. Incident electrons homogeneously illuminate the entire detector (s. fig. 6.6). The spectra of the different pixels are given in color and the model given in black.

comparison would require a more detailed triple charge-sharing model, in particular the influence of the detection threshold E_{thres} on the three-split energies $E_{\text{meas}}/3$.

Energy response

As triple charge-sharing is not considered in the modeled response, the excess rate becomes visible in the model comparison of the full measured energy spectrum, see figure 6.8. Here, instead of performing a fit to the data, all parameters were derived from calibration measurements. For example the energy resolution to electronic noise $\text{FWHM}_{\text{noise}} = 181\,\text{eV}$ is derived from a fit of the noise peak at $E = 0\,\text{keV}$:

$$\Gamma_{\text{px}} = 550\,\text{cps}\ ,\quad U_{\text{BC}} = -100\,\text{V}\ ,\quad t_{\text{min}} = 0.11\,\mu\text{s}\ ,$$
$$E_{\text{thres}} = 1\,\text{keV}\ ,\quad \text{FWHM}_{\text{noise}} = 181\,\text{eV}\ ,\quad \text{FWHM}_{\text{ff}} = 360\,\text{eV}\ , \tag{6.2}$$
$$P_{\text{cs}} = 8.3\,\%\ ,\quad z_{\text{dl}} = 65\,\text{nm}\ \text{and}\quad \vartheta_{\text{p,in}} = 0\,^{\circ}\ .$$

A characteristic rate estimation is visible just below the silicon escape peak $E \approx 17\,\text{keV}$. This is likely related to the simulated scattering model, which incorporates a discrete deadlayer, and where x-ray escape was not considered. It is further discussed in the following section.

Overall the modeled response is in good qualitative agreement with the measurement. Notably, the model assumption of energy-lossless signal pile-up correctly describes the pile-up peak at $E_{\text{meas}} = 39\,\text{keV}$. The largest discrepancies are mostly related to neglecting triple charge-sharing in the model and lead to a shape distortion $< 50\%$.
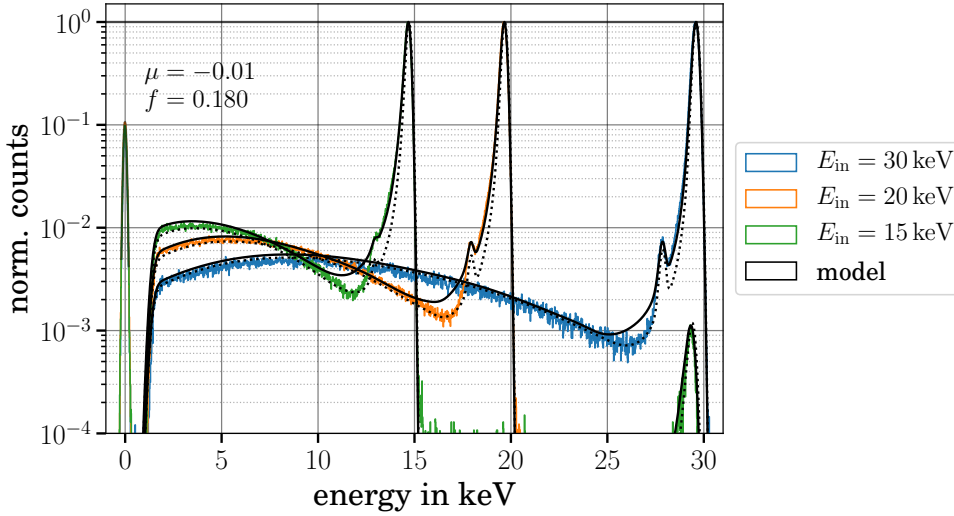
Figure 6.9: Normalized energy spectrum of $E_{kin} = 15/20/30$ keV (blue/orange/green) electrons measured with the "F-02" detector at the SEM. The black solid (dotted) lines are the corresponding model description and based on a $z_{dl} = 65$ nm ($z_{dl} = 40$ nm) detection deadlayer.

6.3.3 Pixel center

In order to separately investigate the detection deadlayer model, the incident electron spot was focused onto the center of the central pixel. The SEM was operated at mag $= 9500$, corresponding to a region of 13.47×10.11 μm, and the measurement repeated for different acceleration voltages $U_{acc} = 15/20/30$ kV.

As charge-sharing only occurs close to a neighboring pixel, the modeled energy response solely contains the response to scattering in silicon and electronic noise. Model parameters are either directly determined from DAQ settings (E_{thres}, t_{min}, etc.) or, for the energy resolution, by fitting the noise peak at $E = 0$. In figure 6.9 the measured spectra and the predicted model results are presented.

The only free model parameter is the detection deadlayer thickness z_{dl}. Assuming a large value $z_{dl} = 65$ nm leads to a rate overestimation directly below the silicon x-ray escape peak, in case of electron with incident energy $E_{kin} = 20$ keV the excess is visible at $E \approx 17$ keV. In contrast, a thin deadlayer $z_{dl} = 45$ nm better describes the minimum, but ensues a mismatch of the peak broadening, as it is affected by the reduced energy loss in the deadlayer E_{dl}. In conclusion the discrete deadlayer cab be determined only with large uncertainties $z_{dl} = 53 \pm 14$ nm.

Previous measurement by [Sie19] at the SEM electron similarly investigated the energy response at the pixel center. Due to large electronic noise, they were however insensitive to this dip. In consequence, this suggests improving the model of electron scattering in silicon and directly translates into improving underlying simulation in KESS (s. sc. 5.3). A reason for the observed discrepancy is connected to modeling of x-rays. Currently, KESS
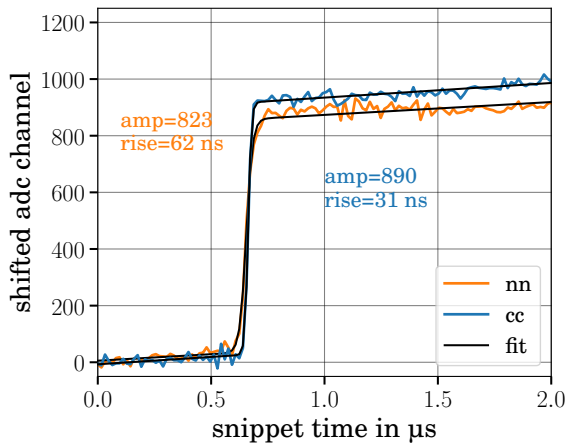
Figure 6.10: Signal waveforms recorded with the DANTE pulse processor for $E_{kin} = 10\,keV$ electrons impinging close to the boundary between the "center" and "north" pixel of the "F-02" detector. Two exemplary signal waveforms are given, in blue for an event in the "center" pixel, and in addition a model fitted (black).

does not include x-ray trajectories and thus two individual simulations with different incident energies where performed. The response is then calculated by superimposing the two spectra: $\Gamma(E_{kin}) + P_{esc}^{Si} \cdot \Gamma(E_{kin} - 1.7\,keV)$ (s. sc. 5.3). Another reason for the discrepancy is the discrete detection deadlayer model (s. sub-sc. 5.2.1). A more realistic scenario would have to consider a continuous deadlayer and the underlying charge-collection process.

6.3.4 Pixel boundary

Electron charge-sharing can be investigated in detail by narrowly focusing the electron beam and measuring the signal waveform at different distances to the intersection of two pixels. In a SEM characterization measurement this is achieved by applying a focus magnitude of mag = 400. The scanning frame $320 \times 240\,\mu m$ was horizontally aligned with the straight boundary between two pixels, such that the registered rate in both pixels was approximately equal. Moreover, the frame height $h = 240\,\mu m$ was chosen large enough to cover a decently large part of the expected charge-sharing region in both directions $h/2 > 5 \cdot r_{cc}$.

Instead of the previously discussed energy spectra and timing a new analysis approach was applied: modeling of the signal waveform. Aside from event timing and amplitude, this method allows to investigate the signal rise-time.

The data was taken in the "wavelist-mode" of the DANTE pulse processors, which records the processors energy estimate, the events timing as well as a snapshot of the underlying signal waveform - 400 samples of the digital output voltage. The waveform does not include the online interpolation and it is given with respect to 16 ns-sampling, a time-frame corresponds to $6.4\,\mu s$.

Unfortunately a coincidence analysis with the recorded data in the "wavelist-mode" is hardly possible, as only a fraction of the expected charge-sharing events 0.3% fall within the coincidence time $t_{coin} = 0.2\,\mu s$. This is likely related to the increased data throughput in the readout mode and thus introduces an artificial dead time after each event.

(a) scatter: energy - position

(b) scatter: rise-time - position
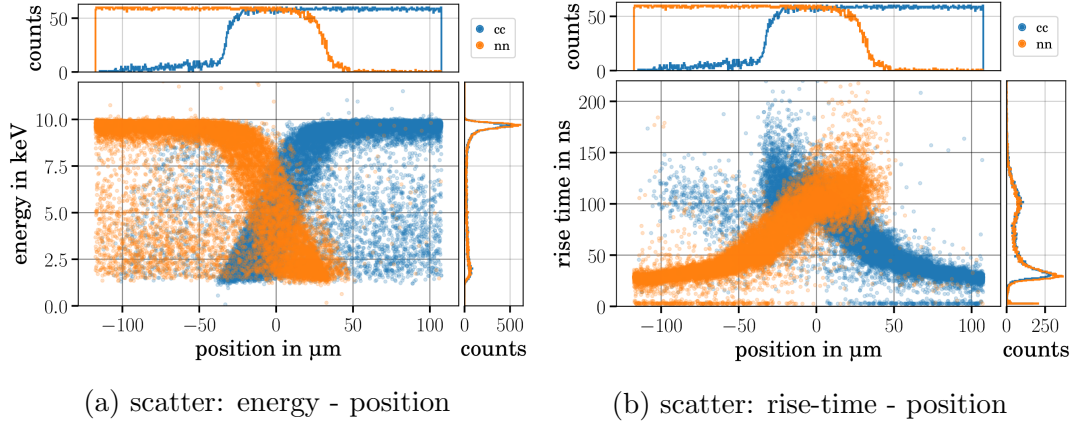
Figure 6.11: Scatter plot of event energy (a) and signal rise-time (b) over scanning position of the SEM. The measurement was performed at the intersection of two pixels with $E_{\text{kin}} = 10\,\text{keV}$ electrons and the "F-02" detector. Both E and t_{rise} are derived by fitting the recorded signal waveforms. Here blue dots are events in the "center" pixel.

In figure 6.10 exemplary signal waveforms in two neighboring pixels are given. The model is based on a sigmoid function, jointly developed with [Des19]. The model is normalized in such a fashion, that the signals rise-time t_{rise} is defined as the time it takes for the signal amplitude to increase from 10% to 90%: $t_{\text{rise}} = t_{90\%} - t_{10\%}$.

Compared to the "center" pixel, the illustrated waveform of the "north" pixel shows a visibly higher rise-time $t_{\text{rise}} = 62\,\text{ns}$ as well as a slightly lower signal amplitude amp $= 823$. This corresponds to the distance Δx to the pixel boundary where the incident electron hits the detector and is better illustrated in the scatter plot of energy E (s. fig. 6.11a) or rise-time t_{rise} (s. fig. 6.11b) over scanning position Δx.

The scatter plots show a distinct impact on the recorded energy and rise-time starting at a distance of $\Delta x = -40\,\mu\text{m}$ from the pixel boundary and ending at $\Delta x = 40\,\mu\text{m}$. Similarly, a small rate increase is visible at $\Delta x = -80\,\mu\text{m}$ in the projections on scanning position. In contrast, this increase is asymmetric and performing the same SEM scan in reverse direction instead showed a rate increase in the other pixel. This hints to a systematic effect of the SEM's scanning procedures.

A caveat of the measurement is spread of the measured energies respective rise-times. At various distances events with the same energy (rise-time) are observed; for example the events with an energy $E = 2\,\text{keV}$ are measured in the central pixel at distances of $\Delta x \in [-40, 0]$. One contribution to this spread is an imperfect alignment of the frame with respect to the boundary. Another process that adds to the spread is the charge deposition process. It leads to a broadening of a few μm (s. fig. ??). Lastly, the SEM's scanning procedure consists of rows and pixels. The dimension of such a pixel, or differently phrased the size of the incident electron beam, contributes to the observed spread.

Of particular interest for charge-sharing is the position were the charge cloud reaches across

the pixel boundary (s. sub-sc. 5.2.3). The cloud radius r_{cc} is defined as half the width $r_{cc} = \text{FWHM}/2$ of the underlying distribution. In terms of the charge-shared fraction it begins at $\approx 12\%$ charge loss and ends at $\approx 88\%$. Neglecting the spread induced by alignment and scattering, a cloud radius of roughly $r_{cc} = 25 \pm 10\,\mu\text{m}$ can be determined. A notable result of this measurement is that all charge-sharing events show a distinct increase of the signal rise-time. Within $\Delta x \in [-40, 40]$ the fitted timing is larger than twice its nominal value

$$t^{cs}_{rise} \gtrsim 2 \cdot t^{nom}_{rise} = 2 \cdot 25\,\text{ns} \ . \tag{6.3}$$

The largest observed rise-times for twin charge-sharing events is $t_{rise} = 150\,\text{ns}$. A similar measurement was performed for electrons with an energy of $E_{kin} = 20\,\text{keV}$ (s. fig. A.17b) as well as for electrons that impinge at the intersection of three pixels (s. fig. A.18b). In consequence, the signal rise-time is an optimal parameter for triggering charge-shared events.

6.4   Conclusion

In the previous sections the energy response for a $r_{px} = 1\,\text{mm}$ detector "F-02" with standard deadlayer technology was investigated. The measurements were performed with x-ray and electron sources and obtained energy responses were compared to prediction with the semi-analytical model (s. sc. 5.3).

Characterization measurements with x-rays (s. sc. 6.2) were in particular used to calibrate the detector and to characterize charge-sharing. Especially low energy x-rays $E < 10\,\text{keV}$ from ^{55}Fe are preferred, as they penetrate deep enough into the detector to neglect the detection deadlayer and back-scattering, while interacting close enough to the surface to show the impact of charge collection. Comparison with semi-analytical model allows determining the charge cloud radius to $r_{cc} = 19 \pm 1.2\,\mu\text{m}$.

Using electrons for characterization requires high-precision source with well determined beam parameters, such as the incident energy and angle of electrons. Of similarly importance is the ability to focus the electron onto a small areas, which may be used to separately investigated detector bulk (deadlayer) from pixel boundary (charge-sharing) effects.

Illuminating the entire detector homogeneously (s. sc. 6.3.2) best emulates the final operation conditions at KATRIN. As the charge-sharing model was derived with respect the homogeneity assumptions, a coincidence analysis allowed to independently determine the charge cloud radius to $r_{cc} = 18.1 \pm 1.2\,\mu\text{m}$ for $E_{kin} = 20\,\text{keV}$ electrons. Within the uncertainty this value agrees with the radius obtained from x-ray characterization. In addition the analysis permitted to investigate triple charge-sharing events - currently not implemented in the model. Compared to data, the modeled energy response hence shows

an underestimation of the low-energy spectrum. Moreover a small dip below the silicon x-ray escape is visible.

This feature was further investigated by focusing the beam on the center of the detector pixel (s. sc. 6.3.3). This suppress the influence of charge-sharing and allow to directly compared the energy deposition model - more accurately, the energy response determined from simulating electron scattering off silicon with KESS. Although a good agreement was found for a discrete deadlayer thickness of $z_{\mathrm{dl}} = 65\,\mathrm{nm}$, the dip is better described by $z_{\mathrm{dl}} = 40\,\mathrm{nm}$. In consequence the discrete deadlayer model only allows to infer an average value of $z_{\mathrm{dl}} = 53 \pm 14\,\mathrm{nm}$ with a large uncertainty. A reduced uncertainty thus requires improvements in the underlying KESS simulation software: a continuous deadlayer model as well as the propagation of x-rays should be considered.

Lastly, the electron beam was focused onto the pixel boundary (s. sc. 6.3.4). Here a novel analysis approach was performed by fitting the signal shape directly to the recorded signal waveforms. The result showed that charge-sharing occurs within the distance $\Delta x/\mu\mathrm{m} \in [-40, 40]$ to the pixel boundary. In addition the fit allows to characterize the signal rise-time of charge-shared events and values up to $t_{\mathrm{rise}} = 150\,\mathrm{ns}$ where measured. In comparison electrons that impinge at $|\Delta x| > 40\mu\mathrm{m}$ - electrons that do not charge-share - show a signal rise-time of about $t_{\mathrm{rise}} = 25\,\mathrm{ns}$. Assuming that a future DAQ system registers the signal rise-time, this would allows discriminating charge-shared events from events that undergo pile-up or back-reflection.

6.5   Further electron sources

For characterizing TRISTAN detectors at KIT a dedicated laboratory was built within the scope of this thesis. In addition to the detector system, described in section 6.1, the laboratory hosts two different electron sources: the high-intensity electron gun (s. sc. 6.5.1) and the photo-electric electron gun (s. sc. 6.5.2). In the following the two setups are briefly introduced, focusing on the experimental features.

6.5.1   High-intensity electron gun

For characterizing the detector response to electrons the incident electron energies E_{kin} as well as their polar angle $\vartheta_{\mathrm{p,in}}$ have to be well defined. With respect to DAQ systematics, it is in addition required to test rate dependent effects.

An electron source that features almost mono energetic (FWHM $= 0.5\,\mathrm{eV}$) electrons $E_{\mathrm{kin}} \in [0.2\,\mathrm{keV}, 20\,\mathrm{keV}]$ and large variety in rate $\Gamma \in [1\,\mathrm{cps}, 10^{16}\,\mathrm{cps}]$ ($I < 1\,\mathrm{mA}$) is the "EGF-3104" electron gun from Kimball Physics [Kim15]. It can be mounted onto the standardized CF40 vacuum flanges and is usable in extreme ultra high vacuum[Hub15].

Internally the electrons are generated on a tantalum cathode by an electric heating current I_{cat}. The cathode and several beam forming electrodes (grid U_{grd}, focus U_{foc} and first anode U_{1an}) are encased by an electrode that is operated at high voltage U_{acc}. It functions

(a) top view (b) front view
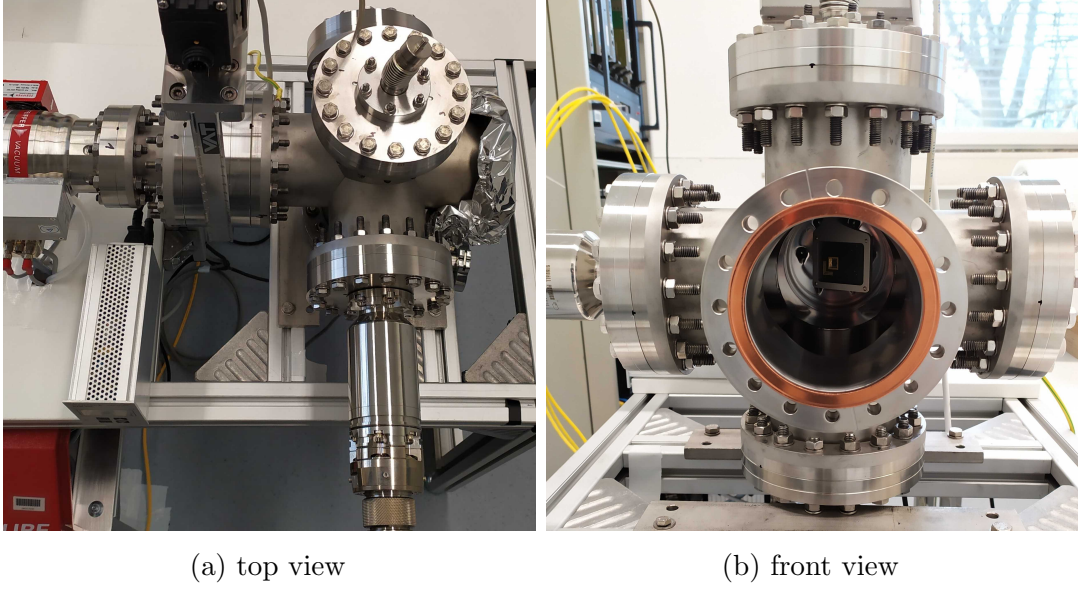
Figure 6.12: Picture of the high-intensity electron gun vacuum setup from the top (left) and from the front (right). The detector is mounted on in the center of the vacuum cross and may be rotated around the vertical axis.

as the acceleration voltage and has to be considered relative to the electric potential at the detector. The produced electrons exit the electron gun in a forward cone with and opening angle of $\theta \approx 22°$ [Hub15] and are accelerated onto the detector with energies relative to the back-frame potential U_{BF}.

In order to enable measurements with different incident polar angles the experimental vacuum setup has been completely redesigned. The detector is mounted a rotatory vertical axis in the center of a CF100 double cross. The electron gun is directly aligned to the detectors central pixel and situated at a distance of roughly $13\,\mathrm{cm}$ (s. fig. 6.12a). First measurements with different electric potentials as well as incident angles were performed. A notable affect of the electron gun was observed at the following potentials:

$$U_{\mathrm{grd}} = 5\,\mathrm{V}\ ,\quad U_{\mathrm{foc}} = 100\,\mathrm{V}\ ,\quad U_{\mathrm{1an}} = 500\,\mathrm{V}\ ,$$
$$U_{\mathrm{acc}}/\mathrm{kV} \in [-0.2, -20]\ \text{and}\quad U_{\mathrm{BF}} = -112\,\mathrm{V}\ . \tag{6.4}$$

The recorded energy spectrum is illustrated in figure 6.13a. Instead of a single electron peak at $E = qU_{\mathrm{acc}} + qU_{\mathrm{BF}}$, two separate maxima at position $E_1 = qU_{\mathrm{acc}} + qU_{\mathrm{foc}} + qU_{\mathrm{BF}}$ and $E_2 = qU_{\mathrm{acc}} - qU_{\mathrm{foc}} + qU_{\mathrm{1an}} - qU_{\mathrm{BF}}$ were observed (s. fig. 6.13a). The effect is least pronounced for the central pixel and it shows a significant higher rate, which leads to the assumption that some of the observed electrons scatter off or originate from the electrodes. Experimentally, this effect could be mitigated by varying the electron gun potentials. A good setting was achieved by increasing the potential at the focus electrode to $U_{\mathrm{foc}} = -500\,\mathrm{V}$ and by setting U_{1an} to zero.

The used "F-12" detector has a radius of $r_{\mathrm{px}} = 0.5\,\mathrm{mm}$ and comes with standard deadlayer

(a) energy spectrum   (b) pixel map
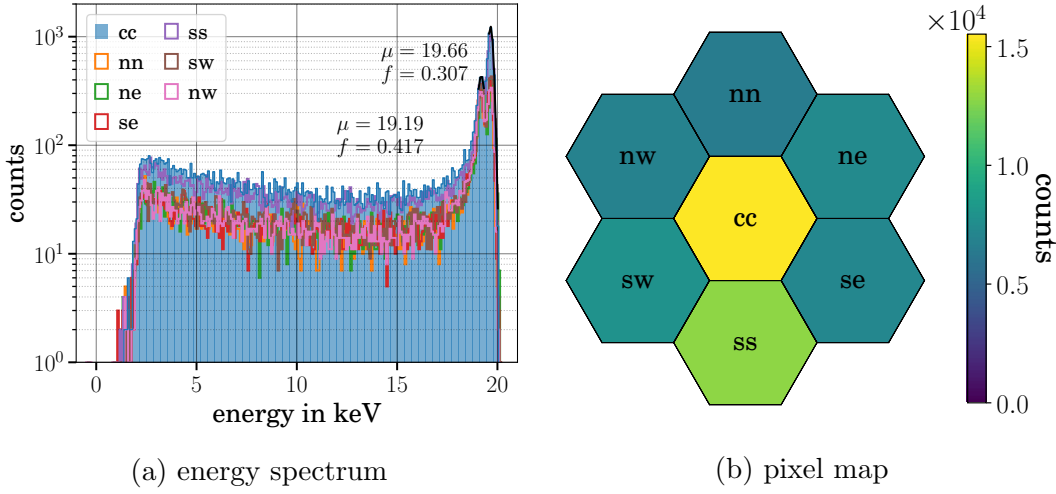
Figure 6.13: Electron energy spectrum measured with the "F-12" detector at the high intensity electron gun setup (a) and the total counts registered illustrated in the pixel map (b). The model depicted in (a) (black) implements the the various electric potentials inherent to the electron gun, notably the registered shift of between the two observed maxima $U_{1\text{an}}$.

technology. A **caveat** of the measurements is that the detector could not be operated, due to an electric short, at nominal supply potentials. Instead the outer drift ring U_{RX} was powered to $U_{\text{RX}} = -21.9\,\text{V}$ and the inner drift ring to $U_{\text{R1}} = -30\,\text{V}$. Thereby the inner ring functions as a barrier and some charges are collected by the outer ring. In effect the sensitive area of the pixels shrank to small fraction.

This should lead to a reduced rate Γ_{px} as well as an increase of charge loss (s. eq. 5.27). However, a coincidence based analysis is not possible here, as the charge loss occurs close to the pixel center and not at the boundary. Using the constant charge cloud radius $r_{\text{cc}} = 19\,\mu\text{m}$ the charge-sharing fraction can be translated to an effective pixel radius of $r_{\text{px}} = 0.15\,\text{mm}$. As a consequence the wrong drift ring settings result in an effective area of only $9\% = (0.15/0.5)^2$ of the total.

While a fit with the semi-analytical model has been tried, the high correlation of fitted parameters do not allow to estimate the detector properties consistently. In order to separate systematics further calibrations are required. For example separating deadlayer induced broadening from electronic noise can be accomplished by analyzing the noise peak (s. e.g. 6.9).

Overall the setup is suited for characterization measurements, as the electrons impinge homogeneously and almost perpendicular onto the detector $\mathcal{O}(1)$. In addition the setup shows good noise conditions, here FWHM $= 307\,\text{eV}$ at $E_{\text{meas}} = 19.7\,\text{keV}$. For future investigations the capability to rotate the detector should be considered and the optimized electron gun potentials used.
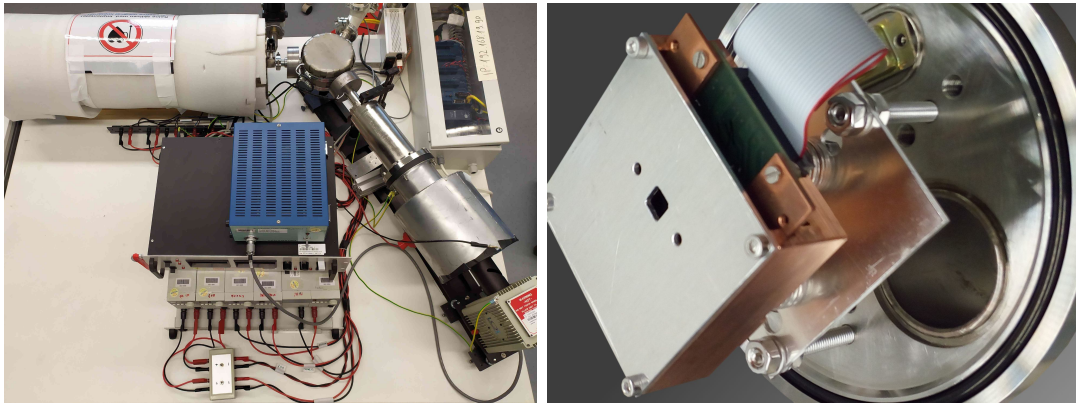
(a) photo electric electron gun

(b) detector mounting flange

Figure 6.14: (a) Picture of the entire photo electric electron gun setup. Electrons are generated on high voltage U_{acc} in the bottom right corner and magnetically guided along the setup to the detector flange on the top left. (b) Close up of the detector flange with mounted detector and its encasing.

6.5.2 Photo electric electron gun

Another source for electrons that has been commissioned is based on the photo electric absorption of ultraviolet light on a gold [Kas98] coated quartz glass in vacuum (s. fig. 6.14a). As an ultraviolet light source $\lambda/\mathrm{nm} \in [185, 400]$ the deuterium lamp "L6565" from Hamamatsu is used.

The gold layer and mounting structure are directly operated on high voltage $U_{\mathrm{acc}}/\mathrm{kV} \in [0, 30]$ and used to accelerate the electrons to high energies. The vacuum setup is designed in an angled fashion $\phi = 120°$, in order to suppress a direct illumination of the detector with ultraviolet light. Consequently, electrons are magnetically guided throughout the setup. In particular the setup includes (s. A.13)

- the rotation magnet, that guides electrons around the angle,

- the two focus magnets, encasing the angle and acting as a magnetic lens,

- the 75 cm long transport magnet, for focusing the beam, and

- two dipole coils, displacing the electron beam in x/y direction.

A picture of the setup is given in figure 6.14a and a close-up of the mounting flange in 6.14b.

An exemplary measurement with the "F-12" detector and $E_{\mathrm{kin}} = 20\,\mathrm{keV}$ electrons is depicted in 6.15a. It shows a good energy resolution FWHM $= 305\,\mathrm{eV}$ and, similar to the high-intensity electron gun (s. sc. 6.5.1), an increased charge-sharing probability P_{cs} due to the inverted drift ring potentials of the detector.

(a) energy spectrum
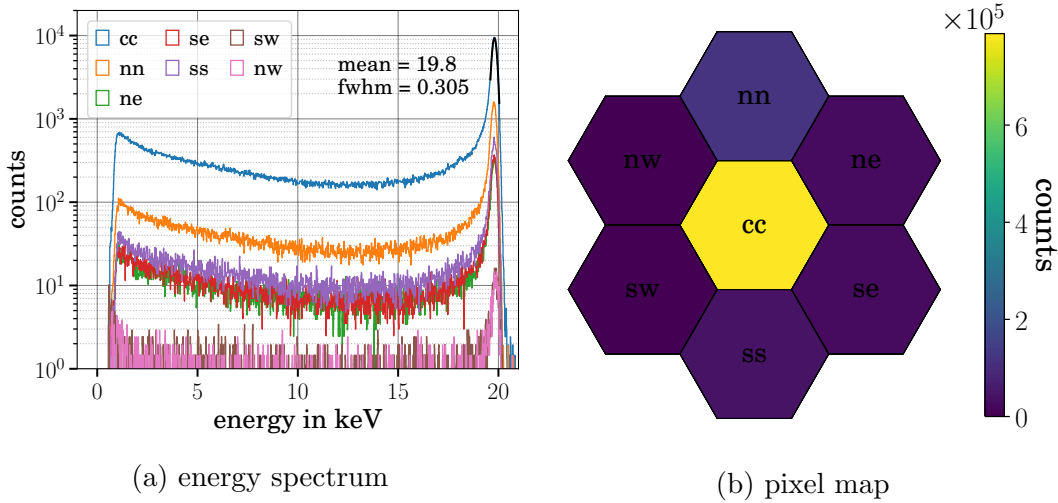
(b) pixel map

Figure 6.15: Electron energy spectrum (a) and pixel map (b) measured by the "F-12" detector within the photo electric electron gun. The incident electron beam has an energy of $E_{\mathrm{kin}} = 20\,\mathrm{keV}$ and its cross section corresponds the size of the pixels diameter.

The measured high rates in the central pixel suggest an electron beam size of roughly $r \approx 5\,\mathrm{mm}$, the same size as the pixel geometry. The spot size is directly related to the dimension of the gold coated quartz glass $r \approx 4.5\,\mathrm{mm}$. The beam's size can be further reduced by fine-tuning the magnetic field currents, however, a high-precision electron spot would require an upgrade of the currently installed power supplies.

Chapter 7

Detector design

The sterile neutrino search at KATRIN is strongly tied to the capabilities of the detector and DAQ system that is currently developed within the TRISTAN project. It is envisioned that the detector system will consist of $n_\mathrm{px} = 3486$ pixels with individual readout channels. The development is separated into several production milestones $n_\mathrm{px} = 7/166/3486$.

In this chapter the impact of detector systematic effects (s. ch. 5) to the sterile neutrino search with KATRIN is discussed in two steps:

- Based on the semi-analytical model from section 5.3 the sterile neutrino sensitivity for various parameters and uncertainties is calculated (s. sc. 7.1). Both the impact of all individual systematic uncertainties and their combined effect is investigated.

- Based on the outcome of these sensitivity studies, an optimal electromagnetic field setting is discussed (s. sc. 7.2). A direct consequence field configuration is the pixel size for the future TRISTAN detector and the available space for instrumentation.

7.1 Sterile neutrino sensitivity

While previous studies on sterile neutrino sensitivities [Mer15a; Mer15b] illustrated the feasibility of discovering sterile neutrinos with KATRIN, the analyses did not include the influence of systematic uncertainties.

The estimation of systematic uncertainties is achieved using the covariance approach [Las15; Dol17]. By default the presented studies show 90% CL contours and the overall normalization is given in accordance with [Mer19]. The expected detector rate, the number of pixels, and the measurement time are fixed to

$$\Gamma_\mathrm{det} = 10^8 \,\mathrm{cps} \, , \quad n_\mathrm{px} = 3486 \text{ and } \quad t_\mathrm{meas} = 3\,\mathrm{y} \, . \tag{7.1}$$

Table 7.1: Values for $\Delta\chi^2$ corresponding to a confidence level % CL and Gaussian coverage in terms of multiple standard deviations (std. dev.). The parameter m denotes the number of estimated parameters.

C.L. (%)	std. dev. (σ)	$\Delta\chi^2$		
		m=1	m=2	m=3
68.27	1.000	1.00	2.30	3.53
90.00	1.645	2.71	4.61	6.25
95.00	1.960	3.84	5.99	7.82
95.45	2.000	4.00	6.18	8.03
99.00	2.576	6.63	9.21	11.34
99.73	3.000	9.00	11.83	14.16

7.1.1 Procedure

The sensitivity estimation is based on a maximum likelihood approach [Tan18]. The likelihood of $L(H)$ describes how probable it is, that measured data at x matches a given hypothesis H:

$$L(H) = P(x|H) \ . \tag{7.2}$$

A typical extension is the introduction of multiple, independent measurements $x \rightarrow \boldsymbol{x} = (x_1, ..., x_n)$, i.e. binned data, where all measurements follow the same hypothesis, i.e. the same probability density function $H \rightarrow f(\boldsymbol{x}|\boldsymbol{\theta})$, with a set of parameters $\boldsymbol{\theta} = (\theta_i, ...\theta_m)$. The likelihood thus becomes the product of the independent measurements:

$$L(\boldsymbol{\theta}) = \prod_{i=1}^{n} f(x_i, \boldsymbol{\theta}) \ . \tag{7.3}$$

Rewriting this equation under the assumption of normal distributed , i.e. $f(x_i, \boldsymbol{\theta}) \rightarrow \exp(-(N_{\text{data},i} - N_{\text{model}}(x_i, \boldsymbol{\theta}))^2/2/\sigma_{\text{data},i}^2)$, yields the so-called χ^2 method:

$$\chi^2(\boldsymbol{\theta}) = -2\ln L(\boldsymbol{\theta}) + const. = \sum_{i=1}^{n} \frac{\left(N_{\text{data},i} - N_{\text{model}}(x_i, \boldsymbol{\theta})\right)^2}{\sigma_{\text{data},i}^2} \ . \tag{7.4}$$

Note that the natural logarithm is used as it facilitates numerical calculation, as well as a factor -2 multiplied, implying a minimization process for χ^2 instead of the maximization for $L(\boldsymbol{\theta})$. Doing an expansion of χ^2 in a single parameter θ around its true value $\hat{\theta}$, one finds, that

$$\chi^2(\theta) = \chi^2(\hat{\theta} \pm \sigma_{\hat{\theta}}) = \chi^2(\hat{\theta}) + 1 = \chi^2_{\text{min}} + \Delta\chi^2 \tag{7.5}$$

has tangent planes at constant values $\Delta\chi^2$. These allow for a geometrical relation between $\Delta\chi^2$ and θ. One often speaks of these planes as confidence levels. The percentage is

calculated according to the coverage of the normal distribution. In table 7.1 typical values of $\Delta\chi^2$ for different numbers of parameters m are noted.

Nuisance parameters

A possibility to include systematic uncertainties, is by using so-called nuisance parameters $\boldsymbol{\nu}$. They are part of the model and assumed free during the minimization of χ^2. Thereby χ^2 is reduced and the impact of model parameters tested. Assuming an asymptotic data set for the measurement [Cow11], i.e. neglecting statistical fluctuations, and deriving it from the same model, at $(\boldsymbol{\theta}', \boldsymbol{\nu}')$, we get:

$$\chi^2(\boldsymbol{\theta}|\boldsymbol{\nu}) = \sum_{i=1}^{n} \frac{\left(\Gamma_{\text{data},i}(\boldsymbol{\theta}'|\boldsymbol{\nu}') - \Gamma_{\text{model},i}(\boldsymbol{\theta}|\boldsymbol{\nu})\right)^2}{\sigma^2_{\text{data},i}(\boldsymbol{\theta}'|\boldsymbol{\nu}')} \ . \tag{7.6}$$
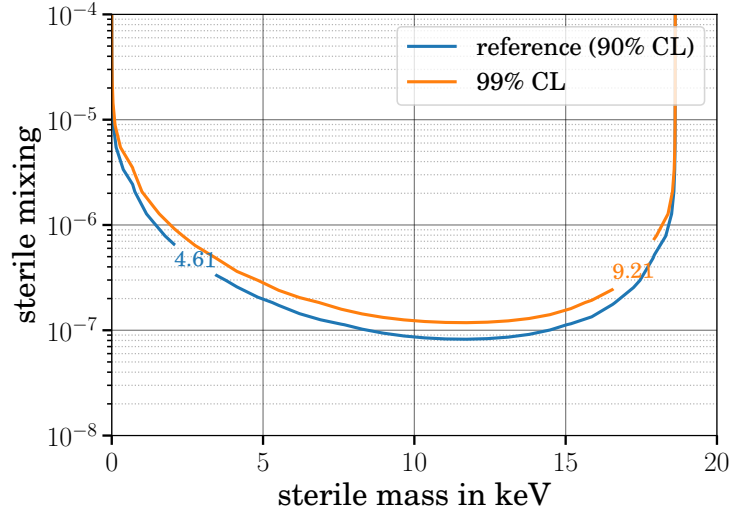
Figure 7.1: Statistical sensitivity to a sterile neutrino at confidence level of 90% CL (blue) and 99% CL (orange). $\Delta\chi^2$ is marginalized over the background rate Γ_{bkg}, the electron detector rate Γ_{det}, and the spectrum endpoint of tritium beta-decay. The 90% CL will be reused in later illustrations and referred to as reference sensitivity.

In figure 7.1 a sterile neutrino sensitivity analysis with $\boldsymbol{\theta} = (m_4, \sin^2\theta)$ and $\boldsymbol{\nu} = (\Gamma_{\text{det}}, \Gamma_{\text{bkg}}, E_0)$ was performed. Γ_{det} is the total rate at the detector, Γ_{bkg} a constant background rate and E_0 the spectrum endpoint. Based on [Mer19], the measurement was derived with respect to $\boldsymbol{\nu}' = (\Gamma_{\text{det}} = 10^8\,\text{cps}, \Gamma_{\text{bkg}} = 1\,\text{cps}, E_0 = 18575\,\text{eV})$ and as a null hypothesis $\boldsymbol{\theta}' = (m_4 = 0\,\text{keV}, \sin^2\theta = 0)$ the non existence of sterile neutrinos is assumed. The figure shows a maximal sensitivity at roughly $m_4 = 12\,\text{keV}$, this relates to the nuisance parameter Γ_{det}. Similar to the overall normalization, it implies a shape-only analysis. Accordingly, the sterile neutrino signature is less prominent at the edges of the beta-decay electron energy spectrum.

Covariance matrix

Relaxing the assumption of bin-to-bin uncorrelated data requires a vectorized approach and thus the usage of a covariance matrix

$$V = \mathrm{Cov}[\vec{y}] = \mathrm{E}[(\vec{y} - \vec{\mu})] \cdot (\vec{y} - \vec{\mu})^T] \; , \tag{7.7}$$

where "$E[\,]$" denotes the expectation value of a variable (its mean value), $\vec{\mu} = (E[y_1], ..E[y_n])$ is a vector of expectations and "$\cdot$" specifies the matrix product, yielding V of size $n \times n$. With respect to correlations equation 7.4 transforms to

$$\chi^2(\boldsymbol{\theta}) = \left(\vec{N}_{\mathrm{data}} - \vec{N}_{\mathrm{model}}(\boldsymbol{\theta})\right)^T \cdot V^{-1} \cdot \left(\vec{N}_{\mathrm{data}} - \vec{N}_{\mathrm{model}}(\boldsymbol{\theta})\right) \; , \tag{7.8}$$

with V^{-1} being the inverse of the covariance matrix.

Mathematically, the covariance matrix is derived from n_{cov} repeated binned measurements $D = (\vec{N}_{\mathrm{data},1}, ..., \vec{N}_{\mathrm{data},n_{\mathrm{cov}}})$:

$$V(\boldsymbol{\theta}'|\vec{\boldsymbol{\eta}}') = \mathrm{Cov}[D(\boldsymbol{\theta}'|\vec{\boldsymbol{\eta}}')] \; , \quad D_{ij} = \Gamma_{\mathrm{data},i}(\boldsymbol{\theta}'|\boldsymbol{\eta}'_j) \; . \tag{7.9}$$

Here $\vec{\boldsymbol{\eta}}'$, an n_{cov} long vector of nuisance parameters, was introduced. They allow an investigation of systematic uncertainties by modifying the generated binned measurements and thereby the calculated covariance matrix. A viable choice for the k-th nuisance parameter $\vec{\eta}'_k$ is a normal distribution with mean $\mu = \hat{\eta}_k$ and a standard deviation of $\sigma = 10\% \cdot \hat{\eta}_k$.

(a) covariance matrix
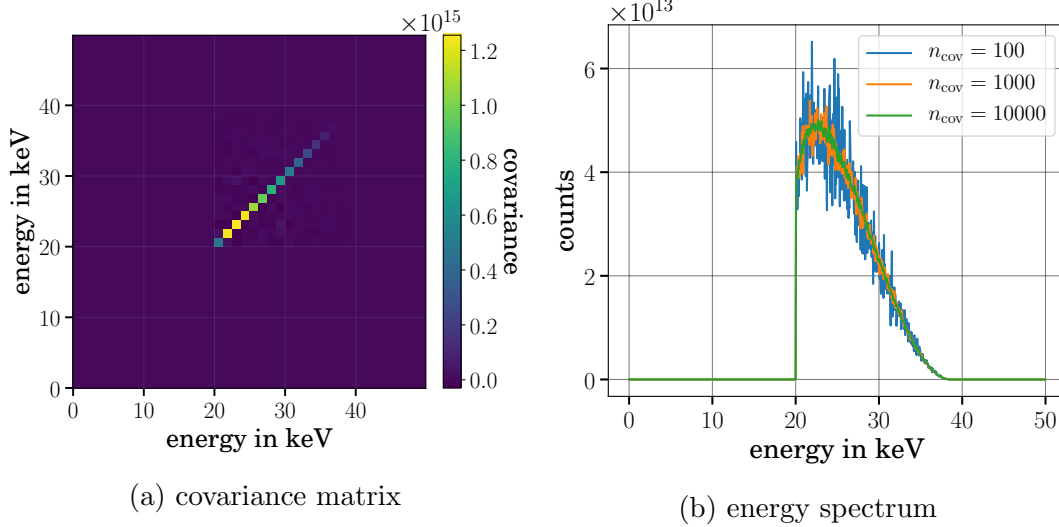
(b) energy spectrum

Figure 7.2: Covariance matrix of the beta-decay electron energy spectrum with $U_{\mathrm{ret}} = 20\,\mathrm{kV}$ post acceleration electrode and $n_{\mathrm{cov}} = 5000$ number of MC repetitions (left). In contrast, on the right the evolution of its diagonal elements at different values of n_{cov} is shown. For illustration, the covariance matrix is displayed with exaggerated energy bins $\Delta E = 1.25\,\mathrm{keV}$.

In figure 7.2a such a covariance matrix and its fluctuations for different numbers of n_{cov} is illustrated. Notably, the figure shows the impact of statistical fluctuations, which is a fully bin-to-bin uncorrelated effect.

7.1.2 Individual study

The systematic sensitivity for sterile neutrinos is studied by calculating a covariance matrix based on systematic parameters p as well as their uncertainties σ_p. The spectrum calculation is based on the semi-analytical model (s. sc. 5.3) and the influence of

- electronic noise ($\text{FWHM}_{\text{noise}}$, $\sigma_{\text{FWHM}_{\text{noise}}}$, E_{thres}, $\sigma_{E_{\text{thres}}}$),

- signal pile-up (t_{min}, $\sigma_{t_{\text{min}}}$),

- charge-sharing (P_{cs}, $\sigma_{P_{\text{cs}}}$), and

- silicon scattering (z_{dl}, $\sigma_{z_{\text{dl}}}$, $\sigma_{\vartheta_{\text{p,in}}}$)

are discussed. In addition, different acceleration voltages U_{ret} are considered.

7.1.2.1 Electronic noise

Electronic noise occurs on the waveform level and introduces fluctuations in the observed signal (s. sc. 5.2.4). Two effects are described in the model: spectrum broadening due to the energy resolution $\text{FWHM}_{\text{noise}}$ and the trigger threshold $E_{\text{kin}} > E_{\text{thres}}$.
In figure 7.3a their impact to a shifted $U_{\text{pae}} = 20\,\text{kV}$ beta-decay spectrum is illustrated. The influence of the energy resolution is especially pronounced at the position of detection threshold E_{thres}, at the starting region of the beta-decay spectrum U_{pae}, and at the spectrum endpoint $E_0 + qU_{\text{pae}}$.
A sensible parameter for the energy resolution is derived from the waveform sensitivity studies in [Mer15b], requiring a resolution better than $\text{FWHM} = 300\,\text{eV}$. The modeled response only considers electronic noise $\text{FWHM} \cong \text{FWHM}_{\text{noise}}$ (no Fano-noise, no dead-layer). The energy threshold is directly connected to the resolution of electronic noise and here a value of $E_{\text{thres}} = 1000\,\text{eV} \approx 3 \cdot \text{FWHM}_{\text{noise}}$ is chosen. For voltage fluctuations a systematic uncertainty of $\sigma = 20\,\text{eV}$ is selected, a conservative value compared to per mil level accuracy of monitoring devices at KATRIN. Together with a default scenario $U_{\text{pae}} = 0\,\text{kV}$, the analysis parameters are:

$$U_{\text{pae}} = 0\,\text{kV} \ , \quad \text{FWHM}_{\text{noise}} = 300 \pm 20\,\text{eV} \ \text{and} \quad E_{\text{thres}} = 1000 \pm 20\,\text{eV} \ . \tag{7.10}$$

The spectrum calculation is now repeated for $n_{\text{cov}} = 1000$-times for the two parameters. However, on each calculation the resolution is randomly selected from a normal distribution with $\mathcal{N}(\mu = \text{FWHM}_{\text{noise}}, \sigma_{\text{FWHM}_{\text{noise}}})$ respective $\mathcal{N}(\mu = E_{\text{thres}}, \sigma_{E_{\text{thres}}})$ for the detection threshold. Based on the set of n_{cov}-calculated energy spectra the covariance matrix is

(a) spectrum

(b) absolute covariance
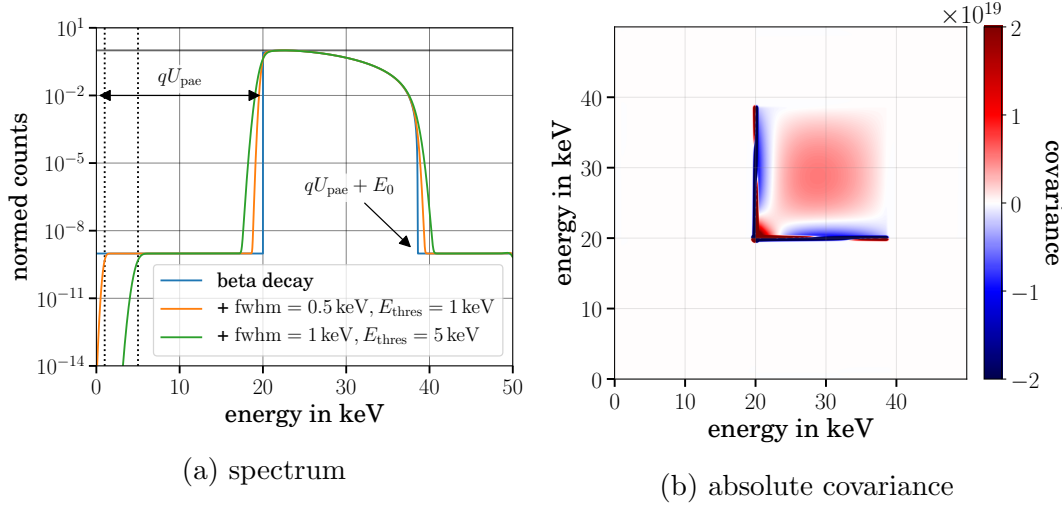
Figure 7.3: (a) Impact of electronic noise to the beta-decay electron energy spectrum measured at the detector. The spectra are normalized to the maximum of the scenario of no noise and the dotted lines illustrate the applied threshold values E_{thres}. (b) Covariance matrix for $\text{FWHM}_{\text{noise}} = 300 \pm 20 \,\text{eV}$, $E_{\text{thres}} = 1000 \pm 20 \,\text{eV}$ and with $n_{\text{cov}} = 500$ repetitions. Here an additional post acceleration of $U_{\text{pae}} = 20 \,\text{kV}$ and constant background rate of $\Gamma_{\text{bkg}} = 1 \,\text{cps}$ are considered.

determined (s. fig. 7.3b). Similar to the impact of electronic noise to the beta-decay spectrum, uncertainties lead to large covariance matrix elements where bin-to-bin count rate differences are large: at E_{thres}, at qU_{pae} and at $qU_{\text{pae}} + E_0$. In contrast, at the maximum position $qU_{\text{pae}} + 2.5 \,\text{keV}$ of the beta-decay spectrum the covariance is accordingly small. The underlying structure at all three position is especially strong pronounced in the correlation matrix in A.19a.

Subsequently the sterile neutrino sensitivity is calculated based on equation 7.8. Here two spectra are compared, a case without and a case with sterile neutrinos $(m_4, \sin^2 \theta)$. Repeating the calculation for different masses and mixing amplitudes along a two dimensional grid gives the systematic sensitivity illustrated in figure 7.4.

With the parameter set in equation 7.10 a loss of the sensitivity at larges masses is observed. This is related to the signature of the sterile neutrino: large masses lead to a signature below the energy threshold $m_4 \cdot c^2 \geq E_0 - E_{\text{thres}}$ and are undetectable. The broadening due to the energy resolution affects an energy range of $\mathcal{O}(300 \,\text{eV})$ and thus affects the sensitivity up to masses of $m_4 > 14 \,\text{keV}$. Notably, a sterile neutrino signature close to the endpoint $m_4 < 14 \,\text{keV}$ is not affected by electronic noise, which is related to the small count rates.

In order to investigate how the sensitivity develops for different model parameters the covariance calculation and sensitivity study is repeated, modifying a single parameter at-a-time compared to the default set in equation 7.10:

- *Uncertainties*: Improving the uncertainty on electronic noise to $\sigma_{\text{FWHM}_{\text{noise}}} = \sigma_{E_{\text{thres}}} =$
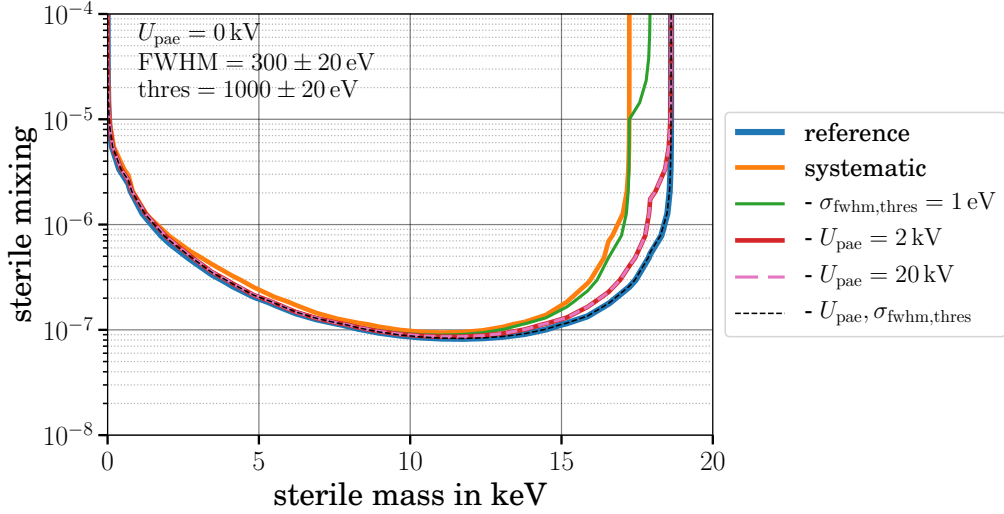
Figure 7.4: Electronic noise sterile neutrino sensitivity study. The reference sterile neutrino sensitive, based on statistical uncertainties only, is shown in blue. The impact of electronic noise with default parameters (upper left) is shown in orange. Green, red and pink highlight different mitigation scenarios, where one parameter of the depicted parameters changes from default. The sensitivity is fully recovered for $U_{\mathrm{pae}} = 2\,\mathrm{kV}$, $\mathrm{FWHM}_{\mathrm{noise}} = 300 \pm 1\,\mathrm{eV}$ and $E_{\mathrm{thres}} = 1000 \pm 1\,\mathrm{keV}$ (black).

$1\,\mathrm{eV}$ only slightly mitigates the observed sensitivity loss at large masses $m_4 \cdot c^2 \approx E_0 - E_{\mathrm{thres}}$. Interestingly, the small uncertainties allow to peer - due to the broadening of the energy resolution - into the spectral shape below the detection threshold $E_{\mathrm{thres}} = 1000\,\mathrm{keV}$ and thus some sensitivity is recovered.

- *Acceleration voltage*: Accelerating the electrons from beta-decay by $U_{\mathrm{pae}} = 2\,\mathrm{kV}$ results in an almost full recovery of the sensitivity. The reason being, that the acceleration is chosen high enough to shift the sterile neutrino signature above the influence of energy resolution and threshold $E_{\mathrm{thres}} + \mathrm{FWHM} < qU_{\mathrm{pae}} + E_0 - m_4$. A further increase of voltage $U_{\mathrm{pae}} = 20\,\mathrm{kV}$ does not improve the sensitivity.

- *Optimized*: Combining an acceleration voltage of $U_{\mathrm{pae}} = 2\,\mathrm{kV}$ with low systematic uncertainties $\sigma_{\mathrm{FWHM}_{\mathrm{noise}}} = \sigma_{E_{\mathrm{thres}}} = 1\,\mathrm{eV}$ allows for a full recovery of the sterile neutrino sensitivity.

In summary, the influence of systematic uncertainties from electronic noise to the sterile neutrino sensitivity can be reduced by selecting acceleration potentials larger than the prevalent noise $qU_{\mathrm{pae}} > E_{\mathrm{thres}} + \mathrm{FWHM}_{\mathrm{noise}}$ and by monitoring voltages that affect an electron's energy with an accuracy of $\sigma = 1\,\mathrm{V}$.

(a) spectrum

(b) covariance
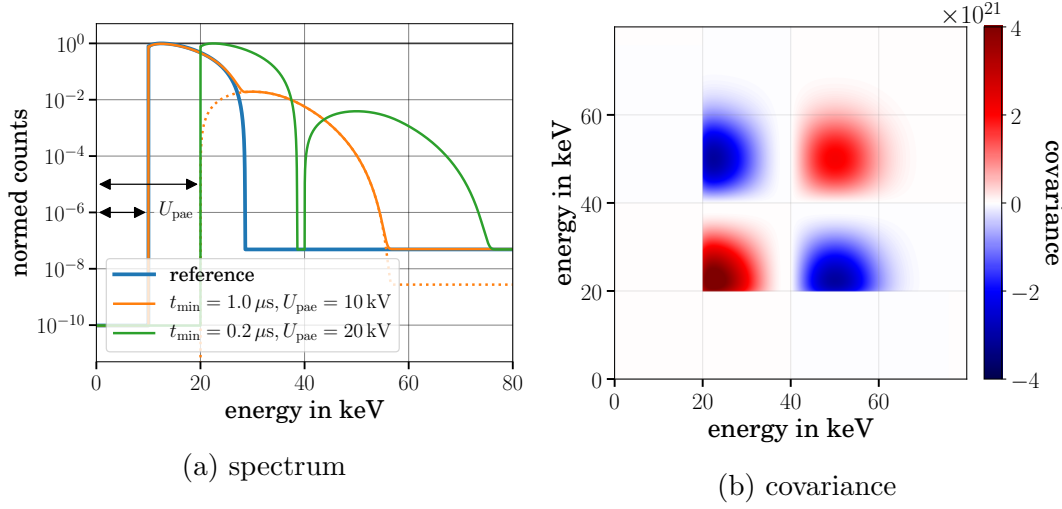
Figure 7.5: (a) Impact of signal pile-up to the detected beta-decay electron energy spectrum for different minimal discrimination times $t_{\min} = 0/0.2/1.0\,\mu$s (blue/orange/-green). The spectra are normalized to the maximum of the reference: no pile-up (blue). Applying a post acceleration $U_{\text{pae}} = 20\,$kV, shifts the region of pile-up events above the spectrum endpoint (green). (b) Respective covariance matrix at $U_{\text{pae}} = 20\,$kV and $t_{\min} = 1.0 \pm 0.1\,\mu$s.

7.1.2.2   Signal pile-up

Signal pile-up occurs when two events hit the detector quickly $\Delta t < \mathcal{O}(1\,\mu$s) after another. As the measured signal is indistinguishable by the DAQ, the detected energy is a superposition of the individual $E = E_1 + \epsilon(\Delta t) \cdot E_2$ events. In the pile-up model the energy-loss of pile-up events $\epsilon = 1$ was neglected. Measurements with DANTE performed in chapter 6 and separately by [Des19] are in good agreement with this assumption.

The probability for pile-up to occur is based on the incident rate at each pixel Γ_{px} and on the chosen signal filter settings, defined by the minimal event discrimination time $t_{\min}$ (s. eq. 5.32 & 7.1). The expected influence of pile-up to the registered electron energy spectrum is illustrated in figure 7.5a. Notably, smaller discrimination times $t_{\min}$ lead to an exponentially scaled reduction of the probability and the minimal energy of pile-up events is given by twice the acceleration voltage:

$$E = (E_1 + qU_{\text{pae}}) + (E_2 + qU_{\text{pae}}) \geq 2 \cdot qU_{\text{pae}} \tag{7.11}$$

Applying a large acceleration potential $qU_{\text{pae}} \geq E_0$ thus leads to a separation in the observed energy spectrum: pure beta-decay electrons have energies $E_{\text{kin}} \in [qU_{\text{pae}}, qU_{\text{pae}}+E_0]$, whereas events that are affect by signal pile-up have a minimal energy of $E_{\text{kin}} \geq 2qU_{\text{pae}}$ (s. fig. 7.5a).

In order to estimate the expected uncertainty on $t_{\min}$ it is important to consider both, the precision of the future DAQs system as well as the stability of KATRINs tritium source
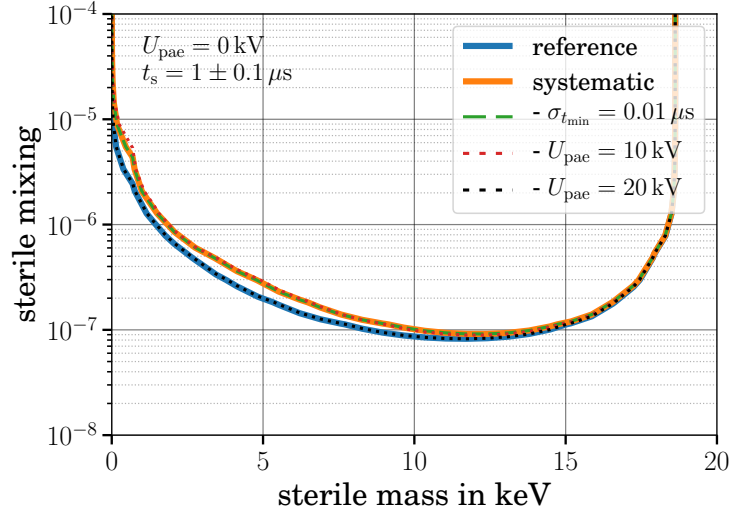
Figure 7.6: Systematic impact of signal pile-up to a sterile neutrino investigation at KATRIN. The reference model without pile-up is given in blue. In orange its projected systematic impact is given: default parameters $U_{\mathrm{pae}} = 0\,\mathrm{kV}$ and $t_{\mathrm{min}} = 1 \pm 0.1\,\mu\mathrm{s}$. The dashed and dotted lines vary a single parameter thereof ($\sigma_{t_{\mathrm{min}}}$ or U_{pae}).

Γ_{src}. The latter affects the pile-up probability in the same fashion as t_{min} and is thus directly correlated. A conservative $10\% = \sigma_{t_{\mathrm{min}}}$ uncertainty was assumed.

Uncertainties on the minimum discrimination time translate to uncertainties on the pile-up probability. In the energy spectrum the amplitude of the pure beta-decay part increases for small t_{min}, whereas the amplitude of the piled-up spectrum region decreases. In conclusion this leads to an uncertainty in the scaling of the two spectral regions, which is directly visible in the covariance matrix (s. fig. 7.5b).

The sensitivity analysis is shown in figure 7.6, with the default parameters

$$U_{\mathrm{pae}} = 0\,\mathrm{kV} \quad \text{and} \quad t_{\mathrm{min}} = 1.0 \pm 0.1\,\mu\mathrm{s}\ . \tag{7.12}$$

The largest impact to the sensitivity is visible at low masses $m_4 < 10\,\mathrm{keV}$, which corresponds to sterile neutrino signatures closer to the spectrum endpoint. This is related to the minimum energy of pile-up events (s. eq. 7.11). For $U_{\mathrm{pae}} = 0\,\mathrm{kV}$ the beta-decay and the pile-up spectra overlap and the position of the maximum shifts from $2.5\,\mathrm{keV}$ (beta-decay) to twice the energy $E = 5\,\mathrm{keV}$. The influence of pile-up broadens and shifts the observed spectrum. This process has a larger impact at regions where the initial beta-decay has low count rates, i.e. closer to the spectrum endpoint.

The sensitivity analysis is repeated by changing only a single parameter at-a-time from the default set in equation 7.12:

- *Uncertainty*: Improving the accuracy to $1\% = \sigma_{t_{\mathrm{min}}}$ does not show any improvement in the sensitivity.

(a) spectrum
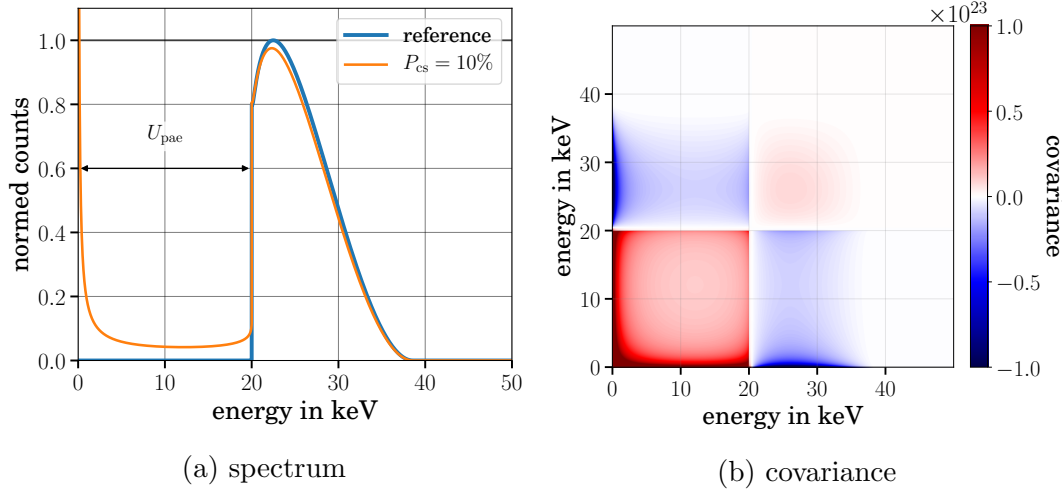
(b) covariance

Figure 7.7: (a) Impact of charge-sharing to the tritium beta-decay spectrum with $U_{\mathrm{pae}} = 20\,\mathrm{kV}$. The pure beta-decay spectrum is given in blue and the in orange a spectrum with $P_{\mathrm{cs}} = 10\,\%$ charge-sharing is shown. (b) Covariance matrix with respect to $P_{\mathrm{cs}} = 10 \pm 1\,\%$ and $U_{\mathrm{pae}} = 20\,\mathrm{kV}$.

- Acceleration voltage: Increasing the acceleration voltage to $U_{\mathrm{pae}} = 10\,\mathrm{kV}$ similar does not improve the sensitivity. However, accelerating the electron by more than the spectrum endpoint $qU_{\mathrm{pae}} > E_0$ leads to a full recovery of the sensitivity. In this case the minimal pile-up energy is large enough to separate the beta-decay signature region from the pile-up spectrum.

In conclusion, pile-up requires high post-acceleration voltages, larger than the spectrum endpoint $qU_{\mathrm{pae}} > E_0$.

7.1.2.3 Charge-sharing

Charge-sharing occurs if an incident electron hits the boundary between pixels. The initial energy is hence similarly split $E_{\mathrm{in}} \rightarrow (E_1, E_2)$ and two separate events observed. In the model charge-sharing between two pixels and for a homogeneous incidence are considered (s. sc. 5.2.3). Characterization measurements however showed, that triple charge-sharing leads to measurable spectrum distortion and should be included in the future (s. fig. 6.7b). The impact of charge-sharing to the beta-decay energy spectrum is depicted in figure 7.7a. Three regions are notable: high count rates at low energies $E < 1\,\mathrm{keV}$, an almost flat shape for $E \in [1\,\mathrm{keV}, qU_{\mathrm{pae}}]$ and a slight rate reduction for $E \in [qU_{\mathrm{pae}}, qU_{\mathrm{pae}} + E_0]$.

Based on equation 5.27, assuming a pixel radius of $r_{\mathrm{px}} = 1.5\,\mathrm{mm}$ and a charge cloud radius $r_{\mathrm{cc}} = 20\,\mu\mathrm{m}$, one expects a charge-sharing probabiltiy of $P_{\mathrm{cs}} = 5.6\,\%$. For a more conservative estimate a slightly higher value $P_{\mathrm{cs}} = 10\,\%$ was selected. As the determination of the probability depends on the estimation of the overall rate a large 10% uncertainty is chosen. The covariance matrix in figure 7.7b reflects the discussed three regions.
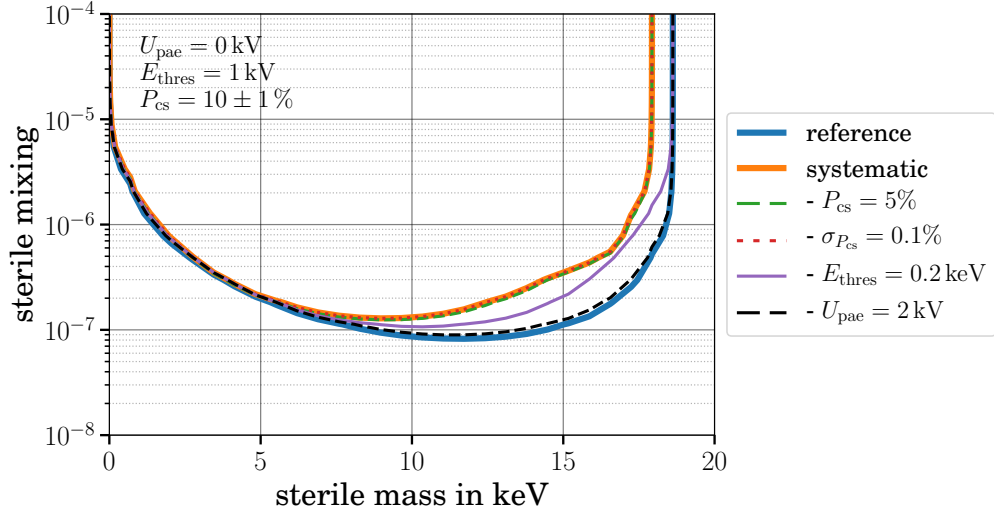
Figure 7.8: Sterile neutrino sensitivity with respect to charge-sharing. The reference model without charge-sharing is given in blue. In orange its projected systematic impact is given, using $U_{\mathrm{pae}} = 0\,\mathrm{kV}$, $E_{\mathrm{thres}} = 1\,\mathrm{keV}$ and $P_{\mathrm{cs}} = 10 \pm 1\,\%$. The other $90\%\,\mathrm{CL}$ curves differ by a single parameter from this set (e.g. $P_{\mathrm{cs}} = 5\,\%$ in green).

Uncertainties on the charge-sharing probability show the largest impact at low energies $E < 1\,\mathrm{keV}$. This region is however not accessible in a typical measurement, due to the energy threshold. For the sensitivity analysis, presented in figure 7.6, the default parameters hence also include a fixed energy threshold:

$$U_{\mathrm{pae}} = 0\,\mathrm{kV}\ , \quad E_{\mathrm{thres}} = 1\,\mathrm{keV} \quad \text{and} \quad P_{\mathrm{cs}} = 10 \pm 1\,\% \ . \tag{7.13}$$

Consequently the sensitivity is lost at sterile neutrino masses $m_4 > E_0 - E_{\mathrm{thres}}$ below the energy threshold. Over the range $m_4 \in [9\,\mathrm{keV}, E_0 - E_{\mathrm{thres}}]$ the sensitivity is slowly recovered. Translated to the sterile neutrino signature the range corresponds to energies $E \in [0, E_0/2]$. As charge-sharing results in split energies, the entire beta-decay spectrum contributes to the observed charge-shared spectrum at low energies. Uncertainties on the charge-sharing probability thus impact the low-energy region more.

The sensitivity analysis was repeated by changing a single parameter at-a-time from the default set in equation 7.13:

- *Probability*: Decreasing the charge-sharing probability to $P_{\mathrm{cs}} = 5\,\%$ does not improve the sensitivity.

- *Uncertainty*: Similarly, a smaller uncertainty $\sigma = 0.1\%$ does not show any improvement.

- *Energy threshold*: Reducing the energy threshold to $E_{\mathrm{thres}} = 200\,\mathrm{eV}$ improves the sensitivity. Here the reduced threshold allows the optimization process to asses the "first region" of charge-sharing $E < 1\,\mathrm{keV}$. During the optimization the steep increase

(a) spectrum

(b) covariance
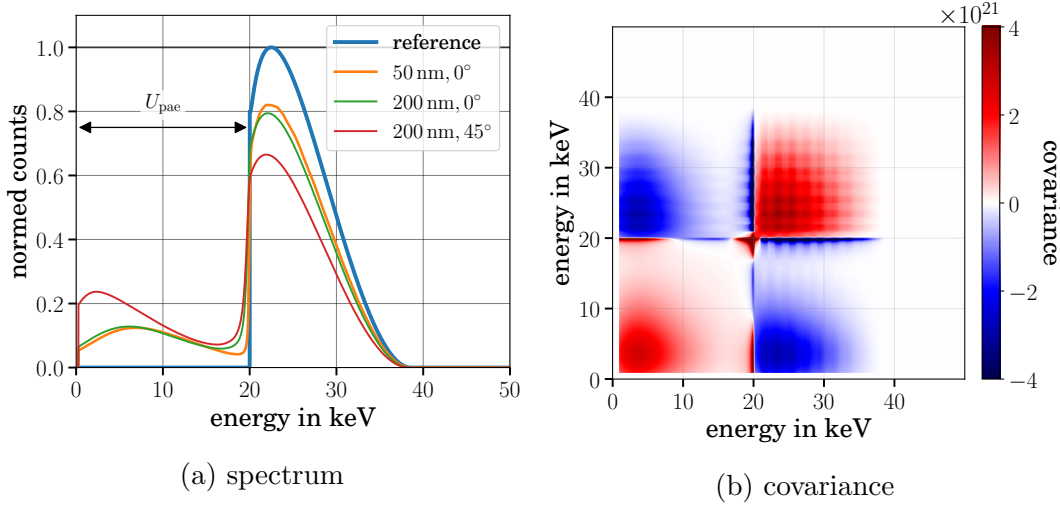
Figure 7.9: (a) Impact of electron scattering in the silicon to the beta-decay electron energy spectrum with $U_{\text{pae}} = 20\,\text{kV}$. The pure beta-decay spectrum is given in blue. A deadlayer $z_{\text{dl}} = 50\,\text{nm}$ and perpendicular incidence $\vartheta_{\text{p,in}} = 0\,°$ is shown in orange. The exemplary impact of a deadlayer with $z_{\text{dl}} = 200\,\text{nm}$ is shown in green and for angle of $\vartheta_{\text{p,in}} = 45\,°$ in red. (b) Covariance matrix with respect to $U_{\text{pae}} = 20\,\text{kV}$, $z_{\text{dl}} = 50 \pm 5\,\text{nm}$ and $\vartheta_{\text{p,in}} = 0 \pm 5\,°$.

allows for better model comparisons and is thus less impacted by the shape-only analysis, i.e. less impacted by the minimization process of the detector rate Γ_{det}.

- *Acceleration voltage*: Increasing the acceleration voltage to $U_{\text{pae}} = 2\,\text{kV} = E_{\text{thres}} + 1\,\text{keV}$ allows for a full recovery of the sensitivity. This is similarly related to the optimization process, the shape-only analysis. In this scenario, however, the acceleration voltage leads to a small range $E \in [E_{\text{thres}}, qU_{\text{pae}}] = [1\,\text{keV}, 2\,\text{keV}]$ that is solely related to charge-sharing. This region constrains the marginalization of the detector rate Γ_{det} and leads to the full recover of the sensitivity.

In conclusion, charge-sharing requires low energy threshold values $E_{\text{thres}} < 1\,\text{keV}$ and a post-acceleration voltage large enough $U_{\text{pae}} > E_{\text{thres}}$ to constrain the shape-only analysis.

7.1.2.4   Scattering

The last systematic that is discussed is the energy deposition process of the incident electrons. The model is based on simulated energy responses with KESS (s. sc. 5.2.1) and the simulation interpolation approach (s. sc. 5.3.2). In summary the model describes the energy deposition of electrons in silicon. Two model parameters where investigated: the detection deadlayer z_{dl} and the incident angle $\vartheta_{\text{p,in}}$ of electrons.

The impact of scattering to the beta-decay spectrum is presented in figure 7.9a. Comparing the realistic scenario of deadlayer thickness $z_{\text{dl}} = 50\,\text{nm}$ and perpendicular incidence

$\vartheta_{\mathrm{p,in}} = 0^{\circ}$ to a pure beta-decay spectrum, a count rate reduction of about 20% is visible at the position of the maximum. This is related to electron back-scattering, they deposit only a small fraction of their initial energy within the detector[1]. The measured energy is further reduced by an energy loss in the detection deadlayer

$$E_{\mathrm{meas}}(E_{\mathrm{in}}, \vartheta_{\mathrm{p,in}}) = E_{\mathrm{in}} - E_{\mathrm{bs}}(E_{\mathrm{in}}, \vartheta_{\mathrm{p,in}}) - E_{\mathrm{dl}}(E_{\mathrm{in}}, \vartheta_{\mathrm{p,in}}) . \tag{7.14}$$

Moreover, the measured energy depends on the initial energy E_{in}, and incident angle $\vartheta_{\mathrm{p,in}}$. For example, electron with an energy $E_{\mathrm{in}} = 3\,\mathrm{keV}$ will lose their entire energy in a $z_{\mathrm{dl}} = 100\,\mathrm{nm}$ thick deadlayer (s. sub-sc. 5.2.1).

For calculating the covariance matrix, the model is evaluated $n_{\mathrm{cov}} = 1000$-times at different deadlayer thicknesses $z_{\mathrm{dl}} = 50 \pm 5\,\mathrm{nm}$ and incident angles $\vartheta_{\mathrm{p,in}} = 0 \pm 5^{\circ}$. In contrast to the previous systematic effects, scattering off silicon is not modeled in an analytic fashion but instead by the simulation interpolation approach (s. sc. 5.3.2). As it is fundamentally based on individual simulations, the derived spectra reflect, to some degree, the statistical uncertainties $\sigma_{\mathrm{sim}} \leq \sqrt{N_{\mathrm{sim}}}$.

The uncertainties of the simulation interpolation become visible in the covariance matrix as periodic structures with $1\,\mathrm{keV}$ spacing (s. fig. 7.9b). The period matches with the underlying simulated responses and is visible at $E \in [qU_{\mathrm{pae}}, qU_{\mathrm{pae}} + E_0]$. As each modeled response is connected with small simulation uncertainties σ_{sim}^i, the calculation process of the covariance matrix (s. eq. 7.7) leads to an increase of the total uncertainty. This effect is further expressed at electron energies $E_{\mathrm{in}} < 5\,\mathrm{keV}$, where they are more likely to lose their entire energy in the deadlayer and thus lead to a reduction of events in the simulated response $N_{\mathrm{sim}} \searrow (\sigma_{\mathrm{sim}}/N_{\mathrm{sim}} \nearrow)$.

The impact of these uncertainties are however suppressed by the χ^2 formalism in the sensitivity analysis (s. eq. 7.8). Here the scattering response is calculated only once. By calculating the difference of the spectrum with and without a sterile neutrino, the model uncertainties cancel-out. Lastly, the marginalization of the detector rate Γ_{det} leads to an averaging of the covariance matrix.

In contrast to the previous studies, a large acceleration voltage is chosen by default. The detector deadlayer $z_{\mathrm{dl}} = 50\,\mathrm{nm}$ is selected in accordance to the characterization measurements in section 6.3.3, and a 10% uncertainty assumed. The incidence of electrons is simplified: instead of a distribution a constant value $\vartheta_{\mathrm{p,in}} = 0^{\circ}$ is used. As the incidence angle is connected to detector and electromagnetic-field alignment, a conservative uncertainty of $\sigma = 5^{\circ}$ is considered for the incidence angle.

For the sensitivity analysis, presented in figure 7.10, the default parameters are:

$$U_{\mathrm{pae}} = 20\,\mathrm{kV} , \quad z_{\mathrm{dl}} = 50 \pm 5\,\mathrm{nm} \text{ and } \quad \vartheta_{\mathrm{p,in}} = 0 \pm 5^{\circ} . \tag{7.15}$$

---

[1]Back-reflection is not considered
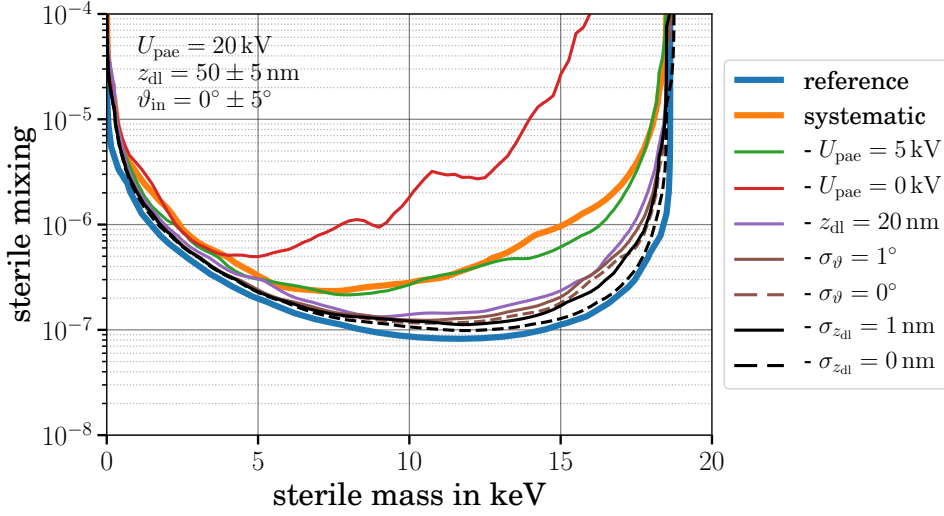
Figure 7.10: Impact of scattering to a sterile neutrino sensitivity. The reference statistic sensitivity without scattering is given in blue. Including the scattering response for the inscribed parameters (top left; $U_{\mathrm{pae}} = 20\,\mathrm{kV}$, $z_{\mathrm{dl}} = 50 \pm 5\,\mathrm{nm}$, $\vartheta_{\mathrm{p,in}} = 0 \pm 5\,^\circ$) is shown in orange. All other $90\%\,\mathrm{CL}$ curves vary in a single parameter from this parameter set.

The uncertainty on the deadlayer z_{dl} and on the incident angle $\vartheta_{\mathrm{p,in}}$ lead to significant sensitivity loss over the entire mass range. High sterile neutrino masses $m_4 > 10\,\mathrm{keV}$ correspond to a signature in the lower energy region $E \in [qU_{\mathrm{pae}}, qU_{\mathrm{pae}} + 10\,\mathrm{keV}]$. Here the spectrum broadening by Fano-like noise $\mathrm{FWHM}_{\mathrm{fano}}(20\,\mathrm{keV}) = 215\,\mathrm{eV}$ and the detection deadlayer affect the sensitivity. In addition, at masses $m_4 > 5\,\mathrm{keV}$ the sterile neutrino signature is obscured by the low energy-tail of back-scattered electrons. The sensitivity is only recovered at low masses $m_4 > 5\,\mathrm{keV}$.

The sensitivity analysis is repeated by changing only a single parameter at-a-time from the default set in equation 7.15:

- *Acceleration voltage*: Decreasing the acceleration voltage to $U_{\mathrm{pae}} = 5\,\mathrm{kV}$ does not show a significant impact to the sensitivity. However, at lower potentials the minimum electron energy decreases and results in lower Fano-noise $\mathrm{FWHM}_{\mathrm{fano}}(5\,\mathrm{keV}) = 108\,\mathrm{eV}$.

  Reducing the voltage further to $U_{\mathrm{pae}} = 0\,\mathrm{kV}$ shows a drastic sensitivity loss. In this case the detection deadlayer acts like a threshold for low energy electrons. Moreover, the shape-only analysis - marginalization over the detector rate Γ_{det}- can not distinguish the pure beta-decay spectrum from the low energy contribution of electron back-scattering.

- *Deadlayer thickness*: Reducing the deadlayer thickness to $z_{\mathrm{dl}} = 20\,\mathrm{nm}$ results in an overall improvement of the sensitivity. A low deadlayer significantly reduces the energy loss, which translates into smaller impact on the spectrum broadening due to uncertainties on deadlayer and incident angle.

- *Alignment*: Improving the uncertainty of the incident angle to $\sigma = 1°$ gives a similar improvement of the sensitivity. Its uncertainty affects the description of back-scattering energy tail and also leads to a virtual deadlayer (s. fig. 7.9a).

  In addition the uncertainty on the incident angle was switched off $\sigma = 0°$, which does not significantly change the sensitivity.

- *Homogeneity*: Lastly, a reduced uncertainty on the detector deadlayer $\sigma = 1\,\text{nm}$ was investigated. In this scenario the sensitive is mostly recovered. This is related to the reduced uncertainty on the spectrum broadening due to the deadlayer.

  Further decreasing the uncertainty on the deadlayer $\sigma = 0\,\text{nm}$ leads to an almost fully recovery of the sensitivity.

In conclusion, for improving the sensitivity to electron scattering at least an acceleration voltages of $U_{\text{pae}} > 5\,\text{keV}$ is required. Equally important is the production of detectors with thin deadlayers $z_{\text{dl}} \leq 20\,\text{nm}$, to characterize the deadlayer homogeneity to $\sigma_{z_{\text{dl}}} \approx 1\,\text{nm}$, and to determine the detector alignment with a $\sigma_{\vartheta_{\text{p,in}}} = 1°$ precision.

7.1.3 Combined study

In the final sterile neutrino measurement a multitude of systematic effects are superimposed to give the registered response. This however leads to large distortions of the measured spectrum and consequently requires a joint analysis. Here the impact of scattering, charge-sharing, electronic noise and signal pile-up are considered and uncertainties on all model parameters investigated together. The model calculation is based on the semi-analytical approach presented in section 5.3.

In the previous section 7.1.2 it was demonstrated that the shape-only sensitivity analysis requires a small region where the pure beta-decay spectrum may be separated from the impact of systematic effect (s. 7.1.2.3). This could be achieved, for example, by applying an electron acceleration voltage. In the combined approach this separation will become more complicated as scattering & charge-sharing both contribute a spectrum tail at low energies $E_{\text{meas}} < E_{\text{in}}$, whereas signal pile-up folds this part back to the energy region $E \in [qU_{\text{pae}}, qU_{\text{pae}} + E_0]$ of beta-decay electrons. In addition, electronic noise limits the measured spectrum above the detection threshold E_{thres} and thus complicates measuring the characteristic increase of charge-sharing $E_{\text{meas}} < 1\,\text{keV}$. Lastly, electronic- and Fano-noise lead to a broadening of the entire energy spectrum.
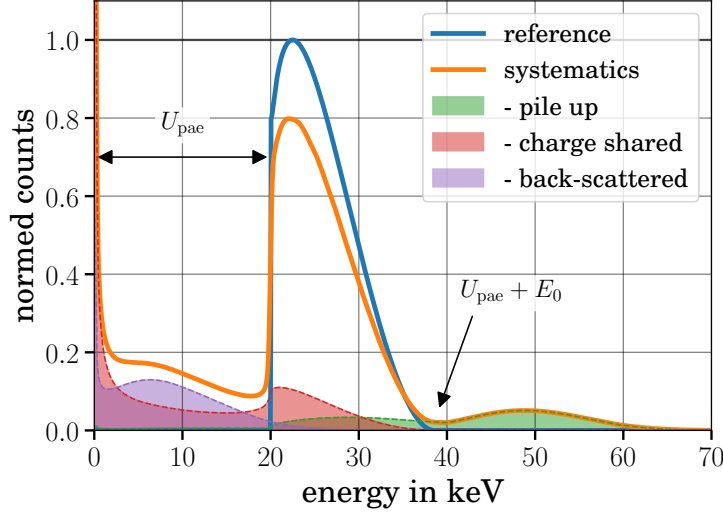
Figure 7.11: Combined impact of detector systematic effects to the tritium beta-decay electron energy spectrum (orange). The pure tritium spectrum given in blue. In addition the contribution of charge-sharing (green), pile-up (red) and the low energy scattering tail (violet) is depicted as shaded areas. For the illustration a zero detection threshold was applied $E_{\mathrm{thres}} = 0\,\mathrm{keV}$.

Without systematic uncertainties

Before discussion of systematic uncertainties, the effect of a perfectly known response is compared to the purely statistical sensitivity. In this first step following parameters are assumed

$$U_{\mathrm{pae}} = 20\,\mathrm{kV}\ , \quad \mathrm{FWHM_{noise}} = 300\,\mathrm{eV}\ , \quad E_{\mathrm{thres}} = 1000\,\mathrm{eV}\ ,$$
$$P_{\mathrm{cs}} = 10\,\%\ , \quad z_{\mathrm{dl}} = 50\,\mathrm{nm}\ \text{and}\ \ \vartheta_{\mathrm{p,in}} = 0\,^{\circ}\ . \tag{7.16}$$

Figure 7.12 shows that even a perfectly known detector response degrades the sterile neutrino sensitivity:

- *Acceleration voltage*: In the case of zero acceleration voltage $U_{\mathrm{pae}} = 0\,\mathrm{kV}$ the high mass regions $m_4 > 10\,\mathrm{keV}$ are especially strongly affected. This stems mainly from the influence of electronic noise (s. sc. 7.1.2.1), further increased by the energy loss in the detection deadlayer and by electron back-scattering.

- *Pile-up*: At low sterile neutrino masses $m_4 < 10\,\mathrm{keV}$ the contribution of signal pile-up is dominant and improving the minimum discrimination time to $t_{\mathrm{min}} = 0.2\,\mu\mathrm{s}$ slightly improves the sensitivity.

- *Back-scattering*: At all masses a small 10% sensitivity degradation is visible. This is mostly related to electron back-scattering (s. fig. 7.10).
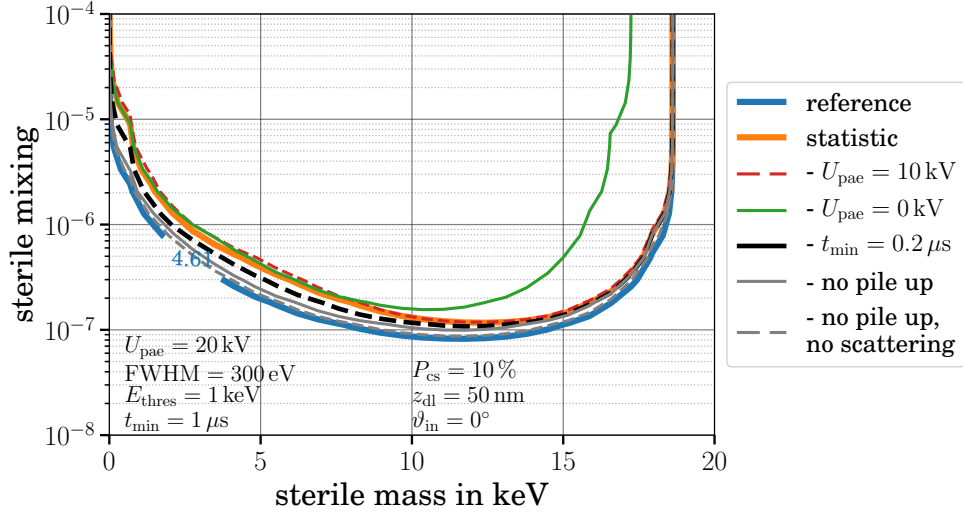
Figure 7.12: Impact of the systematic spectrum response to the statistical sterile neutrino sensitivity. As a reference the sensitivity with the pure beta-decay is given in blue. The default parameters for the detector systematic are inscribed in the figure and the relating 90 % CL given in orange. The other curves differ in a single parameter thereof.

For a full recovery of the sensitivity, the contribution of electron scattering to the modeled detector response has to be switched off.

With systematic uncertainties

In a next step, the impact of uncertainties in the detector response are investigated. Here the following uncertainties are considered simultaneously - a derivation for each value is discussed in section 7.1.2:

$$U_{\mathrm{pae}} = 20\,\mathrm{kV}\ , \quad \mathrm{FWHM}_{\mathrm{noise}} = 300 \pm 20\,\mathrm{eV}\ , \quad E_{\mathrm{thres}} = 1 \pm 0.02\,\mathrm{keV}\ ,$$
$$t_{\mathrm{min}} = 1 \pm 0.1\,\mu\mathrm{s}\ , \quad P_{\mathrm{cs}} = 10 \pm 1\,\%\ , \quad z_{\mathrm{dl}} = 50 \pm 5\,\mathrm{nm}\ \text{and}\quad \vartheta_{\mathrm{p,in}} = 0 \pm 5\,^{\circ}\ . \tag{7.17}$$

A covariance matrix (s. fig. 7.13) was generated by simulating $n_{\mathrm{cov}} = 1000$ spectra, while varying simultaneously all above-mentioned input parameters for each calculation. According to the different energy ranges the covariance matrix is dominated by other systematic effects: at $E \in [E_{\mathrm{thres}}, qU_{\mathrm{pae}}]$ by charge-sharing and back-scattering, at $E \in [qU_{\mathrm{pae}}, qU_{\mathrm{pae}} + E_0]$ by the energy resolution and at $E \in [qU_{\mathrm{pae}} + E_0, 2 \cdot qU_{\mathrm{pae}} + E_0]$ by signal pile-up.

The combined systematic sensitivity study is presented in figure 7.14. The uncertainties on the systematic parameters lead to a stark degradation of sterile neutrino sensitivity. The analysis was repeated several times, changing only a single parameter at-a-time from the default set in equation 7.17:
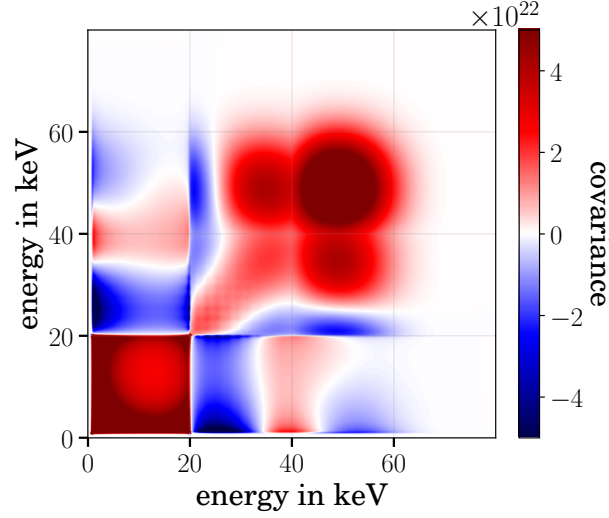
Figure 7.13: Impact of detector systematics to the covariance matrix. The systematic parameters and their uncertainties are given in equation 7.17.

- *Acceleration voltage*: Four different acceleration voltages have been investigated. An increase from $U_{\mathrm{pae}} = 0\,\mathrm{kV}$ to $U_{\mathrm{pae}} = 10\,\mathrm{kV}$ improves the separation of the detection threshold and charge-sharing. Increasing to $U_{\mathrm{pae}} = 20\,\mathrm{kV}$ allows for a better discrimination of the pure beta-decay spectrum and signal pile-up. And the last step, increasing to $U_{\mathrm{pae}} = 30\,\mathrm{kV}$, improves the sensitivity at best by the factor 2. This related to the improved discrimination of systematics, but, to some degree, affected negatively by the increase of Fano-noise.

- *Alignment*: Improving the uncertainty on the incident angle $\sigma_{\vartheta_{\mathrm{p,in}}} = 1^\circ$ shows an overall improvement on the sensitivity.

- *Homogeneity*: A reduced deadlayer uncertainty $\sigma_{z_{\mathrm{dl}}} = 1\,\mathrm{nm}$ leads to a similar improvement of the sensitivity.

- *Detector scattering*: Combining a good alignment $\sigma_{\vartheta_{\mathrm{p,in}}} = 1^\circ$ with good homogeneity $\sigma_{z_{\mathrm{dl}}} = 1\,\mathrm{nm}$ gives a further improvement to the sensitivity. With an overall degradation of approximately a factor 2.

In order to further improve the sensitivity all parameters and their uncertainties where optimized[2]:

$$U_{\mathrm{pae}} = 30\,\mathrm{keV} \pm 1\,\mathrm{eV} \ , \quad \mathrm{FWHM}_{\mathrm{noise}} = 150 \pm 1\,\mathrm{eV} \ , \quad E_{\mathrm{thres}} = 500 \pm 1\,\mathrm{eV} \ ,$$
$$t_{\mathrm{min}} = 100 \pm 10\,\mathrm{ns} \ , \quad P_{\mathrm{cs}} = 10 \pm 1\,\% \ , \quad z_{\mathrm{dl}} = 20 \pm 1\,\mathrm{nm} \ \text{and} \quad \vartheta_{\mathrm{p,in}} = 0 \pm 1^\circ \ . \tag{7.18}$$

---

[2]Here the energy resolution of electronic noise is specifically denoted by $\mathrm{FWHM}_{\mathrm{noise}}$. In combination with Fano-noise the joint resolution for electrons is $\mathrm{FWHM} = 260\,\mathrm{eV}$.
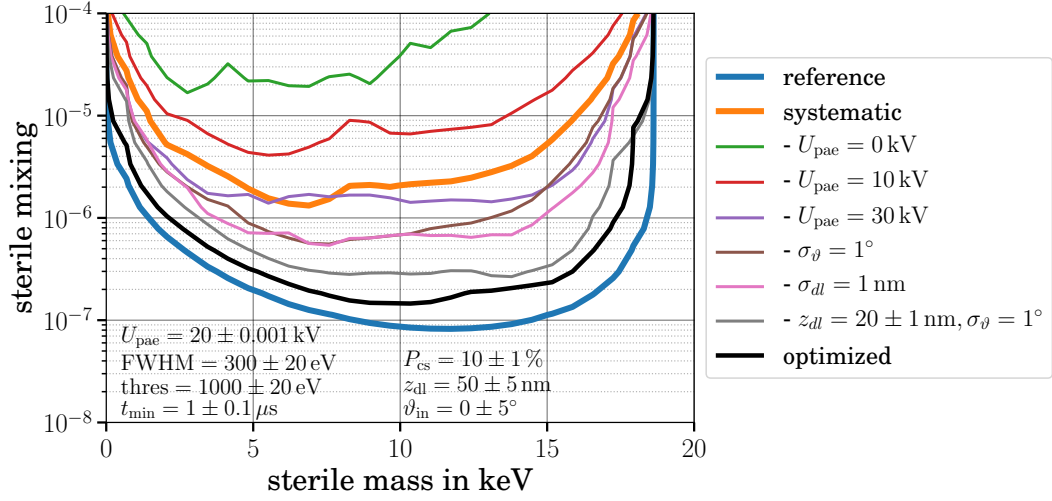
Figure 7.14: Combined impact of detector systematics to the sterile neutrino sensitivity. The reference sensitivity without systematics is colored blue. The model parameters for the combined systematic sensitivity (orange) are inscribed in the figure. The other lines represent variations of the accordingly changed parameters. In addition a highly optimized scenario (black) is given: the underlying parameters are listed in equation 7.18.

Compared to the reference case, the optimized systematic sensitivity shows a degradation by factor of 1.5. However, the influence of electronic noise at masses of $m_4 \approx E_0$, which corresponds to a sterile neutrino signature at $E \approx qU_{\mathrm{pae}}$, is more strongly affected.

In summary, the combined study of systematic uncertainties shows that every detector parameter has to be optimized to high precision (s. eq. 7.18). This corresponds to live-monitoring and characterization tests during a future sterile neutrino measurement. Compared to the individual study on systematic effects (s. sc. 7.1.2), the overall sensitivity degradation is much larger if uncertainties are considered jointly.

However, additional measurements for discriminating systematics from one-another would majorly improve the sensitivity. For example, by vetoing events with large signal rise-times (s. sc. 6.3.4) the impact of charge-sharing could be suppressed. A discrimination of systematic effects based on event-level monitoring would allow to suppress their impact to the sterile neutrino sensitivity.

7.2 Detector magnetic field

The design of a viable detector for a sterile neutrino search with KATRIN is largely dependent on the envisioned electron rates and the reduction of systematics. A consequence is that the detector requires $n_{\mathrm{px}} = 3500$ pixels to handle the high detector rates (s. sc. 4). It is expected that the entire detector section of KATRIN requires a redesign, with an emphasis on optimizing the magnetic and electric field settings. As the TRISTAN detector

size increases compared to the FPD, it has to be positioned behind the detector magnet and an additional magnet is required to ensure perpendicular field lines at the position of the new detector [Kor16].

In the following an optimal magnetic field for the detector position is discussed – with consideration of back-scattering and charge-sharing – and the impact to the re-design of the detector section for TRISTAN shown.

At KATRIN the magnetic field is optimized to allow adiabatic transport of electrons throughout the setup. As a consequence the conservation of magnetic flux ϕ directly relates the local magnetic field B to the area A of the electron beam

$$\phi = \text{const.} = B \cdot A \longleftrightarrow \quad A = \frac{B_{\text{src}} A_{\text{src}}}{B} \ . \tag{7.19}$$

The size of the detector is thus driven by the local magnetic field B_{det} at its position and the area of the detector pixels - in circular approximation - given by

$$A_{\text{px}} \approx r_{\text{px}}^2 \pi \approx \frac{A_{\text{det}}}{n_{\text{px}}} = \frac{1}{n_{\text{px}}} \frac{B_{\text{src}} A_{\text{src}}}{B_{\text{det}}} \ . \tag{7.20}$$

A reasonable magnetic field can be derived with consideration of detector charge-sharing (s. subs. 5.2.3) and back-scattering (s. subs. 5.2.2).

Charge-sharing

Charge-sharing is optimized by relating the charge cloud expansion to the detector pixels size. In approximation the probability of charge-sharing P_{cs} is given by the charge clouds area $r_{\text{cc}}^2 \pi = 40\mu\text{m}^2\pi$ coverage along the pixels perimeter L_{px} (s. eq. 5.25), leading to an inverse proportionality $P_{\text{cs}} \propto 1/r_{\text{px}}$.

Assuming the conservation of magnetic flux (s. eq. 7.20) throughout the beamline, charge-sharing can be related to the pixel size, which is determined by the fixed number of pixels in the flux tube area, which in turn is related to the detector magnetic field B_{det}: $P_{\text{cs}} \propto \sqrt{B_{\text{det}}}$.

In figure 7.15 the magnetic field dependence is illustrated. In addition the energy of the incident electron $E_{\text{in}} \approx E_0 + qU_{\text{pae}}$ is incorporated by adding the average radial scattering position (s. fig. A.2a) to the constant charge cloud radius $r_{\text{cc}} = 20\,\mu\text{m}$ in quadrature.

The probability of charge-sharing increases with the magnetic field and approaches zero at low values B_{det}, implying small magnetic fields for the final setup.
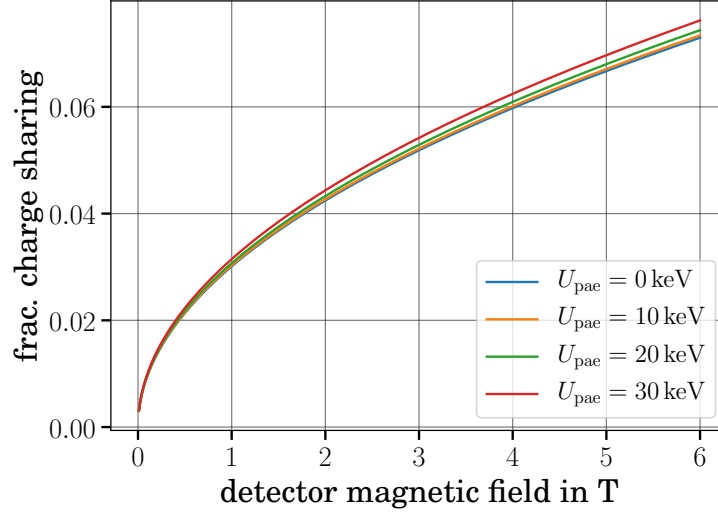
Figure 7.15: Analytic estimation of charge-sharing at different detector magnetic fields and post acceleration voltages. Charge-sharing is mostly independent of U_{pae}, which translates to the contribution of scattering and an electrons incident energy. Lower magnetic fields translate to large detector pixels and reduced charge-sharing.

Back-scattering

Electron *back-scattering* off the detector is optimized with respect to the initial interaction as well as ensuing interactions of back-scattered electrons.

In order to reduce the influence of detector back-scattering the angle of incidence should be close to perpendicular [Ren11; Kor16]. In addition electrons with non-perpendicular incidence experience a virtual increase of the detector deadlayer and thus an increased energy loss E_{dl}.

At KATRIN the incidence angle of an electron is affected by magnetic focusing and reflection (s. eq. 3.7) as well as by boosting the parallel kinetic energy component $E_\parallel$ of electrons with the post acceleration electrode U_{pae}:

$$\vartheta_{\text{p,in}} = \arctan\left(\sqrt{\frac{E_{\text{kin},\perp}^2 + 2m_e E_{\text{kin},\perp}}{(E_{\text{kin},\parallel} + qU_{\text{pae}})^2 + 2m_e(E_{\text{kin},\parallel} + qU_{\text{pae}})}}\right). \tag{7.21}$$

Due to magnetic focusing from the pinch magnet $B_{\text{pch}} = 6\,\text{T}$ to the magnetic field at the detector $B_{\text{det}} = 3.6\,\text{T}$ the incidence angle is restricted to $\vartheta_{\text{p,in}} \lesssim 50.77°$. Insuring that low energy electrons travel through the deadlayer puts a lower limit to the post acceleration electrons. For $z_{\text{dl}} = 50\,\text{nm}$ at least $U_{\text{pae}} = 2\,\text{kV}$ is required. This also slightly decreases the polar angle to $\vartheta_{\text{p,in}} \lesssim 45.6°$.

Optimally the detector should be situated in low magnetic fields and high post acceleration voltages. To be independent of their initial kinetic energy exceedingly high acceleration voltages $qU_{\text{pae}} \gg E_0$ would be required.
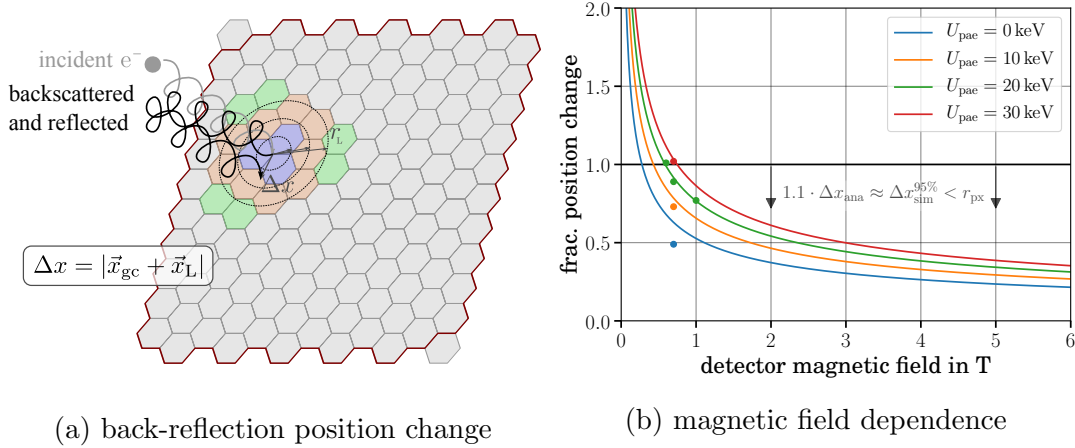
(a) back-reflection position change

(b) magnetic field dependence

Figure 7.16: (a) Illustration of an incident electron hitting at a detector pixel corner. If the cyclotron radius of back-scattered and back reflected electrons is a multiple of the pixel radius, the number of pixel that could be reached vastly increases. (b) Analytic estimation of maximal expected position change $\Delta x \approx 1.4 \cdot r_{\mathrm{L}}$ due to cyclotron motion of back-scattered and back reflected electrons at the detector system for different magnetic field strengths at the detector. The colors represent different acceleration voltages for electrons. For verification several simulations with different settings were performed and the plot includes an upper limit of their 95% position change quantiles $1.1 \cdot \Delta x^{95\%}/r_{\mathrm{px}}$ (points).

Back-reflection

Subsequent events of back-scattered electrons re-impinge onto the detector within a certain inter-event-time $\Delta t = \mathcal{O}(1\,\mu\mathrm{s})$ and at slightly shifted position $\Delta x = \mathcal{O}(1\,\mathrm{mm})$. Δx depends on the local electromagnetic setup, which influences the cyclotron motion as well as the drift of the adiabatic guiding center (s. eq. 5.12).

In order to analytically estimate the positional change the drift component is approximated with a constant factor of 1.4:

$$\Delta x \approx \frac{m_{\mathrm{e}} c \sqrt{\gamma_0^2 - 1}}{e B_{\mathrm{det}}} \cdot 1.4 \;, \tag{7.22}$$

where m_{e} is the electrons rest mass, c the speed of light and γ the relativistic boost factor. For verification the position change was also simulated in KASSIOPEIA, giving a good agreement at high acceleration voltages $U_{\mathrm{pae}} = 10/20/30\,\mathrm{kV}$ (s. fig. 7.16b).

The position change is especially relevant with consideration of multi-pixel events (s. fig. 7.16a). Back-scattering occurs with a probability of $P_{\mathrm{bs}}(\vartheta_{\mathrm{p,in}}) \geq 20\%$, being more likely for shallow incidence angles $\vartheta_{\mathrm{p,in}}$. Therefore it is possible that a single electron back-scatters multiple times n_{bs} off the detector. Electrons with $n_{\mathrm{bs}} \geq 1$ (s. fig. 5.10a) thus deposit their kinetic energy in multiple hits and might impinge on different detector pixels. This increases detector rate and translates to higher DAQ throughput. Even more if multi-pixel

events are considered with next-to-next pixel coincidences. Lastly, background electrons that back-scatter off the acceleration electrodes are more likely to hit the detector, if they are back-reflected with large position changes. A conservative requirement for TRISTAN detector is to ensue small position changes relative to the pixels radius

$$\Delta x/r_{\mathrm{px}} \lessapprox 1 \ . \tag{7.23}$$

In figure 7.16b the fractional position change $\Delta x/r_{\mathrm{px}}$ is given. It uses the described analytic estimations as well as a dedicated simulation with KASSIOPEIA for verification. The simulation has two detector magnets that are tuned in tandem $B_1 = B_2 = 5\,\mathrm{T}$ to give perpendicular field lines at shifted detector positions and a field strength of $B_{\mathrm{det}} = 0.6/0.7/1\,\mathrm{T}$ at the detector surface. The vacuum chamber is correspondingly enlarged [Kor16].

The fractional position change increases inversely proportional to the magnetic field strength B_{det}. Consequently, decreasing the position change requires large magnetic fields $B_{\mathrm{det}} > 0.5\,\mathrm{T}$ and low post acceleration voltages U_{pae}.

Summary
Both, charge-sharing and back-scattering show a dependence on the detector magnetic field B_{det} and prefer low magnetic fields. On the other hand high magnetic fields are preferred by the argument that position change of back-reflected electrons should be limited to less than a pixel radius. Combined this gives a magnetic field of $B_{\mathrm{det}} \geq 0.3\,\mathrm{T}$ for a zero acceleration voltage $U_{\mathrm{pae}} = 0\,\mathrm{kV}$.

The post acceleration voltage should be chosen large enough for electrons to overcome the detection deadlayer. While high values in addition boost the parallel component of electrons and thereby decrease the incidence angle, this leads to an increase of the position change.

In summary optimizing back-scattering and charge-sharing at the same time suggests low magnetic fields at the detector, limited to a minimum value. With respect to systematic sensitivity studies post acceleration potentials between $U_{\mathrm{pae}} = 20 \ldots 30\,\mathrm{kV}$ are preferred. This ensues magnetic fields of $B_{\mathrm{det}} = 0.7 \ldots 0.8\,\mathrm{T}$ and translates to SDD pixel radii of $r_{\mathrm{px}} = 1.5 \ldots 1.6\,\mathrm{mm}$.

7.3 Conclusion

Design criteria for the future TRISTAN where examined with respect to magnetic field optimizations as well as dedicated systematic sensitivity studies. The combination of both allow constraining the parameters of the detector as well as optimizing the electromagnetic fields.

Sensitivity

The systematic sensitivity studies include the effects of electronic noise, signal pile-up, charge-sharing and electron scattering.

Although signal pile-up only slightly affects the sensitivity (s. fig. 7.6), a full mitigation requires operating the detector on high acceleration voltages $qU_{\mathrm{pae}} > E_0$, separating the beta-decay spectrum and piled-up region.

The energy deposition in silicon (scattering) showed the largest impact on the sensitivity (s. fig. 7.10). In order to reduce sensitivity degradation, modest acceleration potentials $U_{\mathrm{pae}} > 5\,\mathrm{kV}$ are required. A further improvement is achieved, if, with almost equal importance, the deadlayer thickness z_{dl}, its homogeneity $\sigma_{z_{\mathrm{dl}}}$ and the alignment $\sigma_{\vartheta_{\mathrm{p,in}}}$ is optimized and monitored with high precision. Improving a single of these parameters would ensue a decent recovery of sensitivity to sterile neutrinos. Experimentally, a decent result would be achieved by improving the detection deadlayer to a thickness of $z_{\mathrm{dl}} < 20\,\mathrm{nm}$, or by monitoring homogeneity with $\sigma_{z_{\mathrm{dl}}} \approx 1\,\mathrm{nm}$ respective $\sigma_{\vartheta_{\mathrm{p,in}}} \approx 1°$ accuracy.

Uncertainties on potential fluctuations of $\sigma = 1\,\mathrm{V}$ on electronic noise and acceleration voltage were tested. Compared to the keV range relevant for the sterile neutrino search, their impact is rather small. However a low detection threshold $E_{\mathrm{thres}} \approx 300\,\mathrm{eV}$, especially for reducing the impact of charge-sharing, is important to improve sensitivity. As the energy threshold is related to electronic noise, an excellent energy resolution $\mathrm{FWHM}_{\mathrm{noise}} \leq 150\,\mathrm{eV}$ is vital[3]. Low electronic noise is equally necessary for discriminating triple charge-sharing events (s. sc. 6.2 & 6.3.2) and for the wavelet-based sensitivity analysis [Mer15b].

Of special importance to the sterile neutrino sensitivity are the combined impact of systematic uncertainties (s. fig. 7.14). For example the detector response is at low energies $E < (qU_{\mathrm{pae}} + E_0)/2$ affected by uncertainties of charge-sharing as well as electron back-scattering. This translates to large elements in the covariance matrix and strongly affects the sensitivity - the shape-only analysis by marginalization over the detector rate Γ_{det}.

In order to mitigate this effect, acceleration voltages larger than the spectrum endpoint $qU_{\mathrm{pae}} > E_0$ are important. The requirement stems from signal pile-up, where the minimum energy of pile-up events is limited by $E > 2 \cdot qU_{\mathrm{pae}}$. High potentials separate the pile-up spectrum from the pure beta-decay spectrum and improve the sensitivity to the sterile neutrino signature.

However, the combined study shows that even strongly optimized detector parameters as well as their uncertainties leads to a sensitivity degradation by a factor 1.5. In consideration of additional systematic effects, such as ADC non-linearity [Dol17], it is important to further discriminate systematic effects from the sterile neutrino signature in the pure beta-decay spectrum. This would suppress the influence systematics and thus allow to reduce the analysis to a smaller subset of effects. At best the remaining systematic effects are easily discriminated from one-another, leading back to an individual sensitivity study

---

[3]This refers to electronic noise broadening only. Combined with Fano-like noise at $E_{\mathrm{in}} = 20\,\mathrm{keV}$ the energy resolution is $262\,\mathrm{eV}$.

for each effect.

An exemplary parameter for triggering charge-shared events is the measurement of the signal rise-time (s. sc. 6.3.4). Accidental pile-up and events from back-reflection could be separated based on model predictions: the inter-event-time of back-reflected electrons for example shows characteristic features (s. sc. 5.2.2).

Detector system

Another approach for constraining the detector system is given in section 7.2, where back-scattering, back-reflection and charge-sharing were discussed with respect to the prevalent magnetic field settings. Assuming acceleration voltages $U_{\mathrm{pae}} = 20\ldots30\,\mathrm{kV}$ above the spectrum endpoint, an optimal magnetic field strength $B_{\mathrm{det}} = 0.7\ldots0.8\,\mathrm{T}$ is determined. Based on magnetic flux conservation this ensues an optimal the SDD pixel size of $r_{\mathrm{px}} = 1.5\ldots1.6\,\mathrm{mm}$.

The principle used in this optimization considers only small position changes $\Delta x < r_{\mathrm{px}}$ of back-scattered and back-reflected electrons. An advantage of this principle is that event triggering in the DAQ only has to consider neighboring events. Moreover it further allows vetoing of background electrons generated close to the detector and thus enables a "golden pixel" selection.

With respect to the low magnetic field strength and the space requirement of operating about 3500 pixel in vacuum, it is likely that the TRISTAN detector will be placed roughly $1\,\mathrm{m}$ to behind the current position of the FPD. In addition a second magnet will be operated in tandem, ensuing perpendicular magnetic field lines (s. fig. 7.17).

Based on simulations with KASSIOPEIA the available space for instrumentation is limited $\Delta z = 60\,\mathrm{cm}$ between the two detector magnet cryostats. Moreover electric and magnetic field operation requires special material selection and safety margins, which further reduces the available space. However, some space for operation is available in radial direction between the cryostats as well as along the beamline after the 2nd detector magnet.

The detector, though, must also fulfill vacuum criteria imposed by the KATRIN MS. The spectrometer is operated at $p \approx 2 \cdot 10^{-11}\,\mathrm{mbar}$ and is directly connected with the detector chamber. It is thus important to restrict additional gas load of detector components. In order to improve vacuum conditions additional vacuum pumps, material selection and a gas-flow optimized design are considered. As a consequence most of the DAQ and instrumentation instruments have to be operated outside the detector chamber.

At the current step of the technical design efforts only the first stage amplification is performed within vacuum and the rest of the DAQ system operated in ambient-air. To further improve the gas load criteria the acceleration electrode is designed as a mask that restricts molecular flow from detector components in direction of the MS.
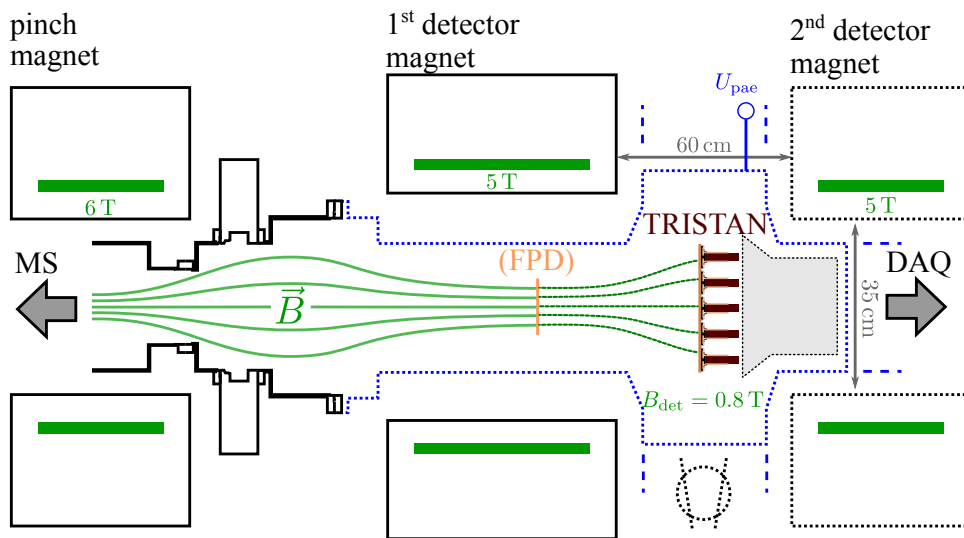
Figure 7.17: Schematic of the KATRIN DS with respect to a future sterile neutrino search TRISTAN detector upgrade. As a reference the current FPD position is marked in orange. The 166px modules are colored in shades of brown and 21 placed side by side in a 5×5 grid. Dotted outlines depict components that have yet to be designed: an additional detector magnet, the detector chamber (blue), additional vacuum pumps, and first stage electronics (gray). Most likely the vacuum chamber will be operated on high voltage and some electronics mounted directly behind the detector within vacuum.

Chapter 8

Sterile neutrinos with First Tritium run

Of particular interest for the KATRIN sterile neutrino measurement during the first tritium campaign is the experience gained from a 1.6 keV deep spectroscopic scan into the tritium beta-decay spectrum ($U_{\mathrm{ret}} \geq E_0 - 1.6$). The measurement was performed with the FPD and the sterile neutrino analysis is centered on an integral measurement [Koe19; Hub20]. This chapter focuses on the probability for measuring an incident electron with the FPD, the detection efficiency. In contrast to previous assumptions [Ang05; Ams15], the efficiency shows a small retardation potential dependency (s. sc. 5.2.2). For the sterile neutrino search it must be thus considered as an additional systematic uncertainty.

8.1   Stability run and model comparison

A core measurement for calibrating the FPD detection efficiency is the stability run with number 40970. It was performed at a retardation potential of $U_{\mathrm{ret}} = 16.975$ kV, with the same electromagnetic field settings as the "1.6 keV" run (s. tb. A.1).

The measured FPD response is illustrated in figure 8.1a. It shows the normalized ring-wise energy spectra of the stability run. The normalization factor of the maximum position is shown in figure 8.1b.

Remarkably the energy spectra of the outer rings show an increased count rate at low energies. This dependency mostly originates from the FPD's radial geometry (the innermost ring has a perimeter of $L_1 \approx 17$ mm, whereas the outermost ring almost twice as large $L_{12} \approx 50$ mm) which affects the probability that back-scattered electrons hit a neighboring pixel (s. fig. 5.10a) as well as the probability of charge sharing (s. fig. A.11).

(a) energy spectra

(b) FPD pixel map
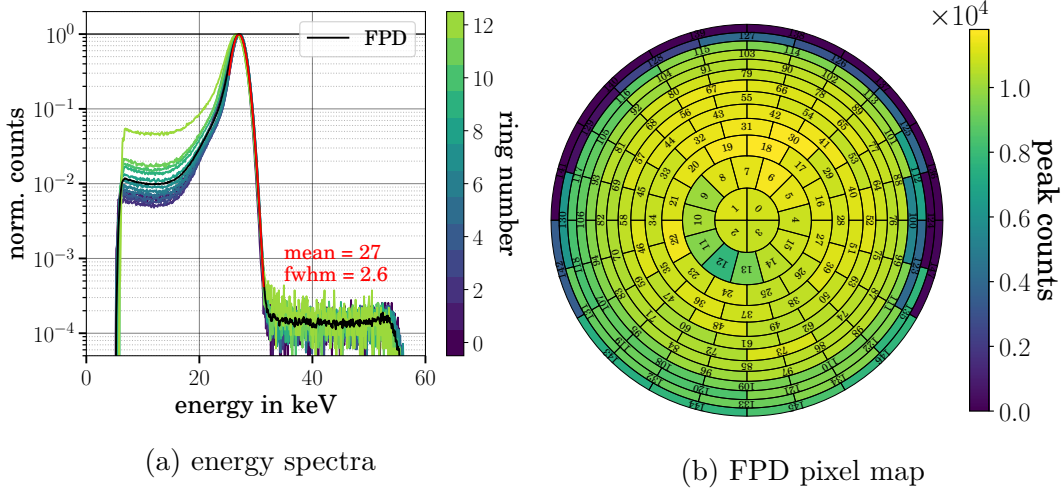
Figure 8.1: (a) Measured energy spectra of the various detector rings (in color) and for the FPD (black) in its entirety. In addition a Gaussian peak fit is added in red. For comparison the spectra are normalized to one at the peak position. (b) Illustration of the normalization factor. Detector pixels with high rates are referred to as the golden pixel selection.

Inter-event-time

The modeling framework consists of a simulation part and a subsequent analysis 5.2. In summary the model encompasses:

- Simulation: Electromagnetic tracking of $N_{sim} = 10^6$ simulated electrons within the SDS. Events are generated in the first PS magnet with energies according to the tritium beta-decay spectrum (s. tab. A.2). The silicon scattering framework includes a detector deadlayer of $z_{dl} = 100\,\text{nm}$ thickness.

- Analysis: The output from the simulation is processed to include Fano-noise. The detector event structure is based on the FPD pixel geometry and the timing resolution $t_{min} = 2 \cdot t_{sh} + t_{ft} = 3.6\,\mu\text{s}$. Multiple energy depositions from events that back-scatter are combined if they are back-reflected to the same pixel and hit the pixel within the time $\Delta t < t_{min}$. Lastly, the impact of charge sharing (s. fig. A.11) and electronic noise with FWHM = 2.6 keV is accounted by using response functions (signal pile-up is not included).

An important quantity for the analysis is the simulated inter-event-time for back-scattered electrons that are reflected back to the detector. In figure 8.2 the simulated and measured inter-event-time of back-reflected electrons is depicted. For experimentally measuring inter-event-times smaller than the time resolution of the FPD, a selection of specific detector pixels and a specific energy region is investigated in the data.

An energy cut of $E \in [0, 14\,\text{keV}]$ removes coincident electron events originating from tritium beta-decay, while the pixel selection - central four FPD pixels - narrows the data
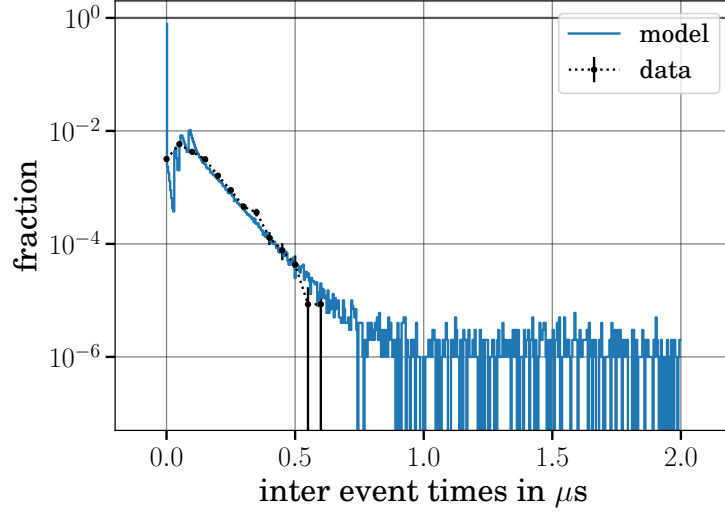
Figure 8.2: Comparison of the modeled inter-event-time for back-scattered electrons (blue) and the inter-event times measured with the FPD (black). The measurement only represents a selection of electron energies $E_{in} \in [0, 14\,keV]$ and events that are detected in the central four pixels of the FPDs. The distribution is accordingly scaled and a statistical uncertainty depicted.

down to electrons that back-scatter of one of the pixels and are subsequently back-reflected an adjacent pixel. Together the expected number of counts scales by a factor of $0.5 \cdot 4/100$. Here the rate reduction in the outer pixels lead to the factor of 100 (s. fig. 8.1b).

The model shows a prominent peak at $\Delta t = 0\,\mu s$, which relates to electrons that do not back-scatter. In the data these events are excluded as only coincident events were selected. In contrast, the measured timing is affected by electrons that are affected by charge-sharing. This leads to an increase of short time $\mathcal{O}(20\,ns)$ and was not considered in the model.

Overall the model is in good agreement with the measured data. Moreover, the analysis proves that it is possible investigate detector back-scattered electrons in-situ.

Radial dependence

The two effects, back-scattering and back-reflection, directly influences the observed energy response. A comparison of the modeled and measured energy spectrum in the first and tenth FPD ring is illustrated in figure 8.3.

Model parameters were chosen according to monitoring devices (e.g. $U_{ret} = 16.975\,kV$) or from similar characterizations measurements (e.g. deadlayer $z_{dl} = 100\,nm$ [Sch14]). The charge cloud radius is extracted from a measurement of [Sch14], who determined a probability of $P_{cs} = 1.5\,\%$ in the first ring and $P_{cs} = 2.6\,\%$ in the tenth ring of the FPD. This would correspond to a charge cloud radius of $r_{cc} = 12\,\mu m$ (s. fig. A.11). The detection threshold is not considered, as it would hide the spectrum shape for $E < E_{thres}$ energies below it.
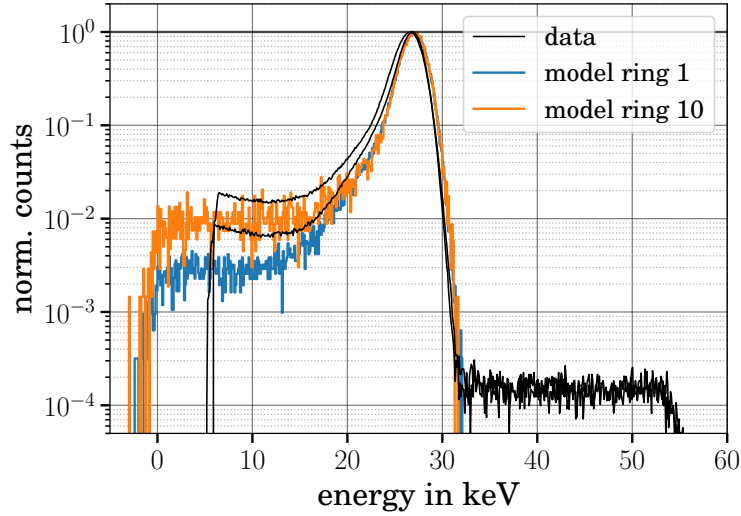
Figure 8.3: Modeled energy response for a potential $U_{\text{ret}} = 17\,\text{kV}$ at the FPD and $N_{\text{sim}} = 10^6$ simulated electrons. In blue (orange) the average spectrum of the first (tenth) ring is depicted. The model includes silicon scattering, back-reflection, charge-sharing, and electronic noise. In addition the respective measured spectra are overlayed in black.

Similar to the data, the model predicts an increase in count rate at low energies for outer FPD detector rings. Quantitatively the low-energy tail as well as the peak-width are underestimated. This is likely related to the energy-loss of peak pile-up (s. fig. A.10). While charge-sharing also contributes to the low energy-tail, a charge cloud radius as large as $r_{\text{cc}} = 100\,\mu\text{m}$ would be necessary (s. fig. A.11) to explain the observed increase.

Rydberg background

With regards to the back-scattering and back-reflection, a special Rydberg background scenario was investigated (s. app. A.3). It is based on highly exited hydrogen atoms, co-called Rydberg atoms, emanating from the steel vessels into the volume of the MS, due to sputtering processes of α-emitters. Background electrons are then created by ionization of Rydberg atoms via black body radiation [Tro19].

These electrons are expected to be generated isotropically in the entire MS vessel with low kinetic energies $\mathcal{O}(\text{meV})$. Accordingly, their energy distribution at the detector ($U_{\text{pae}} = 10\,\text{kV}$) depends on the axial position of creation $qU_{\text{ret}}(z_{\text{in}})$ and shows a small energy spread $\Delta E \lesssim 0.5\,\text{keV}$ (s. fig. A.8a):

$$E_{\text{bkg}} = qU_{\text{ret}}(z_{\text{in}}) + qU_{\text{pae}} + U_{\text{BF}} \ . \tag{8.1}$$

Most important, Rydberg electrons are not affected by back-scattering escape $P_{\text{esc}} = 0\,\%$. A consequence of the maximum energy: even the smallest energy-loss in the detector lead to back-scattering energies below the retardation potential and thus back-reflection.

(a) extrapolation mechanism

(b) relative efficiency
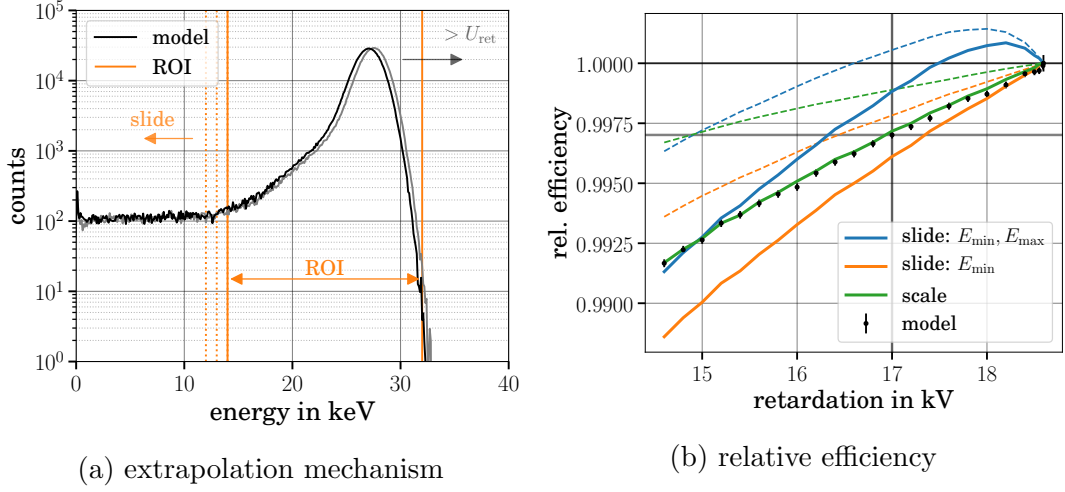
Figure 8.4: (a) Schematic depiction of the ROI and extrapolation mechanism. A single energy response at $U_{\mathrm{ext}} = 17\,\mathrm{kV}$ (black) is used to extrapolate an efficiency for arbitrary U_{ret} (gray) by instead shifting E^*_{min} the ROI bound (orange). (b) Relative modeled efficiency $\epsilon_{\mathrm{roi}} \cdot \epsilon_{\mathrm{esc}}$ for a set of simulated retardation voltages U_{ret} (black). The respective extrapolated results are given for different approaches: sliding lower and upper bound equally (blue), sliding the lower bound (orange), and scaling the lower bound (green, s. eq. 8.5). In dashed line-style solely ϵ_{roi} is given and the cross-hair marks U_{ext} respective $\epsilon_{\mathrm{rel}}(U_{\mathrm{ext}})$.

8.2 Detection efficiency

In order to veto background events, the energy spectrum registered with the FPD is separated into a "region of interest" (ROI) and only events with energies $E_{\mathrm{meas}} \in [E_{\mathrm{min}}, E_{\mathrm{max}}]$ in this region are counted.

The detector efficiency is hence defined by the number N_{roi} of events in this region divided by the total number N_{tot} of electrons that impinge onto the detector:

$$\epsilon_{\mathrm{det}} = \frac{N_{\mathrm{roi}}(U_{\mathrm{ret}})}{N_{\mathrm{tot}}} = \frac{1}{N_{\mathrm{tot}}} \cdot \int_{E_{\mathrm{min}}}^{E_{\mathrm{max}}} \mathrm{d}E \, \frac{\mathrm{d}N(E, U_{\mathrm{ret}})}{\mathrm{d}E} \ . \tag{8.2}$$

However N_{tot} is a priori only known in simulations. In the experiment assessing N_{tot} would require high-precision modeling of systematics with special care for the unobserved spectrum part below the detection threshold.

Consequently the measurement of the detector response only allows to infer a relative efficiency ϵ_{rel}, typically normalized to the spectrum endpoint (s. fig. 8.4a). At KATRIN ϵ_{rel} is further separated into [Eno19]

$$\epsilon_{\mathrm{det}} = \epsilon_{\mathrm{abs}} \cdot \epsilon_{\mathrm{rel}} = \epsilon_{\mathrm{abs}} \cdot \epsilon_{\mathrm{roi}} \cdot \epsilon_{\mathrm{esc}} \cdot \epsilon_{\mathrm{pu}} \ , \tag{8.3}$$

where ϵ_{roi} defines the relative counts within the ROI, ϵ_{esc} describes the escape of detector back-scattered electrons (s. fig. 5.11) and ϵ_{pu} gives the correction for accidental signal pile-up (s. eq. 5.32).

The calculated systematic probabilities are directly connected to the efficiency by $\epsilon_{\mathrm{syst}} = 1 - P_{\mathrm{syst}}$. Lastly, the absolute efficiency ϵ_{abs} is close to unity and absorbed by the normalization factor in sensitivity analyses.

Region-of-interest efficiency

A complication for an experimental determination of ϵ_{roi} is the low electron rates at the spectrum endpoint $U_{\mathrm{ret}} \approx qE_0$. A solution to determine the efficiency is thus based on extrapolating the efficiency from a single detector response performed at distance $qU_{\mathrm{ret}} - E_0 > 1\,\mathrm{keV}$ to the endpoint.

The extrapolation mechanism assumes that the shape of detector response is in first order independent of the retardation potential (s. fig. 8.4a). A single measurement at fixed potential U_{ext} is performed and the extrapolated efficiency determined by modifying the ROI boundaries $[E_{\mathrm{min}}^*, E_{\mathrm{max}}^*]$:

$$\epsilon_{\mathrm{roi}}(U_{\mathrm{ret}}) \approx \epsilon_{\mathrm{roi}}(U_{\mathrm{ext}})|_{E_{\mathrm{min}}^*}^{E_{\mathrm{max}}^*} . \tag{8.4}$$

For KATRIN analyses the so-called sliding-mechanism is implemented, where both boundaries are shifted by $U_{\mathrm{ext}} - U_{\mathrm{ret}}$. As the kinetic energy observed with the FPD is determined $E_0 + qU_{\mathrm{pae}}$ by the spectrum endpoint and post-acceleration, it is more reasonable to fix the upper boundary $E_{\mathrm{max}}^* = E_{\mathrm{max}}$.

Another option is to use a scaling based modification of the ROI boundaries:

$$E_{\mathrm{min}}^* = E_{\mathrm{min}} \cdot \frac{U_{\mathrm{ext}} + U_{\mathrm{pae}}}{U_{\mathrm{ret}} + U_{\mathrm{pae}}} \quad \text{and} \quad E_{\mathrm{max}}^* = E_{\mathrm{max}} . \tag{8.5}$$

Based on a modeled detection efficiency this extrapolation schema gives the best fit (s. fig. 8.4b) and allows to retain the absolute modeled efficiency (s. fig. A.22)

$$\epsilon_{\mathrm{det}}(U_{\mathrm{ret}}) \approx \epsilon_{\mathrm{det}}(U_{\mathrm{ext}})|_{E_{\mathrm{min}}^*}^{E_{\mathrm{max}}} + [P_{\mathrm{esc}}(U_{\mathrm{ext}}) - P_{\mathrm{esc}}(U_{\mathrm{ret}})] , \tag{8.6}$$

by including the probability of electron escape P_{esc} in summation.

Based on the scaling mechanism from equation 8.5, the efficiency ϵ_{roi} for each detector pixel is calculated. The boundaries are $E_{\mathrm{min}} = 14\,\mathrm{keV}$ and $E_{\mathrm{max}} = 32\,\mathrm{keV}$ and the result is illustrated in figure 8.5.

The depicted averaged efficiency of the golden pixel selection[1] shows a reasonable agreement with respect to model considerations (s. sc. 5.4). In particular, the energy-loss of peak pile-up would reduce the efficiency and pixel dependent effects would have to be considered.

---

[1]Detector pixels with low statistics are excluded from the analysis.
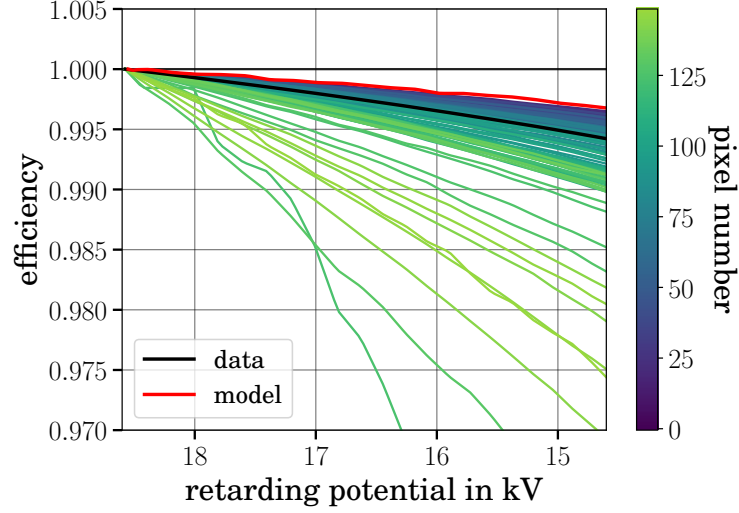
Figure 8.5: Scaling approach based extrapolated ROI efficiency for each detector pixel. In black the averaged value for the golden pixel selection (black) and in red the averaged modeled efficiency $\epsilon_{\mathrm{det}}/\epsilon_{\mathrm{esc}}$ (red) is super-imposed.

At a distance of $1\,\mathrm{keV}$ below the endpoint the efficiency ϵ_{roi} is reduced to 99.875%. Due to the high statistics within the ROI, the systematic uncertainty is estimated by calculating the sample variance of extrapolated efficiencies for the set of golden pixels. The uncertainty is unity at the endpoint and 0.04% at $1\,\mathrm{keV}$ below the endpoint. A conservative uncertainty of $\sigma = 0.1\% \cdot (1 - \epsilon_{\mathrm{roi}})$ is thus suggested.

Sensitivity

For the systematic sterile neutrino analysis the quantitative value as well as the uncertainty thereon have to be considered. A summary plot for the three relative efficiency factors (ϵ_{roi}, ϵ_{esc}, ϵ_{pu}) is given in figure 8.6.

As accidental pile-up is rate dependent its impact increases further into the spectrum and reaches 99.95% at $1\,\mathrm{keV}$ below the endpoint. Its uncertainty depends on the rate estimation and is determined as $\sigma = (1 - \epsilon_{\mathrm{pu}}) \cdot 18\%$ [Eno19].

The modeled efficiency for electron escape at $E_0 - 1\,\mathrm{keV}$ gives a value of 99.89%. In order to estimate the uncertainty, the energy distribution of back-scattered electrons was compared to data from [Ber02] (s. fig. A.3). Here the spectra agree within an uncertainty of $\sigma = 6.8\%$. Assuming a similar accuracy for the simulated angular distribution of back-scattered electrons gives an uncertainty of $\sigma = 10\%$ (summed in quadrature) and $\sigma = 13.6\%$ (absolute sum). For the analysis a conservative uncertainty of $\sigma = 20\% \cdot (1 - \epsilon_{\mathrm{esc}})$ is suggested.

In order to determine the influence of the detection efficiency to the sterile neutrino sensitivity, the systematic uncertainties are considered to be uncorrelated an added in quadrature to the χ^2-function (s. eq. 7.4). The spectrum model incorporates the measurement-time-distribution of the integral scan as well as time-dependent fluctuations
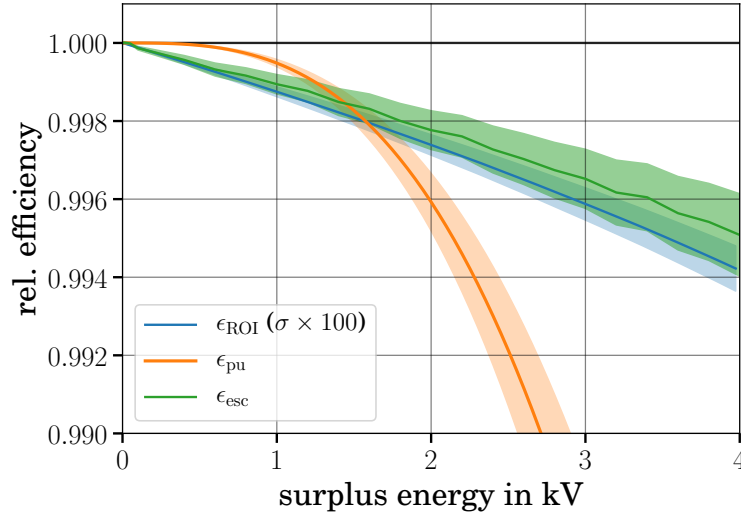
Figure 8.6: Relative detection efficiency of the FPD for a sterile neutrino search in the "1.6 keV" run. The efficiency ϵ_{roi} (blue) & ϵ_{pu} (orange) are given with respect to the average of the golden pixel selection.

of the live-monitoring devices during the "1.6 keV" run [Kat20]. Here the sensitivity analysis is performed with respect to a single effective detector pixel - the golden pixel selection - and the 81 integral scans stacked for each retarding potential.

The resulting modeled sensitivity is shown in figure 8.7. As the uncertainties on the detection efficiencies increase with decreasing potentials U_{ret} (s. fig. 8.6), the sensitivity degradation increases at higher sterile neutrino masses $m_4 > 0.5\,\mathrm{keV}$. The sensitivity loss at $m_4 = 1\,\mathrm{keV}$ due to signal pile-up ϵ_{pu} is about a factor 3 and a factor 2 for electron escape. The low uncertainties on ϵ_{roi} are smaller than the statistical fluctuations and thus do not effect the sensitivity.

The large uncertainty on electron escape is based on the accuracy of the simulated response. Consequently, its influence may be reduced by precision measurements - for example with the RS electron gun. A dedicated simulation (s. fig. A.23a) shows that the probability for electron escape depends both on the surplus energy ΔE as well as the initial polar angle $\vartheta_{\mathrm{p,in}}$ of electrons. In case of a surplus energy $\Delta E = 0$ the escape probability is $P_{\mathrm{esc}} = 0\,\%$, while at $\Delta E = 2.5\,\mathrm{keV}$ & $\vartheta_{\mathrm{p,in}} = 50\,^\circ$ it is $P_{\mathrm{esc}} = 3\,\%$.

In contrast, the influence of signal pile-up depends on the event rate Γ_{px} (s. eq. 5.32). Its accuracy however is limited by rate stability of the tritium source. In addition to the relative detection efficiency, the final sterile neutrino sensitivity investigation with "1.6 keV" run data will incorporate systemic uncertainties for tritium source fluctuations, electron back-scattering off the RW and magnetic trapping in the tritium source [Hub20; Kat20].
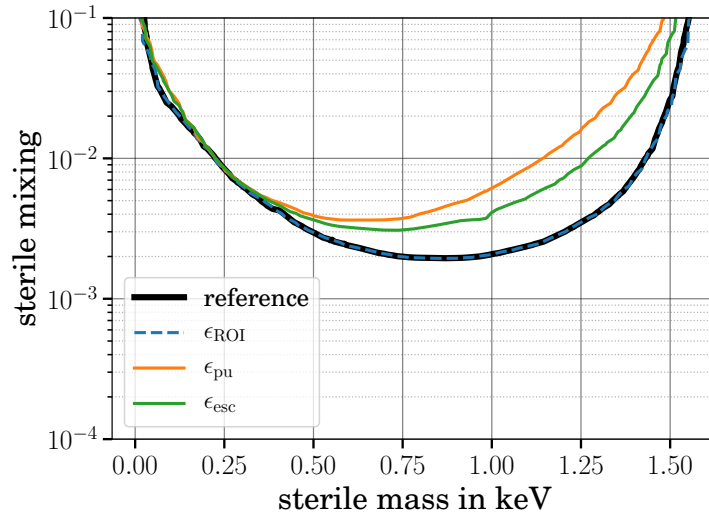
Figure 8.7: Estimated sterile neutrino sensitivity based on MC data with respect to "1.6 keV" run settings [Kat20]. The statistical sensitivity at 90% CL is given in black and the impact of uncorrelated uncertainties on the detection efficiencies is given in color: in blue for ϵ_{roi}, in orange for ϵ_{pu} and in green for ϵ_{esc}.

8.3 Conclusion

In this chapter the detector model was compared with a specific KATRIN calibration measurement for the "1.6 keV" run, a science run dedicated to investigate sterile neutrinos within the last 1.6 keV in the tritium beta-decay spectrum. In contrast to the previous chapter, the semi-analytical model is based on KASSIOPEIA simulation with electromagnetic fields according to the SDS geometry (s. sc. 5.2). In particular, this includes back-reflection of detector back-scattered electrons.

In section 8.1 the consequence of detector back-scattering and back-reflection was investigated with respect to the inter-event-time as well as the position change for back-reflected electrons. Both, short time coincidences and small position changes, may lead to the indistinguishable detector events of a single incident electron. In accordance to the FPD's geometry, the spatial discrimination is better in the outer rings, which leads to an increase of split events and thus results in a radial dependent energy response. This could be well reproduced with the model. A future improvement of the semi-analytical FPD model would have to include energy-loss of signal pile-up. In addition, further charge-sharing characterization measurements are mandatory in order to determine its exact influence.

The impact of detector-related systematics to the integral spectrum is discussed in section 8.2. In contrast to former assumptions [Ang05; Ams15], it is shown that the detection efficiency is both retardation potential as well as radial position depend. This stems largely from back-reflection, which leads to a distortion of the differential spectrum within the region-of-interest. Its contribution is extracted from an independent measurement at $U_{\mathrm{ret}} = 16.975\,\mathrm{kV}$ and it is demonstrated that a scaling based extrapolation approach is

well-suited to recover the efficiency factor ϵ_{roi}. Finally, the influence of uncertainties to the sterile neutrino sensitivity is discussed. Uncorrelated uncertainties on electron escape as well as signal pile-up limit the sensitivity to sterile neutrinos to about $\sin^2 \theta = 6 \cdot 10^{-3}$ at $m_4 = 1\,\mathrm{keV}$. Notably, the uncertainty on electron escape may be reduced by dedicated experimental measurements with the RS electron gun.

Chapter 9

Conclusion

Sterile neutrinos are defined by the generalized SM Lagrangian and may explain many open questions in astroparticle physics. In particular a sterile neutrino mass eigenstate with several keV/c^2 and low mixing angles $\sin^2\theta < 10^{-7}$ is a candidate for DM [Boy19]. Through neutrino oscillation such a particle affects the beta-decay energy spectrum and is hence accessible to the KATRIN experiment. With an unmodified setup a spectroscopic scan into the tritium beta-decay spectrum is, however, limited by the maximal count rate of the FPD. A differential measurement at a by 10^5 reduced source strength - compared to nominal KATRIN operation - would statistically reach sensitivities of $\sin^2\theta = 5 \cdot 10^{-5}$ after several weeks of measurement [Mer19].

Improving the sensitivity thus requires the redesign of the detector system with respect to high count rates as well as excellent energy resolution. The TRISTAN detector system that is currently developed is based on hexagonal SDD pixels and 21 modules with each $n_{px} = 166$ pixels are projected to operated as a joint detector with roughly $n_{px} = 3500$ pixels. The optimized system enables the setup to improve the statistic sterile neutrino sensitivity by several magnitudes, down to $\sin^2\theta = 10^{-7}$ for an effective measurement time of three years [Mer19].

While the tritium source strength would allow for a statistic sensitivity of $\sin^2\theta = 10^{-8}$, the experimental investigation is limited by systematic uncertainties [Mer19]. Within the scope of this thesis several detector systematic effects have been investigated: electron scattering within the detector, back-scattering off the detector as well as back-reflection to it, charge sharing across pixel boundaries, electronic noise and lastly signal pile-up.

In chapter 5 the various systematics are introduced and a detector model is developed. Of special notice is the simulation-interpolation approach that allows transforming simulated responses into calculation-efficient mathematical expression.

Chapter 6 introduces the characterization measurements performed with seven pixel TRISTAN detectors. The laboratory setups comprise high-precision calibration equipment for investigating the detector response to x-rays as well as mono-energetic electrons. It could be shown that the model conforms well with measurements. Improvements would

entail the description of triple boundary charge-sharing, the inclusion of back-reflection in the model, the tracking of x-rays in the simulation and also the implementation of an energy-loss for elastic scattering of electron with silicon.

Design criteria for the final TRISTAN detector are evaluated in chapter 7. Here the influence of systematics was investigated with respect to dedicated sensitivity study and by magnetic field analyses:

- The sensitivity analysis discusses individual as well as the combined impact of systematics. It is demonstrated that the individual effects can be largely mitigated by shifting the tritium beta-decay energy spectrum by the maximal expected decay energy $qU_{\mathrm{pae}} \geq E_0$. In contrast, the combination of systematic effects leads to a sensitivity degradation by more than a factor of 3, even in an optimized case with low and homogeneous detection deadlayer $z_{\mathrm{dl}} = 20 \pm 1\,\mathrm{nm}$. Disentangling systematics, for example by measuring the signal rise-time, is thus essential for the future sterile neutrino measurement.

- Geometric constraints for the detector system where derived from electromagnetic field considerations. Preventing large position displacement of back-reflected or background electrons close to the detector restricts the magnetic field to $B_{\mathrm{det}} = 0.7\ldots0.8\,\mathrm{T}$ and translates to a pixel radius of $r_{\mathrm{px}} = 1.6\ldots1.5\,\mathrm{mm}$.

Finally, the "1.6 keV" run relevant for a first sterile neutrino sensitivity analysis is presented in chapter 8. Focusing on the detector response to back-scattering, back-reflection and charge-sharing, their impact to the observed event timing and recorded energy-spectra is discussed. It was shown that a scaling based extrapolation mechanism is best suited for identifying the ROI efficiency ϵ_{roi} of the FPD and that back-scattered electron escape ϵ_{esc} should be investigated by dedicated calibration measurements. Moreover, the systematic uncertainty on the detection efficiency limits the sterile neutrino sensitivity to about $\sin^2\theta = 5 \cdot 10^{-3}$.

Appendices

A.1 KESS simulation of electron scattering in silicon

(a) lateral direction

(b) radial direction
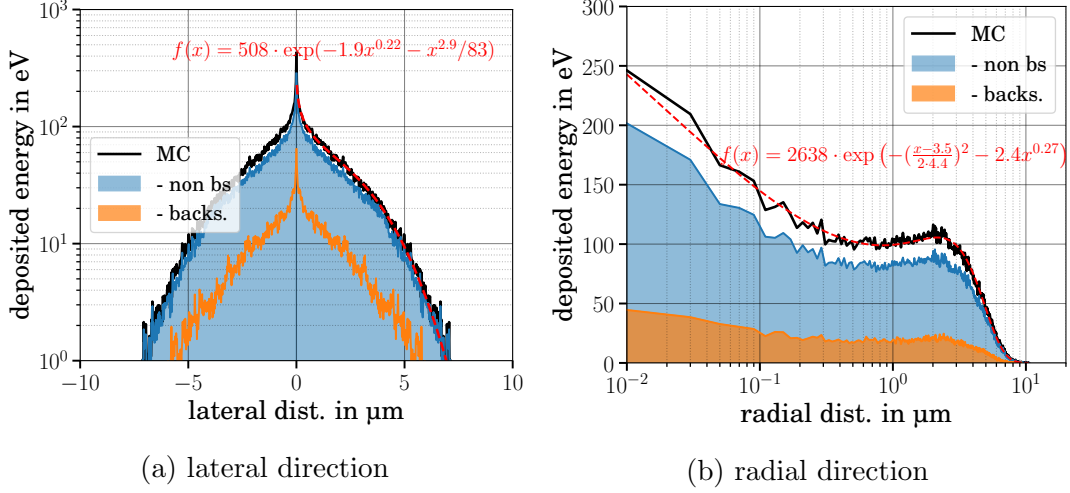
Figure A.1: Simulated energy deposition profile of $E_{\text{kin}} = 30\,\text{keV}$ electrons impinging perpendicularly onto silicon. The simulation counts $N_{\text{sim}} = 10^5$ electrons. In (a) the energy deposition is given for lateral slices along the x-axis and in (b) for slices in radial direction. The integral of the distribution gives the incident energy minus the energy lost due to back-scattering: $E_{\text{dep}} = E_{\text{in}} - E_{\text{bs}}$.

(a) 50% quantile

(b) 90% quantile
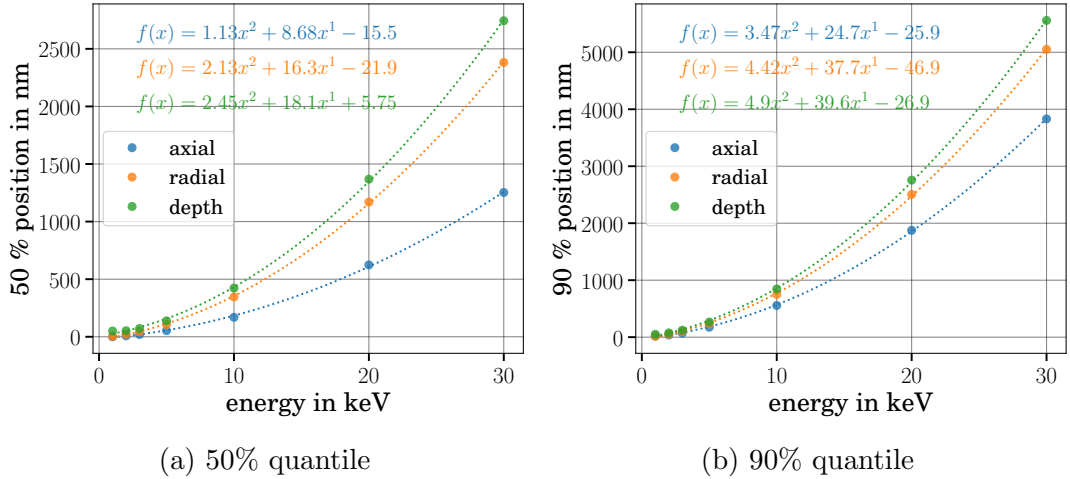
Figure A.2: Average simulated position until 50% (a) respective 90% (b) of the initial electrons energy is deposited in silicon. Every point represents a separate KESS simulation with $N_{\text{sim}} = 10^5$ electrons but for different incident energies E_{kin}. The incident angle is fixed $\vartheta_{\text{p,in}} = 0\,°$ and dotted lines represent second polynomial fits.
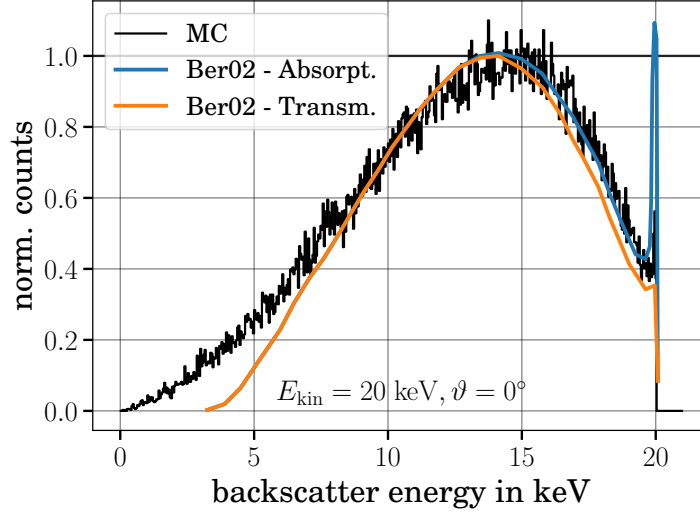
Figure A.3: Back-scattering energy spectrum for initial electrons with $E_{\text{kin}} = 20\,\text{keV}$ that impinge perpendicularly onto silicon. The KESS simulation (black) is based on $N_{\text{sim}} = 10^6$ electrons. In color the spectra spectra for two special silicon lattice orientations are given: anomalous absorption (blue) and transmission (orange) [Ber02]. At KATRIN electrons impinge with angles of about $\vartheta_{\text{p,in}} \in [0°, \vartheta_{\text{max}}]$, with ϑ_{max} limited by reflection at the pinch magnet and the parallel boost by acceleration voltage U_{pae}. In effect this this should lead to a more amorphous response, between anomalous absorption and transmission. The sample variance of the data average to the simulated response gives an uncertainty of $\sigma = 6.8\%$. More conservatively, an uncertainty of $\sigma = 10\%$ is assumed.

A.2 KASSIOPEIA configuration

Table A.1: Electromagnetic field configuration of the 4keV run during the first tritium measurment campaign of KATRIN. The parameters are implemented within an axial symmetric simulation framework. In the simulation the first PS magnet is used for emulating the source magnetic field B_{src} and thus its current differs with respect to the measurement.

component	parameter	comment
PS currents	$I_{\mathrm{ps},1} = 87.9\,\mathrm{A}, I_{\mathrm{ps},2} = 108.8\,\mathrm{A}$	$B_{\mathrm{ps1}} = B_{\mathrm{src}} = 2.52\,\mathrm{T}$
LFCS currents	$I_{\mathrm{ac},1} = 48.2\,\mathrm{A}, I_{\mathrm{ac},2} = 49.5\,\mathrm{A},$ $I_{\mathrm{ac},3} = 90.0\,\mathrm{A}, I_{\mathrm{ac},4} = 52.3\,\mathrm{A},$ $I_{\mathrm{ac},5} = 52.0\,\mathrm{A}, I_{\mathrm{ac},6} = 27.8\,\mathrm{A},$ $I_{\mathrm{ac},7} = 91.8\,\mathrm{A}, I_{\mathrm{ac},8} = 64.7\,\mathrm{A},$ $I_{\mathrm{ac},9} = 63.0\,\mathrm{A}, I_{\mathrm{ac},10} = 13.4\,\mathrm{A},$ $I_{\mathrm{ac},11} = 60.5\,\mathrm{A}, I_{\mathrm{ac},12} = 94.1\,\mathrm{A},$ $I_{\mathrm{ac},13} = 10.1\,\mathrm{A}, I_{\mathrm{ac},14} = 1.1\,\mathrm{A},$ $I_{\mathrm{ac},15} = 1.1\,\mathrm{A}$	$B_{\mathrm{min}} = 6\,\mathrm{Gs}$
EMCS currents	$I_{\mathrm{x}} = 7.85\,\mathrm{A}, I_{\mathrm{y}} = 46.5\,\mathrm{A}$	
MS potentials	$U_{\mathrm{hull}} \in [-14.58\,\mathrm{kV}, -18.58\,\mathrm{kV}],$ $U_{\mathrm{ie}} = -200\,\mathrm{V}, U_{\mathrm{cone}} = -40\,\mathrm{V},$ $U_{\mathrm{ap}} = 0\,\mathrm{V}, U_{\mathrm{gnd}} = 0\,\mathrm{V}$	$U_{\mathrm{ret}} = U_{\mathrm{hull}} + U_{\mathrm{ie}}$
DS currents	$I_{\mathrm{pch}} = 60.9\,\mathrm{A}, I_{\mathrm{det}} = 39.3\,\mathrm{A}$	$B_{\mathrm{pch}} = 4.2\,\mathrm{T}, B_{\mathrm{det}} = 2.52\,\mathrm{T}$
DS potentials	$U_{\mathrm{pae}} = 10\,\mathrm{kV}, U_{\mathrm{BF}} = 120\,\mathrm{V}$	$U_{\mathrm{acc}} = U_{\mathrm{pae}} + U_{\mathrm{BF}}$

Table A.2: KASSIOPEIA simulation electron generator parameters. Two scenarios are distinguished: the beta-decay like and Rydberg background like electron generation.

parameter	KASSIOPEIA generators	
	beta-decay	background
electron energy	$E_{\mathrm{in}} \in [qU_{\mathrm{pae}}, 18.6\,\mathrm{keV}]$ beta-decay	$E_{\mathrm{in}} \in [0, 0.2\,\mathrm{eV}]$ uniform
momentum: azimuth	$\varphi_{\mathrm{p,in}} \in [0°, 360°]$ isotropic	
momentum: polar	$\cos\vartheta_{\mathrm{p,in}} \in [-1, 1]$ isotropic	
position: radius	$r_{\mathrm{in}} \in [0\,\mathrm{mm}, 38\,\mathrm{mm}]$ homogeneous	$r_{\mathrm{in}} \in [0\,\mathrm{mm}, \sqrt{\frac{B(z_{\mathrm{in}})}{\phi}}]$ hom.
position: azimuth	$\varphi_{\mathrm{x,in}} \in [0°, 360°]$ homogeneous	
position: axial	$z_{\mathrm{in}} = -16.465\,\mathrm{m}$ constant	$z_{\mathrm{in}} \in [-1.5\,\mathrm{m}, 11\,\mathrm{m}]$ uniform
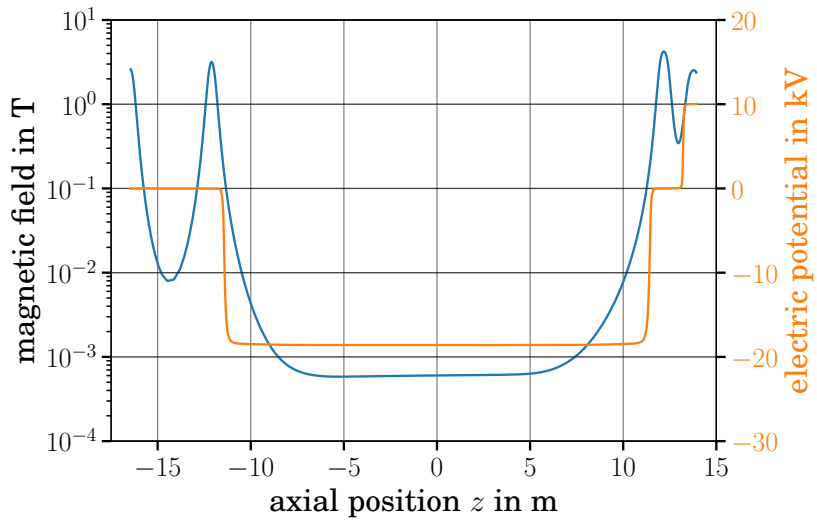
Figure A.4: Electromagnetic fields for a simulated electron along the axial position z. The center of the MS is at $z = 0\,\mathrm{m}$. The exact currents and potentials are listed in table A.1.

A.3 Simulation of background electrons

(a) tritium beta-decay

(b) Rydberg like background
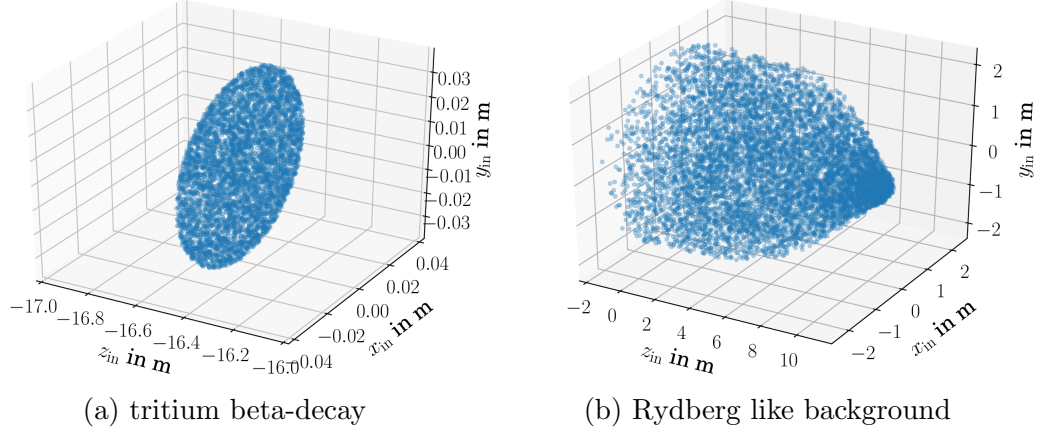
Figure A.5: KASSIOPEIA position generator for the two separate simulation scenarios. Left tritium like electrons created in at the position of the first PS magnet. Right: background like electrons originating from the downstream half of the MS, in accordance to a Rydberg like background.

(a) FPD position shift

(b) FPD inter-event time
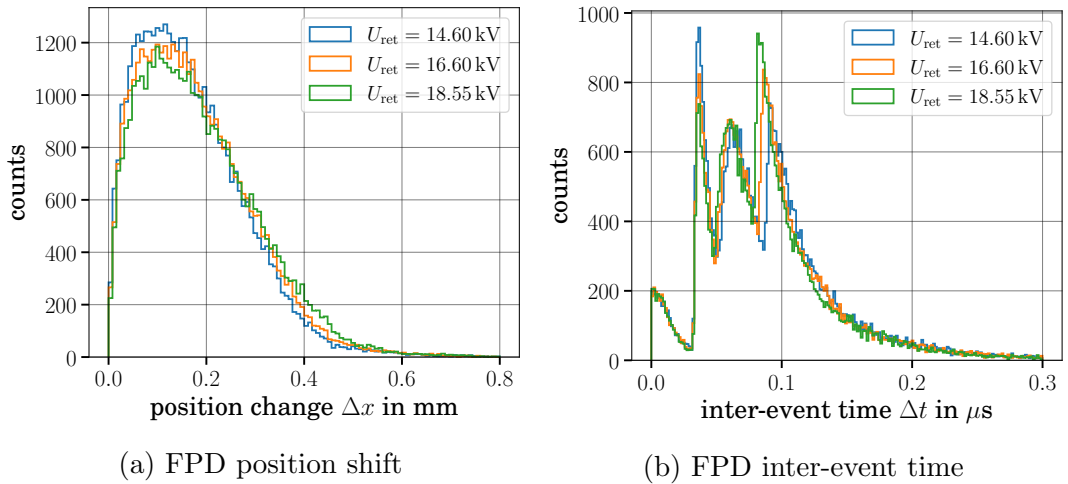
Figure A.6: Rydberg electron background: Position change $\Delta x = x_{\mathrm{fi}} - x_{\mathrm{in}}$ (left) and inter-event times $\Delta t = t_{\mathrm{fi}} - t_{\mathrm{in}}$ (right) for electrons that exit the detector $(x_{\mathrm{in}}, t_{\mathrm{in}})$ due to back-scattering but are back reflected onto it $(x_{\mathrm{in}}, t_{\mathrm{in}})$ (s. fig. 5.3). Both are slightly dependent on the retarding potential values U_{ret}.

(a) incident energy

(b) ring wise rate
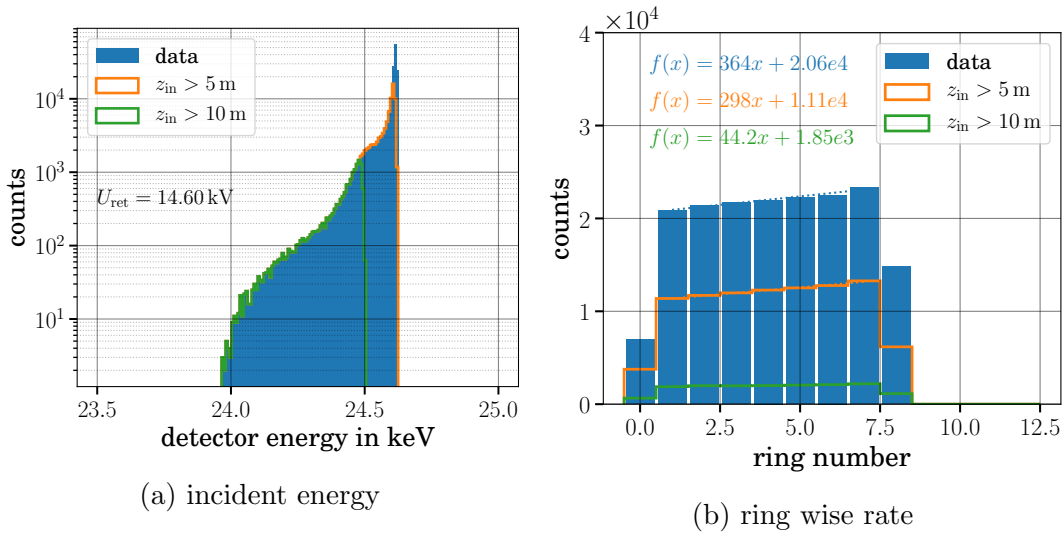
Figure A.8: Rydberg background scenario: Energy and rate of electrons impinging onto the FPD right after being generated. (a) The energy of background electrons show a dependence on generators axial position z_{in}. (b) Electron rate according to the radial position of impact translated to the FPDs ring structure.

(a) FPD event multiplicity

(b) inter-arrival time
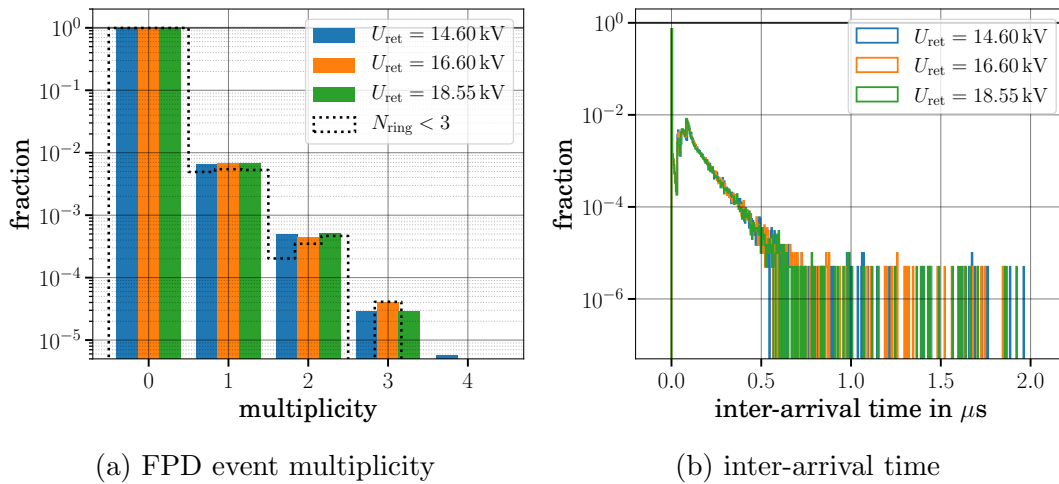
Figure A.7: Rydberg electron background: Overall multiplicity (left) and inter-arrival times (right) of simulated electrons. Here three exemplary retarding potential settings are depicted in color. In addition the multiplicity shows the same distribution but for the innermost FPD rings (+bullseye). The inter-arrival time is calculated relative to the first impingement on the detector and the peak at $t = 0\,\mu\mathrm{s}$ thus corresponds to the $\approx 80\%$ of electrons that don't back-scatter.

A.4 Signal waveform and filter output
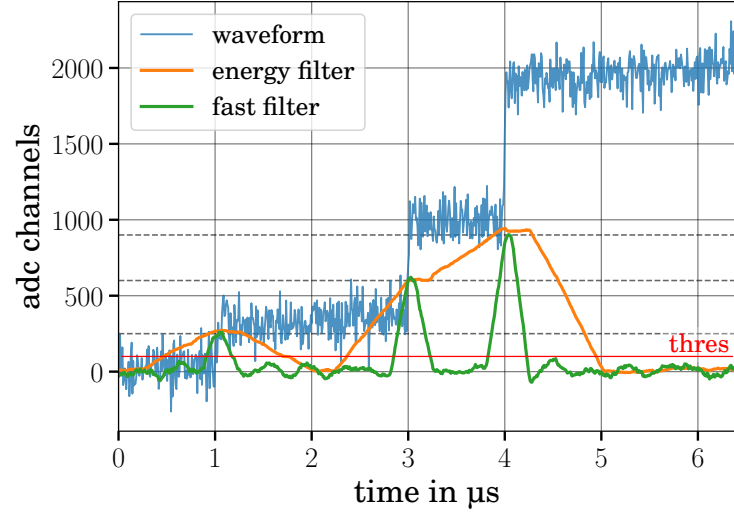
Figure A.9: Simulated waveform (blue) with a $8\,\mathrm{ns}$ samples and three separate events at $t = 1/3/4\,\mu\mathrm{s}$. Their incident energies are denoted by the gray dashed lines and a fixed threshold is denoted in red. In addition the trapezoidal filter output of a trapezoidal filter, using a peaking time of $t_{\mathrm{pk}}^{\mathrm{energy}} = 0.768\,\mu\mathrm{s}$ and $t_{\mathrm{ft}}^{\mathrm{energy}} = 0.256\,\mu\mathrm{s}$ flattop, is depicted in orange. A four times faster filter would be able to discriminated the three events but in turn is more affected by electronic noise.

138
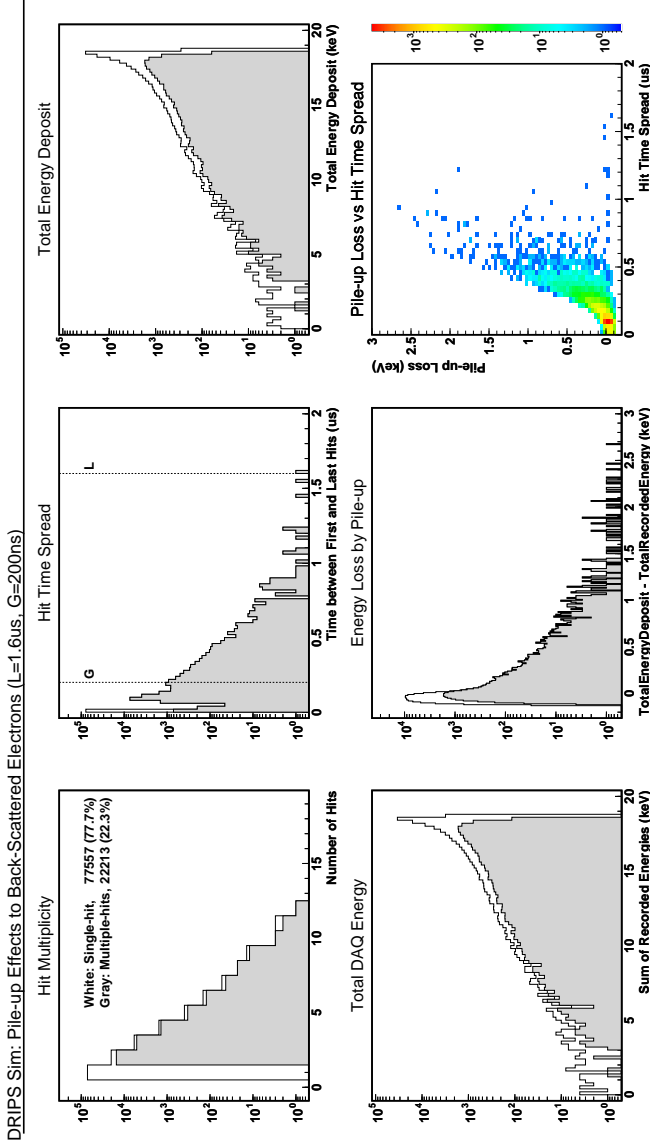
Figure A.10: Exemplary DRIPS DAQ simulation ($t_{\text{sh}} = 1.6\,\mu s$, $t_{\text{ft}} = 0.2\,\mu s$, by S. Enomoto) with electron track data presented in 5.2.2. Electrons that deposit all energy on the first hit are shown as contour histograms. Electrons that back scatter, which leads multiple detector hits, are depicted as gray faced histograms. The top center figure shows the timing structure and equals figure 5.10b. The energy spread illustrated in the bottom center figure is related to the so-called peak pile-up [Eno14; Eno19].

A.5 FPD charge sharing
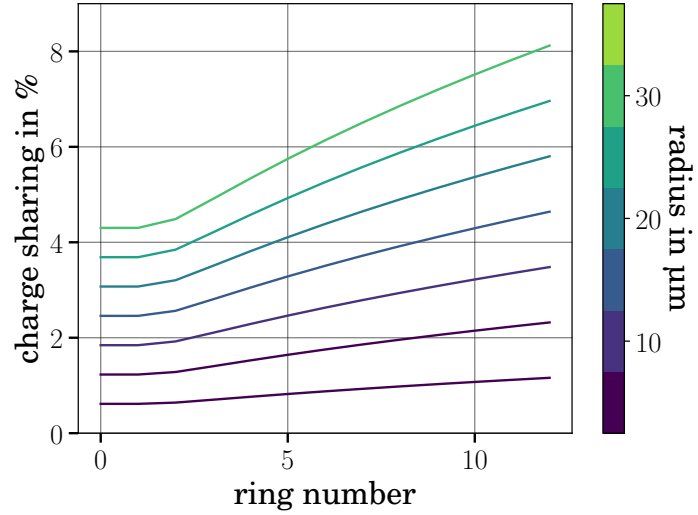
Figure A.11: Charge sharing probability over ring number of the FPD, calculated according to equation 5.25. Due to the geometry of the detector the pixels in the bullseye and ring 1 have the lowest probability of charge sharing. A measurement of charge sharing presented in [Sch14] measures a charge sharing probability of roughly $P_{cs} = 1.5\%$ for the center of the FPD. This would ensue a charge cloud radius of roughly $r_{cc} = 12\,\mu$m.

A.6 Dimensions photo-electric electron gun
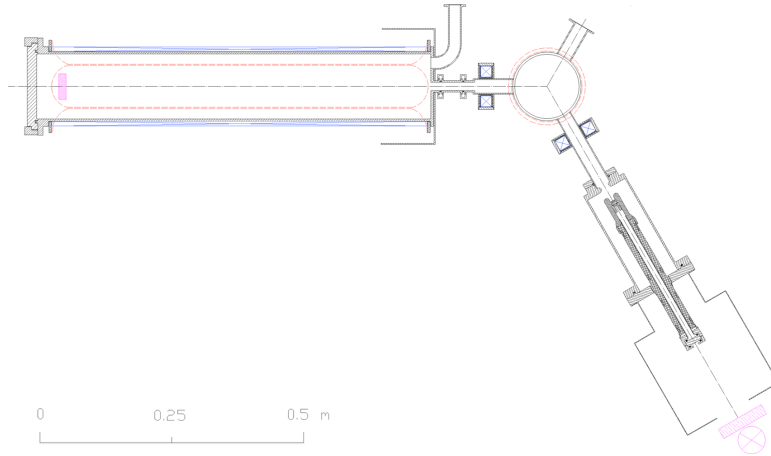
Figure A.12: Dimensions of the photo-electric electron gun.
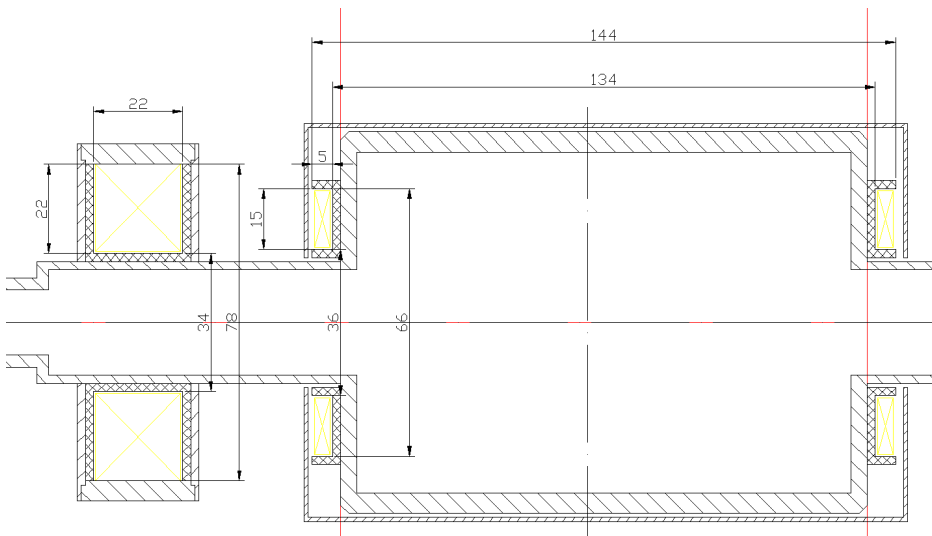
Figure A.13: Dimensions of the focus and rotation magnets.

A.7 Calibration and fast-filter variation

(a) energy spectrum

(b) pixel map
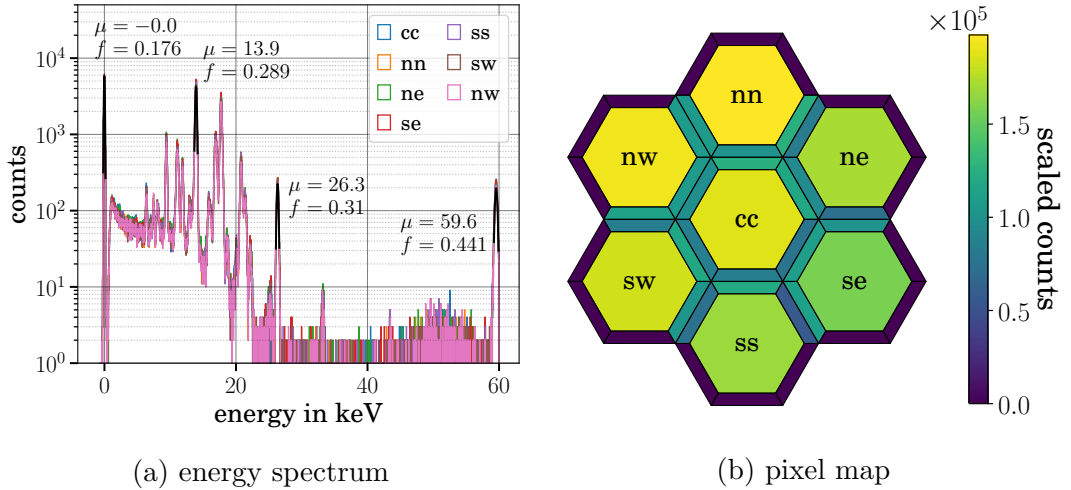
Figure A.14: (a) Measured ^{241}Am energy spectrum with the "F-02" detector. The measurement was performed in the SEM environment and reflects the prevalent electronic noise conditions. Americium has three prominent x-ray lines: $E_{\mathrm{kin}} = 13.9\,\mathrm{keV}$ (37%), $E_{\mathrm{kin}} = 26.3\,\mathrm{keV}$ (2.27%) and $E_{\mathrm{kin}} = 59.5\,\mathrm{keV}$ (35.9%) [Bas06]. From the increased attenuation length at $E_{\mathrm{kin}} = 59.5\,\mathrm{keV}$, it is expected that roughly 95.5% of all x-rays aren't registered but transmitted through the detector (s. fig. 5.17). The peak at $0\,\mathrm{keV}$ is recorded by random sampling with DANTE and thus describes contribution of electronic noise FWHM = 176 eV. The fitted normal distribution of the above lines show an increase of the energy resolution according to its combination with Fano-noise 4.4: $\sigma = \sqrt{\sigma_{\mathrm{el}}^2 + \sigma_{\mathrm{fano}}^2}$. (b) Pixel map of the count rates for each pixel - the coincident charge-shared rate is scaled by 100. Due to the additional spectral lines - from excitation of ambient materials - distinguishing charge-shared events becomes less accurate. This translates into an inaccurate determination of the time correction factor $t_{\mathrm{ch}}^{\mathrm{off}}$ and is visible as slight asymmetries of the charge-shared rates for neighboring pixels.
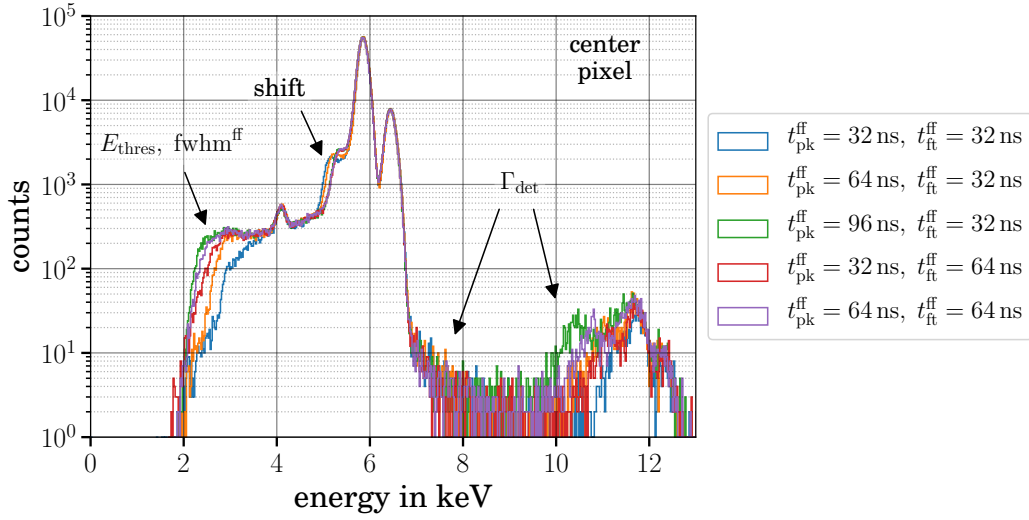
Figure A.15: Impact of the fast filters peaking $t_{\mathrm{ff,pk}}$ and flattop $t_{\mathrm{ff,ft}}$ time to the measurement of an ^{55}Fe x-ray source. Here for a representative pixel only. Both parameters effect the region close the energy threshold as the fast filter is used for event triggering. Furthermore the event discrimination time is given by the fast filter $t_{\mathrm{min}} = 2 \cdot t_{\mathrm{ff,pk}} + t_{\mathrm{ff,ft}}$ and thus affect the observed spectrum above the $E_{\mathrm{kin}}^{K\beta_{1+3}} = 6.49\,\mathrm{keV}$ line (cf. [Des19]).

A.8 Pixel boundary measurements

(a) inter-event time

(b) eta plot
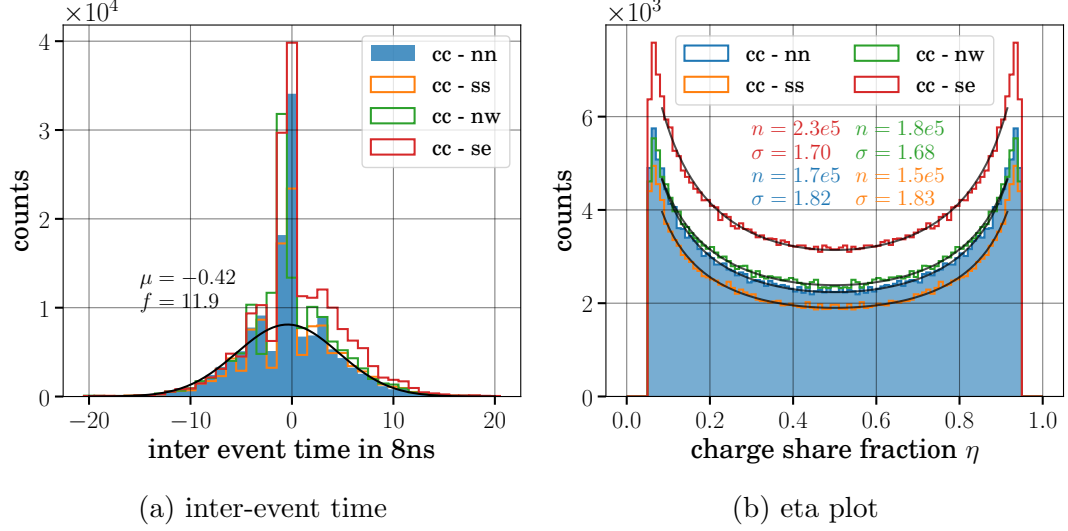
Figure A.16: Pixel boundary measurement with the "F-02" detector and the SEM operated at mag = 400 ($320 \times 240 \, \mu$m). The stage was moved and rotated to measure twin charge sharing between four different pixels: cc-nn, cc-ss, cc-nw, and cc-se. (a) shows the inter-event times of electrons and (b) the charge sharing fraction η. Here the printed normalization n is defined as $t_{\text{meas}} \cdot \Gamma_{\text{px}} \cdot P_{\text{cs}}$ and σ describes the increase of the charge clouds normal distribution: only the charges within $\Delta x \in [-\sigma, \sigma]$ are considered (s. eqs. 5.25 & 5.26), for homogeneous illumination it is defined as $\sigma = 3.5256$.

(a) scatter: energy - position

(b) scatter: rise-time - position
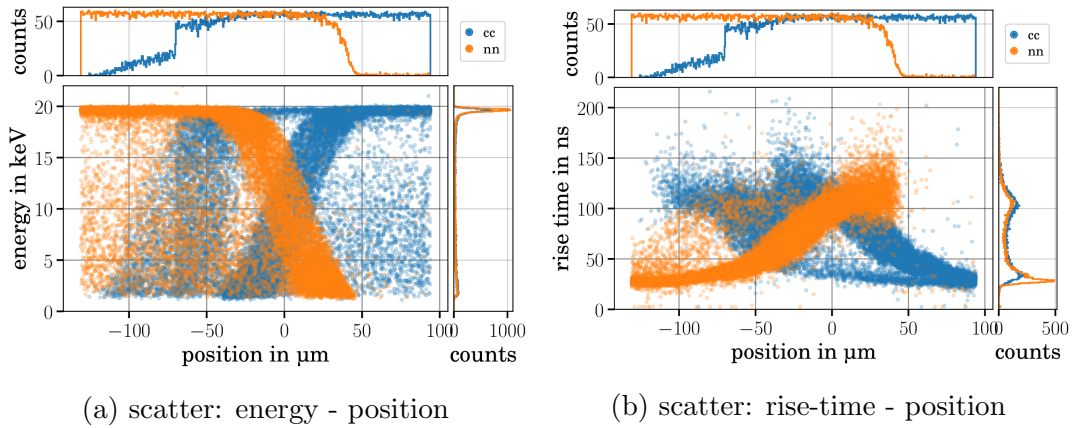
Figure A.17: Scatter plot of event energy (a) and signal rise-time (b) over scanning position of the SEM. The measurement was performed at the intersection of two pixels with $E_{\text{kin}} = 20 \, \text{keV}$ electrons and the "F-02" detector. Both E and t_{rise} are derived by fitting the recorded signal waveforms. Here blue dots are events in the "center" pixel.

(a) scatter: energy - position

(b) scatter: rise-time - position
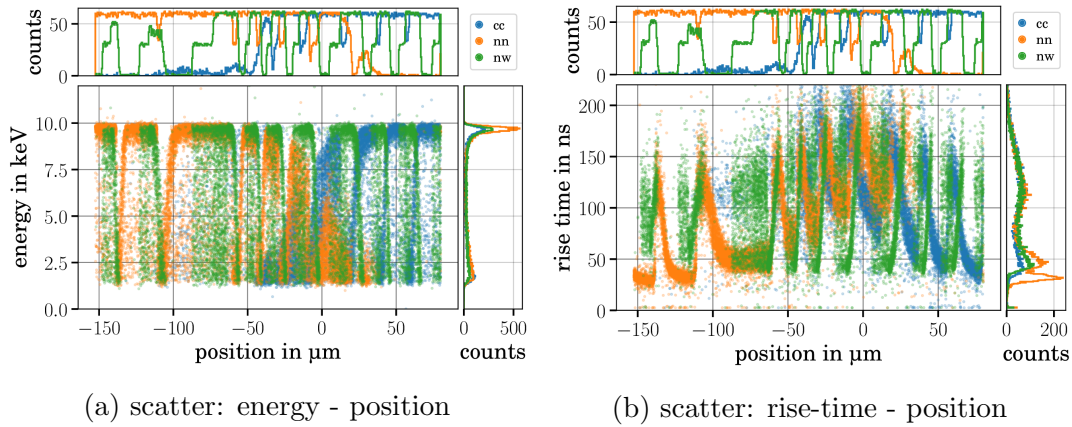
Figure A.18: Scatter plot of event energy (a) and signal rise-time (b) over scanning position of the SEM. The measurement was performed at the intersection of three pixels with $E_{\mathrm{kin}} = 10\,\mathrm{keV}$ electrons and the "F-02" detector. Both E and t_{rise} are derived by fitting the recorded signal waveforms. Here blue dots are events in the "center" pixel. Due to the "Y" shaped pixel intersection geometry a line scan with SEM shows characteristic ramps.

A.9 Sensitivity study correlation matrices

(a) electronic noise
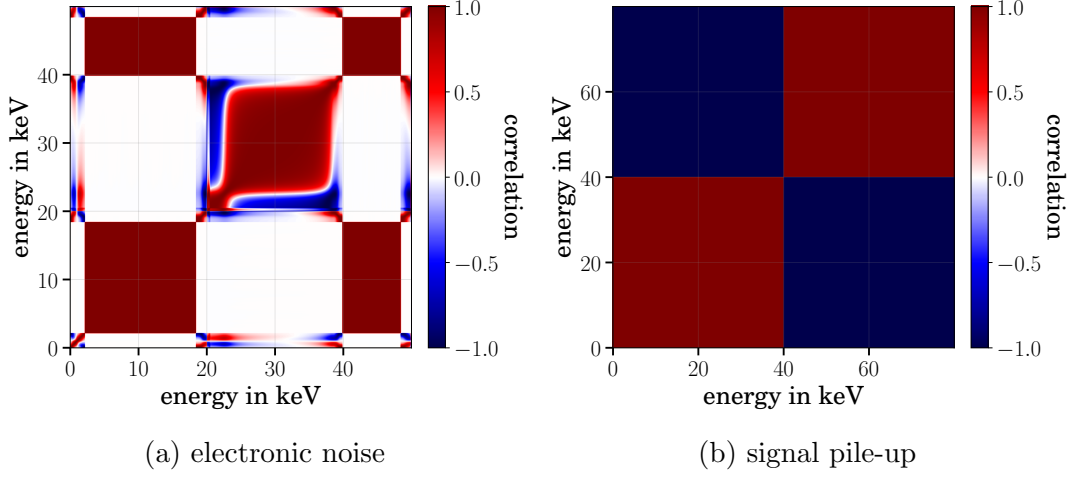
(b) signal pile-up

Figure A.19: (a) Electronic noise correlation matrix for FWHM $= 300 \pm 20\,\text{eV}$, $E_{\text{thres}} = 1000 \pm 20\,\text{keV}$ and with $n_{\text{cov}} = 500$ repetitions. Here an additional post acceleration of $U_{\text{pae}} = 20\,\text{kV}$ and constant background rate of $\Gamma_{\text{bkg}} = 1\,\text{cps}$ are considered. (b) Signal pile-up correlation matrix for a detector rate $\Gamma_{\text{det}} = 10^8\,\text{cps}$, $n_{\text{px}} = 3500$ number of pixels and a discrimination time of $t_{\text{min}} = 1.0 \pm 0.1\,\mu\text{s}$. The spectrum was post accelerated by $U_{\text{pae}} = 20\,\text{kV}$.

(a) charge sharing

(b) scattering off silicon
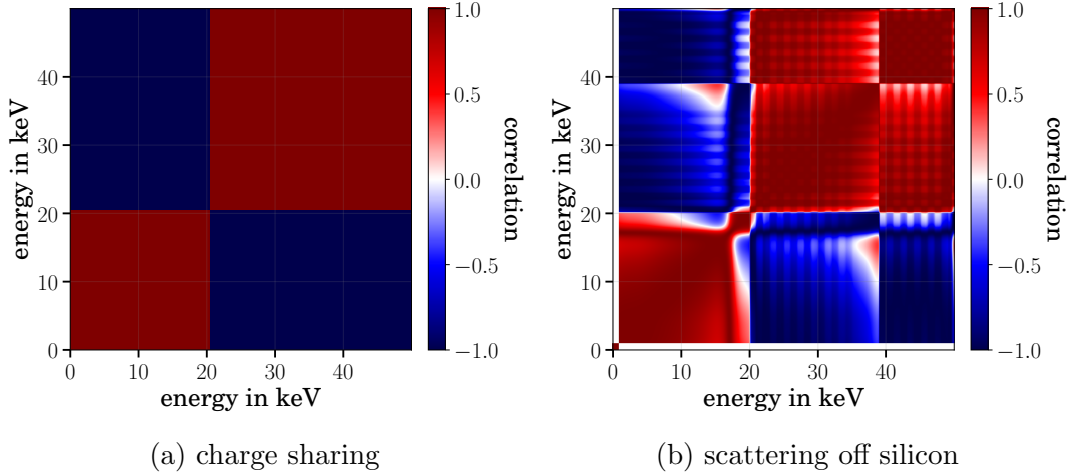
Figure A.20: (a) Charge sharing correlation matrix for $U_{\text{pae}} = 20\,\text{kV}$ post acceleration, a detection threshold of $E_{\text{thres}} = 0\,\text{keV}$ and $P_{\text{cs}} = 10 \pm 1\,\%$ probability for charge sharing. (b) Scattering correlation matrix for $U_{\text{pae}} = 20\,\text{kV}$ post acceleration, a deadlayer of $z_{\text{dl}} = 50 \pm 5\,\text{nm}$ and $\vartheta_{\text{p,in}} = 0 \pm 5\,°$ perpendicular incidence.
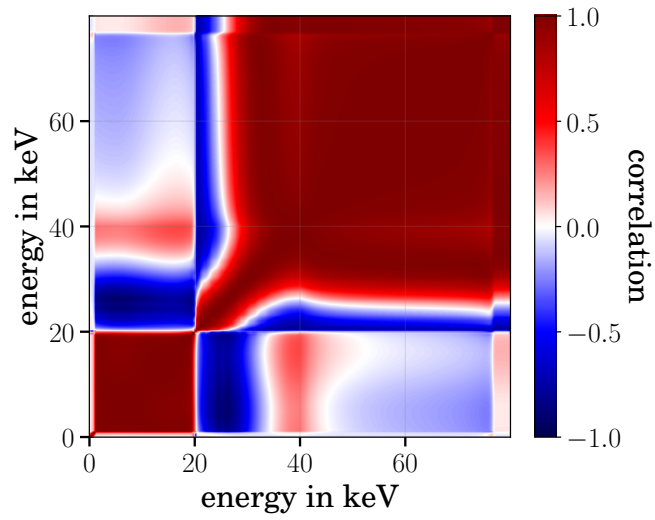
Figure A.21: Correlation matrix with respect to a combination of detector related systematics: silicon scattering, charge sharing, electronic noise and signal pile-up. Here the spectrum is shifted due to post acceleration $U_{\mathrm{pae}} = 20\,\mathrm{kV}$.

A.10 FPD detection efficiency
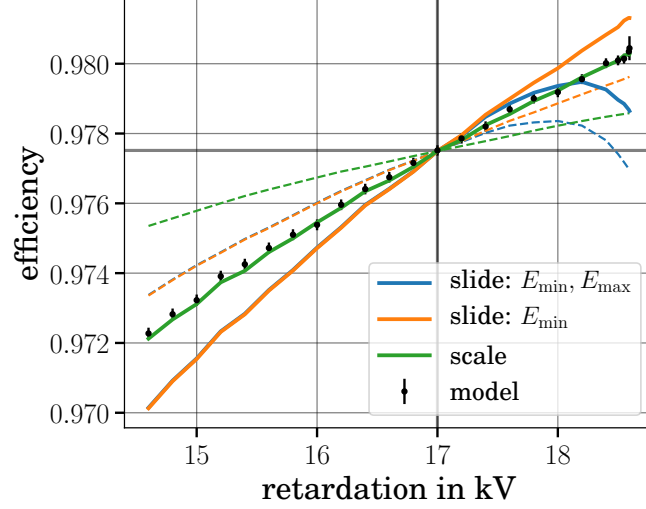
Figure A.22: Modeled absolute detection efficiency ϵ_{det} (black). In color the extrapolation result of the cross-hair marked reference $(U_{ext}, \epsilon_{det} (U_{ext}))$ response is given for three different approaches: sliding both boundaries (blue), sliding the lower boundary (orange) and scaling the lower boundary (green). The dashed line represent the ϵ_{roi} only and the solid lines is corrected by electron escape (s. eq. 8.6).

(a) $P_{ref}(\Delta E)$

(b) $P_{ref}(\vartheta_{p,in})$
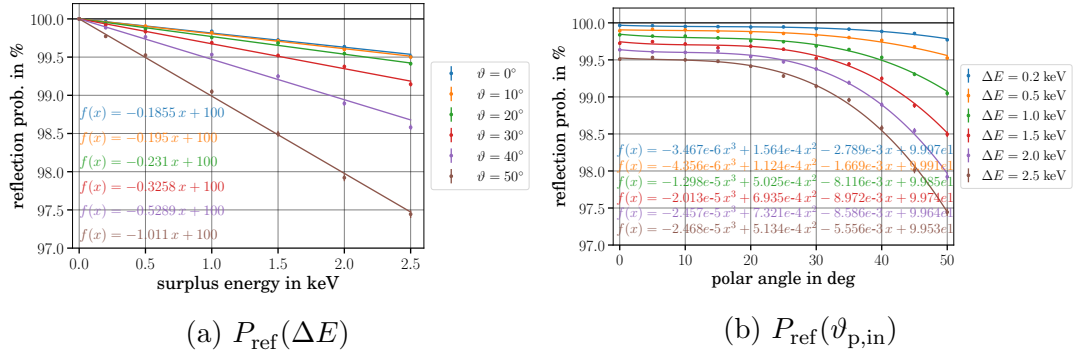
Figure A.23: KASSIOPEIA simulation with mono-energetic E_{in} electrons, with fixed initial polar angle $\vartheta_{p,in}$ and fixed retardation potential $U_{ret} = 18.6\,\text{kV}$. The simulation was repeated for various surplus energies $\Delta E = E_{in} - U_{ret} = 0.2/0.5/1.0/1.5/2.0/2.5\,\text{keV}$ as well as initial polar angles $\vartheta_{p,in} = 0/5/\ldots/50°$. The figures show the probability for back-scattered electrons to be back-reflected $P_{ref} = 1 - P_{esc}$ (dots). In (a) it is presented as a function of the surplus energy and of the polar angle in (b). Errors reflect the statistical uncertainty for $N_{sim} = 10^5$ simulated electrons, generated in the tuned first PS magnet (s. sc. 5.1). The solid lines correspond to polynomial fits.

Glossary

Λ-CDM Lambda Cold Dark Matter model, also referred to as standard cosmological model.. 8, 11

νMSM neutrino Minimal Standard Model. 13

"F-02" TRISTAN seven pixel detector with $r_\mathrm{px} = 1\,\mathrm{mm}$ and standard entrance window technology. 71, 78, 81–85, 141, 143, 144

"F-12" TRISTAN seven pixel detector with $r_\mathrm{px} = 0.5\,\mathrm{mm}$ and standard entrance window technology. 87–90

ADC Analog to Digital Converter. 32, 34, 59, 72, 114

adu Analog Digital Unit. 32

boson Elementary particle for conveying interaction forces. 1

CKrS Condensed Krypton Source. 18

CMB Cosmic Microwave Background. 11, 13

CMU Carnegie Mellon University. 34

CPS Cryogenic Pumping Section. 15–18

CUBE charge sensitive preamplifier from XGLab. 71–73

D-Sub D-Subminiature. 72, 73

DANTE digital pulse processor from XGLab. 72, 73, 83, 98, 141

DAQ Data Acquisition (system). 2, 17, 20, 27, 34, 35, 41, 43, 50, 51, 53, 58–60, 64, 70, 74, 75, 82, 86, 91, 98, 112, 115, 138

DE Dark Energy. 8

DM Dark Matter. 8, 13, 14, 28, 127

DPS Differential Pumping Section. 16–18

DS Detector Section. 41, 116, 133

EMCS Earth Magnetic field Compensation System. 19, 133

FBM Forward Beam Monitor. 18

fermion Elementary matter particle. 1

FPD Focal Plane Detector. 17, 19–21, 29, 35–37, 41–43, 50, 51, 53–55, 58, 59, 61, 70, 110, 115–122, 124, 125, 127, 128, 135, 136, 139

FPGA Field Programmable Gate Array. 20

FSD Final State Distribution. 26

FTICR Fourier Transformation Ion Cyclotron Resonance. 18

FTL First Level Trigger. 20

HLL HalbLeiterLabor München (semiconductor laboratory) part of the MPG. 34, 71, 77

IE Inner Electrode system. 20

IPE Institute for Data Processing and Electronics. 34

KASSIOPEIA Particle tracking software developed at KATRIN. 37–40, 43, 53, 70, 112, 113, 115, 125, 133, 135, 147

KATRIN KArlsruhe TRitium Neutrino experiment. vii, 1, 2, 15–17, 19–22, 24, 26–29, 34–37, 40, 41, 43, 48, 53, 62, 66, 70, 71, 78, 85, 91, 95, 98, 99, 109–111, 115–117, 121, 122, 125, 127, 132, 133, 150

KESS Katrin Electron Silicon Scattering. 43, 44, 63, 66, 69, 70, 82, 86, 102, 131, 132

KIT Karlsruhe Institute of Technology. 15, 34, 86

KNM1 KATRIN Neutrino Mass (campaign). 25

KSETA Karlsruhe School of Elementary and Astroparticle Physics: Science and Technology. v

LARA LAser RAman spectroscopy system. 18

LFCS Low Field Correction System. 19, 133

LS Loop System. 18

MAC-E Magnetic Adiabatic Collimation with Electrostatic filter. 19, 22

MC Monte Carlo. 26, 67, 70, 94, 125

MobSU Mobile Sensor Unit. 19

MonSpec Main Spectrometer. 17, 19, 20

MPP Max-Planck-Institute for Physics (Werner-Heisenberg-Institut) in Munich part of MPG. 34

MS Main Spectrometer. 15, 17, 19, 20, 22–25, 29, 40, 41, 48, 51, 59, 115, 120, 133–135

MTD Measurement Time Distribution. 23–26

nJFET Negative Junction gate Field-Effect Transistor. 35

PAE Post Acceleration Electrode. 20, 21, 40, 48, 49, 52

PCB Printed Circuit Board. 71

PoliMi Politecnico di Milano (Polytechnic University of Milan). 34

ppm Parts Per Million. 20

PS Pre Spectrometer. 17, 19, 40, 118, 133, 135, 147

R&D Research & Developement. 34

ROI Region-Of-Interest. 121–123, 128

RS Rear Section. 16, 17, 25, 124, 126

RW Rear Wall. 17, 49, 51, 124

SDD Silicon Drift Detector. 27, 31, 33–35, 40, 45, 71, 73, 77, 78, 113, 115, 127

SDS Spectrometer and Detector Section. 16, 40, 41, 49, 118, 125

SEM Scanning Electron Microscope. 77–79, 81–84, 141, 143, 144

SM Standard Model of particle physics. It describes all matter and interactions as elementary particles. 1, 3, 6–8, 13, 15, 127

SMA SubMiniature version A. 72, 73

STL Second Level Trigger. 20

STS Source and Transport Section. 16, 19, 40, 42, 51, 53, 78

TLK Tritium Laboratory Karlsruhe. 15

TOF Time-Of-Flight. 25

TRISTAN TRitium Investigation on STerile (A) Neutrinos. vii, 2, 19, 20, 30, 34–37, 40, 54, 55, 59, 60, 71, 72, 78, 86, 91, 109, 110, 113, 115, 116, 127, 128

TUM Technische Universität München (Technical University of Munich). 34

UNIMIB Università degli Studi di Milano-Bicocca (University of Milano-Bicocca). 34

UV Ultra Violet. 17

WDM Warm Dark Matter. 13, 14

WGTS Windowless Gaseous Tritium Source. 15–18, 21, 22, 24, 25, 41, 42

XGLab X and Gamma ray electronics LAB, a spin-off company from the Politecnico di Milano and currently part of BRUKER. 34, 71, 72

XML eXtensible Markup Language. 38

Bibliography

[Aad12]   G. Aad, T. Abajyan, B. Abbott, et al. "Observation of a new particle in the search for the Standard Model Higgs boson with the ATLAS detector at the LHC". In: *Physics Letters B* 716.1 (2012), pp. 1–29. DOI: 10.1016/j.physletb. 2012.08.020.

[Abe12]   Y. Abe, C. Aberle, T. Akiri, et al. "Indication of Reactor $\overline{\nu}_e$ Disappearance in the Double Chooz Experiment". In: *Phys. Rev. Lett.* 108 (Mar. 2012), p. 131801. DOI: 10.1103/PhysRevLett.108.131801.

[Abe14]   K. Abe, J. Adam, H. Aihara, et al. "Precise Measurement of the Neutrino Mixing Parameter θ_{23} from Muon Neutrino Disappearance in an Off-Axis Beam". In: *Phys. Rev. Lett.* 112 (2014), p. 181801. DOI: 10.1103/PhysRevLett. 112.181801.

[Adh16]   R. Adhikari et al. "A White Paper on keV Sterile Neutrino Dark Matter". In: *Submitted to: White paper* (Feb. 2016). Ed. by M. Drewes et al. arXiv: 1602.04816 [hep-ph].

[Aga10]   N. Agafonova et al. "Observation of a first candidate event in the {OPERA} experiment in the {CNGS} beam". In: *Physics Letters B* 691.3 (2010), pp. 138–145. DOI: 10.1016/j.physletb.2010.06.022.

[Agh18]   N. Aghanim, Y. Akrami, M. Ashdown, et al. "Planck 2018 results. VI. Cosmological parameters". In: (July 2018). arXiv: 1807.06209 [astro-ph.CO].

[Ahn06]   M. H. Ahn, E. Aliu, S. Andringa, et al. "Measurement of neutrino oscillation by the K2K experiment". In: *Phys. Rev. D* 74 (Oct. 2006), p. 072003. DOI: 10.1103/PhysRevD.74.072003.

[Ahn12]   J. K. Ahn, S. Chebotaryov, J. H. Choi, et al. "Observation of Reactor Electron Antineutrinos Disappearance in the RENO Experiment". In: *Phys. Rev. Lett.* 108 (May 2012), p. 191802. DOI: 10.1103/PhysRevLett.108.191802.

[Ake19a]   M. Aker, K. Altenmüller, M. Arenz, et al. "First operation of the KATRIN experiment with tritium". In: (Sept. 2019). arXiv: 1909.06069 [physics.ins-det].

[Ake19b]   M. Aker, K. Altenmüller, M. Arenz, et al. "An improved upper limit on the neutrino mass from a direct kinematic method by KATRIN". In: (Sept. 2019). arXiv: 1909.06048 [hep-ex].

[Ale05]   S. Schael et al. "Precision electroweak measurements on the Z resonance". In: *Phys. Rept.* 427 (2006), pp. 257–454. DOI: 10.1016/j.physrep.2005.12.006.

[Ali80]   R. C. Alig, S. Bloom, and C. W. Struck. "Scattering by ionization and phonon emission in semiconductors". In: *Phys. Rev. B* 22 (1980), pp. 5565–5582. DOI: 10.1103/PhysRevB.22.5565.

[Alt19]   K. Altenmüller. "Search for sterile neutrinos in β-decays". PhD thesis. Technical University of Munich and University Paris-Saclay, 2019.

[Ams15]   J. F. Amsbaugh, J. Barrett, A. Beglarian, et al. "Focal-plane detector system for the KATRIN experiment". In: *Nuclear Instruments and Methods in Physics Research Section A: Accelerators, Spectrometers, Detectors and Associated Equipment* 778 (2015), pp. 40–60. DOI: 10.1016/j.nima.2014.12.116.

[An12]   F. P. An, J. Z. Bai, A. B. Balantekin, et al. "Observation of Electron-Antineutrino Disappearance at Daya Bay". In: *Phys. Rev. Lett.* 108 (2012), p. 171803. DOI: 10.1103/PhysRevLett.108.171803.

[Ang05]   J. Angrik et al. "KATRIN Design Report 2004". In: *FZKA Scientific Report 7090* (2005).

[Are18a]   M. Arenz, W.-J. Baek, M. Beck, et al. "First transmission of electrons and ions through the KATRIN beamline". In: *Journal of Instrumentation* 13.04 (Apr. 2018), P04020–P04020. DOI: 10.1088/1748-0221/13/04/p04020.

[Are18b]   M. Arenz, W.-J. Baek, M. Beck, et al. "Calibration of high voltages at the ppm level by the difference of ^{83m}Kr conversion electron lines at the KATRIN experiment". In: *The European Physical Journal C* 78.5 (May 2018), p. 368. DOI: 10.1140/epjc/s10052-018-5832-y.

[Are18c]   M. Arenz, W.-J. Baek, M. Beck, et al. "The KATRIN superconducting magnets: overview and first performance results". In: *Journal of Instrumentation* 13.08 (Aug. 2018), T08005–T08005. DOI: 10.1088/1748-0221/13/08/t08005.

[Arn83]   G. Arnison et al. "Experimental Observation of Lepton Pairs of Invariant Mass Around 95-GeV/c**2 at the CERN SPS Collider". In: *Phys. Lett.* 126B (1983), pp. 398–410. DOI: 10.1016/0370-2693(83)90188-0.

[Asa05a]   T. Asaka, S. Blanchet, and M. Shaposhnikov. "The νMSM, dark matter and neutrino masses". In: *Physics Letters B* 631 (2005), pp. 151–156. DOI: 10.1016/j.physletb.2005.09.070.

[Asa05b]   T. Asaka and M. Shaposhnikov. "The νMSM, dark matter and baryon asymmetry of the universe". In: *Physics Letters B* 620.1—2 (2005), pp. 17–26. DOI: 10.1016/j.physletb.2005.06.020.

[Ase11]   V. N. Aseev, A. I. Belesev, A. I. Berlev, et al. "Upper limit on the electron antineutrino mass from the Troitsk experiment". In: *Phys. Rev. D* 84 (2011), p. 112003. DOI: 10.1103/PhysRevD.84.112003.

[Bab14]   M. Babutzka. "Design and development for the Rearsection of the KATRIN experiment". PhD thesis. Karlsruhe Institut für Technologie, 2014. DOI: 10.5445/IR/1000045598.

[Bag83]   P. Bagnaia et al. "Evidence for $Z^0 \rightarrow e^+ + e^-$ at the CERN p$\bar{\text{p}}$ Collider". In: *Phys. Lett.* 129B (1983), pp. 130–140. DOI: 10.1016/0370-2693(83)90744-X.

[Ban83]   M. Banner et al. "Observation of Single Isolated Electrons of High Transverse Momentum in Events with Missing Transverse Energy at the CERN anti-p p Collider". In: *Phys. Lett.* 122B (1983), pp. 476–485. DOI: 10.1016/0370-2693(83)91605-2.

[Bas06]   M. S. Basunia. "Nuclear Data Sheets for $A = 241$". In: *Nuclear Data Sheets* 107 (Aug. 2006), p. 3323.

[Bau13]   S. Bauer, R. Berendes, F. Hochschulz, et al. "Next generation KATRIN high precision voltage divider for voltages up to 65kV". In: *Journal of Instrumentation* 8.10 (Oct. 2013), P10026–P10026. DOI: 10.1088/1748-0221/8/10/p10026.

[Beh17]   J. Behrens. "Design and commissioning of a mono-energetic photoelectron source and active background reduction by magnetic pulse at the KATRIN experiment". PhD thesis. Westfälische Wilhelms-Universität Münster, 2017.

[Ber02]   D. Berger and H. Niedrig. "Energy distribution of electron backscattering from crystals and relation to electron backscattering patterns and electron channeling patterns". In: *Scanning* 24.2 (2002), pp. 70–74. DOI: 10.1002/sca.4950240204.

[Ber10]   M. J. Berger, J. H. Hubbell, S. M. Seltzer, et al. *XCOM: Photon Cross Sections Database.* Comp. software. 2010. DOI: 10.18434/T48G6X.

[Bet30]   H. Bethe. "Zur Theorie des Durchgangs schneller Korpuskularstrahlen durch Materie". In: *Annalen der Physik* 397.3 (1930), pp. 325–400. DOI: 10.1002/andp.19303970303.

[Boh13]   N. Bohr. "On the constitution of atoms and molecules". In: *The London, Edinburgh, and Dublin Philosophical Magazine and Journal of Science* 26.151 (1913), pp. 1–25. DOI: 10.1080/14786441308634955.

[Bor06]   B. Bornschein. "The closed tritium cycle of KATRIN". In: *Progress in Particle and Nuclear Physics* 57 (2006), pp. 38–48. DOI: 10.1016/j.ppnp.2005.12.004.

[Bor11]   B. Bornschein. "Between Fusion and Cosmology – The Future of the Tritium Laboratory Karlsruhe". In: *Fusion Science and Technology* 60.3 (2011), pp. 1088–1091. DOI: 10.13182/FST11-A12604.

[Boy19]   A. Boyarsky, M. Drewes, T. Lasserre, et al. "Sterile neutrino Dark Matter". In: *Progress in Particle and Nuclear Physics* 104 (2019), pp. 1–45. DOI: 10.1016/j.ppnp.2018.07.004.

[Bra05]   W. H. Bragg and R. Kleeman. "XXXIX. On the α particles of radium, and their loss of range in passing through various atoms and molecules". In: *The London, Edinburgh, and Dublin Philosophical Magazine and Journal of Science* 10.57 (1905), pp. 318–340. DOI: 10.1080/14786440509463378.

[Bro26]   L. de Broglie. "Mécanique quantique et ondulatoire". In: *Onde et mouvements* (1926).

[Cha12]   S. Chatrchyan, V. Khachatryan, A.M. Sirunyan, et al. "Observation of a new boson at a mass of 125 GeV with the CMS experiment at the LHC". In: *Physics Letters B* 716.1 (2012), pp. 30–61. DOI: 10.1016/j.physletb.2012.08.021.

[Cha14]   J. Chadwick. "Intensitätsverteilung im magnetischen Spektrum der Betas-trahlen von Radium B+C". In: *Verhandlungen der Deutschen Physikalischen Gesellschaft* 16 (1914), pp. 383–391.

[Cha32]   J. Chadwick. "Possible Existence of a Neutron". In: *Nature* 129 (1932), p. 312. DOI: 10.1038/129312a0.

[Clo06]   C. Clowe, M. Bradač, A. H. Gonzalez, et al. "A Direct Empirical Proof of the Existence of Dark Matter". In: *The Astrophysical Journal* 648.2 (Aug. 2006), pp. L109–L113. DOI: 10.1086/508162.

[Cor00]   E. Corbelli and P. Salucci. "The extended rotation curve and the dark matter halo of M33". In: *Monthly Notices of the Royal Astronomical Society* 311.2 (Jan. 2000), pp. 441–447. DOI: 10.1046/j.1365-8711.2000.03075.x.

[Cow11]   G. Cowan et al. "Asymptotic formulae for likelihood-based tests of new physics". In: *The European Physical Journal C* 71.2 (2011), pp. 1–19. DOI: 10.1140/epjc/s10052-011-1554-0.

[Cow56]   C. L. Cowan et al. "Detection of the Free Neutrino: a Confirmation". In: *Science* 124.3212 (1956), pp. 103–104. DOI: 10.1126/science.124.3212.103.

[Da54]   R. H. Dalitz. "Decay of τ Mesons of Known Charge". In: *Phys. Rev.* 94 (May 1954), pp. 1046–1051. DOI: 10.1103/PhysRev.94.1046.

[Dan62]   G. Danby, J.-M. Gaillard, K. Goulianos, et al. "Observation of High-Energy Neutrino Reactions and the Existence of Two Kinds of Neutrinos". In: *Phys. Rev. Lett.* 9 (1962), pp. 36–44. DOI: 10.1103/PhysRevLett.9.36.

[Dav68]   R. Davis, D. S. Harmer, and K. C. Hoffman. "Search for Neutrinos from the Sun". In: *Phys. Rev. Lett.* 20 (1968), pp. 1205–1209. DOI: 10.1103/PhysRevLett.20.1205.

[Dec89]   D. Decamp et al. "Determination of the Number of Light Neutrino Species". In: *Phys. Lett.* B231 (1989), pp. 519–529. DOI: 10.1016/0370-2693(89)90704-1.

[Des19]   M. Descher. "High rate systematic effects for keV sterile neutrino searches at KATRIN". MA thesis. Karlsruher Institut für Technologie, 2019.

[Dir27]   P. A. M. Dirac and N. H. D. Bohr. "The quantum theory of the emission and absorption of radiation". In: *Proceedings of the Royal Society of London. Series A, Containing Papers of a Mathematical and Physical Character* 114.767 (1927), pp. 243–265. DOI: 10.1098/rspa.1927.0039.

[Dol16]   K. Dolde. "Detector and read-out development to search for sterile neutrinos with KATRIN". MA thesis. Karlsruher Institut für Technologie, 2016.

[Dol17]   K. Dolde, S. Mertens, D. Radford, et al. "Impact of ADC non-linearities on the sensitivity to sterile keV neutrinos with a KATRIN-like experiment". In: *Nuclear Instruments and Methods in Physics Research Section A: Accelerators, Spectrometers, Detectors and Associated Equipment* 848 (2017), pp. 127–136. DOI: 10.1016/j.nima.2016.12.015.

[Dre13]   M. Drews. "The phenomenology of right handed neutrinos". In: *International Journal of Modern Physics E* 22.08 (2013), p. 1330019. DOI: 10.1142/S0218301313300191.

[Dre19]   M. Drewes. "Auf dem Weg zu neuen Ufern". In: *Physik Journal* 18, Nr. 2 (2019).

[Eck19]   G. Ecker. *Particles, Fields, Quanta: From Quantum Mechanics to the Standard Model of Particle Physics.* Springer International Publishing, 2019. ISBN: 978-3-030-14479-1. DOI: 10.1007/978-3-030-14479-1_1.

[Ell17]   E. Ellinger, N. Haußmann, K. Helbing, et al. "Monitoring the KATRIN source properties within the beamline". In: *Journal of Physics: Conference Series* 888 (Sept. 2017), p. 012229. DOI: 10.1088/1742-6596/888/1/012229.

[Eno14]   S. Enomoto. *Simple Analytical Models of Signal Pile-up.* Tech. rep. 2014.

[Eno19]   S. Enomoto. *Detector Count Corrections for First Tritium.* Tech. rep. 2019.

[Erh14]   M. Erhard, S. Bauer, A. Beglarian, et al. "High-voltage monitoring with a solenoid retarding spectrometer at the KATRIN experiment". In: *Journal of Instrumentation* 9.06 (June 2014), P06022–P06022. DOI: 10.1088/1748-0221/9/06/p06022.

[Erh16]   M. G. Erhard. "Influence of the magnetic field on the transmission characteristics and the neutrino mass systematic of the KATRIN experiment". PhD thesis. Karlsruhe Institute of Technology, 2016. DOI: 10.5445/IR/1000065003.

[Erh18]   M. Erhard, J. Behrens, S. Bauer, et al. "Technical design and commissioning of the KATRIN large-volume air coil system". In: *Journal of Instrumentation* 13.02 (Feb. 2018), P02003–P02003. DOI: 10.1088/1748-0221/13/02/p02003.

[Est19]   I. Esteban, M. C. Gonzalez-Garcia, A. Hernandez-Cabezudo, et al. "Global analysis of three-flavour neutrino oscillations: synergies and tensions in the determination of θ_23, δ_{CP}, and the mass ordering". In: *Journal of High Energy Physics* 2019.1 (Jan. 2019), p. 106. DOI: 10.1007/JHEP01(2019)106.

[Fab76] S. M. Faber and R. E. Jackson. "Velocity dispersions and mass-to-light ratios for elliptical galaxies". In: *The Astrophysical Journal* 204 (Mar. 1976), pp. 668–683. DOI: 10.1086/154215.

[Fan47] U. Fano. "Ionization Yield of Radiations. II. The Fluctuations of the Number of Ions". In: *Phys. Rev.* 72 (1947), pp. 26–29. DOI: 10.1103/PhysRev.72.26.

[Fer34] E. Fermi. "Versuch einer Theorie der β-Strahlen. I". In: *Zeitschrift für Physik* 88.3 (1934), pp. 161–177. DOI: 10.1007/BF01351864.

[Fer50] E. Fermi. *Nuclear Physics*. University of Chicago Press, 1950. ISBN: 978-0226243658.

[Fey58] R. P. Feynman and M. Gell-Mann. "Theory of the Fermi Interaction". In: *Phys. Rev.* 109 (Jan. 1958), pp. 193–198. DOI: 10.1103/PhysRev.109.193.

[Fis14] S. Fischer. "Commissioning of the KATRIN Raman system and durability studies of optical coatings in glove box and tritium atmospheres". PhD thesis. Karlsruhe Institut für Technologie, 2014. DOI: 10.5445/IR/1000043697.

[Fla03] B. Flatt and J. Wolf. "Design of the KATRIN pre-spectrometer". In: *Nuclear Physics B - Proceedings Supplements* 118 (2003), p. 483. DOI: 10.1016/S0920-5632(03)01373-2.

[Fuk03] M. Fukugita and T. Yanagida. *Physics of Neutrinos*. Springer-Verlag Berlin Heidelberg GmbH, 2003. ISBN: 978-3-642-07851-4.

[Fuk98] Y. Fukuda et al. "Evidence for Oscillation of Atmospheric Neutrinos". In: *Phys. Rev. Lett.* 81 (1998), pp. 1562–1567. DOI: 10.1103/PhysRevLett.81.1562.

[Fur17] D. Furse, S. Groh, N. Trost, et al. "Kassiopeia: a modern, extensible C++ particle tracking package". In: *New Journal of Physics* 19.5 (May 2017), p. 053012. DOI: 10.1088/1367-2630/aa6950.

[Gan16] A. Gando, Y. Gando, T. Hachiya, et al. "Search for Majorana Neutrinos Near the Inverted Mass Hierarchy Region with KamLAND-Zen". In: *Phys. Rev. Lett.* 117 (Aug. 2016), p. 082503. DOI: 10.1103/PhysRevLett.117.082503.

[Gar57] R. L. Garwin, L. M. Lederman, and M. Weinrich. "Observations of the Failure of Conservation of Parity and Charge Conjugation in Meson Decays: the Magnetic Moment of the Free Muon". In: *Phys. Rev.* 105 (Feb. 1957), pp. 1415–1417. DOI: 10.1103/PhysRev.105.1415.

[Gat84] E. Gatti and P. Rehak. "Semiconductor drift chamber — An application of a novel charge transport scheme". In: *Nuclear Instruments and Methods in Physics Research* 225.3 (1984), pp. 608–614. DOI: 10.1016/0167-5087(84)90113-3.

[Gat87] E. Gatti, A. Longoni, P. Rehak, et al. "Dynamics of electrons in drift detectors". In: *Nuclear Instruments and Methods in Physics Research Section A: Accelerators, Spectrometers, Detectors and Associated Equipment* 253.3 (1987), pp. 393–399. DOI: 10.1016/0168-9002(87)90522-5.

[Gem01]   H. Gemmeke. *The Auger fluorescence detector electronics*. 27th Internat.Cosmic Ray Conf., Hamburg, August 7-15, 2001 ; ICRC 2001 Katlenburg-Lindau : Copernicus Ges., 2001 CD-ROM. 51.02.04; LK 01. 2001.

[Ger22]   W. Gerlach and O. Stern. "Der experimentelle Nachweis der Richtungsquantelung im Magnetfeld". In: *Zeitschrift für Physik* 9.1 (Dec. 1922), pp. 349–352. DOI: 10.1007/BF01326983.

[Gil10]   W. Gil, J. Bonn, B. Bornschein, et al. "The Cryogenic Pumping Section of the KATRIN Experiment". In: *IEEE Transactions on Applied Superconductivity* 20.3 (2010), pp. 316–319. DOI: 10.1109/TASC.2009.2038581.

[Gla59]   S. L. Glashow. "The renormalizability of vector meson interactions". In: *Nucl. Phys.* 10 (1959), pp. 107–117. DOI: 10.1016/0029-5582(59)90196-8.

[Glu13]   F. Glück, G. Drexlin, B. Leiber, et al. "Electromagnetic design of the large-volume air coil system of the KATRIN experiment". In: *New Journal of Physics* 15.8 (2013), p. 083025. DOI: 10.1088/1367-2630/15/8/083025.

[Gol58]   M. Goldhaber, L. Grodzins, and A. W. Sunyar. "Helicity of Neutrinos". In: *Phys. Rev.* 109 (Feb. 1958), pp. 1015–1017. DOI: 10.1103/PhysRev.109.1015.

[Gro11]   S. Grohmann et al. "Precise temperature measurement at 30 K in the KATRIN source cryostat". In: *Cryogenics* 51.8 (2011), pp. 438–445. DOI: 10.1016/j.cryogenics.2011.05.001.

[Gro15]   S. Groh. "Modeling of the response function and measurement of transmission properties of the KATRIN experiment". PhD thesis. Karlsruher Institut für Technologie, 2015. DOI: 10.5445/IR/1000046546.

[Hac15]   M. Hackenjos. "Die differentielle Pumpstrecke des KATRIN-Experiments- Inbetriebnahme und Charakterisierung des supraleitenden Magnetsystems". MA thesis. Karlsruhe Institut für Technologie, 2015.

[Hac17]   M. T. Hackenjos. "KATRIN "First Light" - Commissioning and Modelling of the Beamline". PhD thesis. Karlsruhe Institute of Technology, 2017. DOI: 10.5445/IR/1000078933.

[Han17]   V. Hannen, I. Heese, C. Weinheimer, et al. "Deconvolution of the energy loss function of the KATRIN experiment". In: *Astroparticle Physics* 89 (2017), pp. 30–38. DOI: 10.1016/j.astropartphys.2017.01.010.

[Has73]   F. J. Hasert, S. Kabe, W. Krenz, et al. "Observation of neutrino-like interactions without muon or electron in the gargamelle neutrino experiment". In: *Physics Letters B* 46.1 (1973), pp. 138–140. DOI: 10.1016/0370-2693(73)90499-1.

[Hei25]   W Heisenberg. "Über quantentheoretische Umdeutung kinematischer und mechanischer Beziehungen". In: *Zeitschrift für Physik* 33 (July 1925), pp. 879–893.

[Hin12] G. F. Hinshaw, D. Larson, E. Komatsu, et al. "Nine-year Wilkinson Microwave Anisotropy Probe (WMAP) Observations: Cosmological Results". In: 208.2 (Sept. 2013), p. 19. DOI: 10.1088/0067-0049/208/2/19.

[Hir87] K. Hirata, T. Kajita, M. Koshiba, et al. "Observation of a neutrino burst from the supernova SN1987A". In: *Phys. Rev. Lett.* 58 (Apr. 1987), pp. 1490–1493. DOI: 10.1103/PhysRevLett.58.1490.

[Hub15] A. Huber. "Search for keV-Scale Sterile Neutrinos with KATRIN". MA thesis. Karlsruher Institut für Technologie, 2015.

[Hub20] A. Huber. "Analysis of first KATRIN data and searches for keV-scale sterile neutrinos (working title)". PhD thesis. Karlsruhe Institute of Technology, 2020.

[Hub29] E. Hubble. "A relation between distance and radial velocity among extragalactic nebulae". In: *Proceedings of the National Academy of Sciences* 15.3 (1929), pp. 168–173. DOI: 10.1073/pnas.15.3.168.

[Ini07] K. Iniewski, H. Chen, G. Bindley, et al. "Modeling charge-sharing effects in pixellated CZT detectors". In: 6 (Oct. 2007), pp. 4608–4611. DOI: 10.1109/NSSMIC.2007.4437135.

[Jan15] A. Jansen. "The cryogenic pumping section of the KATRIN experiment - Design studies and experiments for the commissioning". PhD thesis. Karlsruhe Institut für Technologie, 2015. DOI: 10.5445/IR/1000047146.

[Jeo19] Japan JEOL Ltd. *Specification: JSM-IT300 InTouchScope^{TM} Scanning Electron Microscope*. Tech. rep. 2019.

[Jun08] H. Junde. "Nuclear Data Sheets for $A = 55$". In: *Nuclear Data Sheets* 109 (Apr. 2008), pp. 787–942. DOI: 10.1016/j.nds.2008.03.001.

[Kas98] V. Kasperovich and V. V. Kresin. "Ultraviolet photoabsorption spectra of silver and gold nanoclusters". In: *Philosophical Magazine B* 78.4 (1998), pp. 385–396. DOI: 10.1080/13642819808206735.

[Kat20] A. Huber, C. Karl, C. Kohler, et al. *Search for keV-scale Sterile Neutrinos with the First Tritium Campaign of KATRIN*. unpublished manuscript. 2020.

[Kim15] USA Kimball Physics Inc. *Specification: EGF-3104 electron gun and EGPS-3104 power supply*. Tech. rep. 2015.

[Kle14] M. Kleesiek. "A Data-Analysis and Sensitivity-Optimization Framework for the KATRIN Experiment". PhD thesis. Karlsruhe Institut für Technologie, 2014. DOI: 10.5445/IR/1000043301.

[Kle19] M. Kleesiek, J. Behrens, G. Drexlin, et al. "β-Decay spectrum, response function and statistical model for neutrino mass measurements with the KATRIN experiment". In: *The European Physical Journal C* 79.3 (Mar. 2019), p. 204. DOI: 10.1140/epjc/s10052-019-6686-7.

[Kle19b]   M. Klein. "Tritium ions in KATRIN: blocking, removal and detection". PhD thesis. Karlsruhe Institute of Technology, 2019. DOI: 10.5445/IR/1000093526.

[Kly99]   A. Klypin et al. "Where Are the Missing Galactic Satellites?" In: *The Astrophysical Journal* 522 (1999), p. 82. DOI: 10.1086/307643.

[Kod01]   K. Kodama et al. "Observation of tau neutrino interactions". In: *Physics Letters B* 504.3 (2001), pp. 218–224. DOI: 10.1016/S0370-2693(01)00307-0.

[Koe19]   L. Köllenberger. "Model Building and Search for keV-Scale Sterile Neutrinos with the KATRIN-Experiment". MA thesis. Karlsruhe Institute of Technology, 2019.

[Kor16]   M. Korzeczek. "eV- & keV-sterile neutrino studies with KATRIN". MA thesis. Karlsruher Institut für Technologie, 2016.

[Kos12]   A. Kosmider. "Tritium Retention Techniques in the KATRIN Transport Section and Commissioning of its DPS2-F Cryostat". PhD thesis. Karlsruhe Institute of Technology, 2012. DOI: 10.5445/IR/1000028959.

[Kra05]   Ch. Kraus, B. Bornschein, L. Bornschein, et al. "Final results from phase II of the Mainz neutrino mass searchin tritium β decay". In: *The European Physical Journal C - Particles and Fields* 40.4 (2005), pp. 447–468. DOI: 10.1140/epjc/s2005-02139-7.

[Kra16]   M. Kraus. "Energy-Scale Systematics at the KATRIN Main Spectrometer". PhD thesis. Karlsruhe Institute of Technology, 2016. DOI: 10.5445/IR/1000054447.

[Kuc18]   L. Kuckert, F. Heizmann, G. Drexlin, et al. "Modelling of gas dynamical properties of the Katrin tritium source and implications for the neutrino mass measurement". In: *Vacuum* 158 (2018), pp. 195–205. DOI: 10.1016/j.vacuum.2018.09.036.

[Las15]   T. Lasserre. *Covariance matrix approach*. Tech. rep. 2015.

[Lec01]   P. Lechner, C. Fiorini, R. Hartmann, et al. "Silicon drift detectors for high count rate X-ray spectroscopy at room temperature". In: *Nuclear Instruments and Methods in Physics Research Section A: Accelerators, Spectrometers, Detectors and Associated Equipment* 458.1 (2001), pp. 281–287. DOI: 10.1016/S0168-9002(00)00872-X.

[Lec96]   P. Lechner, S. Eckbauer, R. Hartmann, et al. "Silicon drift detectors for high resolution room temperature X-ray spectroscopy". In: *Nuclear Instruments and Methods in Physics Research Section A: Accelerators, Spectrometers, Detectors and Associated Equipment* 377.2 (Aug. 1996), pp. 346–351. DOI: 10.1016/0168-9002(96)00210-0.

[Lec98]   P. Lechner. "Zur Ionisationsstatistik in Silicium". PhD thesis. Technische Universität München, 1998.

[Lee56]   T. D. Lee and C. N. Yang. "Question of Parity Conservation in Weak Interactions". In: *Phys. Rev.* 104 (Oct. 1956), pp. 254–258. DOI: 10.1103/PhysRev.104.254.

[Lem27]   G. Lemaître. "Un Univers homogène de masse constante et de rayon croissant rendant compte de la vitesse radiale des nébuleuses extra-galactiques". In: *Annales de la Société Scientifique de Bruxelles* 47 (Jan. 1927), pp. 49–59.

[Let18]   J. Letnev, W. Hazenbiller, A. Osipowicz, et al. "Technical design and commissioning of a sensor net for fine-meshed measuring of the magnetic field at the KATRIN spectrometer". In: *Journal of Instrumentation* 13.08 (Aug. 2018), T08010–T08010. DOI: 10.1088/1748-0221/13/08/t08010.

[Lok15]   A. V. Lokhov and F. V. Tkachov. "Confidence intervals with a priori parameter bounds". In: *Physics of Particles and Nuclei* 46.3 (May 2015), pp. 347–365. DOI: 10.1134/S1063779615030089.

[Lor02]   Thomas J. Loredo and Donald Q. Lamb. "Bayesian analysis of neutrinos observed from supernova SN 1987A". In: *Phys. Rev. D* 65 (Feb. 2002), p. 063002. DOI: 10.1103/PhysRevD.65.063002.

[Lou19]   A. Loureiro, A. Cuceu, F. B. Abdalla, et al. "Upper Bound of Neutrino Masses from Combined Cosmological Observations and Particle Physics Experiments". In: *Phys. Rev. Lett.* 123 (Aug. 2019), p. 081301. DOI: 10.1103/PhysRevLett.123.081301.

[Lov12]   M. R. Lovell, V. Eke, C. S. Frenk, et al. "The Haloes of Bright Satellite Galaxies in a Warm Dark Matter Universe". In: *Monthly Notices of the Royal Astronomical Society* 420 (2012), pp. 2318–2324. DOI: 10.1111/j.1365-2966.2011.20200.x.

[Luc00]   "Comprehensive Review and Critical Evaluation of the Half-Life of Tritium". In: *J. Res. Natl. Inst. Stand. Technol.* 105(4) (2000), pp. 541–9. DOI: 10.6028/jres.105.043.

[Lut07]   Gerhard Lutz. *Semiconductor Radiation Detectors : Device Physics.* Springer Berlin Heidelberg, 2007. ISBN: 9783540716792. DOI: 10.1007/978-3-540-71679-2.

[Mak62]   Z. Maki, M. Nakagawa, and S. Sakata. "Remarks on the Unified Model of Elementary Particles". In: *Progress of Theoretical Physics* 28 (1962), pp. 870–880. DOI: 10.1143/PTP.28.870.

[Mat02]   K. Mathiesona et al. "Charge sharing in silicon pixel detectors". In: *Nuclear Instruments and Methods in Physics Research Section A: Accelerators, Spectrometers, Detectors and Associated Equipment* 487 (2002), pp. 113–122. DOI: 10.1016/S0168-9002(02)00954-3.

[Mer15a]   S. Mertens, T. Lasserre, S. Groh, et al. "Sensitivity of next-generation tritium beta-decay experiments for keV-scale sterile neutrinos". In: *Journal of Cosmology and Astroparticle Physics* 2015.02 (2015), p. 020. DOI: 10.1088/1475-7516/2015/02/020.

[Mer15b]   S. Mertens, K. Dolde, M. Korzeczek, et al. "Wavelet approach to search for sterile neutrinos in tritium β-decay spectra". In: *Phys. Rev. D* 91 (2015), p. 042005. DOI: 10.1103/PhysRevD.91.042005.

[Mer19]   S. Mertens, A. Alborini, K. Altenmüller, et al. "A novel detector system for KATRIN to search for keV-scale sterile neutrinos". In: *Journal of Physics G: Nuclear and Particle Physics* 46.6 (May 2019), p. 065203. DOI: 10.1088/1361-6471/ab12fe.

[Mic06]   D. G. Michael, P. Adamson, T. Alexopoulos, et al. "Observation of Muon Neutrino Disappearance with the MINOS Detectors in the NuMI Neutrino Beam". In: *Phys. Rev. Lett.* 97 (Nov. 2006), p. 191801. DOI: 10.1103/PhysRevLett.97.191801.

[Mik86]   S. P. Mikheyev and A. Y. Smirnov. "Resonance Amplification of Oscillations in Matter and Spectroscopy of Solar Neutrinos". In: *Soviet Journal of Nuclear Physics* 42 (1985), pp. 913–917. DOI: 10.1007/BF02508049.

[Mye15]   E. G. Myers et al. "Atomic Masses of Tritium and Helium-3". In: *Phys. Rev. Lett.* 114.1 (2015), p. 013003. DOI: 10.1103/PhysRevLett.114.013003.

[Noe18]   E. Noether. "Invariante Variationsprobleme". In: *Nachrichten von der Gesellschaft der Wissenschaften zu Göttingen, Mathematisch-Physikalische Klasse* 1918 (1918), pp. 235–257.

[Obe19]   J. Oberauer and Lothar Oberauer. *Neutrinophysik*. Springer Spectrum, 2019. ISBN: 978-3-662-59335-6.

[Osi01]   A. Osipowicz et al. "KATRIN: A Next generation tritium beta decay experiment with sub-eV sensitivity for the electron neutrino mass. Letter of intent". In: (Sept. 2001). arXiv: hep-ex/0109033 [hep-ex].

[Osi12]   A Osipowicz et al. "A mobile magnetic sensor unit for the KATRIN main spectrometer". In: *Journal of Instrumentation* 7.06 (June 2012), T06002–T06002. DOI: 10.1088/1748-0221/7/06/t06002.

[Ott08]   E. W. Otten and C. Weinheimer. "Neutrino mass limit from tritium β decay". In: *Reports on Progress in Physics* 71.8 (July 2008), p. 086201. DOI: 10.1088/0034-4885/71/8/086201.

[Paa92]   G. Paál, I. Horváth, and B. Lukács. "Inflation and compactification from Galaxy redshifts?" In: *Astrophysics and Space Science* 191.1 (May 1992), pp. 107–124. DOI: 10.1007/BF00644200.

[Pau30]   W. Pauli. *Scientific Correspondence with Bohr, Einstein, Heisenberg a.o. Volume II: 1930–1939.* Meyenn, K.v., 1985. ISBN: 978-3-540-78801-0.

[Pon57]   B. Pontecorvo. "Mesonium and anti-mesonium". In: *Soviet Physics Journal of Experimental and Theoretical Physics* 6 (1957), p. 429.

[Pop00]   M. Popp. "Untersuchung und analytische Modellierung der Systemantwort von pn-CCD Detektoren". PhD thesis. Ludwig-Maximilians-Universität München, 2000.

[Pra12]   M. Prall, P. Renschler, F. Glück, et al. "The KATRIN pre-spectrometer at reduced filter energy". In: *New Journal of Physics* 14.7 (July 2012), p. 073054. DOI: 10.1088/1367-2630/14/7/073054.

[Pri15]   F. Priester, M. Sturm, and B. Bornschein. "Commissioning and detailed results of KATRIN inner loop tritium processing system at Tritium Laboratory Karlsruhe". In: *Vacuum* 116 (2015), pp. 42–47. DOI: 10.1016/j.vacuum.2015.02.030.

[Rei13]   J. C. Reich. "Magnetic Field Inhomogeneities and Their Influence on Transmission and Background at the KATRIN Main Spectrometer". PhD thesis. Karlsruhe Institute of Technology, 2013. DOI: 10.5445/IR/1000033076.

[Ren11]   P. Renschler. "KESS - A new Monte Carlo simulation code for low-energy electron interactions in silicon detectors". PhD thesis. Karlsruher Institut für Technologie, 2011. DOI: 10.5445/IR/1000024959.

[Rob91]   R. G. H. Robertson, T. J. Bowles, G. J. Stephenson, et al. "Limit on $\bar{\nu}_e$ mass from observation of the β decay of molecular tritium". In: *Phys. Rev. Lett.* 67 (Aug. 1991), pp. 957–960. DOI: 10.1103/PhysRevLett.67.957.

[Rod52]   G. W. Rodeback and J. S. Allen. "Neutrino Recoils Following the Capture of Orbital Electrons in A^{37}". In: *Phys. Rev.* 86 (May 1952), pp. 446–450. DOI: 10.1103/PhysRev.86.446.

[Roe13]   M. Röllig, F. Priester, M. Babutzka, et al. "Activity monitoring of a gaseous tritium source by beta induced X-ray spectrometry". In: *Fusion Engineering and Design* 88.6–8 (2013), pp. 1263–1266. DOI: 10.1016/j.fusengdes.2012.11.001.

[Roe19]   C. Röttele. "Tritium suppression factor of the KATRIN transport section". PhD thesis. Karlsruhe Institute of Technology, 2019. DOI: 10.5445/IR/1000096733.

[Rut11]   E. Rutherford. "LXXIX. The scattering of α and β particles by matter and the structure of the atom". In: *The London, Edinburgh, and Dublin Philosophical Magazine and Journal of Science* 21.125 (1911), pp. 669–688. DOI: 10.1080/14786440508637080.

[Sak67]   A. D. Sakharov. "Violation of CP Invariance, C asymmetry, and baryon asymmetry of the universe". In: *Pisma Zh. Eksp. Teor. Fiz.* 5 (1967), pp. 32–35. DOI: 10.1070/PU1991v034n05ABEH002497.

[Sal59]   A. Salam and J. C. Ward. "Weak and electromagnetic interactions". In: *Il Nuovo Cimento (1955-1965)* 11.4 (Feb. 1959), pp. 568–577. DOI: 10.1007/BF02726525.

[Sch13]   M. Schlösser, H. Seitz, S. Rupp, et al. "In-Line Calibration of Raman Systems for Analysis of Gas Mixtures of Hydrogen Isotopologues with Sub-Percent Accuracy". In: *Analytical Chemistry* 85.5 (2013), pp. 2739–2745. DOI: 10.1021/ac3032433.

[Sch14]   J. Schwarz. "The detector system of the KATRIN experiment - Implementation and first measurements with the spectrometer". PhD thesis. Karlsruhe Institut für Technologie, 2014. DOI: 10.5445/IR/1000042772.

[Sch16b]   K. Schönung. "Development of a Rear Wall for the KATRIN Rear Section and investigation of tritium compatibility of Rear Section components". PhD thesis. Karlsruhe Institute of Technology, 2016.

[Sch26]   E. Schrödinger. "Quantisierung als Eigenwertproblem". In: *Annalen der Physik* 384.4 (1926), pp. 361–376. DOI: 10.1002/andp.19263840404.

[Sei19]   H. Seitz-Moskaliuk. "Characterisation of the KATRIN tritium source and evaluation of systematic effects". PhD thesis. Karlsruher Institut für Technologie, 2019. DOI: 10.5445/IR/1000090748.

[Sha13]   Mikhail Shaposhnikov. "Neutrino physics within and beyond the three flavour oscillation". In: *Journal of Physics: Conference Series* 408 (2013), p. 012015. DOI: 10.1088/1742-6596/408/1/012015.

[Sie19]   D. Siegmann. "Investigation of the Detector Response to Electrons of the TRISTAN Prototype Detectors". MA thesis. Technical University of Munich, 2019.

[Sko06]   C. Skordis et al. "Large Scale Structure in Bekenstein's Theory of Relativistic Modified Newtonian Dynamics". In: *Phys. Rev. Lett.* 96 (Jan. 2006), p. 011301. DOI: 10.1103/PhysRevLett.96.011301.

[Sle15]   M. Slezák. "Monitoring of the energy scale in the KATRIN neutrino experiment". PhD thesis. Czech Academy of Sciences, 2015.

[Stu10]   M. Sturm. "Aufbau und Test des Inner-Loop-Systems der Tritiumquelle von KATRIN". PhD thesis. Karlsruher Institut für Technologie, 2010. DOI: 10.5445/IR/1000019355.

[Sud94]   E. C. G. Sudarshan and R. E. Marshak. "Origin of the Universal V-A theory". In: *AIP Conference Proceedings* 300.1 (1994), pp. 110–124. DOI: 10.1063/1.45454.

[Tan18]   M. Tanabashi, K. Hagiwara, K. Hikasa, et al. "Review of Particle Physics". In: *Phys. Rev. D* 98 (Aug. 2018), p. 030001. DOI: 10.1103/PhysRevD.98.030001.

[Tay98]   A. N. Taylor, S. Dye, T. J. Broadhurst, et al. "Gravitational Lens Magnification and the Mass of Abell 1689". In: *The Astrophysical Journal* 501.2 (July 1998), pp. 539–553. DOI: 10.1086/305827.

[Ter03]   Dick Teresi. *Lost Discoveries: The Ancient Roots of Modern Science–From the Babylonians to the Maya*. Simon & Schuster, 2003. ISBN: 978-0-743-24379-7.

[Tho97]   J. J. Thomson. "Cathode Rays". In: *Philosophical Magazine* 44 (1897), p. 293.

[Thu09]   T. Thümmler, R. Marx, and C. Weinheimer. "Precision high voltage divider for the KATRIN experiment". In: *New Journal of Physics* 11.10 (Oct. 2009), p. 103007. DOI: 10.1088/1367-2630/11/10/103007.

[Tro19]   N. R.-M. Trost. "Modeling and measurement of Rydberg-State mediated Background at the KATRIN Main Spectrometer". PhD thesis. Karlsruhe Institute of Technology, 2019.

[Ubi09]   M. Ubieto-Díaz, D. Rodríguez, S. Lukic, et al. "A broad-band FT-ICR Penning trap system for KATRIN". In: *International Journal of Mass Spectrometry* 288.1–3 (2009), pp. 1–5. DOI: 10.1016/j.ijms.2009.07.003.

[Urb19]   Korbinian Urban. "Application of a TRISTAN Silicon Drift Detector as Forward Beam Monitor in KATRIN". MA thesis. Technical University of Munich, 2019.

[Val10]   K. Valerius. "The wire electrode system for the KATRIN main spectrometer". In: *Progress in Particle and Nuclear Physics* 64.2 (2010), pp. 291–293. DOI: 10.1016/j.ppnp.2009.12.032.

[Vel19]   A. Veloni, N. Miridakis, and E. Boukouvala. *Digital and Statistical Signal Processing*. CRC Press, 2019. ISBN: 9781138580060.

[Wan09]   N. Wandkowsky. "Design and Background Simulations for the KATRIN Main Spectrometer and Air Coil System". MA thesis. Karlsruhe Institut für Technologie, 2009.

[Wei67]   S. Weinberg. "A Model of Leptons". In: *Phys. Rev. Lett.* 19 (Nov. 1967), pp. 1264–1266. DOI: 10.1103/PhysRevLett.19.1264.

[Wie97]   E. Wiechert. "Schriften". In: *Physikalisch-Ökonomischen Gesellschaft zu Königsberg* 38 Jg. No. 1 (1897), pp. 3–6.

[Wol78]   L. Wolfenstein. "Neutrino oscillations in matter". In: *Phys. Rev. D* 17 (1978), pp. 2369–2374. DOI: 10.1103/PhysRevD.17.2369.

[Wu57]   C. S. Wu, E. Ambler, R. W. Hayward, et al. "Experimental Test of Parity Conservation in Beta Decay". In: *Phys. Rev.* 105 (Feb. 1957), pp. 1413–1415. DOI: 10.1103/PhysRev.105.1413.

[XGL18]   XGLab S.R.L. *User manual of DANTE Digital Pulse Processor Board Version: DPP-4552, revision: 2.2*. Tech. rep. Apr. 2018.

[Zbo13]   M. Zbořil, S. Bauer, M. Beck, et al. "Ultra-stable implanted 83 Rb/ 83 m Kr electron sources for the energy scale monitoring in the KATRIN experiment". In: *Journal of Instrumentation* 8.03 (2013), P03009. DOI: 10.1088/1748-0221/8/03/P03009.

[Zub11]   K. Zuber. *Neutrino Physics*. CRC Press LLC, 2011. ISBN: 978-1-420-06472-8.

[Zwi33]   F. Zwicky. "Die Rotverschiebung von extragalaktischen Nebeln". In: *Helvetica Physica Acta* 6 (Jan. 1933), pp. 110–127. DOI: 10.1007/s10714-008-0707-4.